December 2019

Experimental, Theoretical and Numerical Evaluation of Wicking Models for Liquid Imbibition in Dry Porous Wicks

Mohammad Amin Faghihi Zarandi
University of Wisconsin-Milwaukee

EXPERIMENTAL, THEORETICAL AND NUMERICAL EVALUATION OF WICKING MODELS FOR LIQUID IMBIBITION IN DRY POROUS WICKS

by

Mohammad Amin Faghihi Zarandi

A Dissertation Submitted in

Partial Fulfillment of the

Requirements for the Degree of

Doctor of Philosophy

in Engineering

at

The University of Wisconsin- Milwaukee

December 2019

ABSTRACT

EXPERIMENTAL, THEORETICAL, AND NUMERICAL EVALUATION OF WICKING MODELS FOR LIQUID IMBIBITION IN DRY POROUS WICKS

by

Mohammad Amin Faghihi Zarandi

University of Wisconsin- Milwaukee, 2019

Under the Supervision of Professor Krishna M. Pillai

Nowadays commercial wicks are utilized by consumer product companies in several important commercial applications including Tiki® Brand torches, the passive lubricants of machine gears, propellant management device, and fragrance dispersion units. Spontaneous imbibition of a liquid into porous wicks, also called wicking, is modeled using the single-phase Darcy's law after assuming a sharp flow-front marked by full saturation behind the front. An analytical expression for the height of the wicking flow-front as a function of time is tested through comprehensive experiments using different wicks and an oil as the wicking liquid. We proposed a model based on sharp liquid-front where a good match with the experimental data was achieved. However the proposed model based on the sharp liquid-front fails to account for partial saturations in the wicks. As a result we applied the Richards equation to predict partial liquid saturations in wicks where the equation is solved numerically in 2-D using COMSOL and analytically in 1-D using Mathematica for glass-fiber wicks after treating them as transversely-isotropic porous media. As a novel

contribution, the relative permeability and capillary pressure are determined directly from pore-scale simulations in wick microstructure using the state-of-the-art software GeoDict. The saturation along the wick length is determined experimentally through a new liquid-N_2 based freezing technique. After including the gravity effect, good agreements between the numerical/analytical predictions and experimental results are achieved in saturation distributions. We also validated the Richards equation based model while predicting absorbed liquid-mass into the wick as function of time.

A series of wicking experiments with wicks procured from our industrial partners were conducted where the use of a dyed liquid revealed essentially three types of macroscopic (visual) fronts—sharp, semi-sharp, and diffuse. The particulate wicks (i.e. the wicks formed by sintering polymer beads) invariably formed sharp fronts, while the fibrous wicks (i.e. wicks formed from fibers) formed either semi-sharp or diffuse fronts. The porosity was also found to play a role—the lower-porosity fibrous wicks displayed semi-sharp fronts, while the higher-porosity fibrous wicks caused the fronts to be diffuse. A study of SEM (Scanning Electron Microscopy) micrographs revealed that the latter behavior was caused by clustering of fibers thus leading to the formation of an inhomogeneous porous medium (perhaps promoting finger formation on micro-fronts). The experiments also revealed that the visually-observed fronts, for most parts, achieved a good match with the fronts estimated through the sharp-front mass gain formula. (Such a match was found to be lacking in the fibrous wicks displaying diffuse fronts.) We also investigated two parameters of interest to the users of wicks: 1) steady-state (SS) height reached by the visual front at very large times, 2) the liquid supply rate when the front is near the top. The parameters estimated using our sharp-front model matched well with the experimentally-observed ones.

Finally we conducted a CFD simulation using FLUENT where the flow of wicking liquid

through a 2D microstructure made of ellipses of varying aspect ratio was modeled. A series of microstructures were created by varying the ellipse aspect ratio from 1:1 (20*20 μm) to 1:64 (20*1280 μm), with lower values representing particulate porous media and the higher values representing fibrous porous media. To study the effect of porosity, two values of 50% and 70% were considered. The flow simulation in particulate porous media produced somewhat even micro-fronts that indicate a flat visual (macroscopic) front. On the other hand, simulations in fibrous porous media produced highly uneven micro-fronts that point to a semi-sharp or diffuse visual fronts. Increasing the porosity results in clustering of solid phase and leads to further increase in the unevenness of micro-fronts, thus pointing to purely diffuse visual fronts. The evolution of saturation plots along the flow direction, obtained using a grid superimposed on fluid distribution pictures, was also studied and the predictions matched our previous experimental and numerical observations, i.e., particulate media create sharp fronts while fibrous media create diffuse fronts.

TABLE OF CONTENTS

LIST OF FIGURES

LIST OF TABLES

LIST OF NOMENCLATURE

A_w= wick cross section area

B = Closure variable (2nd order tensor)

b = Closure variable (vector)

D = Modified diffusivity coefficient (m^2/s)

D_f = Diameter of fiber

D = Closure variable (2nd order tensor)

d = Closure variable (vector)

D_g= Diffusivity coefficient (m^2/s)

D_{ij}= Capillary diffusivity tensor

g = Acceleration due to gravity

h = Elevation (m)

h_f = height of the liquid front

H_{ss} = Steady State height (m)

I = Unity tensor

$\hat{\imath}, \hat{\jmath}, \hat{k}$=Unit vectors along the x, y, and z coordinate axes, respectively

K = Permeability of porous medium (m^2)

K_h = Hydraulic conductivity tensor for an anisotropic porous medium

k_r = Relative permeability of the wick

L = Length of the wick

l = lattice vector

m_{liq} = mass of absorbed liquid into the wick

m_{dry} = mass each part of the dry wick

n_{fs} = Unit vector normal to the liquid-solid interface

p = Hydrodynamic fluid pressure (Pa)

p_{atm}= Atmospheric pressure

p_s= Suction pressure

p_C = Capillary pressure

P= Modified pressure (Pa)

$\tilde{\mathbf{p}}_f$ = Pressure deviations

Q= Flow rate at the top of the wick

r_{fb}= Radius of fiber

R_w= Radius of the wicks

S_{fs} = Fluid entrance and exit areas of the REV

S_w = Saturation wetting phase

t = Time

V = Total volume of the wicks

V = Velocity

$\tilde{\mathbf{v}}_f$ = Velocity deviations

Greek Letters

Θ = Contact angle

μ = Viscosity of the liquid [kg/(m s)]

ε = Porosity of the wicks

γ = surface tension of the liquid (N/m)

ρ_{fbr} = density of glass fibers (kg/m3)

ρ_{liq} = density of the liquid (kg/m3)

ρ = Liquid density (kg/m3)

∇ = Gradient operator

Φ = An arbitrary function used for volume averaging

Subscripts

f = Liquid phase

s = Solid phase

ACKNOWLEDGMENTS

I would like to thank my advisor, Prof. Krishna M. Pillai for guiding, supporting, leading and encouraging me over the years. Prof. Pillai as a tremendous researcher, mentor and instructor has the attitude and the substance of a genius. He will be one of my best role models for a professional scholar. I hope that we could be as lively, enthusiastic, supporting, and energetic as he is. I also want to thank the members of my PhD committee Dr. Hector Bravo, Dr. Ilya Avdeev, Dr. Shangping Xu and Dr. Yongjin Sung for their helpful advice, brilliant comments, and suggestions in general.

Lastly and most importantly, my deepest gratitude goes to my family for their love and support. My lovely wife, Shiva Salehi, who has always supported and encouraged me, and sacrificed many things to be with me over this long journey. My parents, Mehdi Faghihi Zarandi and Zahra Ashrafzadeh, who have supported me from tens of thousands of miles away with their love and hearth warming messages.

Chapter 1: Introduction and Background

1-1 Introduction

Imbibition in a porous medium is defined as the displacement of a non-wetting fluid by a wetting one. Wicking is a special type of imbibition where a liquid displaces air in a dry porous medium under the driving force of the capillary suction pressure. Of the many methods available to model the wicking phenomenon mathematically [1], depending on the type of liquid front, the following three approaches are most popular due to their simplicity and ease in determining all of the necessary material parameters.

1-2 Wicking models

In the first, older method, the porous medium undergoing wicking is assumed to be as a wick of parallel capillary tubes aligned with the flow direction. This capillary-type modeling approach was first proposed by Lucas[2], Bell and Cameron [3], Washburn [4] and later adopted successfully by others [5-11]. They ignored the inertia and gravity effects and used the momentum balance equation to derive an analytical solution for the liquid-front height, h, as a function of time, t, in a vertical capillary tube [1, 12-14], and presented an equation for the relation between this height and time as

$$h = ct^n \qquad (1)$$

This theoretical relationship, called the Washburn equation (also known as the Lucas-Washburn equation), has the value of n to be 0.5 while c has been shown to be a function of various properties including surface tension, contact angle, and the hydraulic radius of capillaries. The accuracy of this equation can be gauged by the fact that the experimentally determined value of n has been

observed to be in the range 0.46 to 0.48 [15]. Several researchers [15-20] included the neglected physical effects, including the gravitational and inertial effects in the capillary model to modify it. Experimental research has demonstrated that the modified capillary model is more accurate than the traditional Washburn equation [17, 19-21]. Because of its long history, simplicity, and accuracy, the Washburn equation continues to enjoy the steady support of researchers, particularly among the chemistry and textile-based research communities.

Despite the popularity of the capillary model, it has a few drawbacks. One of its major deficiencies is that it is based on the Hagen–Poiseuille flow model of wick of parallel capillary tubes[22], which means that it is used to predict only one-dimensional (1D) wicking flows as the parallel capillary tubes are supposed to be aligned with the flow direction. As a result, it cannot predict two-dimensional (2D) or three-dimensional (3D) flows in wicks with complex shapes. The real intricate microstructure of a porous medium is substituted with an imaginary structure made from a wick of capillary tubes. Moreover, the different pores in a real medium are connected to each other, unlike the capillary models where the capillary tubes are not interconnected [22]. Therefore, this model will not represent the true circuitous, interconnected flows at pore scales seen in real porous media and hence will always require the use of some kind of additional fitting parameter such as the hydraulic radius or capillary diameter [22].

Another more recent (and scientifically more in step with the field of flow modeling in porous media) method to model wicking of liquids into porous media is based on using Darcy's law [23-27]. In 1856, Henry Darcy [28] reported his empirical formula for flow in a porous medium based on his investigation of the relationship between water, flow-rate through a sand column and the pressure gradient through a hydraulic resistance term. Darcy's law method proposed a simple relation between the average velocity of a liquid and the pressure gradient in a fully-saturated

porous medium [26]. The relatively recent method to model the wicking flow using Darcy's law are built on the assumption that a clearly-identifiable liquid front travels in the porous medium during wicking, and that saturation in the region behind the liquid-front is 100% (i.e., all the pore space is occupied by the wicking liquid) [29]. Pillai et al. continue to develop the Darcy's law–based model for predicting and modeling liquid absorption in porous media [20, 22, 30-32] . Furthermore, the application of Darcy's law allows researchers to model and predict the two-dimensional (2D) and three-dimensional (3D) wicking flows in intricately shaped wicks [31]. Some porous materials, consisting of elongated pores aligned in a certain direction, are characterized as anisotropic porous media. The examples of such media found in wicking applications include fiber mats made from unidirectional fibers, woven or stitched fabrics made from fiber wicks, and paper made from oriented fibers [1]. Once again, the Darcy's law based models are amenable to the prediction of wicking in such media.

Despite the sharp liquid-front assumption used in the derivations of the Washburn and Darcy's law-based equations, both have been shown to work quite well for 1D applications while the latter for 2D or 3D wicking flows [29, 33-35]. In contrast, both the Washburn's equation and Darcy's law based method are not applicable where a sharp liquid-front cannot be observed during wicking and the wetting of the wick is marked by partial saturation.

In 1931 Richards [36] proposed a model for diffusion of moisture in unsaturated regions of soil. On using Richards equation, partial saturation and multidimensional analysis can be done as this equation characterizes two-phase flow in porous media as a diffusive, continuum-based model [1]. By Applying Richards equation we can predict the diffusive saturation field throughout a porous medium as a function of time. The detail of this model will be presented in this thesis. Recently Gruener et al. [37] simulated the progress of water front in nanoporous glass (Vycor) by

using a pore network model where a *broadening/diffusing* of the front was observed. In order to have a model that mimics the characteristics of their medium, Gruener et al. modeled the medium by a network of capillaries of the same length but different radii, where they found that water moving faster through thin capillaries and hence creating a diffusive front. However, their computer simulation found the mean rise-level (the overall average) following the predictions of the Lucas-Washburn equation by being proportional to square root of time [38] [39] [40].

Chapter 2: Liquid Front Type Characterization

2-1 Introduction

Knowing the type liquid front is very important in proposing the correct type of governing equations for the wicking process. The type of liquid front helps us to adapt the most related and accurate governing equations. In addition, knowing the type liquid-front leads to an accurate study of the wicking process and to proposing correct parameters and dimensionless numbers related to the wicking process. During the spontaneous imbibition of a liquid into dry porous wicks, the liquid travels in the wicks in broadly two different forms: either with a sharp front, or with a diffusive front. In the sharp-front case, the saturation in the region immediately behind the liquid front can be approximated to be 100% (i.e., all the available pore space is occupied by the absorbed liquid) and this saturation precipitously drops to 0% (i.e., all the available pore space is occupied by air) in a very narrow region. In contrast, in the diffusive-front case, the wetting of the wick is marked by a zone of partial saturation (i.e., the saturation changing from 100% to 0% in a broad region). In this chapter, the main goal is investigating the type of front appearing in the considered wicks. Hence, we set up a wicking experiment in which we put the vertically-aligned wicks one by one in touch with a liquid dyed red.

2-2 Study of liquid fronts during the wicking process

In order to have a comprehensive and reliable investigation, we decided to study a relatively large sample of six (6) wicks made from the sintering of polymer beads (to be called sintered-beads wicks) and twelve (12) wicks made from fibers (to be referred to as fibrous wicks) shown in Figure 1. The former are named from **B1** to **B6** while the latter are named from **F1** to

F12[1]. The glass fiber wicks in Figure 1(a) to (h) were supplied by Lamplight Farm Inc. at Menomonee Falls, and the wicks (i) to (r) were supplied by S. C. Johnson at Racine during our collaboration with them.

[1] The names of the wicks and the test liquid will not be revealed due to the confidentiality agreements.

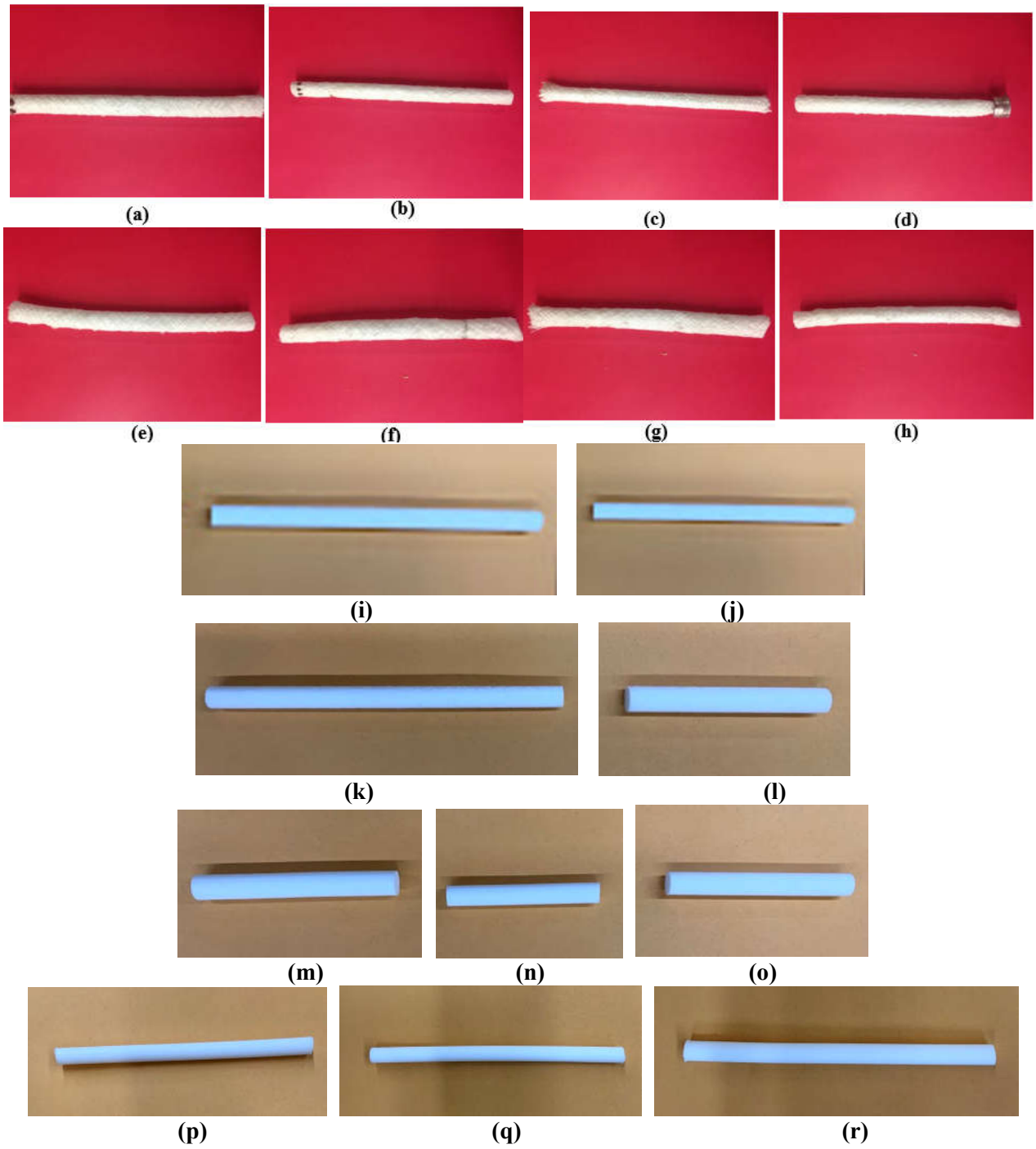

Figure 1 Photographs of the eighteen investigated cylindrical wicks made of polymer beads and fibers (a) to (l) correspond to fibrous wicks F1 to F12 and (m) to (r) correspond to sintered-polymer beads B1 to B6, respectively

2-2-1 Wicking experiment result

To find the type liquid front during the wicking process in the investigated wicks, we used a special type of dye to be added to the wicking liquid and this dye helped us to track and observe the type of liquid front easily. As the liquid rose up into the wicks, we were able to determine its front type visually. The result of the wicking experiment are shown in Figure *2* for the investigated wicks. As is evident, all the wicks made from polymer beads (B1 to B6) displayed remarkably *sharp* fronts. In contrast, only 5 wicks made from fibers (F1, F2, F5, F8 and F12) displayed mildly sharp fronts (to be called the *semi-sharp* fronts) compared to those for B1 to B6. (Note that the region behind the fronts in the latter is not as red as for the B1 to B6 wicks). Hence the saturation behind the fronts in the latter can be deemed to be somewhat less than 100 %.) The remaining fibrous wicks (F3, F4, F6, F7, and F9 to F11) displayed significant finger formation and uneven saturation distributions. Hence, their wicking fronts can only be called the *diffuse* fronts.

(B1)

(B2)

(B3)

(B4)

(B5)

(B6)

(F1)

(F2)

(F3)

(F4)

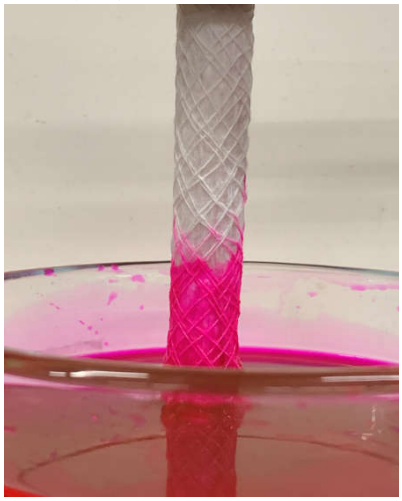

(F5)

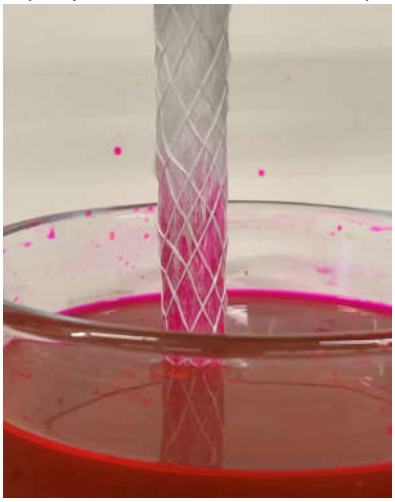

(F6)

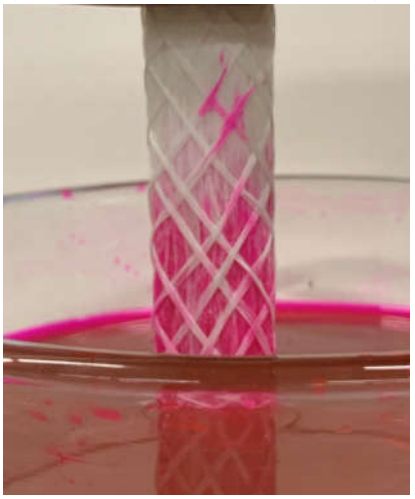

(F7)

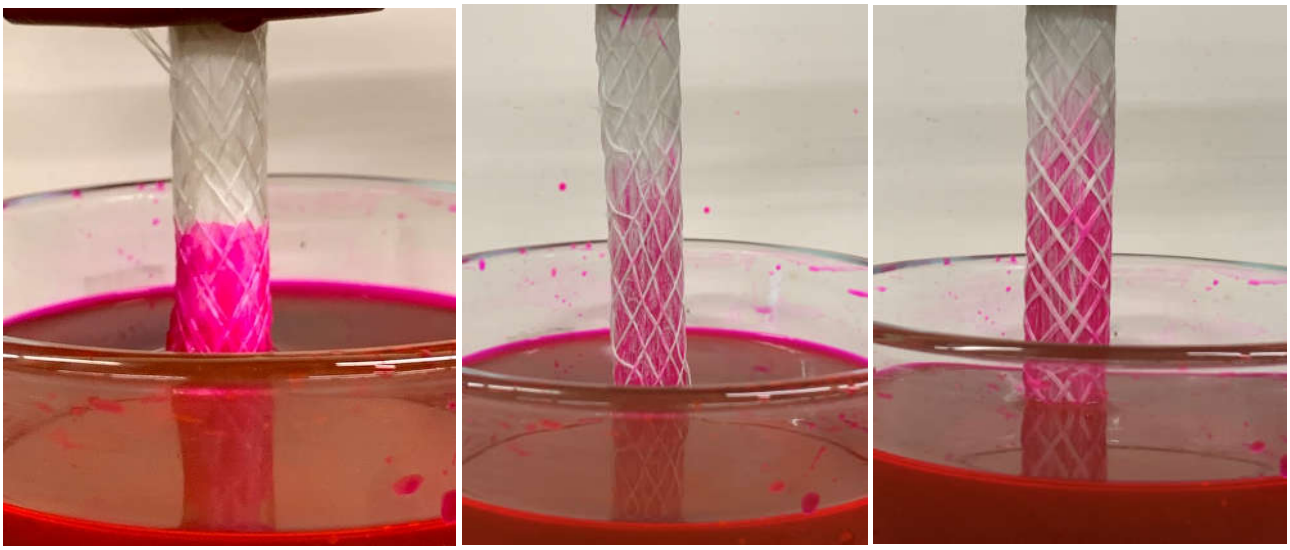

(F8) **(F9)** **(F10)**

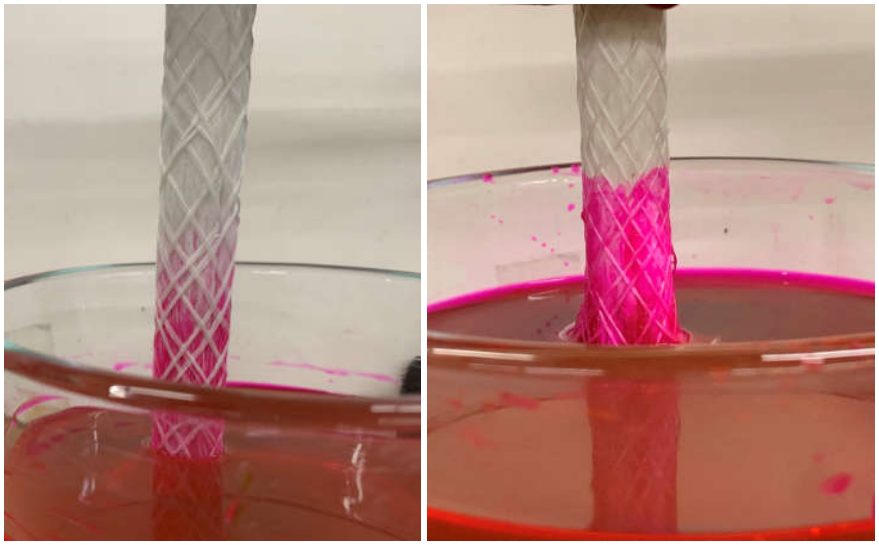

(F11) **(F12)**

Figure 2 Results of the wicking experiment conducted to determine the type of flow front for the sintered beads (B1 to B6) and fibrous wicks (F1 to F12). The wicks made of beads (B1 to B6) display *sharp* fronts, the fibrous wicks F1, F2, F5, F8 and F12 display *semi-sharp* fronts, while the fibrous wicks F3, F4, F6, F7, and F9 to F11 display *diffuse* fronts.

2-3 Preliminary investigation of different types of liquid front

It is instructive to study the changes in the wicking fronts of wicks showing diffusive fronts.

In this regard, we did two different investigations to find this different behavior in terms of form

of liquid front in the selected wicks. First, in terms of visual comparison, we chose the two wicks F3 and F4 to investigate the reason behind their different types of front compare to the sintered-beads wicks and the other fibrous wicks. Figure 3 describes the changes in the liquid front formation and progress with time. As we can see, initially, the front is sharp, which then turns into a semi-sharp one, and finally takes the form of a diffusive front with fingers. This indicates that as *the front moves farther away the source of liquid* (i.e., the liquid surface), the front changes from being sharp to being semi-sharp to finally being diffuse. This implies that as the availability of liquid to the front becomes more difficult (because of the increase in viscous resistance due to the enlargement of the flow path of a liquid element), the front has the tendency to become increasingly more diffuse in the fibrous wicks F3 and F4.

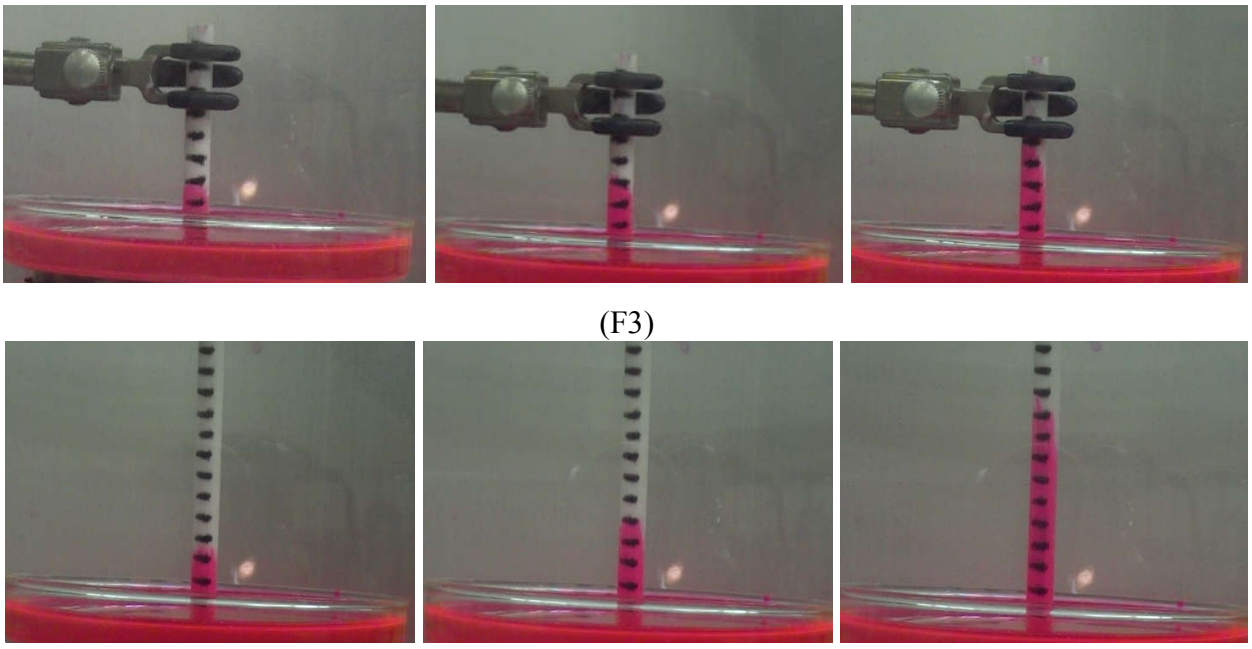

(F3)

(F4)

Figure 3 Different stages of liquid-front formation in the fibrous wicks F3 and F4

Second, we will explore the microstructural causes of this divergent morphological behavior of the fronts. For this comparison, we picked one wick from each type of the wicks, B4,

sintered-beads wick, F2 and F4, fibrous wick made of short fibers with lower and higher porosity, respectively. In order to find the mystery behind these three different front types, we acquired Micro-CT (Computed Tomography) images of the longitudinal sections of three different wicks displaying three different front types. As can be concluded from Figure 4-a for the wicks B1 to B6, a homogeneous particulate structure of a wick made from polymer beads leads to a sharp front as the pore space get filled by the wicking liquid uniformly without the presence of any local inhomogeneities that leads to preferential climbing of tiny micro-fronts, thus causing a 'diffusion' of the front. Let us now consider the fibrous wicks F1 and F2. The wicks F1 and F2 made of short parallel fibers with the lower porosity[1] values (Figure 4-b), the liquid-air interface, as we saw earlier, is very close to forming a sharp front. In this type of wicks, apparently the short length of fibers and their closer packing overcome the effect of local inhomogeneities. In contrast, in the wicks F3 and F4 made of short parallel fibers with higher porosity values (Figure 4-c), factors such as fiber clustering cause the liquid front to transform from the initial sharp type to the diffusive type, and the looser packing of fibers apparently intensifies this process.

It is instructive to discuss the impact of the porosity a little bit more. A study of Table 1 (Page 33) and Table 9 (Page 80) reveal that the porosity of the wicks B1 to B6 is between 35 to 51%, those of the wicks F1 and F2 is from 60% to 65%, and those of the wicks F3 and F4 is 85% each. So one can see that as the porosity increases, the front type changes from sharp to semi-sharp to diffuse. One can argue that if the porosity is low, then the particles and fibers are closer to each other and more homogeneously distributed, and hence the tiny micro-fronts climb uniformly in the interstitial channels to generate a sharper macro-front. On the other hand when the porosity is high, the fibers tend to cluster with big gaps between the clusters, and as a result, the micro-fronts climb

[1] Porosity is defined as the ratio of the void-space volume between fibers to the total volume of the wick

preferentially along the clusters, thereby leading to finger formation and a diffuse macro-front. This hypothesis needs to be tested further in future, either through a Navier-Stokes flow simulation within the wick microstructure obtained from μ-CT, or through a pore network model simulation conducted on a pore network reconstructed from the 2D SEM or 3D μ-CT images.

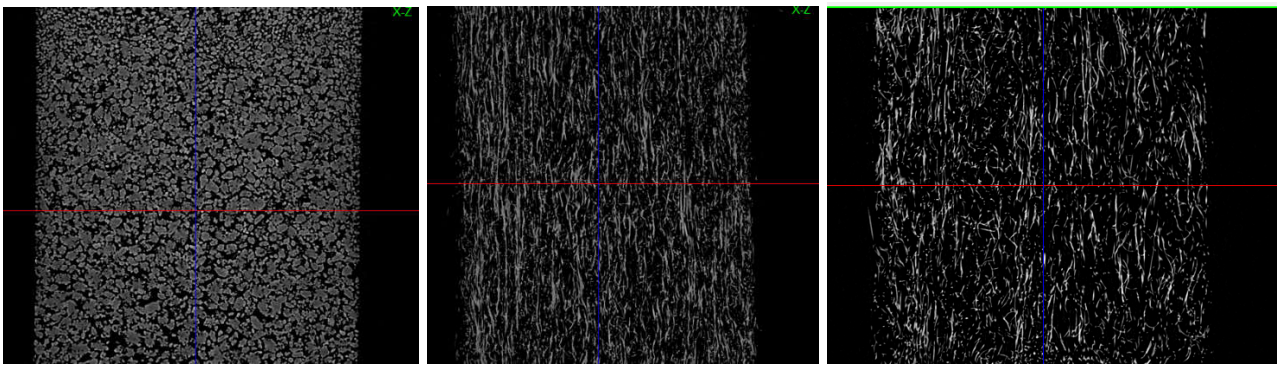

Figure 4 Micro-CT images acquired for three different wicks: (a) sintered-beads wick B4 (b) Fibrous wick F2 (with a low porosity) (c) Fibrous wicks F4 (with a higher porosity)

2-4 Conclusion

In this chapter the first question was: can one observe sharp liquid-fronts in all the wicks? If not, then how many of them will display a diffuse front? To answer this preliminary, a wicking experiment was conducted where a red dyed liquid was spontaneously imbibed by the selected wicks in a vertical configuration. Overall, three categories of fronts were observed. The sintered-beads wicks (B1 to B6) unfailingly showed a sharp front during these experiments. The fibrous wicks, F1, F2, F5, F8 and F12, displayed slightly-perturbed sharp fronts which were deemed to fall into an intermediate category of semi-sharp fronts. The remaining fibrous wicks, F3, F4, F6, F7, and F9 to F11, displayed the diffuse fronts that were characterized by the presence of large fingers. The SEM images of the sintered-beads wicks and some of the fibrous wicks reveal that the presence of aligned fibers in the latter is the cause of fudges in the liquid front—the local

clustering of fibers lead to speeding of liquid compared to the high porosity regions, thereby leading to the blurring of the front. A correlation with porosity is also observed—the arc of rising porosity from the sintered-beads wicks (B1 to B6) to the lower-porosity fibrous wicks (F1 to F2) to the higher-porosity fibrous wicks (F3 to F4) corresponds to progressive ‘diffusing’ of the front from being sharp to semi-sharp to diffuse, respectively.

Chapter 3: Sharp-Front Approach

3-1 Introduction

In this chapter, as we found that some of the investigated wicks have sharp liquid fronts, we will discuss about the usefulness and application of sharp front approach and we will focus our investigation just on the wicks with sharp liquid fronts.

The Washburn's equation, using the sharp-front approximation, is a popular approach to model spontaneous imbibition of a wetting liquid (also called wicking) into a porous medium and has a history of achieving satisfying match with the experimental results after employing a couple of adjustable parameters including hydraulic radius and tortuosity [2, 4]. The equation is also called the capillary model in literature since a porous substrate is assumed to be consisting of a wick of aligned capillary tubes and the movement of wetting liquids into porous media is modeled as the capillary-pressure driven flow of liquids through a wick of parallel capillary tubes [23]. Since pores in a real porous medium are connected to each other, the wicking flows are often complex and three-dimensional (3D). However, the capillary model, because of its basis in parallel tubes aligned along a certain direction, can be used to predict wicking only along one direction (i.e., only 1D flows), which means the prediction of two-dimensional (2D) or three-dimensional (3D) wicking flows in wicks with complex shapes is not possible [23].

Furthermore, the Washburn's equation neglects physical effects, including the gravitational and inertial effects, which makes it less applicable; even though, there have been various modifications in order to make it an accurate model [19-21, 41, 42].

In order to overcome the disadvantages of the Washburn's equation, recently a more versatile wicking-prediction method based on Darcy's law has been proposed [20, 22-26, 31]. The

Darcy's law, which is a crucial equation to model flows in porous media, is a simple linear relationship between the pressure gradient and the average velocity of a liquid. This modeling approach using Darcy's law is based on the assumption that a sharp liquid-front travels in the porous medium during wicking and the saturation in the region behind the liquid-front is 100% (i.e., all the pore space is occupied by the absorbed liquid) [29]. Here the suction pressure at the front is created due to surface energy considerations and the liquid flow in the saturated region constitutes single-phase flow in porous media [43].

In this chapter, the Darcy's law–based approach, using the single-phase flow assumption behind a clearly defined liquid front, is used to predict liquid absorption into different types of wicks made of either aligned fibers or polymer beads. We develop a new theoretical expression to predict the height of the liquid-front as a function of time in transversely-isotropic wicks. The proposed analytical formula is compared with the experimental results based on mass absorption history and is found to be as applicable, if not more so, than the conventional Washburn equation.

3-2 Mathematical Model

During wicking, we assume that all of the pore space within a wick behind the moving front is occupied by a single fluid or phase. As a result, we assume the region behind the liquid front is fully saturated and the saturation jumps from one to zero over a very small distance[1]. It implies that the single-phase Darcy's law is the momentum equation for the flow of a single liquid;

[1] Such an assumption also forces us to assume that no second phase (air) is trapped behind the moving sharp liquid-air front. As was described in the reference [29. Masoodi, R. and K.M. Pillai, *Single-Phase (Sharp-Interface) Models for Wicking*, in *Wicking in Porous Materials: Traditional and Modern Modeling Approaches*. 2012, CRC Press. p. 97-129.], the sharp-front assumption presupposes a high-Capillary number liquid-wetting process characterized by small pockets of trapped residual air phase behind the moving front. The trapped phase quickly gets mobilized in the form of tiny bubbles which moves quickly towards the front to burst there. Hence the fully-saturated region behind the sharp-front is reasonable.

its form in an anisotropic porous medium is given [26] as

$$\tilde{V} = -\frac{\bar{\bar{K}}}{\mu}.\tilde{\nabla}P \qquad (1)$$

where $\tilde{V}$ is the volume-averaged liquid velocity (also called the Darcy velocity) and $\bar{\bar{K}}$ is the permeability tensor of the transversely-isotropic wick[1] and it is of the form $K\underline{\underline{I}}$ (with $\underline{\underline{I}}$ being the diagonal unity tensor) for the isotropic wicks made of polymer beads. The pore-averaged modified pressure, P, which includes the effect of gravity-induced hydrostatic variation in pressure, is defined as

$$P = p + \rho g h \qquad (2)$$

such that p is the ordinary liquid (hydrodynamic) pressure and h is the height of a point within the fully-wetted (saturated) wick (Figure 5)

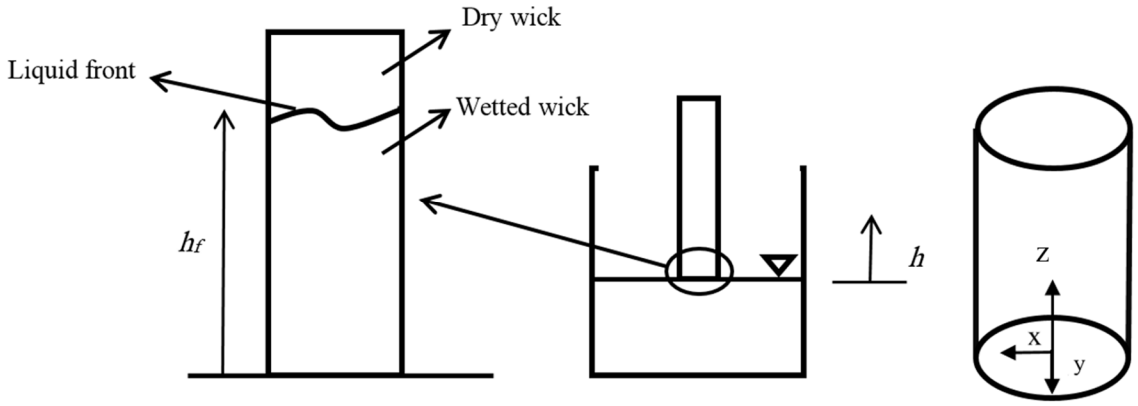

Figure 5 A schematic of the 1D flow and liquid-front position in a glass-fiber wick. Here x is the coordinate along the fiber axis, while y and z are transverse to it.

Due to the tensor nature of the permeability for wicks made of aligned fibers, Eq. 1 can be expressed as

[1] Permeability can be either a scalar quantity, as in the case of an isotropic porous medium or it can be a second-order tensor, as in the case of an anisotropic medium.

$$\begin{bmatrix} V_x \\ V_y \\ V_z \end{bmatrix} = -\frac{1}{\mu}\begin{bmatrix} K_x & 0 & 0 \\ 0 & K_y & 0 \\ 0 & 0 & K_z \end{bmatrix}\begin{bmatrix} \partial_x P \\ \partial_y P \\ \partial_z P \end{bmatrix} \qquad (3)$$

such that V_x, V_y, V_z are the x, y and z components of the volume-averaged velocity vector $\tilde{\mathrm{V}}$. Since the three principal directions of $\bar{\bar{\mathrm{K}}}$ coincide with the three coordinate directions shown in Figure 5, the matrix representation of $\bar{\bar{\mathrm{K}}}$ is diagonal in nature with K_x, K_y, K_z being the three principal components. Note that a typical wick with parallel, aligned fibers and wicks with polymer beads, respectively, are the transversely-isotropic and isotropic type porous media. (For the fibrous wicks, here the direction *z* is along the fibers, while the across directions x and y, due to symmetry about the fiber axis, are equivalent to each other.) The resultant velocity components can be resolved as

$$V_x = -\frac{K_x}{\mu}\partial_x P \qquad (4)$$

$$V_y = -\frac{K_y}{\mu}\partial_y P \qquad (5)$$

$$V_z = -\frac{K_z}{\mu}\partial_z P \qquad (6)$$

Another governing equation for the flow of an incompressible liquid in a solid porous medium is the macroscopic mass-balance equation, the manipulation of which yields an elliptic equation for pressure:

$$\tilde{\nabla}.\tilde{V} = 0 \rightarrow \partial_x V_x + \partial_y V_y + \partial_z V_z = 0 \rightarrow -\frac{K_x}{\mu}\partial_x{}^2 P - \frac{K_y}{\mu}\partial_y{}^2 P - \frac{K_z}{\mu}\partial_z{}^2 P = 0 \quad (7)$$

The last step is due to the use of Eqs. 4, 5 and 6 in the mass balance equation. If we assume the velocities in the transverse-to-the-fiber-axis direction (i.e., y and x directions) to be negligible (i.e., $V_y = V_x = 0$), the pressure equation simplifies to

$$\frac{d^2P}{dz^2} = 0 \qquad (8)$$

which has a general solution of the form

$$P(z) = az + b \qquad (9)$$

The constants a and b are evaluated using the boundary conditions (b.c.s) in terms of the modified pressure, P. However, the b.c.s in terms of the pore averaged hydrodynamic pressure, p, are

$$p = p_{atm} \quad \text{at} \quad z = 0 \qquad (10a)$$

$$p = p_{atm} - p_s \quad \text{at} \quad z = h_f \qquad (10b)$$

where h_f is the height of the liquid front during wicking (Figure 5). Note that the capillary action results in the creation of the suction (or capillary) pressure, p_s, at the liquid-front at $h=h_f$ which is responsible for the vertical absorption of the liquid column along the wick during wicking.

Let us define the b.c.s in term of the pore-averaged modified pressure, P, in the wetting liquid. On using Eq. 2 with Eq. 9 above, we get

$$P = p_{atm} \quad at \quad z = 0 \qquad (11a)$$

$$P = p_{atm} + \rho g h_f - p_s \quad at \quad z = h_f \qquad (11b)$$

The use of these b.c.s in the general solution, Eq. 9, results in the following expression for the modified pressure:

$$P(z) = p_{atm} + \rho g z - p_s \frac{z}{h_f} \qquad (12)$$

Note that this solution is valid for the range $0 \leq h \leq h_f(t)$ where the liquid-front height, h_f, is a function of time.

The following derivation is similar to the one proposed by Masoodi and Pillai [31] earlier for an isotropic wick. Except for a few subtle differences (such as the permeability, K, for the isotropic medium being replaced with the z component principal permeability, K_z), other features are the same—it is replicated here for the purposes of enhancing readability. If we relate the Darcy velocity (Eq. 1) at the liquid-front, $z = h_f$, with the liquid-front speed, $\frac{dh_f}{dt}$, the liquid-front location, h_f , can be derived from

$$\frac{dh_f}{dt} = -Vz\,(z = hf)/\varepsilon = -\frac{K_z}{\varepsilon\mu}\frac{dp}{dz} \tag{13}$$

where $\mathbf{V_z}$ is the Darcy velocity component along the h direction (Figure 5). Furthermore, the use of Eq. 13 in Eq. 14 results in

$$\frac{dh_f}{dt} = -\frac{K_z}{\varepsilon\mu}\left(\frac{p_s}{h_f} - \rho g\right) \tag{14}$$

This is an ordinary differential equation. After applying the separation of variables and subsequently integrating Eq.1 by applying the initial condition$h_f\,(t = 0) = 0$, we get

$$p_s\, ln\left|\frac{p_s}{p_s - \rho g h_f}\right| - \rho g h_f = \frac{\rho^2 g^2 K_z}{\varepsilon\mu} t \tag{15}$$

where p_s is the suction pressure. This is the final implicit equation for the liquid-front height as a function of time.

If we neglect the effect of gravity, integration of Eq. 15 leads to an alternate expression for h_f as

$$h_f = \sqrt{\frac{2K_z p_s}{\varepsilon\mu}}\sqrt{t} \tag{16}$$

which is identical in form to the Washburn Equation and is similar to what was obtained before for isotropic porous wicks [20].

Now, if we do include the effect of the gravity for our case, notwithstanding the fact that Eq. 15 is in an implicit form, it can be converted to a more accessible, explicit form by using the Lambert function [22]. By dividing all terms in Eq. 15 by $-p_s$ and on subtracting 1 from both sides, it turns into

$$ln\left|\frac{p_s-\rho gh_f}{p_s}\right| + \frac{\rho gh_f}{p_s} - 1 = -\frac{\rho^2 g^2 K_z}{p_s \varepsilon \mu} t - 1 \qquad (17)$$

Taking the exponential of both sides, we rearrange it as

$$\left(\frac{\rho gh_f}{p_s} - 1\right) e^{\frac{\rho gh_f}{p_s}-1} = -e^{-\frac{\rho^2 g^2 K_z}{p_s \varepsilon \mu} t-1} \qquad (18)$$

which is similar to the Lambert function. The Lambert function, which is also known by the names of omega function or product logarithm, is a set of functions that are branches of the inverse relation of the function [44, 45] given below:

$$f(w) = We^W \qquad (19)$$

The general approach for solving Eq. 20 is to move all the unknowns to one side of the equation and transform it into the form $y = W(z)e^{W(z)}$. Then the function W, the Lambert function, returns the value of x through the relation

$$y = W(z)e^{W(z)} \leftrightarrow z = W(y) \qquad (20)$$

Accordingly, on applying the proposed approach to Eq.19 results in

$$\frac{\rho gh_f}{p_s} - 1 = W(-e^{\frac{\rho^2 g^2 K_z}{p_s \varepsilon \mu} t-1}) \qquad (21)$$

which is easily manipulated into an explicit relation for the liquid-front height as a function of time as

$$h_f = \frac{p_s}{\rho g}\left[1 + W(-e^{-1-\frac{\rho^2 g^2 K_z}{\varepsilon \mu p_s} t})\right] \quad (22)$$

Once the location of the liquid-front is known, the following equation can be used to estimate the absorbed liquid mass, m, as a function of time

$$m(t) = \varepsilon \rho \pi {R_w}^2 h_f \quad (23)$$

after exploiting the assumption of 100% saturation behind the liquid front. (Here R_w is the radius of the wick and ρ is the density liquid.) In the same way, Eq. 23 can be used to estimate the liquid-front height as a function of time once the mass of wicked liquid is known as a function of time.

On studying Eq. 22, one notices that we have not yet presented a method to estimate the capillary suction pressure, p_s. In a porous medium, the imbibition of wetting liquids into a porous medium under sharp-front conditions is caused by the formation of a capillary pressure at the liquid front. The capillary suction pressure is the difference between surface energies of the dry and wet solid matrices. Using an energy balance model [29], the expression for the capillary pressure for flow along fibers is given as

$$p_s = \frac{2(1-\varepsilon)\gamma \cos\theta}{\varepsilon r_{fb}} \quad (24)$$

while for the wicks made of sintered beads, the following expression [46] is deemed appropriate

$$\boldsymbol{p_s = \frac{2\,\gamma \cos\theta}{R_e}} \quad (25)$$

Here r_{fb} is the radius of fibers, R_e is the equivalent capillary radius, γ is the surface tension of the liquid and Θ is the contact angle between the solid-phase surface and the test liquid.

3-3 Porous Wicks Characterization

In order to investigate the efficacy of theoretical models to predict wicking of liquids through porous wicks, first we need to characterize the wicks in terms of the involved parameters. The parameters such as the properties of the fibrous porous medium [porosity (ε), axial permeability (K_z), fiber or bead diameter (D)], properties of the wetting liquid [viscosity (μ), surface tension (γ)] and finally, the property related to the interaction between the solid and liquid phases [contact angle (Θ)] were characterized accurately. For the rigorous testing of the proposed model, *these properties were all measured independently and none of them was used as a fitting parameter.*

We did our investigation on two batch of wicks separately. The first batch included wicks B1 to B6 and F1 to F4 and the second batch included F5 to F12. Also, two different type of liquids were used as the wicking liquid. The wicking liquid used for the first batch is a type of coconut oil and the second liquid is a hydrocarbon solvent containing cycloalkanes, alkanes and aromatics. All the above-described properties were characterized at room temperature (22˚C± 2˚C). In the following sub-sections, the progress of liquid-front as a function of time and the procedures for measuring the mentioned properties are described in detail.

3-3-1 Measurement of Fiber and Bead Diameter

The diameter of fibers is one of the quantities which has a critical effect on the properties employed in our wicking model such as the porosity or the permeability. The diameter of the fibers used in the studied wicks, F1, F2, F5, F8 and F12 were measured carefully under an optical microscope and their values are presented in Table 1.

For the sintered-beads wicks B1 to B6, the effective radius of the channels formed between squished beads is one of the primary quantities which has a critical effect on the capillary suction

pressure employed in our wicking models.

The SEM images (Figure 6) reveal that the sintered-beads wicks are made through some type of sintering process which causes the beads to join and morph into a foam-like structure. Hence, when the wick was sectioned for microscopy, instead of seeing clear-cut round particles with recognizable diameters, we observed 2D sections of the complex 3D microstructures. As the solid-phase distribution in these sections is quite complex and consists of lumps with different characteristic sizes, we needed to find the equivalent capillary radius, R_e, of the channels formed between the particles (which also gives one an idea about the bead size or diameter). This radius [43] is computed through

$$R_e = 2\frac{A_{int,s}}{P_{int,s}}\frac{\varepsilon}{1-\varepsilon} \tag{26}$$

where $A_{int,s}$ is the sectional areas of solid particles and $P_{int,s}$ is the total perimeter of the solid particles.

In order to calculate R_e, we needed to have a very accurate image of the cross-section of the wick. Hence, we acquired these images using the scanning electron microscope (SEM) that are shown in Figure 6.

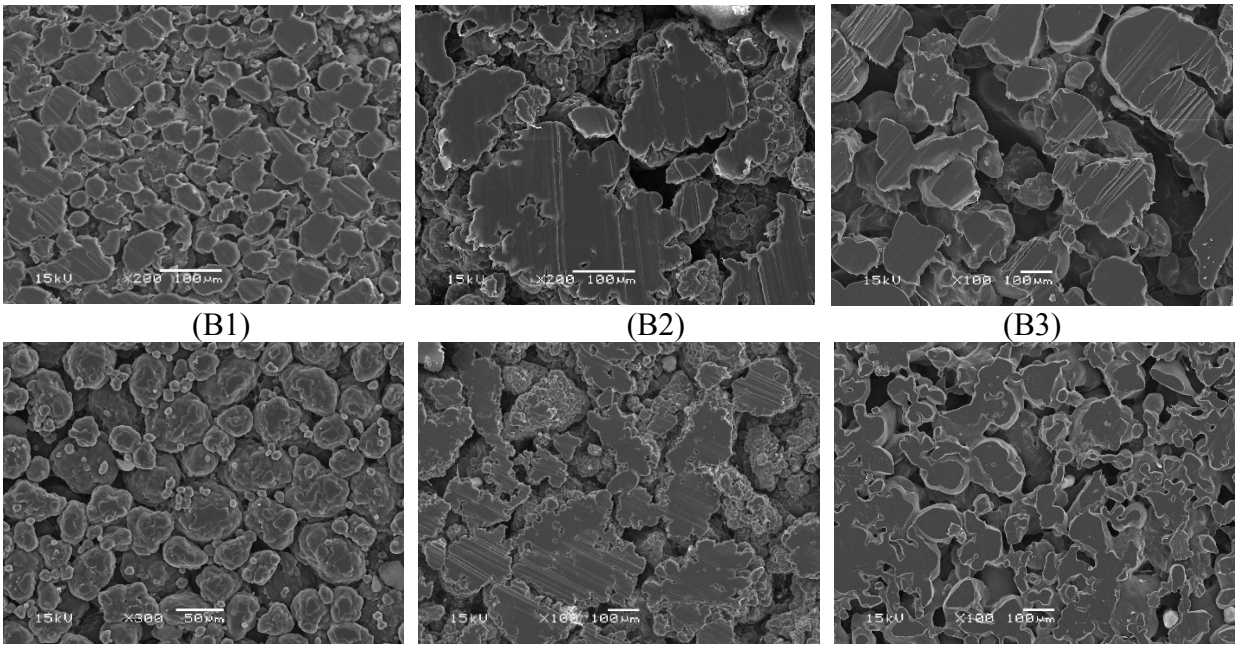

(B1) (B2) (B3)

(B4) (B5) (B6)

Figure 6: SEM of the cross-sections of samples of the sintered-beads wicks. The photographs correspond to the wicks B1 to B6, respectively.

After obtaining the SEM images, we needed to separate the solid phase from the voids in order to have a separate image of just the solid phase. We imported the solid-phase marked image into COMSOL, the multi-physics software, in order to use its image processing feature to calculate the area and perimeter of the marked area. The equivalent capillary radii, R_e, for the investigated wicks was then calculated using Eqn. 26 (see Table 1 for the results).

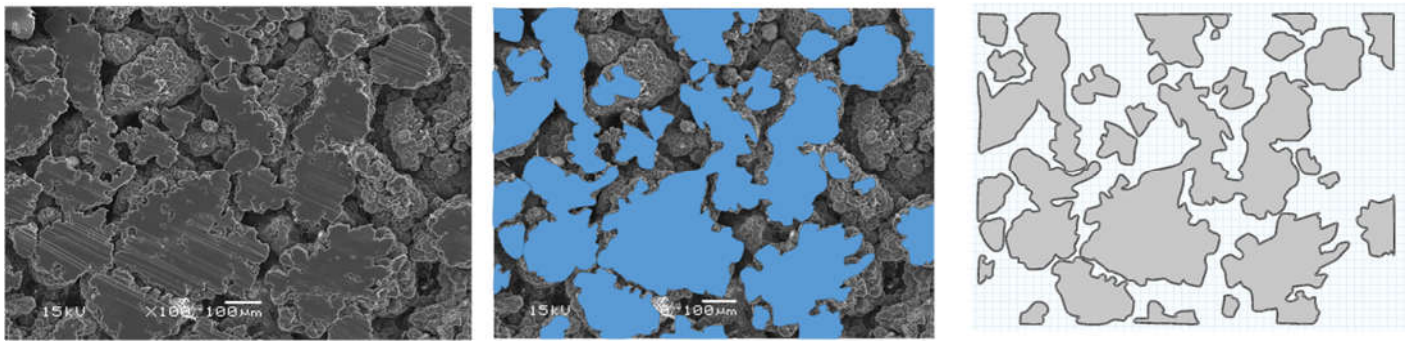

Figure 7: Image processing the SEM images to find the equivalent capillary radius: (left) original image, (middle) identification of the sectioned solid phase, (right) using a grid to quantify the void region and do further image processing.

3-3-2 Porosity Measurement

Porosity is defined as the ratio of the void-space volume between fibers to the total volume of the wick. As we investigated two different type of wicks, made of fibers and polymer beads, the characterization is done separately for each type.

3-3-2-1 Fibrous Wicks

For measuring the porosity of the wicks made of aligned glass fibers, we use two different methods: 1-Dipping Method 2- Micrograph Method. In the dipping method, as the wick has a cylindrical shape, we first estimated the volume of a piece of wick by measuring its height and radius. Later, it is immersed in the liquid kept in a graduated cylinder (Figure 8) and the volume of fibers is estimated by noting the rise in the liquid level caused by the submergence. (The wick sample is kept for a sufficiently long time and shaken while submerged to shake lose any trapped air bubbles.) Using the wick-piece and fiber volumes, the porosity can be estimated using the formula

$$\boldsymbol{\varepsilon = \frac{V_v}{V} = 1 - \frac{V_{fr}}{V}} \qquad (27)$$

in which V_{fr} is the volume of the fibers, V_v is the volume of the inter-fiber void spaces, and V is the total volume of the wick sample.

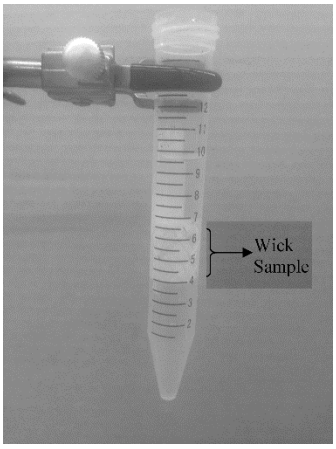

Figure 8 The dipping method involves measuring the porosity by measuring the volume of liquid displaced by a wick piece submerged in a liquid kept in a graduated cylinder

In the micrograph method for measuring the porosity, a section of the wick across its axis is studied under an optical micrograph and the porosity is estimated from the ratio of the total cross-section area of the fibers and that of the inter-fiber void space. Since the fibers in the dry wick are moveable, it is not possible to apply this method without first 'locking' the fibers in their place. This was accomplished by dipping one end of the wick in a pool of curing epoxy (Figure 9a) and then allowing it to fully wet and finally cure into a hard 'composite'. Later, the samples cast in epoxy are polished with progressively finer sanding papers (1200, 800, 600, 240, 120 μm grains) such that the fibers cross-sections are clearly visible in the cross-section Figure 9b). The corresponding micrographs are shown in Figure 10 for the five investigated wicks.

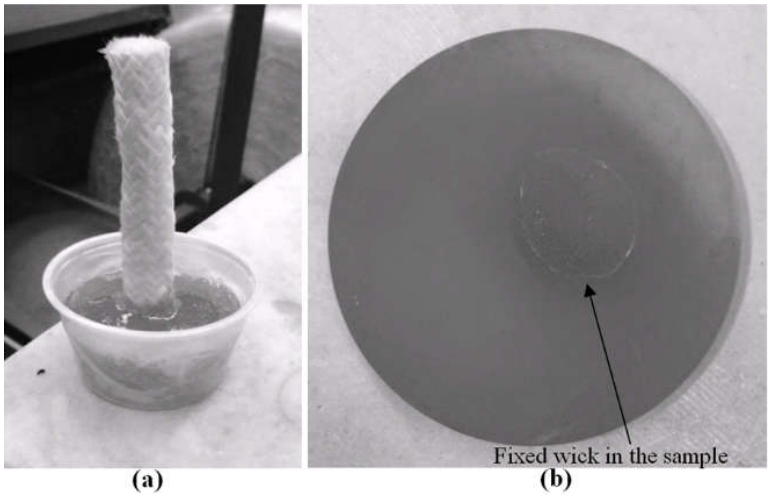

Figure 9 Preparation of a wick sample for making micrograph (a) Dunking a glass fiber wick into epoxy in order to lock the fibers in their places inside the sample (b) Polished and grounded sample ready for producing the micrograph

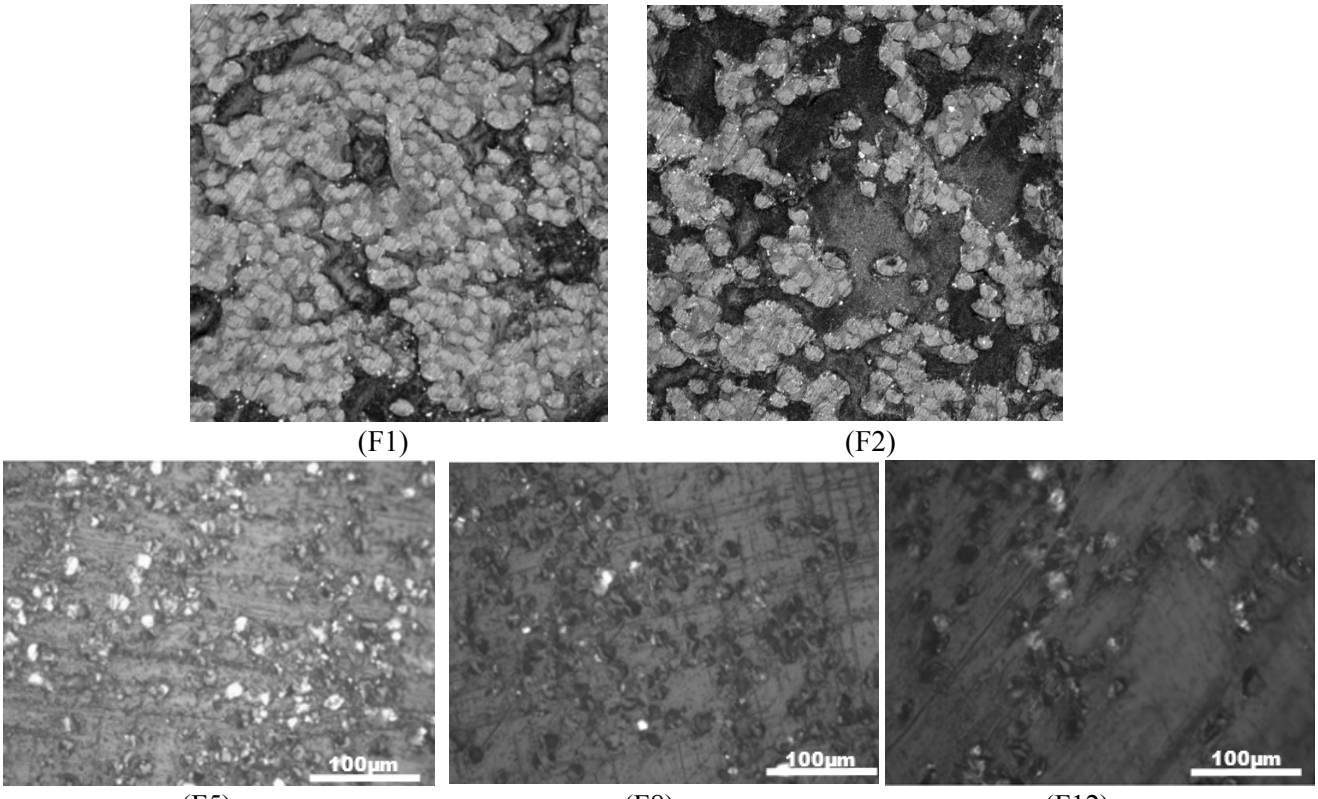

(F1) (F2)

(F5) (F8) (F12)

Figure 10 Typical optical micrographs of the cross-sections of wicks samples cast in epoxy for measuring porosity ($\varepsilon = \frac{V_v}{V} = \frac{\text{Area}_{\text{matrix}}}{\text{Area}_{\text{total}}}$) . The spotty dark spots represent fiber cross-sections while the lighter background is the epoxy matrix. The photographs correspond to the wicks F1, F2, F5, F8 and F12, respectively

By importing the micrograph images into COMSOL, the porosity was obtained as the ratio of pore area to total area after using the inbuilt image processing features of the software. The values of the porosity obtained from the two mentioned methods are presented in Table 1. In order to have repeatable values, each measurement was done five times. As it can be seen from Table 1, all the porosity values were measured with 95% confidence interval[1]. As the values for the porosity provided in Table 1 demonstrate, there is good correlation between the values obtained from the two separate porosity measuring methods for some wicks. However, some divergence in the values is observed for some other wicks. The reason for such differences is perhaps related to the presence of inhomogeneities inside the porous medium (i.e., the wick). Instead of the ideal arrangement of fibers in a parallel, equidistant fashion, one such inhomogeneity could be caused by local fiber clustering in the considered portions of the micrographs (see Figure 10). The possible reasons for this inhomogeneity could be: (a) squeezing of the wick during the making of the epoxy samples, (b) unavoidable kinking of fibers along their axes, etc.

3-3-2-2 Polymer bead Wicks

For measuring the porosity of our wicks, we decided to use the area-based approach rather than the volume-based approach. (In the former, the porosity is obtained from a section as the ratio of the void area to the total area; in the latter, it is obtained from a volume as the ratio of the void volume to the total volume.) For the fibrous wicks, we acquired the micrographs shown in Figure 10 using the procedure described in detail in our earlier paper [48]. For the sintered-beads wicks, we used the SEM images that were acquired for measuring the equivalent capillary radius as

[1] The 95 % confidence interval represents the range the wicks property will fall in 95 % of times. 47. Wheeler, A.J. and A.R. Ganji, *Introduction to engineering experimentation*. 1996: Prentice Hall New Jersey.

described in the last sub-section. For these wicks, we did not use the dipping method, as the SEM based methods has enough accuracy and are reliable.

As we did with the sintered-beads wicks, we were able to find the area of the marked regions (Figure 7) as solid area by using COMSOL. This enabled us to find porosity through using the formula

$$\boldsymbol{\varepsilon} = 1 - \frac{\boldsymbol{V_S}}{\boldsymbol{V}} = 1 - \frac{\boldsymbol{Area}_{\boldsymbol{solid}}}{\boldsymbol{Area}_{\boldsymbol{total}}} \quad (1)$$

The corresponding results for porosity of the fibrous and sintered-beads wicks are presented in Table 1.

3-3-3 Measurement of Surface Tension & Contact Angle

A tensiometer, shown in Figure 11a, is used to measure both the surface tension and contact angle. It was used to measure the surface tension of the liquid using the Wilhelmy plate method where the force resulting from the suspension of a small plate is measured. Here, as in the measurement of the permeability and porosity, the surface-tension measurement is repeated ten times in order to have representative, repeatable data; the final values with the corresponding 95 % confidence intervals are displayed in Table 1.

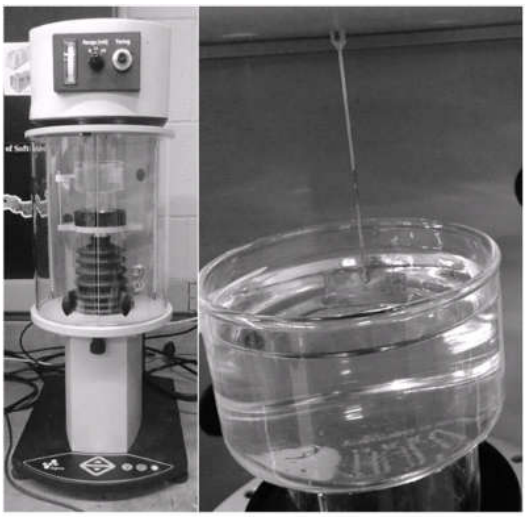

Figure 11 (a) The tensiometer (also known as DCA or the dynamic contact-angle analyzer) used for measuring the surface tension and contact angle (b) A Wilhelmy plate inserted into the liquid in order to measure the surface tension using changes in the downward force (transmitted through the tiny rod) with the help of a sensitive micro-balance

In order to measure the contact angle, one of the properties quantifying the interaction between the wicks and the wicking liquid, the tensiometer is utilized once again. The measurement speed (i.e., the speed at which the sample is dipped into the liquid) was set to 5 mm/min to minimize the viscous and inertial effects. The average values of the advancing and receding contact angles, obtained from twenty repeated up-and-down-traverse measurements for the 95 % confidence interval values of the contact angle, are presented in Table 1. For the second batch of the wicks (B1 to B6 and F1 to F4), since we could not get a flat surface of the solid phase that makes our wicks, we decided to use a whole wick to estimate the contact angle. The same concept as that used in the Wilhelmy-plate technique was employed where the liquid film attached to its perimeter creates a downward force that is proportional to the cosine of the contact angle. To obtain an accurate value for contact angel, we need to ensure that the liquid is not being imbibed by the wick during the measurement process. Hence, As it is shown in Figure 12, we left all our

wicks submerged in the wicking liquid for some time to make sure that they are completely saturated with the liquid. Also we used a dyed liquid to make sure visually that the wicks are fully saturated and no wicking happens during the measurement. The final averaged contact-angle was discovered to be very close to the zero for all the mentioned wicks. This implies that the wicks were wetted perfectly by the chosen test liquid.

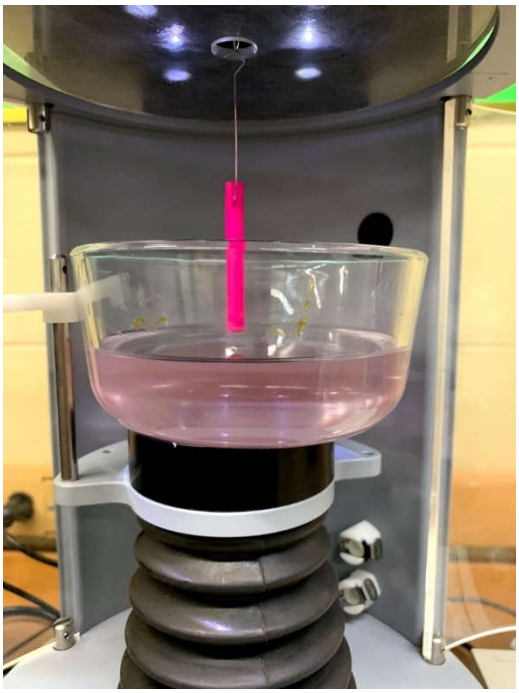

Figure 12. The tensiometer (also called DCA or the dynamic contact angle analyzer) used for measuring the contact angle

Table 1 **.** Measured Properties of the fibrous wicks, F1, F2, F5, F8 and F12, and wicks made of polymer beads B1 to B6 (Each measured property is shown along with a 95% confidence interval.)

Wick	Fiber Diameter (µm)	Equivalent Capillary Radius (µm)	Porosity (Micrograph/ SEM Methods)	Porosity (Dipping Method)	Contact Angle (Degree)
F1	23.15±0.27	NA	0.65±0.021	0.63±0.035	0
F2	43.88±0.65	NA	0.60±0.08	0.58±0.084	0
F5	19.46±0.56	NA	0.72±0.07	0.74±0.03	74.11±3.98
F8	25.63±0.87	NA	0.62±0.02	0.62±0.03	68.28±3.13
F12	24.69±0.95	NA	0.59±0.01	0.59±0.01	64.03±2.48
B1	NA	6.67	0.37±0.02	NA	0
B2	NA	7.95	0.43±0.065	NA	0
B3	NA	20.43	0.49±0.012	NA	0
B4	NA	6.12	0.35±0.019	NA	0
B5	NA	11.8	0.47±0.08	NA	0
B6	NA	10.03	0.51±0.065	NA	0

3-3-4 Viscosity measurement

One of the important properties of the liquid is its dynamic viscosity, which is directly used in Darcy's law. The five measurements of the viscosity of the used liquid for the corresponding 95 % confidence interval were done using the Brookfield viscometer with a rotating cylinder [49]; the average values for both the liquids are presented in Table 2.

Table 2 Measured values of the surface tension and viscosity of the wicking liquid at room temperature using the tensiometer and Brookfield viscometer, respectively.

	Density (kg/m^3)	**Surface Tension (mN/m)**	**Viscosity (mPa.s)**
Wicking Liquid 1	931	36.16 ± 0.095	3.61 ± 0.28
Wicking Liquid 2	872	27.39 ± 0.018	2.175 ± 0.073

3-3-5 Permeability measurement

The permeability of wicks can be determined by: a) an experimental method appropriate for such tow-scale systems, b) formerly developed theoretical models, and c) numerical simulations based on solving the Stokes flow equations and Whitaker's closure formulation

equations. The results derived from all these methods have been compared to bolster the accuracy and find an agreement among them. Among the mentioned three methods, the theoretical and numerical methods were done just on some selected wicks to evaluate their accuracy and reliability, but the experimental method was done for all the wicks. Hence, the tables in which the permeability values are presented, the theoretical and numerical values are just for wicks F7, F8, F10, F11, and F12. In order to preserve the consistency, the permeability values acquired theoretically and numerically for wicks F7, F10 and F11 are presented in this section; although these wicks display diffusive fronts.

3-3-5-1 Permeability measurement methods

3-3-5-1-1 Theoretical models

The expressions for permeability of a fibrous porous media can be divided into different categories, including completely empirical models, phenomenological flow models (for cylindrical fiber-like, conduit-type or tube-type geometries), statistical models, network models, deterministic models based on Stokes flow, and flow-around-submerged-objects models [46]. Most of current theoretical models for permeability are generally of the form

$$K = {D_f}^2 f(\varepsilon) \qquad (28)$$

where ε is the porosity and $D_{f\ or\ b}$ is the fiber or bead diameter and $f(\varepsilon)$ is a function of porosity .

The fibrous wicks are often idealized as stacks of aligned parallel fibers which create a transversely-isotropic porous medium. In the theoretical models considered here, we have included not only those pertaining to parallel fibers but also those who have been derived for other types of porous media with different microstructures such as the particulate (soil-like) media. Hence the permeability models tested in this chapter have been categorized as the

general models developed for isotropic porous media, the models that were developed for the flow axial to parallel fibers, and the models for the flow transverse to parallel fibers.

List of $f(\varepsilon)$:

3-3-5-1-1-1 General models

Kozeny-Carman [26]

$$\frac{1}{180}\frac{\varepsilon^3}{(1-\varepsilon)^2} \tag{29}$$

Davies [34]

$$\frac{1}{64(1-\varepsilon)^{1.5}[1+56(1-\varepsilon)^3]} \tag{30}$$

Chen [35]

$$0.129\frac{\varepsilon}{(1-\varepsilon)}\ln\frac{0.64}{(1-\varepsilon)^2} \tag{31}$$

Tomadakis and Robertson [50]

$$\frac{\varepsilon}{8\ln^2\varepsilon}\frac{(\varepsilon-0.11)^{2.785}}{0.912[(1.785)\varepsilon-0.11]^2} \tag{32}$$

3-3-5-1-1-2 Flow axial to parallel fibers

Berdichevski and Cai [51]

$$\frac{1}{32(1-\varepsilon)}\left[\ln\frac{1}{(1-\varepsilon)^2}-\varepsilon(2+\varepsilon)\right] \tag{33}$$

Gebart [52]

$$\frac{2}{53}\frac{\varepsilon^3}{(1-\varepsilon)^2} \tag{34}$$

3-3-5-1-1-3 Flow transverse to parallel fibers

Berdichevski and Cai [51]:

$$\frac{1}{32(1-\varepsilon)}\left[\ln\frac{1}{(1-\varepsilon)^2}-\frac{\varepsilon(2-\varepsilon)}{1+(1-\varepsilon)^2}\right] \qquad (35)$$

Gebart [52]:

$$\frac{4}{9\pi\sqrt{6}}\left[\left(\sqrt{\frac{1-\varepsilon_{fmin}}{1-\varepsilon_f}}-1\right)^{\frac{5}{2}}\right] \text{ as } \quad \varepsilon_{fmin}=1-\frac{\pi}{2\sqrt{3}} \qquad (36)$$

Bruschke and Advani (square unit-cell: Figure 13) [53]:

$$\frac{1}{3}\frac{(1-{l_h}^2)^2}{l_h}\left(\frac{3\tan^{-1}\left(\sqrt{(1+l_h)/(1-l_h)}\right)}{\sqrt{1-{l_h}^2}}+\frac{1}{2}{l_h}^2+1\right)^{-1} \qquad (37)$$

Where

$${l_h}^2=\frac{2\sqrt{3}}{\pi}(1-\varepsilon) \qquad (38)$$

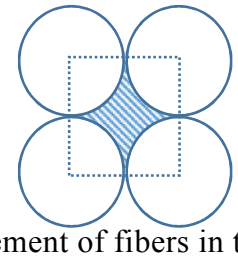

Figure 13- Arrangement of fibers in the square unit-cell for [53].

Bruschke and Advani (hexagonal unit-cell: Figure 14) [53]:

$$\frac{1}{3\sqrt{3}}\frac{(1-{l_h}^2)^2}{l_h}\left(\frac{3\tan^{-1}\left(\sqrt{(1+l_h)/(1-l_h)}\right)}{\sqrt{1-{l_h}^2}}+\frac{1}{2}{l_h}^2+1\right)^{-1} \qquad (39)$$

where

$${l_h}^2=\frac{2\sqrt{3}}{\pi}(1-\varepsilon) \qquad (40)$$

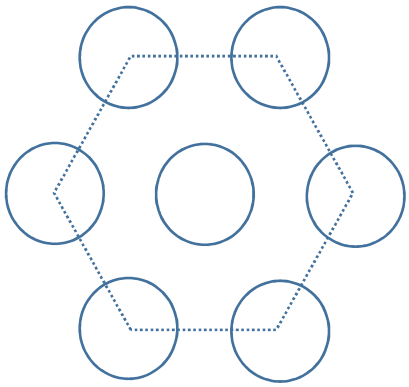

Figure 14- Arrangement of fibers in the hexagonal unit-cell for [53].

For the determination of permeability using the theoretical models, and also using the two numerical simulation methods to be described subsequently, we need the twin parameters of the porosity and average fiber-diameter to be provided after accurate characterization. For testing the accuracy of the theoretical as well as numerical simulation models, these properties were measured independently (Table 1and Table 9) and *neither of them were used as a fitting parameter.*

The comparison between the permeability predicted by both the theoretical models and numerical simulation results is presented later in the section for results and conclusion.

3-3-5-1-2 Numerical simulation methods for permeability estimation

Here we will describe the salient features of the physics involved in estimating the permeability of our fibrous porous media using numerical simulations.

3-3-5-1-2-1 Stokes flow simulation (GeoDict)

In this section, we will briefly describe our method for using the commercial software called GeoDict [54] which relies on simulating Stokes flow through a unit-cell to estimate the medium permeability. The novelty here is the use of the geometry generating feature of the software to create a unit-cell suitable for our medium.

The continuity and Navier–Stokes equations for simulating flow are given by:

$$\nabla.\vec{V} = 0 \qquad (41)$$

$$\rho\left(\frac{\partial}{\partial t} + \vec{V}.\nabla\right)\vec{V} = -\nabla p + \mu\nabla^2\vec{V} \qquad (42)$$

Here ∇p is the local pressure gradient, $\vec{V}$ is the point-wise velocity while μ is the fluid viscosity. Since we are interested in slow, creeping flows through a porous medium, the particle-based Reynolds number is less than or equal to 1. In such a flow regime, the inertia terms in the Navier-Stokes equation can be neglected and the resulting Stokes equation representing our momentum-balance equation is given as

$$\nabla p = \mu\nabla^2\vec{V} \qquad (43)$$

In such a case of microscopic flow, the Darcy's law [28, 33-35] can be used to the scale-up flow through the fibrous porous medium as

$$\langle\vec{V}\rangle = -\frac{\mathbf{K}}{\mu}.\nabla\langle p\rangle^i \qquad (44)$$

where $\langle\vec{V}\rangle$ is the volume-averaged flow velocity and, $\langle p\rangle^i$ is the pore-averaged pressure. **K**, the permeability of the porous medium, is a second-order tensor for our case of aligned fibers and has units of m^2.

Here, we describe the usage of the software GeoDict, developed at Fraunhofer-IWTM Germany [54], in solving the Stokes flow equations, given by Eqns 41 and 42, to predict the flow in a unit cell and to thus estimate the permeability of our tow-level porous medium. While using GeoDict, we decided to generate our 3D unit-cell resembling the fibrous medium at hand, rather than getting our 3-D microstructure directly through a micro-CT scanner as the latter process has been quite problematic and expensive (both in terms of time and money) in the

past for us.

In GeoDict, we firstly need to create our particular geometry which is a unit-cell containing randomly-packed parallel glass fibers. The unit-cell is generated in GeoDict by a voxel-based code in which each voxel in the domain is either “empty” or “filled”. In our case, the fluid domain and solid fibers are represented by empty and filled voxels, respectively. In order to generate a unit-cell that conforms to the macroscopic and microscopic properties of our porous medium, we needed to input the fiber diameter, the porosity, and the orientation matrix of the fibers. Then Geodict starts to randomly pack the aligned fibers inside a cube-like unit-cell. In Figure 15, top views of the thus-generated unit cells of the five different wicks investigated by us are shown. The generated microstructures have the size of 200×200×200 voxels in which the dimension of each voxel is 2μm.

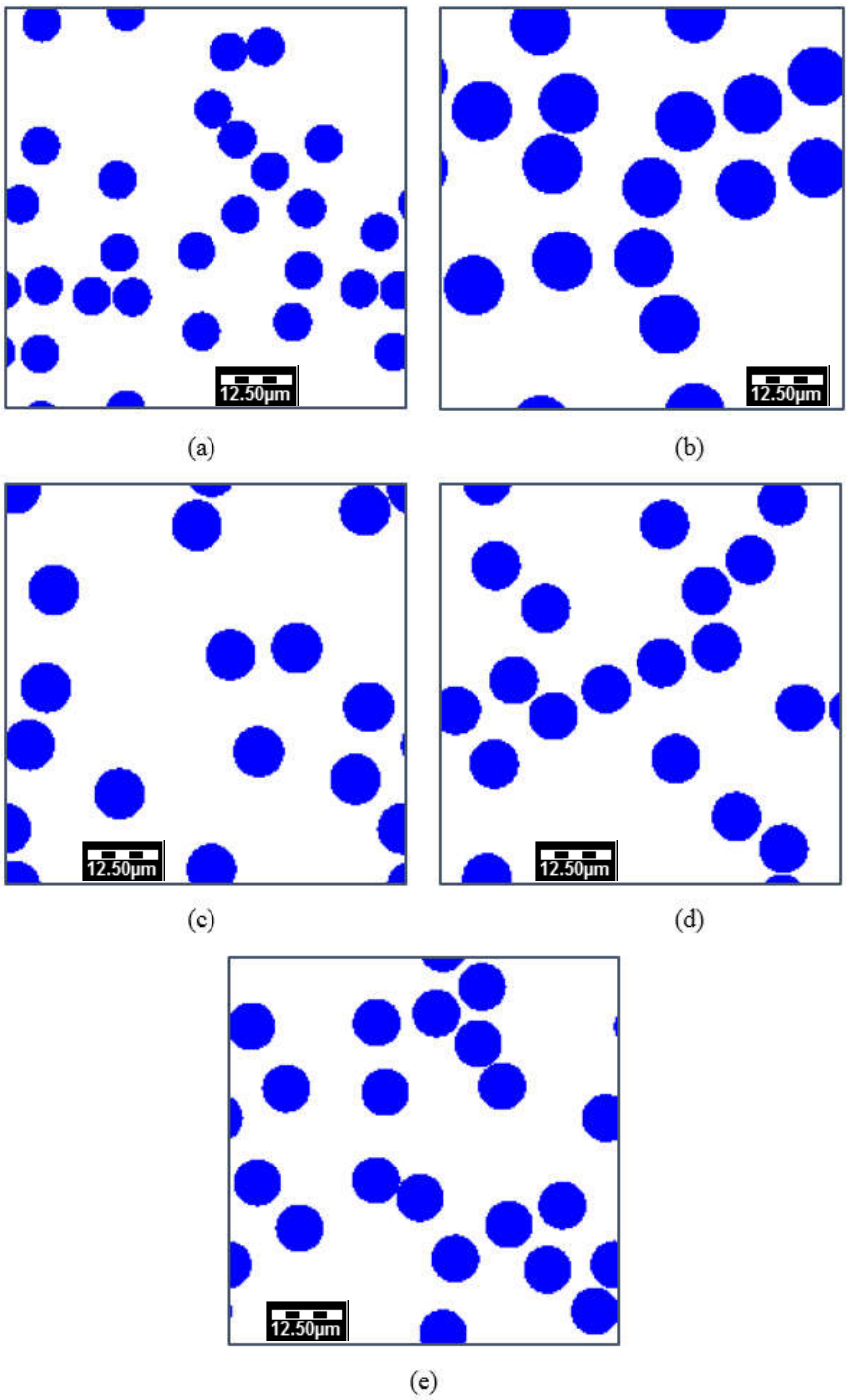

Figure 15. Two-dimensional (2-D) top views of the virtually-created unit cells for 5 different glass-fiber wicks: a) Wick F7, b) Wick F8, c) Wick F10, d) Wick F11, e) Wick F12. The domain size is of 200×200×200 voxels in which each voxel is of dimension 2µm.

The result of the solved Stokes flow for the considered five fibrous wicks cases, shown in

Figure 15, are presented in the results section where the numerical permeabilities are compared with the experimental and theoretical values. In order to have the results that are independent of the randomness used for generating the unit-cells, we have repeated our simulations for three different unit-cell geometries created by GeoDict for each case of F7, F8, F10, F11 and F12, and presented the results that are averages of the three permeabilities.

3-3-5-1-2-2 Closure formulation (COMSOL)

The formulation developed by Whitaker [55], based on the volume averaging method, is used in this numerical model employed for estimating the glass fiber permeability. The flow variables in the pore region of a representative averaging volume (REV)[1] are averaged and the values are used in the macroscopic flow-field. Two types of averaging can be defined for an arbitrary flow variable, φ, as follows.

Phase Average:

$$\langle \varphi \rangle = \frac{1}{V} \int_{V_f} \varphi \, dV \tag{45}$$

Intrinsic-Phase Average (or Pore Average):

$$\langle \varphi \rangle^f = \frac{1}{V_f} \int_{V_f} \varphi \, dV \tag{46}$$

Here V represents the REV volume while V_f represents fluid volume (which is equal to the pore volume) in case of single-phase flow within the REV. For the low-Reynolds number (Stokes) flows between the fibers, the boundary value problem for solving the velocity and

[1] REVs are the averaging volumes used for estimating the averaged flow variable (such as fluid velocities and pressures). Typically, the REVs are supposed to be much larger than the size of individual particles or fibers.

pressure fields associated with the Stokes and continuity equations can be expressed as

$$0 = -\nabla p_f + \rho_f \mathbf{g} + \nabla^2 \mathbf{v}_f \tag{47}$$

$$\nabla . \mathbf{v}_f = 0 \tag{48}$$

$$\text{B.C.1} \quad \mathbf{v}_f = 0 \quad \text{on} \quad S_{fs} \tag{49}$$

$$\text{B.C.2} \quad \mathbf{v}_f = f(\mathbf{r}, t) \quad \text{on} \quad S_{fe} \tag{50}$$

where S_{fs} represents the fluid-solid interface area within the REV while S_{fe} stands for the fluid entrance and exit areas of the REV. Using the volume averaging method prescribed in [55], one can apply some volume averaging theorems to all the additive terms of Eqns. (21) and (22) to obtain the final macroscopic momentum equation for porous-media flows in the form of Darcy's law. During this process of scaling-up, the pressure and velocity terms are decomposed in terms of their intrinsic-phase averages, $\langle p_f \rangle^f$ and $\langle \mathbf{v}_f \rangle^f$, and the corresponding deviations, $\tilde{\mathrm{p}}_f$ and $\tilde{\mathrm{v}}_f$:

$$p_f = \left\langle p_f \right\rangle^f + \tilde{p}_f \tag{51}$$

$$\mathbf{v}_f = \left\langle \mathbf{v}_f \right\rangle^f + \tilde{\mathbf{v}}_f \tag{52}$$

The use of Eqns. (51) and (52) during the volume averaging process results in the following equation set to solve for the pressure and velocity deviations:

$$0 = -\nabla \tilde{p}_f + \mu_f \nabla^2 \tilde{\mathbf{v}}_f - \frac{1}{V_f} \left\{ \int_{S_{fs}} \mathbf{n}_{fs} . \left(-\mathbf{I}\, \tilde{p}_f + \mu_f \nabla \tilde{\mathbf{v}}_f \right) dS \right\} \tag{53}$$

$$\nabla . \tilde{\mathbf{v}}_f = 0 \tag{54}$$

B.C.1 $$\tilde{\mathbf{v}}_f = -\left\langle \mathbf{v}_f \right\rangle^f \quad \text{on} \quad S_{fs} \tag{55}$$

B.C.2 $$\tilde{\mathbf{v}}_f = f(\mathbf{r}, t) \quad \text{on} \quad S_{fe} \tag{56}$$

Note that Eqns. (53) and (54) are obtained from manipulating the momentum (Stokes) and continuity equations, respectively. Later, $\tilde{p}_f$ and $\tilde{\mathbf{v}}_f$ are defined in terms of the corresponding pore-averaged flow velocity as

$$\begin{aligned} \tilde{p}_f &= \mu_f \, \mathbf{b}_f . \left\langle \mathbf{v}_f \right\rangle^f \\ \tilde{\mathbf{v}}_f &= \mathbf{B}_f . \left\langle \mathbf{v}_f \right\rangle^f \end{aligned} \tag{57}$$

On substituting Eqn. (57) in Eqns. (53) and (54), the governing equations for the closure variables, $\mathbf{b}_f$ and $\mathbf{B}_f$, can be developed as

$$0 = -\nabla \mathbf{b}_f + \mu_f \nabla^2 \mathbf{B}_f - \frac{1}{V_f} \left\{ \int_{S_{fs}} \mathbf{n}_{fs} . \left(-\mathbf{I}\, \mathbf{b}_f + \nabla \mathbf{B}_f \right) dS \right\} \tag{58}$$

$$\nabla . \mathbf{B}_f = 0 \tag{59}$$

Note that $\mathbf{b}_f$ is a vector while $\mathbf{B}_f$ is a second-order tensor. This formulation, called the closure formulation as it closes a macroscopic momentum equation containing the local $\tilde{p}_f$ and $\tilde{\mathbf{v}}_f$ variables [55], allows the permeability tensor to be estimated in terms of the closure variables as

$$\frac{1}{V_f}\int_{S_{fs}} \mathbf{n}_{fs}.\left(-\mathbf{I}\,\mathbf{b}_f + \nabla \mathbf{B}_f\right) dS = -\varepsilon_f \mathbf{K}^{-1} \qquad (60)$$

Use of this definition in Eqn. (58) leads to

$$0 = -\nabla \mathbf{b}_f + \nabla^2 \mathbf{B}_f + \varepsilon_f\, \mathbf{K}^{-1} \qquad (61)$$

At this point, $\mathbf{b}_f$ and $\mathbf{B}_f$ can be replaced with $\mathbf{d}_f$ and $\mathbf{D}_f$ [55] through the transformations

$$\begin{aligned} \mathbf{d}_f &= \varepsilon_f{}^{-1}\mathbf{b}_f.\mathbf{K} \\ \mathbf{D}_f &= \varepsilon_f{}^{-1}\mathbf{B}_f^0.\mathbf{K} \\ \mathbf{B}_f^0 &= \mathbf{B}_f + \mathbf{I} \end{aligned} \qquad (62)$$

On using these expressions, one can transform the pore level 'momentum' equation, Eqn. (61), as

$$0 = -\nabla \mathbf{d}_f + \nabla^2 \mathbf{D}_f + \mathbf{I} \qquad (63)$$

and the pore level 'continuity' equation, given by Eqn. (59), can be transformed to

$$\nabla . \mathbf{D}_f = 0 \qquad (64)$$

Note that the closure formulation described by Eqns. (63) and (64) is similar in structure to the Stokes boundary-value problem that can be solved in an REV [55].

In Stokes flow, the pressure and velocity fields within the REV are controlled by the boundary conditions at the fluid-solid interface, Eqns. (49), and at the entrance and exit regions of REV, Eqn. (50). The first boundary condition on the fluid-solid interface, Eqn. (55), can be expressed in terms of the transformed closure variables as

B.C. 1 $\qquad \mathbf{D}_f = 0 \quad$ on $\quad S_{fs} \qquad (65)$

The second boundary condition given by Eqn. (56) is troublesome since it involves the use of an unknown function, *f*, to assign deviations at the entrance and exits of the REV [55]. This problem was made manageable by solving the closure problem in a periodic unit-cell instead of the full-fledged REV. The corresponding periodicity conditions for the velocity and pressure deviations can be prescribed in terms of the closure variables as

B.C. 2

$$\mathbf{D}_f(\mathbf{r} + l_i) = \mathbf{D}_f(\mathbf{r}) \tag{66}$$

$$\mathbf{d}_f(\mathbf{r} + l_i) = \mathbf{d}_f(\mathbf{r}) \tag{67}$$

Here r represents the position vector of any point on the unit-cell boundary, while l_i are the lattice vectors with $i \in \{1, 2, 3\}$ that express the spatially periodic nature of the unit cell in the 3-D space. These periodicity conditions imply that the opposite sides of a rectangular unit-cell have the same values of the $\mathbf{D}_f$ and $\mathbf{d}_f$ components.

The transformed closure variable $\mathbf{D}_f$ is first estimated within the unit cell by solving the closure formulation given by the boundary value problem listed in terms of Eqns. (63) to (67). Then one can estimate the permeability tensor, **K**, using the relation

$$\mathbf{K} = \varepsilon_f \left\langle \mathbf{D}_f \right\rangle^f \tag{68}$$

where $\mathbf{D}_f$ is volume integrated in the pore region of the unit-cell [56]. *Note that the whole of the permeability tensor can be determined from one simulation, rather than three separate* 1D *flow simulations required to determine permeabilities along the x, y and z directions in the Stokes flow simulations of the last section.*

In order to solve the closure formulation using the multiphysics software COMSOL, we first needed to create our 3D unit-cells for the glass fiber wicks. In order to have the same unit-

cell geometries as what we had created earlier using GoeDict, we exported the 3D geometries, created by 'extruding' the 2D geometries of glass fiber wicks shown in Figure 15, into COMSOL. Since we wanted to solve the closure formulation in the pore space of the unit cells, we had to subtract the volume of glass fibers from the volume of the unit cell in order to obtain the pore space geometries shown in Figure 16.

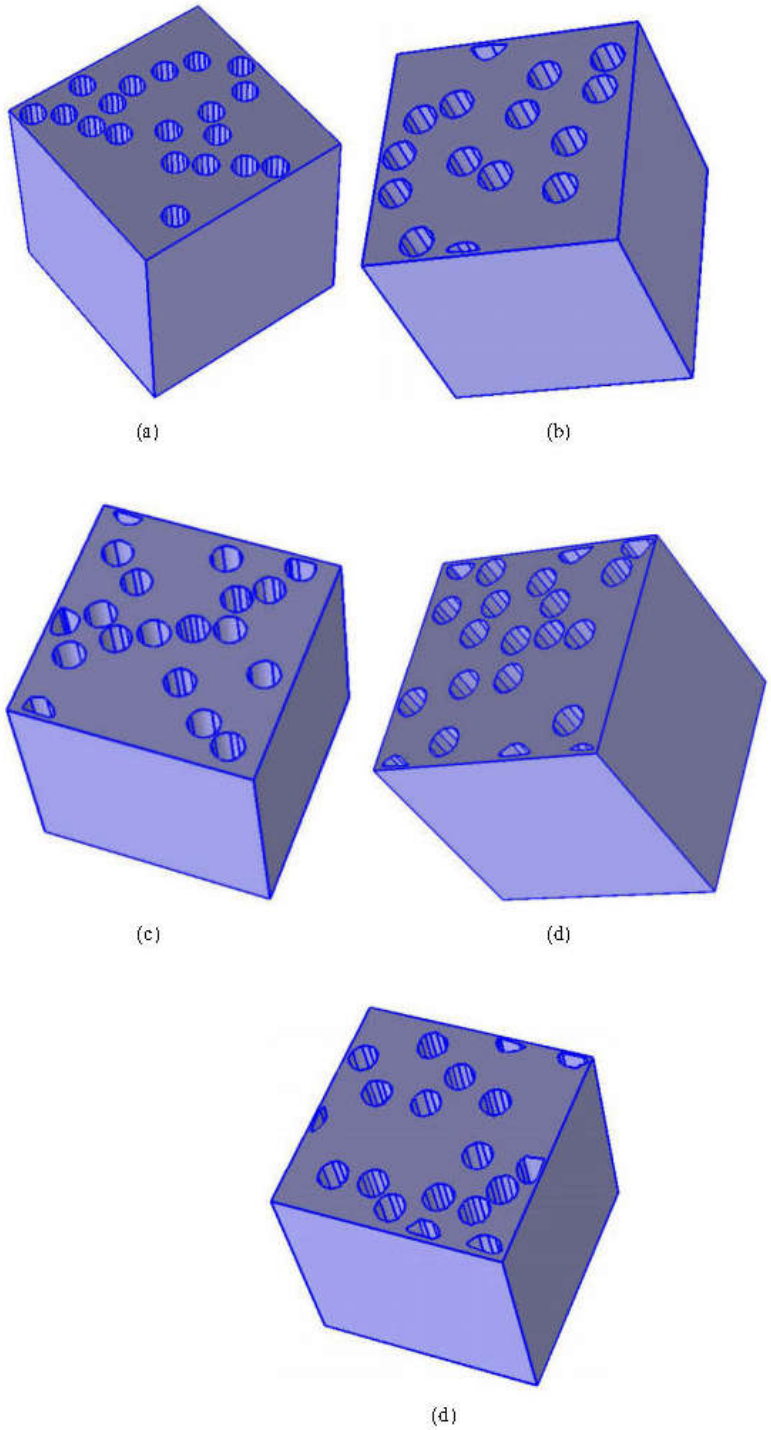

Figure 16. 3D Geometries of void spaces carved out of unit cells of glass-fiber wicks imported into COMSOL: a) Wick F7, b) Wick F8, c) Wick F10, d) Wick F11, e) Wick F12

3-3-5-1-3 Experimental methods

By choosing the rigorously-derived theoretical and numerical models in the previous sections, we hope to obtain accurate permeability values. However, it is always doubtful if the permeability obtained from such theoretical and numerical models will match 100% with the actual permeability of a real porous wick. This divergence will happen because the fibers inside the tows may suffer from many imperfections in their spatial arrangements as well as their geometries, including random clustering, crookedness or waviness, non-uniform cross-sectional areas of fibers, and a scatter in fiber diameter and bead size, and length values. Therefore, it is important to conduct experiments in order to validate the results of numerical simulations and confirm the predictions of the theoretical permeability models.

In order to measure the permeability of a porous medium, several methods have been developed (see chapter 4 of [46]). For the investigated wicks, we choose to apply the falling-head method to measure the permeability. The shape and small size of the wick samples allows us to apply the falling-head method very well. Many permeability measurement techniques, especially for fabrics and fiber mats used in LCM (Liquid Composite Molding), involve forcing a high-pressure liquid to pass through a porous sample [57-60]. In contrast, our chosen technique is a gentle gravity-driven method that does not use high applied pressures and hence does not cause any flow-induced compression or deformation in the wicks.

The falling-head method is based on the flow of a liquid through a short sample of a wick which is connected to a burette. As shown in Figure 17, the setup is held vertical to enable the gravity-driven liquid flow through the porous wicks. As the head at the inlet decreases, the inlet pressure driving the flow decreases with time. The burette is filled with a test liquid that has its density and viscosity measured. A small sample of each type of the wicks is attached to the output

end of the burette. If the initial height of the liquid column (or the height of the meniscus shown in Figure 17) in the burette is h1 at time t = t_1, and the height reduces to h_2 at the end of the experiment at time t = t_2, then the axial permeability of the wick, Kz, can be estimated through the formula

$$K_z = \frac{\mu a L}{\rho g A (t_2 - t_1)} ln \frac{h_1}{h_2} \tag{69}$$

where A is the cross-section area of the wick sample while a is the cross-section area of the burette.

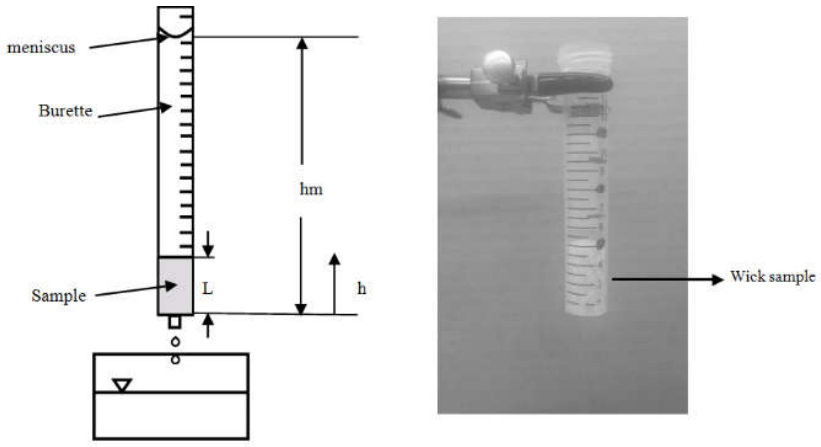

Figure 17- The falling-head permeameter used for measuring the permeability of small fiberous wick samples [46, 48]:(b) Schematic, (c) photo

Two separate approaches were adopted to measure one permeability along the fiber-tow axis and the other across it. For along the fiber axis measurement, a segment of the wick was cut and inserted inside the burette. (Note that the wick diameters were smaller than the inner diameter of the burette, and hence the wick segments could be inserted without any squeezing.) The gap present between the segment and burette walls was eliminated through the use of a viscous sealant that did not penetrate into the wick.

In order to measure the permeability in the direction transverse to parallel fibers (i.e., along

x and y directions), we felt the need to create a wick of fibers rectangular in cross-section so that the transverse flows can be easily administered, and the permeability measured accurately using the falling-head permeameter. (Note that if a segment of fiber wick of circular cross-section is used as the 'sample' in Figure 18, then uniform cross-flow cannot be insured.) Hence, we took fibers out of our wicks and packed them uniformly into a rectangular duct made of Plexiglas shown in Figure 18. (During the process of making such 'square wicks', we try to keep the porosity the same as that of our wicks in order to have their permeability close to those of the considered wicks.) On each side of this duct we made openings which served as inlets and outlets and which enabled us to do the falling-head permeameter experiment along the x and y directions that are transverse to the fiber axes.

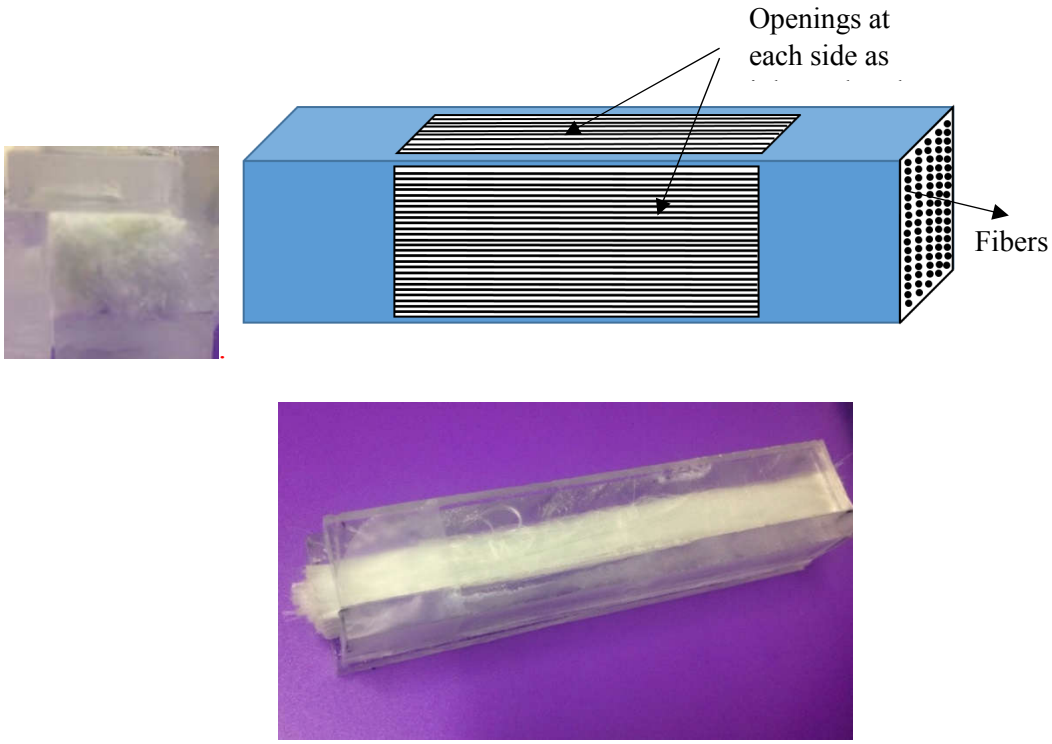

Figure 18. Two views and a schematic of a custom-built plexiglass duct filled with glass fibers representing our specially-created fiber wick with a rectangular cross-section. The schematic shows the two windows on adjacent sides for flow transverse to the fibers along the x and y directions that are orthogonal to each other.

In order to make sure that the measured values for permeability are accurate and repeatable, each test was repeated five times for each wick.

As mentioned earlier, we acquired the numerical and theoretical permeability values for some selected wicks, and estimated experimental permeability values for the rest of wicks, disregarding the type of their liquid fronts, observed. The permeability values as well as the 95 % confidence interval for wicks F1, F2 and B1 to B6 are presented in Table 3.

Table 3 Measured Properties of the sintered-beads wicks, and the fibrous wicks F1 and F2 (Each measured property is shown along with a95% confidence interval)

	Permeability K_z (m^2)
Wick F1	2.74 ×10-10± 5.61 E –11
Wick F2	2.61 ×10-13± 2.12 E –11
Wick B1	2.38×10-13±3.65×10-14
Wick B2	7.64×10-13±1.26×10-14
Wick B3	1.78×10-11±6.36×10-12
Wick B4	2.21×10-12±1.98×10-14
Wick B5	3.59×10-13±5.01×10-15
Wick B6	2.19×10-13±4.65×10-14

3-3-5-2 Results and discussion

3-3-5-2-1 Performance of theoretical models

3-3-5-2-1-1 Flow along the parallel fibers

As we assumed the fibers inside the fibrous wick to be parallel and aligned along the z direction, a theoretical permeability model based on the analytical solution of flow along the

axes of parallel fibers is considered as a benchmark for the permeability along the z direction (K_z). The permeability values calculated from the earlier described numerical models and the experiments are presented in Table 4. A remarkable closeness can be seen between the permeability predictions by the two numerical models on the one hand, and the numerical predictions and experimental results on the other. It is to be remembered that getting a match within an order of magnitude is often considered quite creditable in any permeability study. However, in this work, *we are getting values that not only fall within the same order of magnitude, but also match up to the first digit before the decimal point*. Hence this effort to simulate the permeability along the fibers can be considered to be extraordinarily accurate. In comparison, the values predicted by the Berdichevski and Cai model and the Gebart model are rather lackluster—they are less than half of the experimental values, though they achieve parity in the orders of magnitude. Hence this study highlights the need to develop more accurate analytical models for permeability of flow along the fibers in fibrous wicks.

Table 4 : For flow along the parallel fibers, comparing the permeability values (Units: 10^{-10} m^2) obtained from the numerical simulations and theoretical models with those from the experiments.

	K_z (Stokes flow)	**K_z (Closure)**	**K_z (Experiments)**	**Berdichevski and Cai**	**Gebart**
Wick F7	2.64	2.59	2.36 ± .60	1.33	1.11
Wick F8	2.35	2.41	2.73 ± .29	1.00	.83
Wick F10	1.96	1.99	2.06 ± .19	.88	.68
Wick F11	1.73	1.72	1.78 ± .28	.75	.56
Wick F12	1.75	1.69	1.74 ± .29	1.12	1

3-3-5-2-1-2 Flow transverse to parallel fibers

Let us now test the models to predict the permeability for flow transverse to the fibers. Since the z axis is along the aligned fibers, the x and y axes are the two perpendicular directions transverse to the fiber alignment direction. The permeability in these two directions as obtained by the numerical methods and analytical models are compared with the experimental values in Table 5. Straightaway one can notice that the transverse permeability is one order of magnitude smaller compared to the longitudinal one (10^{-11} m^2 versus 10^{-10} m^2). Also, this time the numerical methods are not that accurate in their predictions. Even the theoretical models are similar in nature. However, *no particular trend can be discerned while comparing various results*. But the Berdichevski and Cai model seem to be over predicting, the Bruschke and Advani model is in general under predicting, while the Gebart model is lying between these two extremes. For the Bruschke and Advani model, the square unit-cell approach seems to be more accurate compared to the hexagonal unit-cell one. It is heartening to note that most of the models, whether numerical or analytical, furnish permeability values that fall within an order of magnitude of the experimental results. It is also worth noting that except for wick F11, the K_x and K_y values are fairly close to each other, as it should be.

Table 5 : For flow transvers to parallel fibers, comparing the permeability values (Units: 10^{-11} m^2) obtained from the numerical simulations and theoretical models with those from the experiments

	K_x Stokes Flow	K_y Stokes Flow	K_x Closure	K_y Closure	K_x Experiments	K_y Experiments	Gebart	Berdichevski - Cai	Bruschke – Advani Square unit cell	Bruschke – Advani Hexagonal unit cell
Wick F7	5.36	5.14	2.73	3.79	1.76 ± .13	2.24 ± .82	6.84	9.23	1.79	1.03
Wick F8	7.07	5.46	5.43	6.36	4.32 ± .35	3.98 ± .44	5.12	6.91	1.33	0.78
Wick F10	3.89	5.98	3.28	2.99	6.43 ± .31	5.92 ± .70	4.49	6.17	1.38	0.80
Wick F11	4.43	3.77	1.80	2.99	9.43 ± .45	1.25 ± .53	3.82	5.30	1.29	0.75
Wick F12	5.78	6.35	4.70	3.43	6.47 ± .64	7.15 ± .24	5.75	7.81	1.57	0.91

3-3-5-2-1-3 General models

Among the theoretical models for permeability, there are some which can be considered as generic models, and which have not been developed for anisotropic porous media. Just out of curiosity, we decided to present their predictions in order to see how close they are to the experimental results as well other models presented so far. Three such models, which can be characterized as being semi-empirical in nature, are considered here. The Kozney-Carmen model [26] developed for isotropic porous media such as soil or sand is considered first. Then the models by Davies [34] and Chen [35] are considered next, which are for the general cases of fibrous porous media without considering any specific flow direction. Tomadakis-Robertson model, developed for randomly overlapping fiber structures, is considered finally [50]. The permeability determined by these general models for the investigated wicks are given in Table 6. It is interesting to note that the values predicted by Chen are one order of magnitude higher than the other three models and more in line with the values seen in Table 4. Hence, in general, the Kozeny-Carman, Davies and Tomadakis-Robertson models predict the

permeabilities that are approximately one-tenth of the experimental values listed in Table 4 for the along-the-fiber-axis flow, but are in line with the experimental values given in Table 5 for across-the-fiber-axis flow.

Table 6 : Permeability values (Units: 10^{-10} m^2) estimated using the general theoretical models for isotropic porous media after taking the porosity and particle-size diameter values from Table 4

	Kozeny-Carman	**Davies**	**Chen**	**Tomadakis- Robertson**
Wick F7	.79	1.06	11.94	.78
Wick F8	.60	.79	8.94	1.04
Wick F10	.51	.69	8.30	.64
Wick F11	.43	.58	7.33	.52
Wick F12	.66	.89	10.21	.86

As can be seen from the tables discussed in the last section, the generic permeability models (such as the Kozeny-Carmen model that have been developed for isotropic porous media such as soil or sand) are applicable to the transverse flows seen in the packed aligned fibers inside fiber tows. For flows along the fibers, only Chen's model seem to yield values that are an order of magnitude within the experimental values. In contrast, there is a satisfying agreement with experiments for the predictions of specialized theoretical models that have been developed specifically for flow along and transverse to parallel fibers. Hence, if we are careful in selecting our theoretical model, it can give us the permeability values that are accurate within an order of magnitude.

An important takeaway from this investigation is the remarkable accuracy of the two numerical methods used to estimate the fiber-tow permeability, especially for flows along the fibers. The main inputs for the Stokes-Flow simulation done using GeoDict and the closure formulation solved using COMSOL are the local tow-level porosity and fiber diameter, which

can be easily obtained from the micrographs of composites made using fiber wicks. The innovation of using the 3-D unit cells created by random placement of parallel fibers, without taking recourse to the expensive and time-consuming method of using a micro-CT to generate a real 3-D unit cell, seems to be quite accurate—it also indicates that the factors such as kinkiness of fibers inside a fiber wick, scatter in fiber length and diameter, clustering, etc. are perhaps not that important for permeability determination. The present research also puts at the same level the two numerical methods employed to determine permeability from the micrograph inputs. Recall however that the main advantage of the closure-based numerical method is its estimation of the permeability tensor from the software-generated unit-cells in *one* simulation, without the need for conducting multiple numerical experiments as in the case of the Stokes-flow based simulation method.

3-4 Results and Discussion

It is important to assess the accuracy of our theoretical model based on the sharp-front assumption for predicting the height of the wetted region in the wicks. Therefore, we evaluate our theoretical model against the experimental results by finding the height of liquid front experimentally. In order to measure the height of the liquid-front as a function of time, the final liquid-mass taken up by the wicks is measured from a vertically-rising wicking experiment designed using a balance and a wetting liquid. For repeatability, the wicking experiment is performed some times for each of the wicks with a new, dry sample used for each of the experiments. The comparison between experimental and theoretical model can be done through two different methods. In the first method, which we will explain in the section 3-4-1-2, all the experimental result will be plotted alongside the theoretical results for Wicks F5, F8 and F12 after conducting experiments. In the section 3-4-2-2 and 3-4-2-3, in order to evaluate the accuracy of

the sharp-front model, we set up a composite experiment where we determine the progress of the sharp front in the wicks using two different methods: (a) through the visually observed means, (b) through the absorbed-mass calculations. In the former, we tracked the progression of the front visually and obtained the height of the front using the indicator lines marked on the wicks. In the latter, we estimated the height of wicking front experimentally and a curve was fitted on the experimental results. Then they were compared with the theoretical results. This comparison was be done for the fibrous wicks F1 and F2, and the sintered beads wicks B1 to B6.

3-4-1 Sharp front model evaluation for Wicks F5, F8 and F12

3-4-1-1 Mass-Gain Measurement

To validate our theoretical model for the wicking of a liquid into a porous wick, an experiment is developed that involved estimating the height of liquid-front, h_f, as a function of time, t.

It was not possible to detect clearly the movement of a transparent wicking liquid in a white wick made of glass fibers, hence h_f vs t could not be recorded directly through visual observations. However, according to Eq. 23, there is a linear relation between h_f and m, the mass of the liquid absorbed by the wick. Therefore, instead of measuring the height of the progressing liquid-front in our experiment, we measured the imbibed mass of the liquid as a function of time. As shown in Figure 19, the weight gain in the wicks due to liquid imbibition is recorded with time by using a balance at room temperature (22.5°C±2°C) and atmospheric pressure (101±2 kPa). (Note that the weight gain by the wick is equal to the weight lost by the liquid container.) Later, using Eq. 23, the weight gain data was transformed into the liquid-front height data.

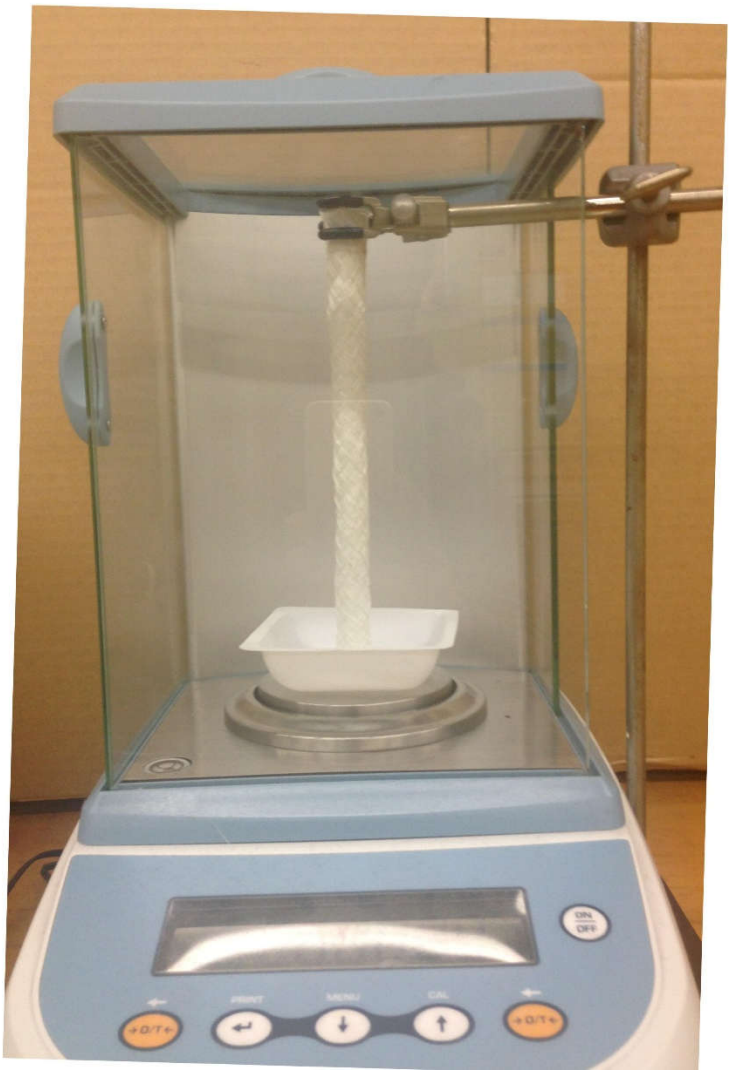

Figure 19 Experimental setup for measuring the mass of liquid spontaneously imbibed by the wick using a sensitive balance. The time corresponding to a measurement was measured using a stop-watch.

3-4-1-2 Liquid absorption experiment and comparison with the proposed theoretical model for wicks F5, F8 and F12

The results of the wicking experiment for the investigated wicks in the form of a comparison between the theoretical predictions and experimental results of the liquid-front height as a function of time are presented in Figure 20. Note that, in order to conduct a comprehensive, repeatable study of the wicking of a liquid into the investigated fibrous wicks, six experiments for

the wicks F5 andF8, and four experiments for the wick F12 were done. In Figure 20, the experimental data are plotted using six different signs for the wicks F5 and F8, and four different signs for the wicks F12, representing the result of repeated mass gain experiment for each type of the wicks, and the proposed theoretical model is plotted using a solid curve. (Note that the slope of these curves in these figures is equal to the speed of the liquid front.) As Figure 20 a, b, and c demonstrate, the theoretical proposed model has a good agreement with the imbibition flow experiments conducted with wicks F5, F8 and F12.

From the study of Figures Figure 20, it is clear that our sharp-interface model is able to predict wicking most satisfactorily only in wicks F5, F8 and F12.

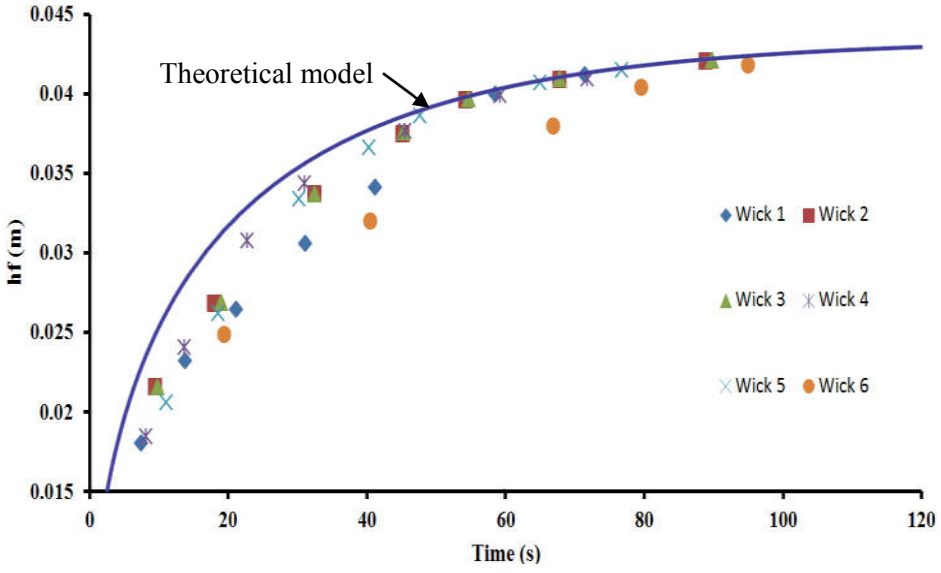

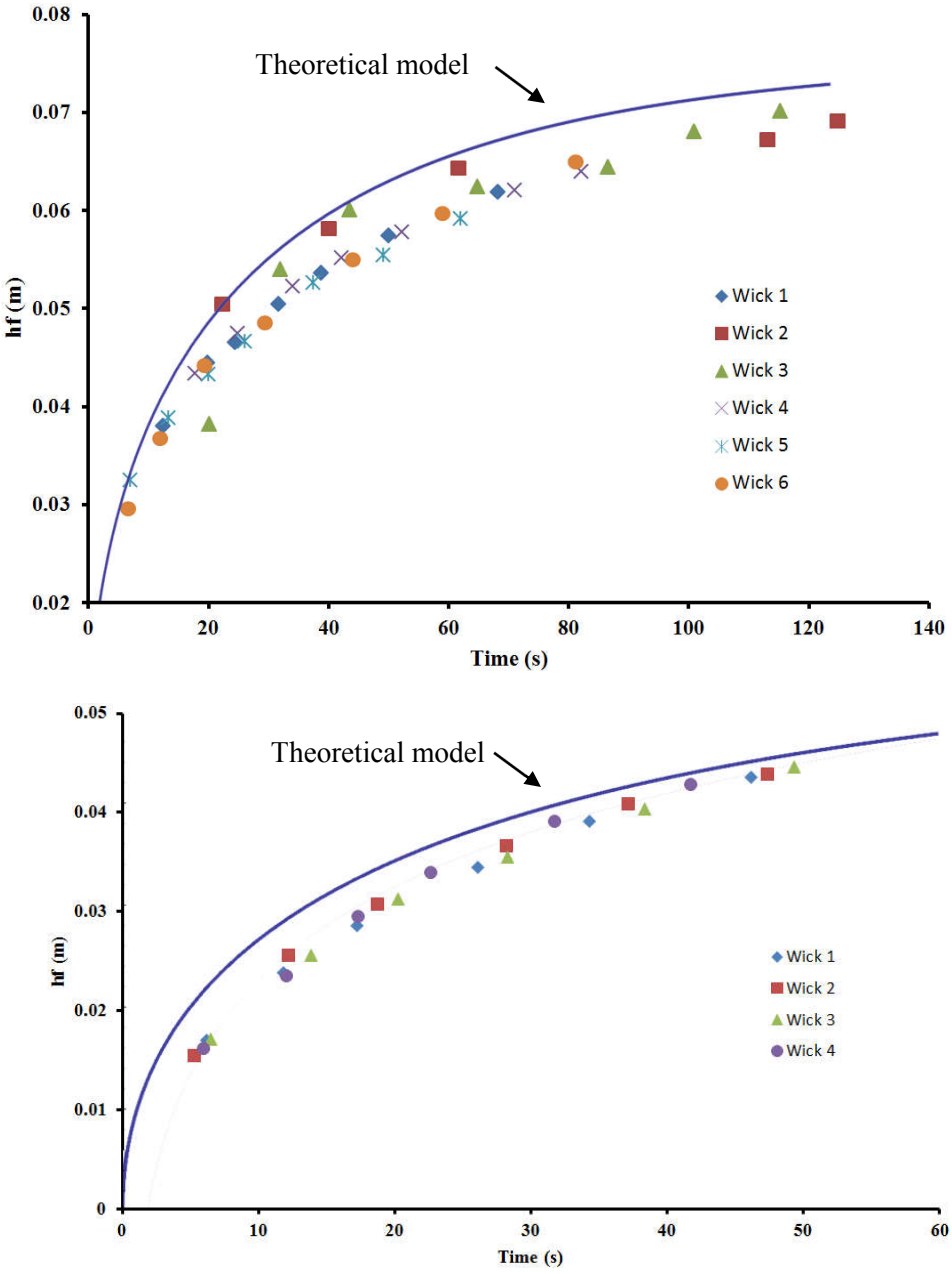

Figure 20 The proposed theoretical model for predicting the height of liquid-front as a function of time during wicking. The model is compared with the experimental data for the wicks F5, F8 and F12

The legends show the number of wicks that we repeated the mass gain experiment for each type of the wicks

It is notable that our model based on sharp-front assumption is quite good in providing an excellent upper bound for wicks F5, F8, and F12 in Figure 20. Moreover, our model, summarized by Eqns (22) and (23), is quite powerful as it clearly and explicitly outlines how parameters (such

as the porosity and permeability; liquid properties such as the density, viscosity, surface tension and contact angle; and the average fiber radius) affect the rising of liquids in wicks.

3-4-2 Sharp front model evaluation for Wicks F1, F2, and B1 to B6

3-4-2-1 Mass-Gain Measurement

In the same way that we did in section 3-4-1-1, for the rest of wicks, we measured the imbibed mass of the liquid as a function of time, as shown in Figure *21*, where the weight gain in the wick due to liquid imbibition is equated to reduction in the weight of the beaker containing the liquid and resting on top of the balance. Such a weight gain was recorded as a function of time by using a balance kept at room temperature (22.5°C±2°C) and atmospheric pressure (101±2 kPa). Later, using Eqn. 23, the weight gain data was transformed into the liquid-front height data. In order to promote repeatability as well as to evaluate the scatter, we repeated each experiment 3 times for each wick in order to obtain the average and the 95 % confidence interval.

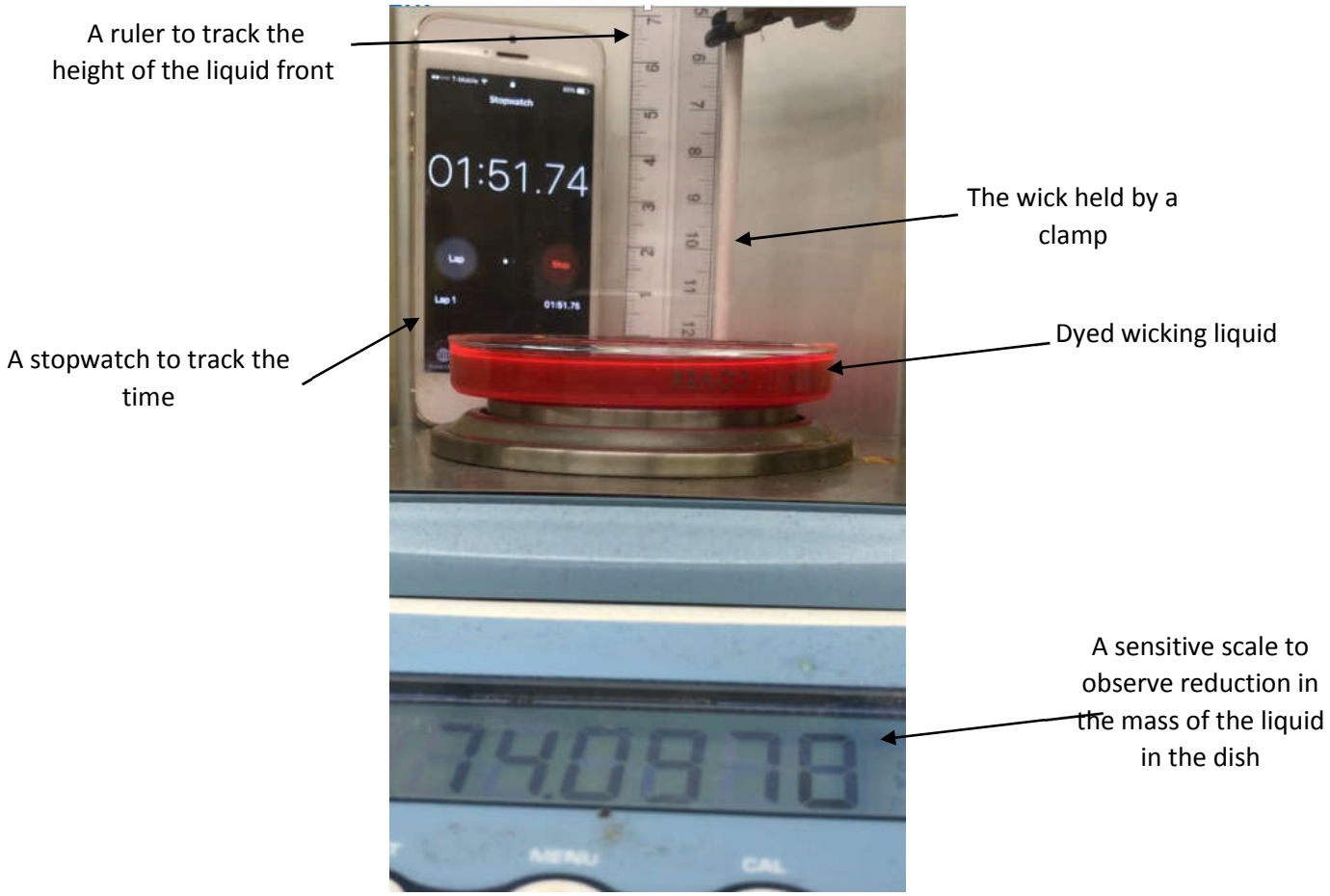

Figure 21: Experimental setup for measuring the mass of liquid spontaneously imbibed by a wick using a sensitive balance. The time corresponding to a measurement was measured using a stop-watch.

3-4-2-2 Visual measurement

Tracking of the liquid front was possible through the addition of a special type of red dye to the wicking fluid, which was then taken in by the white porous wicks. Hence, it was possible to detect clearly the movement of the dyed wicking liquid in both the fibrous and sintered-beads wicks. Precise height of the liquid front was measured by using equidistant markers on the sample placed every 5mm as shown in Figure 22. Thus the climb of the liquid front could be tracked over

time during wicking, and hence h_f vs t could be recorded directly through visual observations.

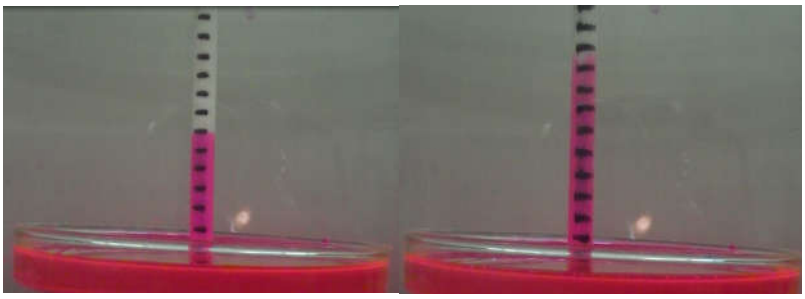

(a) (b)

Figure 22: Measuring the liquid-front height through a visually recording of the wicking-fluid front movement with the help of a linear scale with bars 5mm apart. The three front types: (a) sharp front, (b) semi-sharp front

3-4-2-3 Comparison of the mass-based and visual results

Here we compare the mass-based and visual results for the evolution of the liquid-front height. As mentioned earlier, the main purpose here is to test the basic hypothesis of the sharp-front model, i.e., *all the pores behind the liquid-front are completely filled* so that the liquid mass obtained using Eqn. (22) yields an h_f that matches the actual visually-observed h_f.

As can be seen from Figure 23, all the six sintered-beads wicks (B1 to B6), which have sharp-fronts, show a good match between h_f obtained from the two approaches. Hence we can surmise that for the sintered-beads wicks, not only do we get perfectly defined liquid fronts, but also have the pores of the porous medium behind the front completely filled with the test liquid.

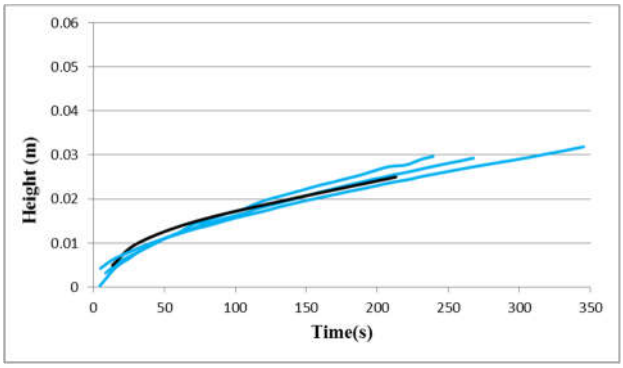

(B1)

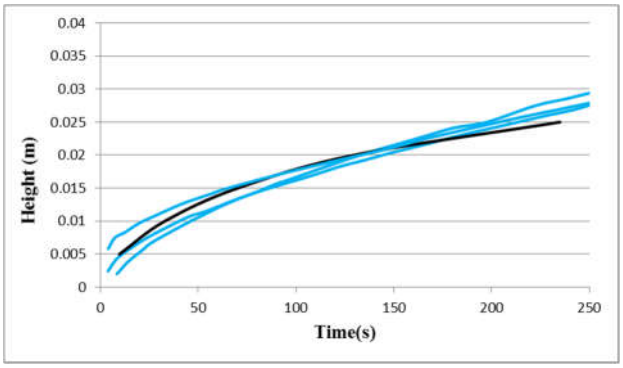

(B2)

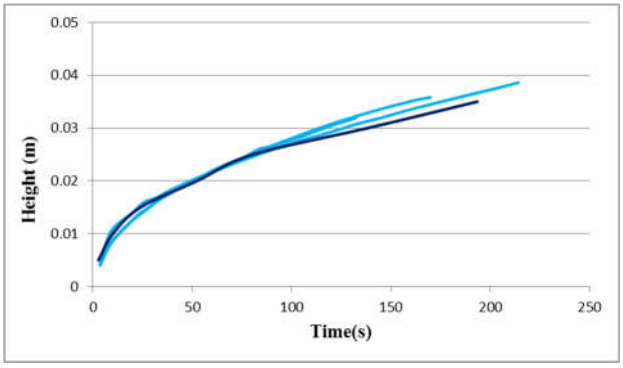

(B3)

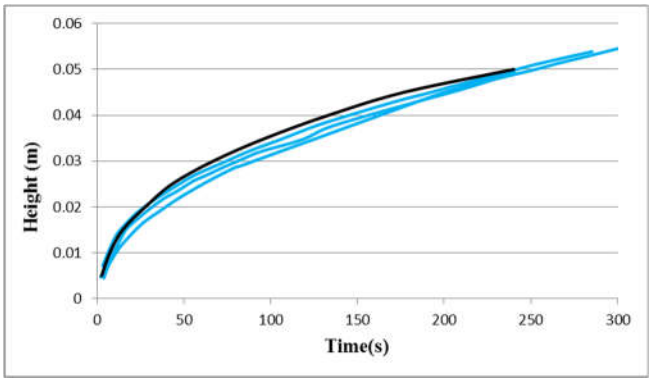

(B4)

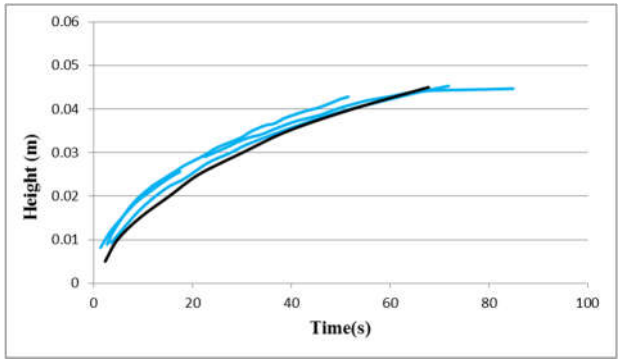

(B5)

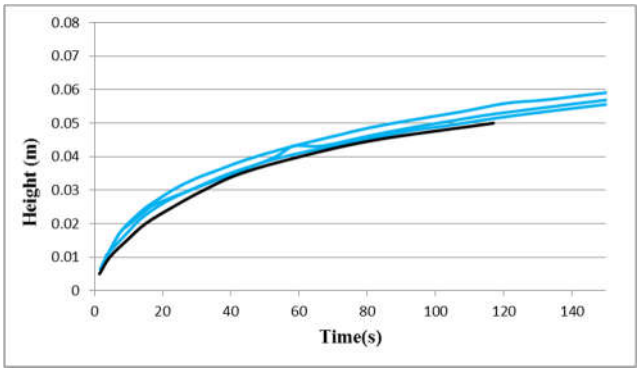

(B6)

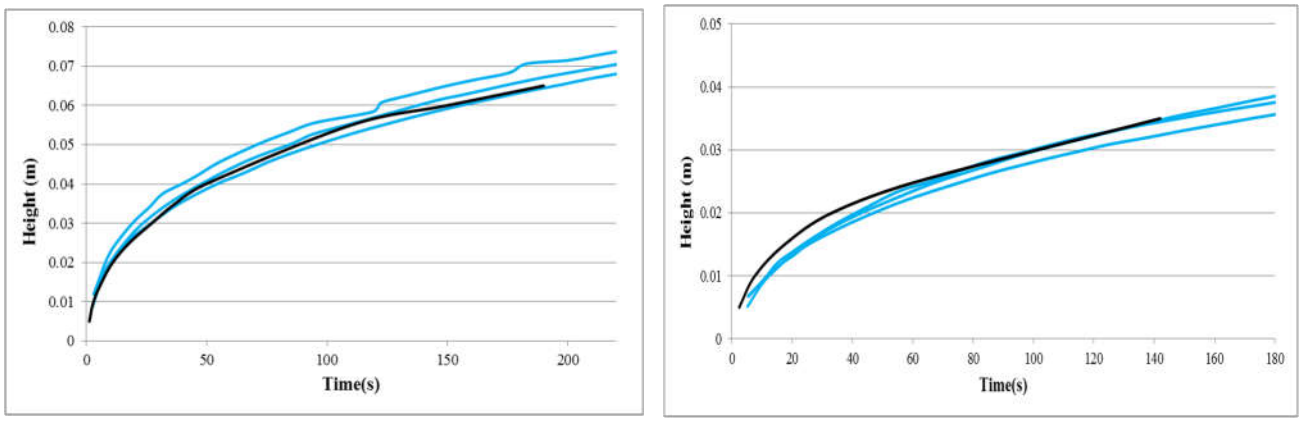

Figure 23: Comparison between the multiple mass-based results and the single visual result. The wick names B1 to B6 and F1 and F2 are given below the respective h_f vs t plots.

3-4-2-4 Comparison of Predictions of Sharp-Front Model with Experimental Results

3-4-2-4-1 Comparing Predictions with the Average Absorbed-Mass Results

To investigate the accuracy of our sharp-front model to predict the height of the liquid front as a function of time for the present set of wicks, we compared the theoretical predictions with the experimental results. Since we observed quite a satisfying correlation between the h_f vs t results obtained from the absorbed-mass and visual approaches for almost all cases, here the predictions of the sharp-front model are compared *only* with the results obtained from the mass-based experiments. Since we repeated our absorbed-mass experiments three times for each wick, in order to have an effective comparison of the theoretical results with the experimental ones, we fitted a curve on all the three sets of experimental results in order to have only one curve for comparison. (As an example, Figure 24 compares the fitted curve with the raw data of all the three experimental cases for the fibrous wicks B1).

As seen in Figure25, the heights of liquid front as predicted by the sharp-front model have a fairly good match with experimental results for all the wicks made from sintered beads (wicks B1-B6). And surprisingly, the sharp-front model performs quite well even for the wicks with semi-sharp fronts (wicks F1 and F2).

These satisfying agreements between the experimental and theoretical results for the wicks with sharp and semi-sharp fronts, *reconfirm* the ability of the sharp-front model to predict the actual height of the liquid front in the wicks. (Some previous examples of successful predictions in other wick-types are listed in [20, 29, 31, 48].)

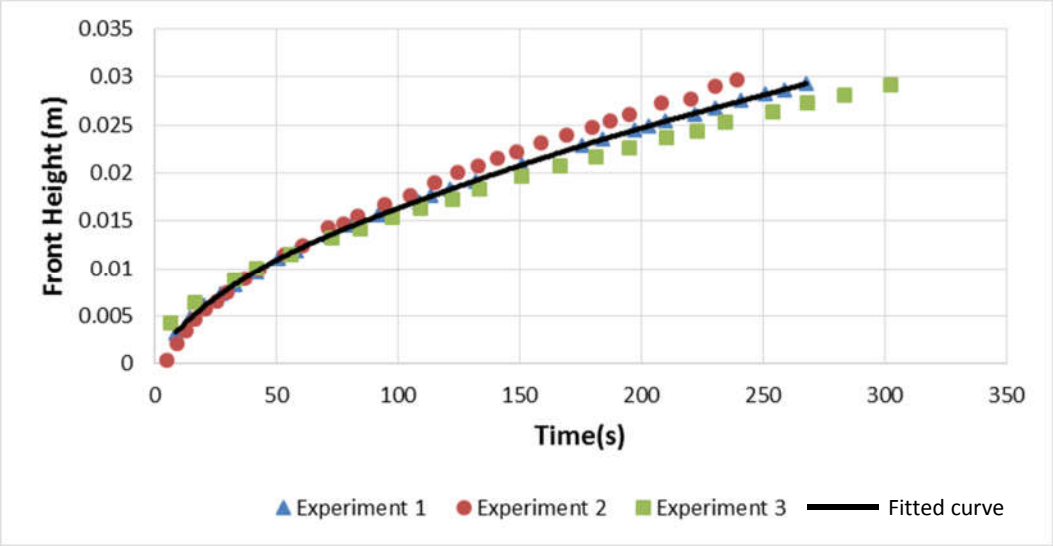

Figure 24: Comparison between the raw data from the three conducted experiments vs the fitted curve for the fibrous wick B1

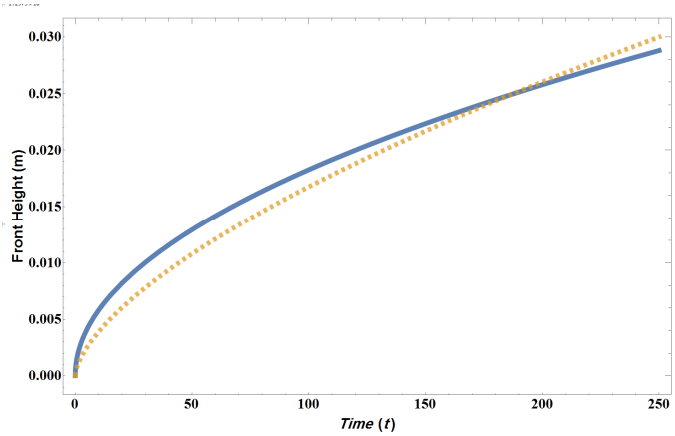

(B1)

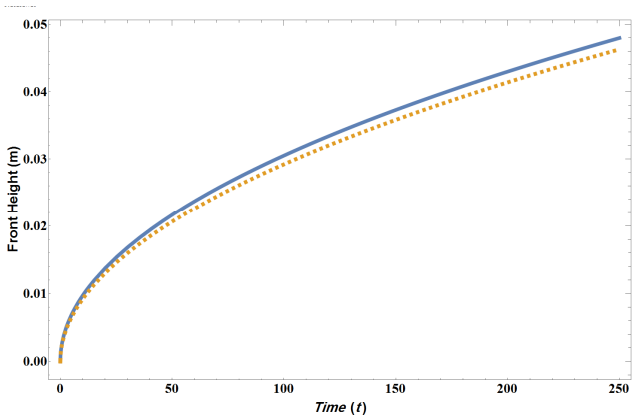

(B2)

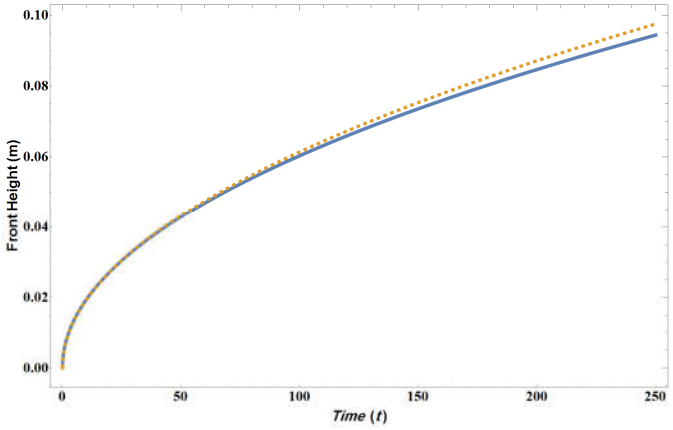

(B3)

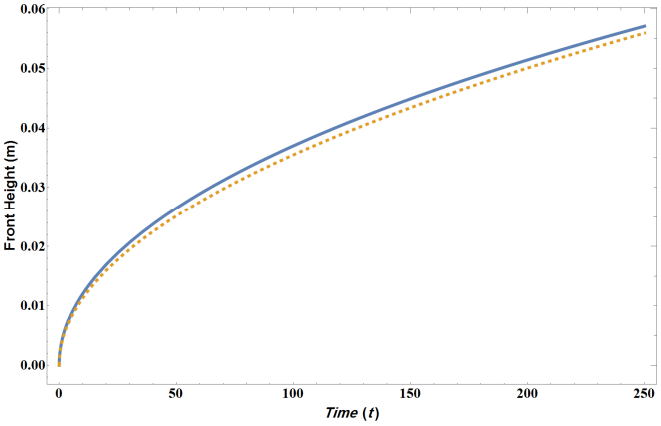

(B4)

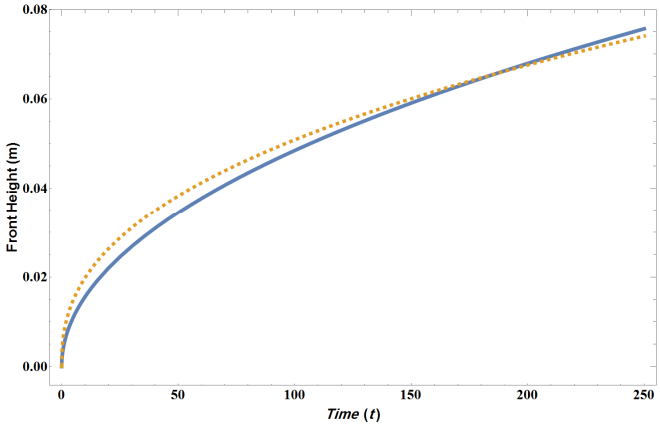

(B5)

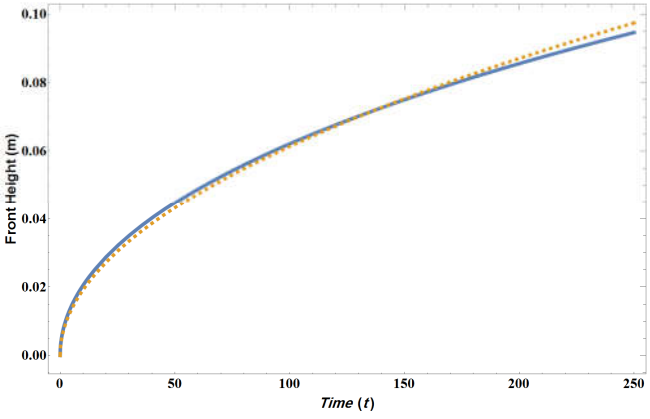

(B6)

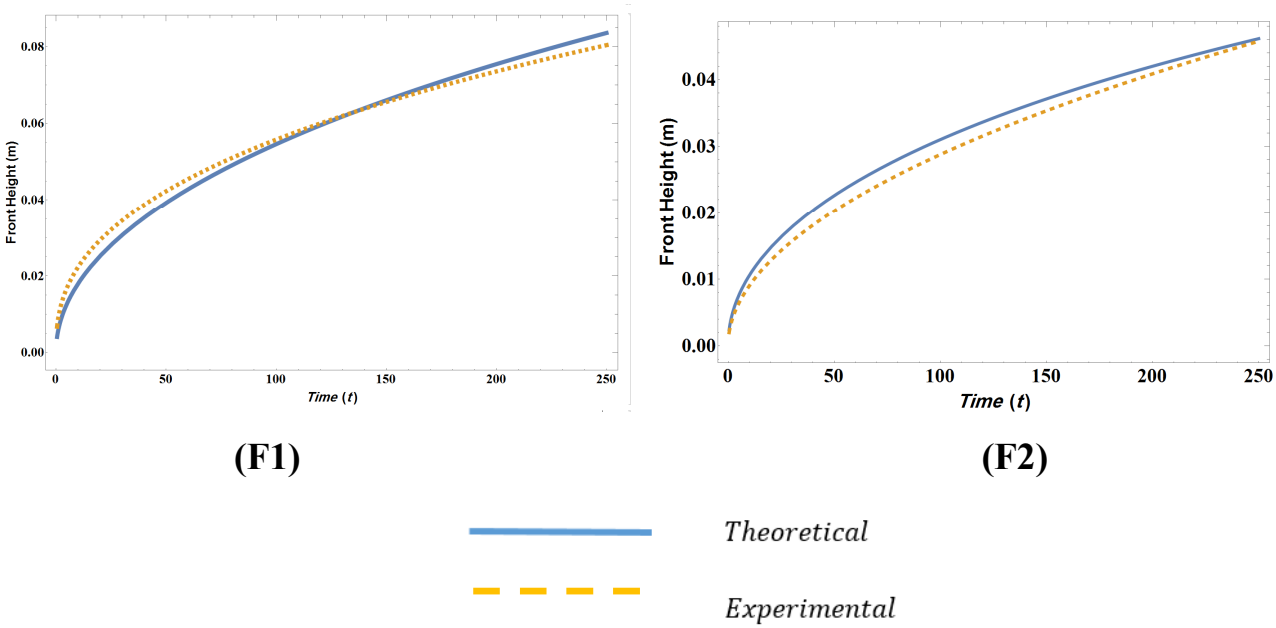

Figure25: The sharp-front model, while predicting the height of liquid-front as a function of time during wicking, is compared with the fitted experimental data for different wicks considered here.

3-4-2-4-2 Comparing Predictions with Visual Result

In order to have an enhanced validation of our sharp-front model, we made another comparison to show the degree of agreement between the theoretically predicted front-height and the visually measured one for each wick at an arbitrary time from the start of the wicking. The comparison is shown in Figure 26.

(B1)(35 sec)

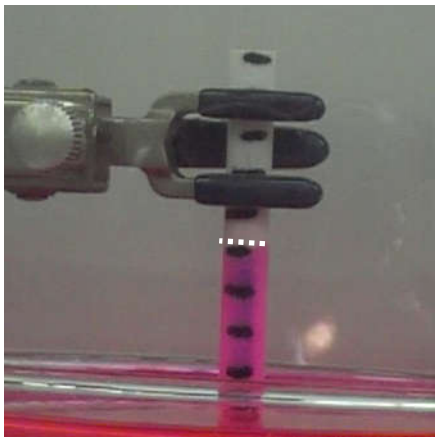

(B2)(40 sec)

(B3)(20 sec)

(B4)(30 sec)

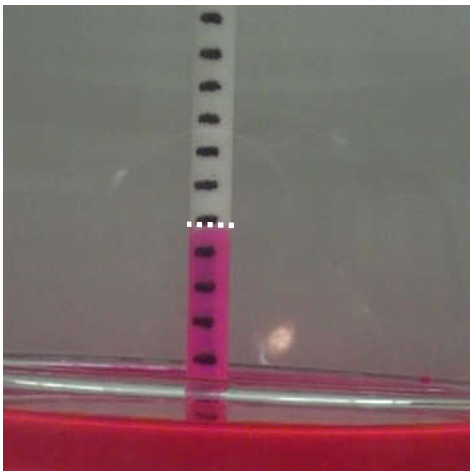

(B5)(35 sec)

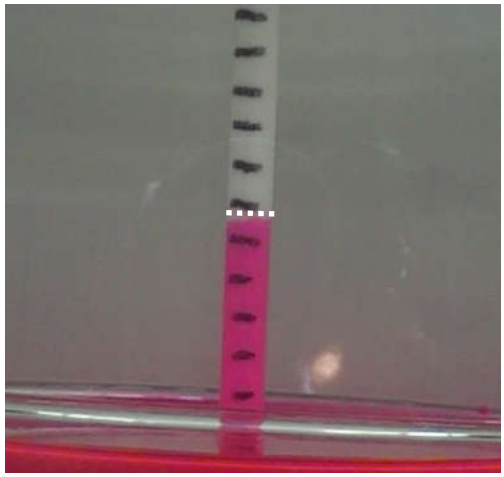

(B6)(40 sec)

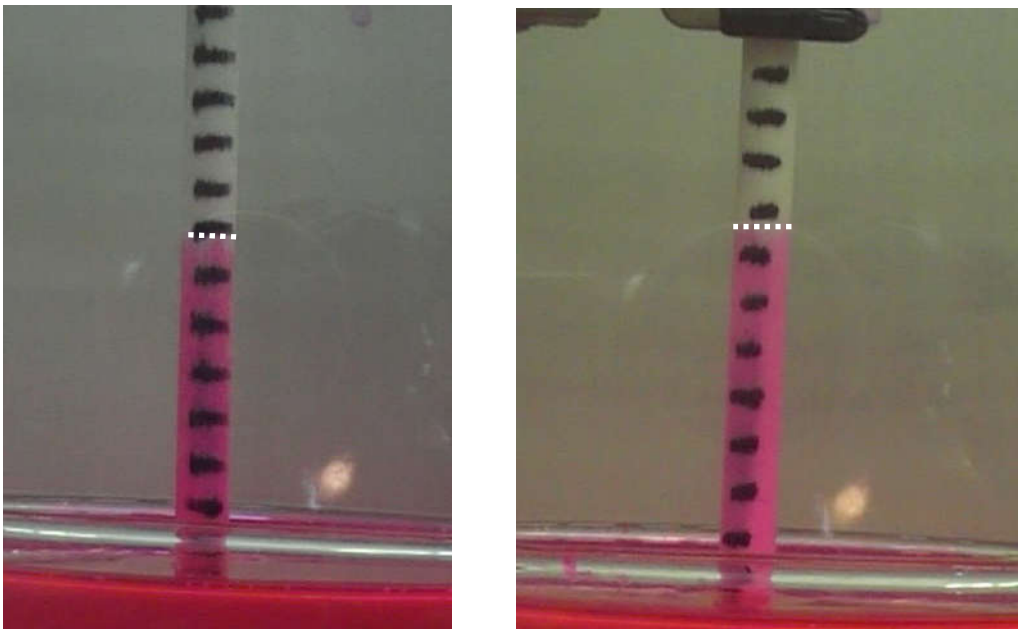

(F1)(40 sec) **(F2)(35 sec)**

Figure 26: Super imposition of the theoretically obtained values for liquid-front height at arbitrary times (shown by white bars) on the snap-shot of wicking for the sintered-beads wicks B1 to B6 and the fibrous wicks F1 and F2.

Figure 26 results reinforce the results observed in Figure25 , i.e., the sharp-front model does a very good job of predicting the rising height of liquid front during wicking for all of the cases of the sintered-beads wicks. What is encouraging to see is that the model is also effective when the fronts are semi-sharp in the fibrous wicks F1 and F2. This is borne by both the corresponding pictures of Figure 26 where the model does an excellent job of predicting the upper boundary of the wetted region.

3-5 Some Applications of Sharp-Front Model

Here we will employ the sharp-front model to discuss the relevance and utility of two important quantities: one, the steady-state height of the liquid front and, two, the flow rate at the

top of the wick. These quantities are often quite important for the users of industrial wicks and can help them in selecting the right wick(s) from a whole set of wicks offered by suppliers.

3-5-1 Steady-state height

Steady-state height (SSH) is the height that the liquid front attains asymptotically after the front speed slows down to zero as the downward gravity force balances the upwards suction force in a wick. SSH is an important parameter if a wick is to be used in the vertically oriented condition. Since the wicks are used essentially to deliver liquids to the wick top from the liquid pool below, it is clear that the wick will fail in this task if SSH is smaller than the wick length. (This is for the worst-case scenario where the liquid level in a container has fallen to its lowest limit and it is barely touching the lower surface of the wick.)

In this regard, the length of a wick relative to SSH plays an important role as sufficient length (< SSH) ensures complete wetting of the whole wick and the fluid can be delivered to the top of the wick for any particular application that it is designed for. A long wick (where length ≥ SSH) may cause low or zero delivery of the liquid as the capillary force is not able to raise the wicking fluid to the top of the wick by overcoming the gravity.

When the liquid is not moving during this steady-state condition, the upward pull on liquid column by the suction pressure is balanced exactly by the downward weight of the column:

$$P_s = \rho g H_{ss} \qquad (70)$$

Here H_{ss} is the mathematical symbol for SSH. The expression for P_s is different for different wicks depending on differences in their microstructures. The suction (capillary pressure) for a porous medium made of parallel fibers and beads are defined (Chapter 5 of [1]), respectively, as

Parallel Fibers $$P_s = 2\frac{1-\varepsilon}{\varepsilon}\frac{\gamma \cos\theta}{R_f} \qquad (71)$$

Beads $$P_s = 2\frac{\gamma \cos\theta}{R_e} \quad (72)$$

On substituting the Eqns 71 and 72 in the Eqn 70, two different expressions for SSH are achieved:

Parallel Fibers $$H_{ss} = 2\frac{(1-\varepsilon)\gamma cos\theta}{\varepsilon R_f \rho g} \quad (73)$$

Beads $$H_{ss} = \frac{2\gamma cos\theta}{\boldsymbol{R_e}\rho g} \quad (74)$$

On using Eqns. 73 and 74, the values of SSHs attained in various wicks are presented in Table 7. Note that they are also compared with the actual lengths of the wicks. The liquid-front speed slows down increasingly as the front comes closer to the final steady-state height. This also means that if the wick length is close to its SSH, the front will take a long time to reach the top.

On studying the table, we find that the wick B1 has the highest SSH compared to its length. Moreover, we have seen that it generates well-defined sharp fronts. Hence, we can surmise that this wick will not ever be dry—the liquid will always reach the top and keep the wick fully wet.

3-5-2 Flow rate at the top of the wick

Wicks are typically used to deliver liquids from a lower level to a higher level in order to replenish the depletion of liquids due to evaporation or some other means. The rate of fluid delivery at the top of the wick, to be called the wick-top flow-rate here, is another important parameter because in many applications, it is essential to deliver a specified amount of liquid in a given time at the ends of the porous wick. Wick-top flow-rate is the rate at which the liquid is traveling through the wick as the liquid front nears the top. This is indicative of the replenishing rate of the wick when a little top portion dries up after the periodic discharge due to natural evaporation or forced evaporation by devices such as the piezoelectric membrane-activated device. Since the

whole length of the wick is used for these computations, this wick-top flow-rate corresponds to the condition when the liquid level in the supply container has fallen to the lowest possible level. Hence this parameter corresponds to the most difficult wicking condition possible when the liquid has to traverse through the *whole* length of the wick.

In the sharp-front model by using Darcy's law, the flow-rate per unit area is given as

$$v = \frac{K}{\mu}\left(\frac{P_s}{H} - \rho g\right) \tag{75}$$

where K is the permeability of the porous medium, H is the height of the wick top above the liquid-pool surface in a container , μ is the fluid viscosity, and ρ is the liquid density. Hence the flow rate at the top of the wick can be estimated to be

$$Q = A_w \frac{K}{\mu}\left(\frac{P_s}{H} - \rho g\right) \tag{76}$$

such that A_w is the wick cross-section area. On substituting Eqns. 71 and 72 in Eqn. 76, the top flow-rate for the investigated fibrous and sintered-beads wicks, respectively, can be deduced to be

$$Q = A_w \frac{K}{\mu}\left(2\frac{1-\varepsilon}{\varepsilon}\frac{\gamma \cos\theta}{R_f H} - \rho g\right) \tag{77}$$

$$Q = A_w \frac{K}{\mu}\left(2\frac{\gamma \cos\theta}{R_e H} - \rho g\right) \tag{78}$$

By using Eqns. 77 and 78, and by entering the actual height of the wicks as the parameter "H", the wick-top flow-rates for all the wicks are estimated. (See Table 4 for the listing.). In addition, from the mass-gain experiments, we are able to obtain mass flow-rates at different heights from the slope of the m(t) vs t plots. By dividing with the liquid density, we can get the corresponding volume flow-rates. We use this approach to get the experimental value of the wick-top flow rate in Table 7. As we can see, the formulas (77) and (78), for the most parts, are

able to predict the wick-top flow rate to an order of magnitude.

Table 7: The steady-state heights as predicted by the sharp-front model for the investigated wicks. The third column lists the wick length for comparison

	H_{ss} (m)	Wick length (m)
Wick B1	1.1392	0.05
Wick B2	0.9558	0.05
Wick B3	0.3722	0.05
Wick B4	0.2643	0.10
Wick B5	0.6429	0.10
Wick B6	0.7580	0.10
Wick F1	0.3524	0.10
Wick F2	0.2706	0.10

Table 8: The flow rate at the top of the wicks (i.e., the wick-top flow-rates) as predicted by the sharp-front model in comparison with the values obtained from the mass-gain experiments.

	Wick-top flow rate (m^3/s) Theoretical	Wick-top flow rate (m^3/s) Experimental
Wick B1	1.34E-09	1.21E-9 ± 1.7E-10
Wick B2	4.93E-09	3.20E-09 ± 2.05E-10
Wick B3	1.05E-08	1.39E-08 ± 1.17E-9
Wick B4	4.35E-09	6.01E-09 ± 2.03E-10
Wick B5	5.89E-09	4.25E-09 ± 3.26E-10
Wick B6	7.09E-08	7.47E-08 ± 1.31E-9
Wick F1	1.47E-08	2.76E-8 ± 1.02E-9
Wick F2	7.83E-09	6.18E-09 ± 4.5E-10

3-6 Summary and Conclusions

In this chapter, a theoretical model for wicking of a liquid into different types of wicks, is developed based on the sharp-front or plug-flow assumption with single-phase Darcy flow occurring behind a clearly-defined liquid front. Such an approach is superior to the traditional Washburn equation based approach derived from unidirectional capillary tubes as it allows one to model wicking in 2-D and 3-D geometries. The newness of the formulation lies in the fact that it was developed for wicking along fibers of a transversely-isotropic porous wick made from wicks of parallel glass fibers. (This is in contrast to the previously published formulations for sintered wicks that act as isotropic porous media.[20]) The simplification of the permeability tensor for this system leads to a straight-forward development of a formula for the liquid-front height as a function of time. Later, the liquid-front height was shown to be directly obtainable from the mass of the liquid absorbed by the wick as a function of time.

The proposed theoretical model is tested against the results of mass-gain experiments designed to study wicking of a liquid in vertical wicks. For some wicks, an extra comparison is presented between: The results of mass-gain experiments and the result of visually tracked liquid front. For all the sintered-beads wicks with sharp fronts and a couple of fibrous wicks with semi-sharp fronts, a good comparison is obtained. This indicates that 100% saturation behind the liquid front for these wicks is a good approximation. In order to avoid the usage of any fitting parameters, all the parameters involved in the problem were measured independently. They included the properties of the fibrous and sintered beads porous wicks [porosity, axial permeability, fiber diameter], properties of the wetting liquid [viscosity, surface tension] and finally, the property related to the interaction between the solid and liquid phases [contact angle]. Estimation of the axial permeability, measured using the falling head permeameter, involved developing a novel

formula using the flow formulation for a transversely-isotropic fibrous wick.

From the comparison of the experimental results with the theoretical predictions, it was observed that the proposed theoretical model is able to predict wicking most satisfactorily. Our proposed model is powerful as it clearly and explicitly explain the dependence of liquid rise in wicks to the fluid and porous media properties.

After observing an excellent performance by the sharp-front model in the 6 polymer sintered-beads wicks and 2 fibrous wicks, we use it to derive some parameters often found necessary for industrial applications of cylindrical wicks. The parameters are the steady-state height of the front (i.e., the maximum height that the wicking liquid could reach), and the flow-rate at the top of the wicks (which gives the rate of liquid supply to the wick top). The predicted values of the steady-state height is found to be at least 2 or 3 times longer than the actual lengths of most wicks, which assures us that the wick is going to be completely saturated during its operation. The sharp-front model is able to predict the flow-rate at wick-top quite well (within the order of magnitude) for all the wicks.

Chapter 4: Diffuse-front Model

Before presenting our diffuse-front model from Sec. 4-2 onward, we present the limitation of the sharp-front model for certain wicks in Sec. 4-1.

4-1 Preface

As observed in chapter 2, the wicking experiments showed that the wicking process happens with diffusive liquid-front in the fibrous wicks F3, F4, F6, F7, and F9 to F11. In the previous chapter by comparing the experimental results from the mass-gained experiment with the results obtained from the predictions of the theoretical model, it was observed that the sharp-front model is able to predict the progress of front height in most wicks with sharp and semi- sharp fronts, i.e., wicks B1 to B6, and F1 and F2. Now, In order to evaluate the usefulness of the sharp front model and its applicability for the diffuse-front wicks, we first characterize the wicks. Then, we evaluate the accuracy of the developed sharp-front theoretical model, by comparing the predicted values with experimental results.

4-1-1 Characterization of wicks showing diffuse front

In the same way we characterized the properties of wicks showing sharp fronts, we characterize the rest of the wicks, all fibrous wicks showing diffusive liquid fronts.

4-1-1-1 Measurement of Fiber Diameter

The diameter of the fibers used in the studied wicks, F3, F4, F6, F7, and F9 to F11 were measured carefully under an optical microscope and their values are presented in Table 9.

4-1-1-2 Porosity Measurement

For measuring the porosity, again, we use two different methods: 1-Dipping Method 2-

Micrograph Method and the procedures are exactly as explained in chapter 3. All the presented porosity values in Table 9 were measured with 95% confidence interval. The corresponding micrographs for wicks F3, F4, F6, F7, and F9 to F11 are shown in Figure 27 for the seven investigated wicks.

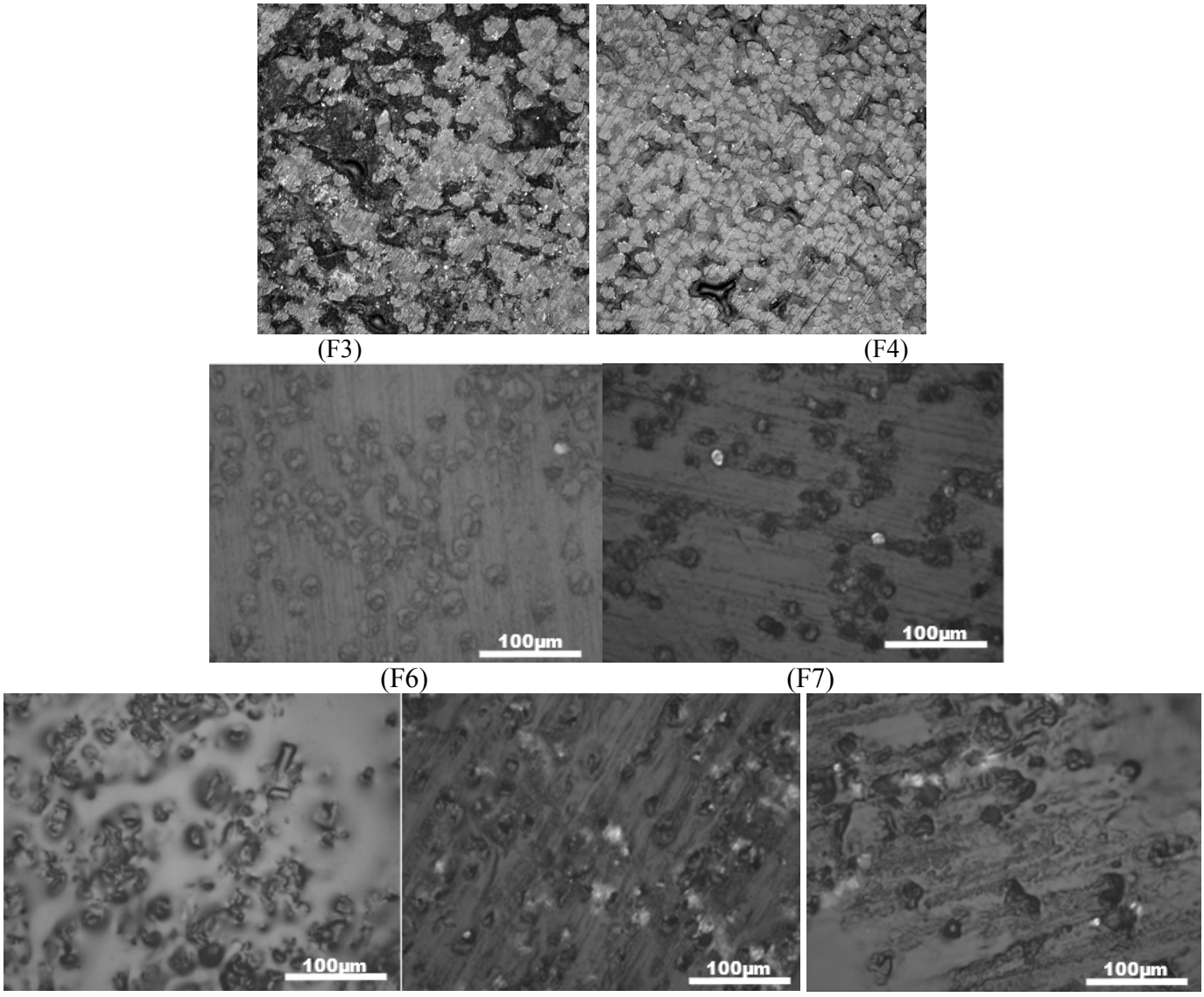

Figure 27 Typical optical micrographs of the cross-sections of wicks samples cast in epoxy for measuring the porosity ($\varepsilon = \frac{V_v}{V} = \frac{\text{Area}_{\text{matrix}}}{\text{Area}_{\text{total}}}$) . The spotty dark spots represent fiber cross-sections while the lighter background is the epoxy matrix. The photographs correspond to the wicks F3, F4, F6, F7, F9 to F11, respectively

4-1-1-3 Measurement of Surface Tension, Viscosity & Contact Angle

As we used the same type liquid throughout our investigation for each batch of the wicks (independent of the type of liquid front), the values for surface tension and viscosity can been found from Table 1. The process of measuring contact angles is the same as explained in section 3-3-3.

4-1-1-4 Permeability Measurement

The permeability values for fibrous wicks F7, F10 and F11 were explained in detail in the section 3-3-5. We followed the same experimental procedure for fibrous wicks F3, F4, F6 and F9. In order to use the falling head permeameter in the most accurate way (which requires the flow of liquid to be just in one direction), we covered the lateral side of the cylindrical wicks with special type of glue (Figure 28) before running the test. This prevented the radial flow of the liquid and generated the required 1D flow along the wick axis. Each test was repeated five times to generate the average as well as the scatter (95% confidence interval) in the permeability values.

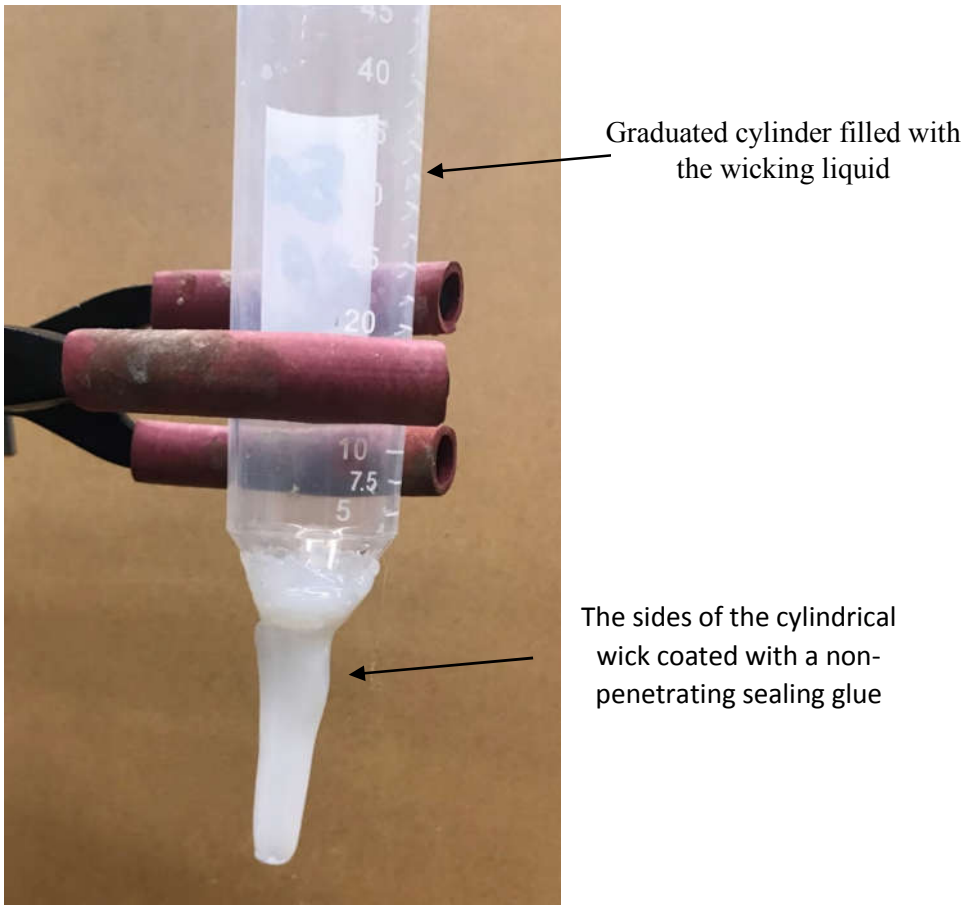

Figure 28: A custom-made falling head permeameter used for measuring the permeability of the wicks

Table 9 **.** Measured Properties of the eight investigated wicks (Each measured property is shown along with a 95% confidence interval.)

Wick	Fiber Diameter (µm)	Porosity (Micrograph Method)	Porosity (Dipping Method)	Contact Angle (Degree)	Permeability (m^2)
F3	21.81±1.28	0.85±0.08	0.83±0.04	0	1.25E-11±2.5E-12
F4	25.22±0.85	0.85±0.03	0.84±0.06	0	8.15E-11±5.31E-12
F6	29.93±0.937	0.85±0.07	0.82±0.02	81.33±0.74	3.35E-10±6.72 E-11
F7	22.08±0.55	0.79±0.05	0.79±0.07	80.06±4.12	3.92E-10±4.70 E-11
F9	19.47±0.39	0.81±0.02	0.81±0.01	87.13±1.26	3.83E-10±7.19 E-11
F10	24.77±0.52	0.81±0.02	0.81±0.01	82.85±4.46	3.81E-10±8.27 E-11
F11	25.58±1.39	0.74±0.08	0.77±0.01	80.25±3.12	3.94 E-10±7.05 E-11

4-1-2 Theoretical Model

In order to predict the height of liquid front as a function of time, we used the same theoretical model, Eqn 22 (Page 22). The predict values will be compared with experimental results to evaluate the accuracy and applicability of this model.

4-1-3 Results and Discussion

To investigate the accuracy of our sharp-front model to predict the height of the liquid front as a function of time for the present set of wicks, we compared the theoretical predictions with the experimental results. We follow the same procedure that we did in previous chapter. Hence, first, for wicks F6, F7, and F9 to F11, we compare the theoretical results with all the experimental result obtained from mass gain experiment. Second, for wicks F3 and F4, we conduct both mass gain experiment and tracking the progression of liquid front visually. After comparing the visual result with the result of mass gain experiments, we fitted a curve on the result of mass gain experiments to be compared with theoretical result. In addition, we made another set of comparison between theoretical result and the visual result. All the procedure of conducting mass gain experiment, tracking the liquid visually, curve fitting is done in the same way as that of chapter 3. Hence, we just present the comparison sections.

4-1-3-1 Sharp-front model evaluation for wicks F3, F4, F6, F7, and F9 to F11

4-1-3-1-1 Comparison of Predictions of Sharp-Front Model with mass-based Experimental Results

As shown in Figure 29, for wicks F7 and F9, the theoretical model initially over-predicts the wicked height marked by large deviations. However, as the time progresses, the theoretical curve asymptotically merges with the experimental data points. In fact, the experimental data seem to behave bilinearly—initial linear rise followed by another linear rise of the lower slope.

Though the match is not as satisfying as the previous cases of having sharp fronts, the theoretical curve seems to provide an excellent upper bound to the experimental data. The behavior of wicks F10 and F11 shown in Figure 30 follows a similar trend, but perhaps to a lesser extent. Initially, the experimentally data diverges from the theoretical curve. But as the time progresses, a good match is reached asymptotically.

The behavior of wick F6 in Figure 31 is markedly different from the wicks studied till now. It seems that the theoretical model under predicts the wicking height till about 10 seconds, and then exhibits the usual trend of over predicting the wicking height seen in the other wicks. It is also surprising to note that the experimental data for wick F6 demonstrates a linear trend unlike the bilinear trend seen for the other wicks.

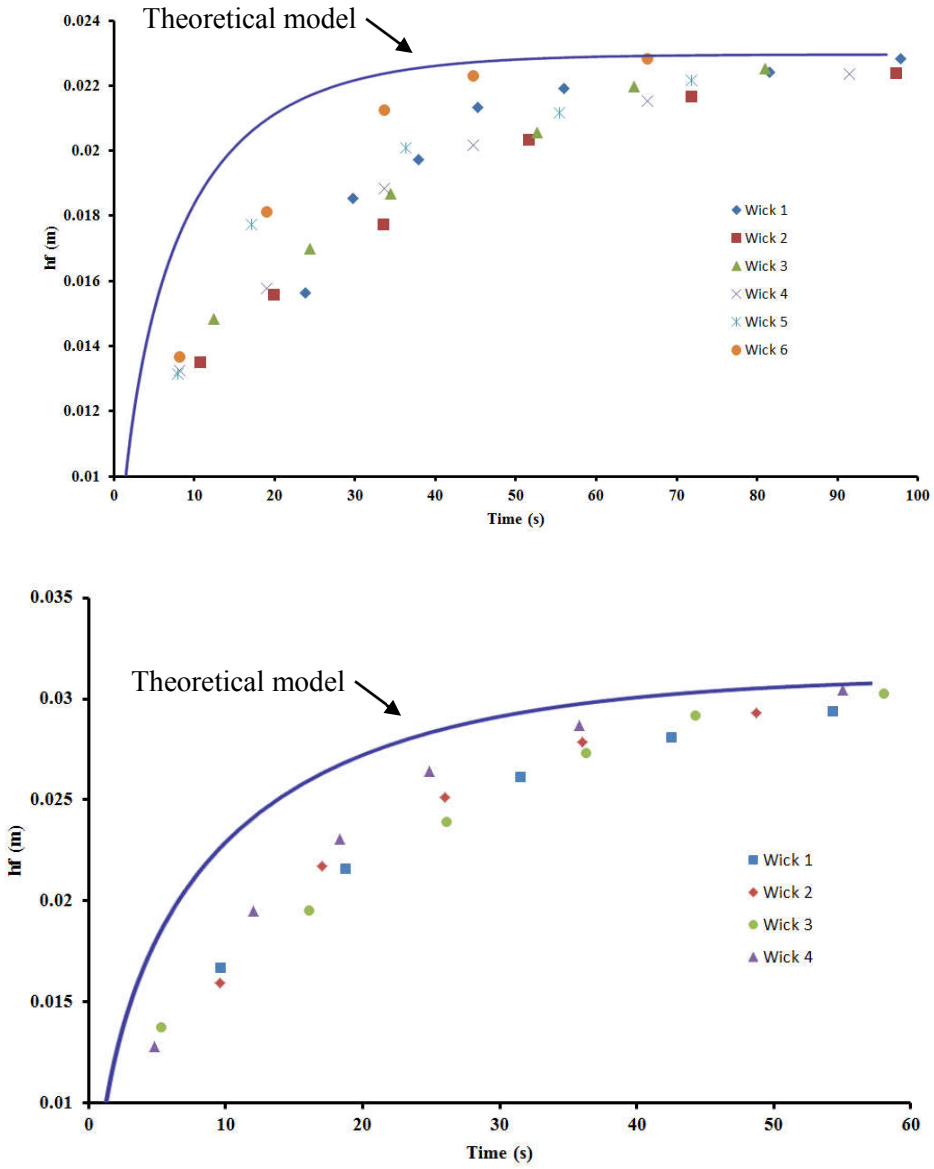

Figure 29 The proposed theoretical model for predicting the height of liquid-front as a function of time during wicking. The model is compared with the experimental data for the wicks F7 and F9. The legends show the number of wicks that we repeated the mass gain experiment for each type of the wicks

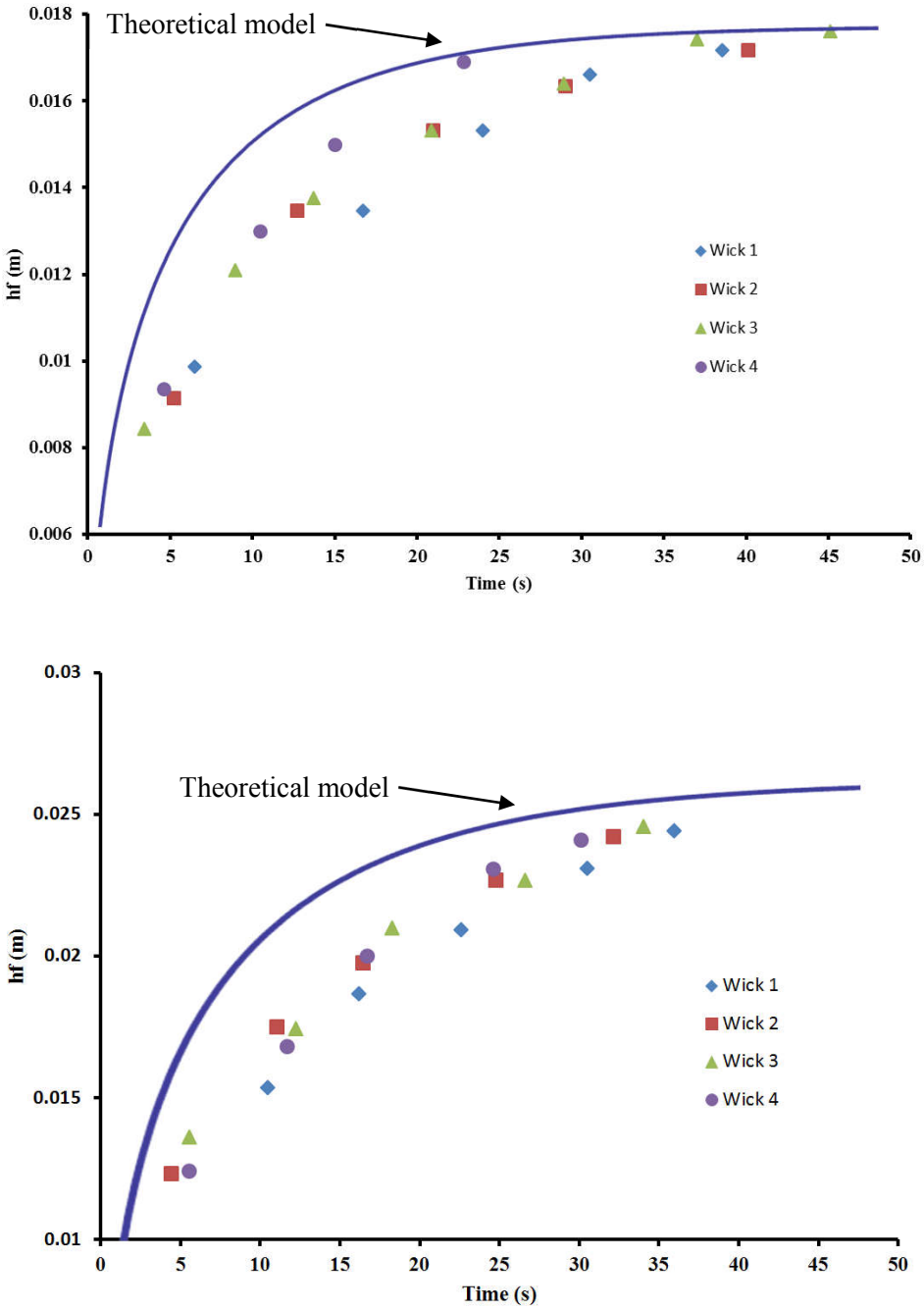

Figure 30 The proposed theoretical model for predicting the height of liquid-front as a function of time during wicking. The model is compared with the experimental data for the wicks F10 and F11

The legends show the number of wicks that we repeated the mass gain experiment for each type of the wicks

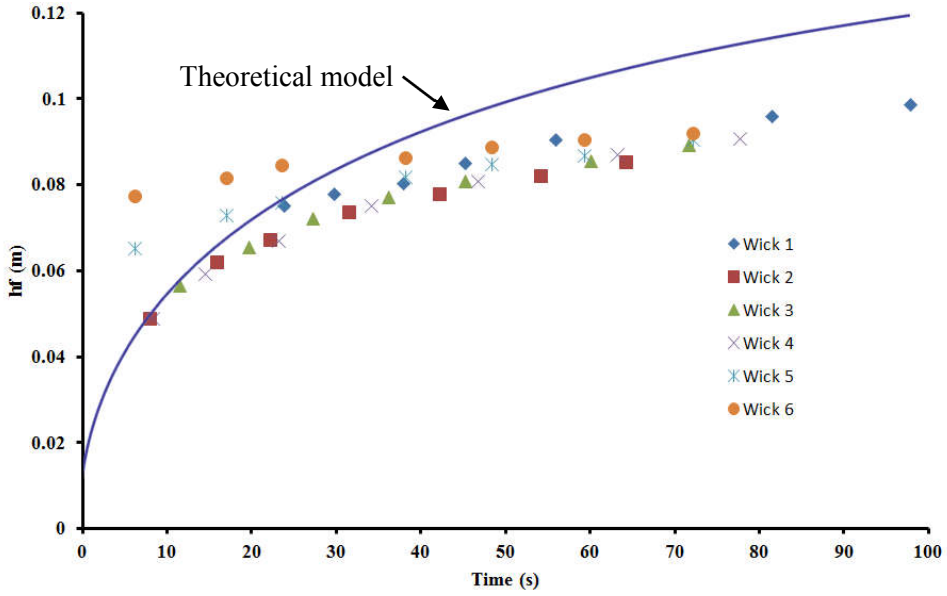

Figure 31 The proposed theoretical model for predicting the height of liquid-front as a function of time during wicking. The model is compared with the experimental data for wick F6
The legends show the number of wicks that we repeated the mass gain experiment for each type of the wicks

4-1-3-2 Sharp front model evaluation for Wicks F3 and F4

4-1-3-2-1 Comparison of the mass-based and visual results

In contrast to the fibrous wicks which display the semi-sharp fronts (F1 and F2), the diffuse-front wicks (F3 and F4), the present wicks, do not show such a good match between the mass-based and visual results: the visual results are clearly different from the mass-based ones.

We also would like to report on the phenomenon of the liquid fronts fading as it moves away from the source of the liquid. As seen from Figure 32, the reason the visual lines for the fibrous wicks F3 and F4 are shorter compared to the other wicks, is the fast transformation of the liquid-front from a sharp one to a diffusive one. Initially, as the liquid front is sharp we were able to track the movement of the front easily, but when the front turned into diffusive

front, we were not able to track the liquid-front visually and hence we had to cut short the process of data gathering.

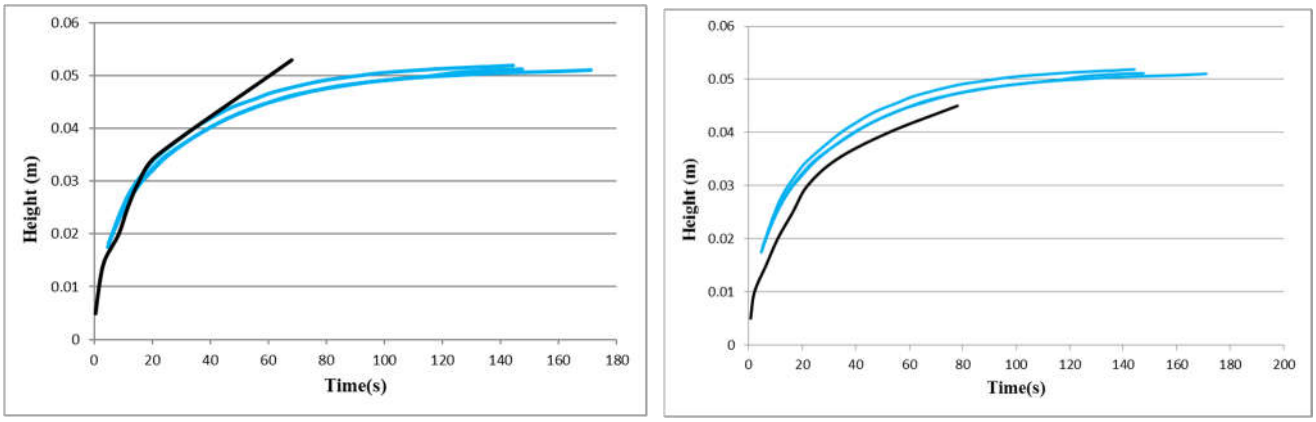

(F3) (F4)

Liquid-mass absorption estimation

Visual estimation

Figure 32: Comparison between the multiple mass-based results and the single visual result. The wick names F3 and F4 are given below the respective h_f vs t plots

4-1-3-2-2 Comparison of Predictions of Sharp-Front Model with Experimental Results

4-1-3-2-2-1 Comparing Predictions with the Average Absorbed-Mass Results

As seen in Figure33, the model is not able to predict the liquid-front height accurately for the wicks with diffuse fronts (wicks F3 and F4)—for the first 25 seconds, it has a good correlation with experimental results; but beyond that point it over predicts the height.

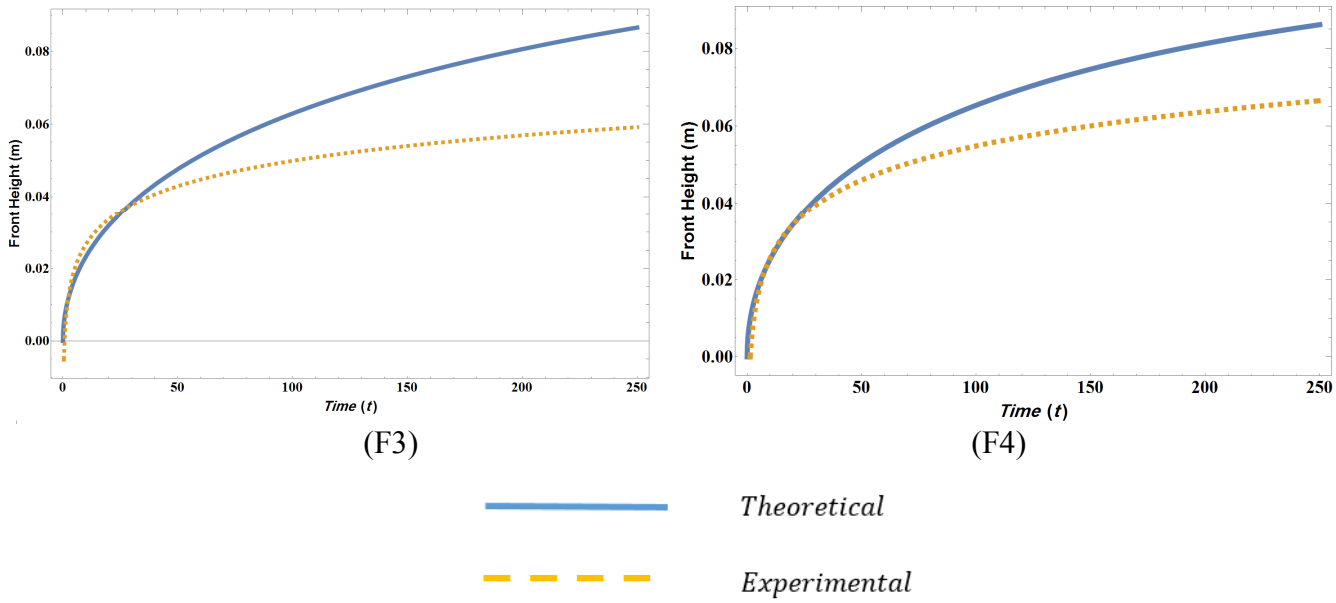

Figure33: The sharp-front model, while predicting the height of liquid-front as a function of time during wicking, is compared with the fitted experimental data for wicks F3 and F4 considered here.

4-1-3-2-2-2 Comparing theoretical predictions with visual result

Like the latter comparison, for the wicks F3 and F4, the sharp-front model basically fails—the comparison in Figure 34 shows a big difference between the predicted and experimentally observed 'height' of the liquid front. In fact, the dash corresponding the prediction lies somewhere in the middle of large smeared region (where the saturation progressively decreases from 100% to 0% over a significant length of the wick). This observation essentially reinforces the large difference in the curves seen in Figure33.

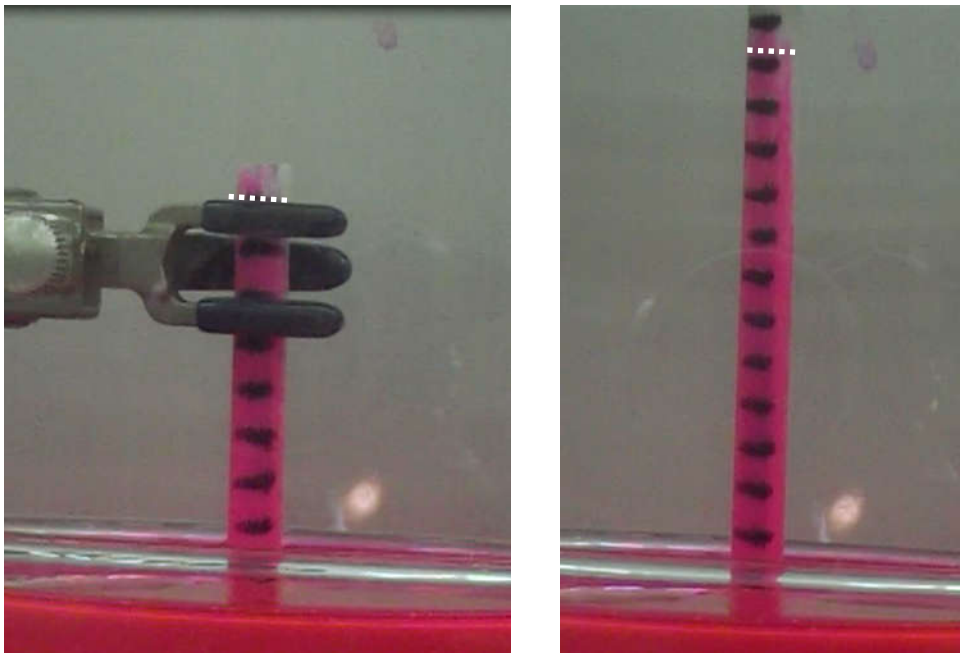

(F3)(75 sec) (F4)(83 sec)

Figure 34: Super imposition of the theoretically obtained values for liquid-front height at arbitrary times (shown by white bars) on the snap-shot of wicking for fibrous wicks F1 to F4

4-1-4 Conclusion

The most obvious conclusion form all the comparison is that the sharp front model fails in prediction of height of liquid front as a function of time for wicks having diffusive front during the wicking process. Here we would like to offer some possible reasons for the divergence of our theoretical model in general from the experimental results. One reason could be the generally higher contact angles, and hence corresponding lower wettability, of the wick + liquid system. This may affect the ability of the wetting phase to displace the non-wetting phase (air) in the porous wick and thus create a sharp-front liquid front. Another reason could be the phenomenon of fiber clustering in the fibrous wicks. From the study of micrographs of various wicks shown in Figure 10, it is clear that the fibers are not distributed equidistantly creating a homogeneous porous medium—rather they are present in the form of groups or clusters leading to local inhomogeneities.

Derivation of Eq. 22 is based on the assumption that the wicks are homogeneous—local clustering leads to the breakdown of this assumption and thus undermines the efficacy the proposed model. Another reason is that fiber clustering leads to preferential climbing of the liquid along these narrow ‘channels’ due to higher capillary pressures (see Figure 35). This could lead to smudging of the sharp saturation change near the liquid front, thereby violating the 100% to 0% step-down in saturation near the front (mandatory for our sharp-front assumption). Under these circumstances, the efficacy of the model proposed in Eq. 22 is in question, and one is perhaps advised to apply the Richards equation (see Chapter 6 of [1]) for modeling wicking under such smudged-front conditions.

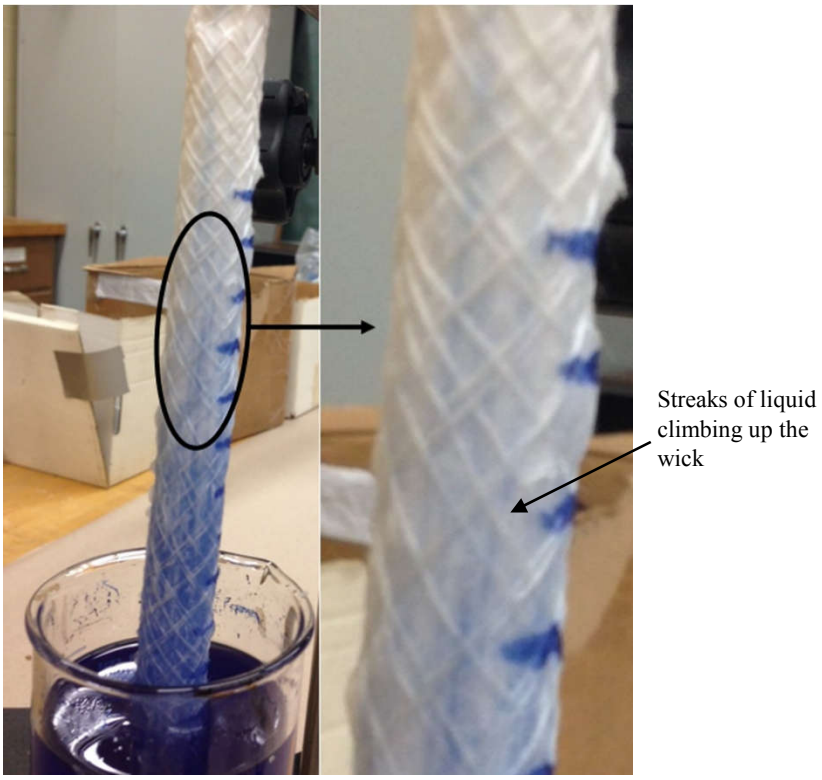

Figure 35 Presence of streaks of liquid in the wicks led to a partial-saturation region above the liquid surface. The phenomena can be attributed to fiber clustering that created higher capillary (suction) pressures at the liquid-air interface, leading to pulling up of liquids along those narrower capillary 'channels'

4-2 Introduction

In chapter 3, we developed a sharp-front model to predict spontaneous imbibition of liquids in fibrous wicks which had a good correlation with experimental results in predicting the absorbed mass of liquid, but had a big difference with experimental results in failing to account for partial saturation in the wick and in predicting the actual height of the liquid-front. Though the liquid was observed to have wicked till the top of the 20-cm-tall wick Figure 35, the height of the saturated region was predicted by our model to be only a few millimeters!

The partial saturation seems to be occurring due to fiber clustering, as shown in Figure 36,

which result in local inhomogeneity within the wick, with the fiber clusters acting as channels for the wicked liquid to travel to wick top due to higher local capillary (suction) pressures. Under such conditions, the saturation of the wetting phase, after starting with a value of unity in a fully saturated zone near the wick bottom, gradually drops to zero as one goes higher in the dry portions of the wick.

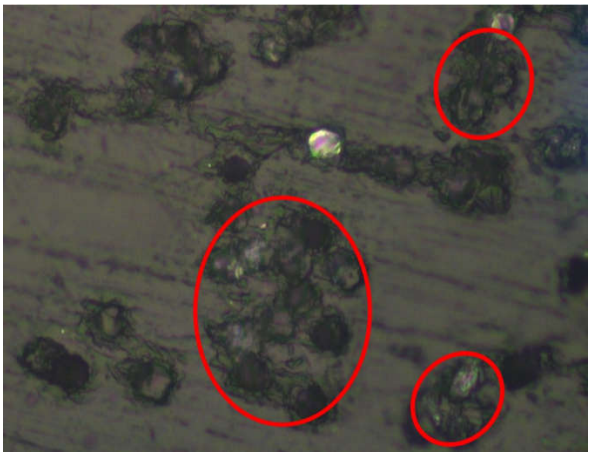

Figure 36 Fiber clustering in the investigated wicks caused local inhomogeneity, leading to upward travel of the imbibed liquid along the channels created by fiber-clusters, and thus resulting in partial saturation along the wick axis

Richards [36] proposed a model for diffusion of moisture in unsaturated regions of soil. Richards equation is used for modeling unsaturated flows in porous media where the motion of only liquid is predicted using the variable saturation while the other phase present in the porous medium, the air, is assumed to be at atmospheric pressure and stationary. Richards equation is an elliptic equation (like the heat equation) that predicts the diffusive saturation field throughout a porous medium as a function of time. In this chapter, we used Richards equation to investigate its ability to predict the saturation distribution of the imbibed liquid into the fibrous wick. This equation is highly non-linear because of the dependence of important parameters, such as the capillary pressure and relative permeability, on local saturation in porous media that varies

spatially as well as temporally in the wick. As a result, it requires using a numerical approach to predict saturation distributions.

In past few decades, Richards equation as a useful tool for predicting partial saturation has been solved numerically and analytically using various numerical schemes such as the finite difference method, the finite element method, and the boundary element method for different cases of porous media, especially soils [61-70]. For fibrous media, Jaganathan *et al.* [71] solved Richards equation in one dimension for inclined fibrous sheets (which had been examined formerly by Landeryou et al.[45]) and were able to predict the region of partial saturation. Furthermore, they validated their partial saturation predictions experimentally. In order to determine saturations at different heights, they cut strips corresponding to different heights along a thin fibrous sheet and then weighed them [1].

In this chapter, the Richards equation is used to predict liquid saturations inside the fibrous wicks made of aligned fibers. In order to find the saturation levels of the liquid in a transversely-isotropic porous medium with a principal direction of the permeability tensor aligned with the flow direction as a function of time and location, we developed and solved an expression based on Richards equation. In addition, in order to have a precise comparison between experimental results and numerical outcomes, we solved the Richards equation as a partial differential equation numerically in 2-D using COMSOL and analytically in 1-D using Mathematica. All the related properties such as capillary pressure and relative permeability equations as a function of saturation were calculated *directly* for our particular fibrous porous medium using the state-of-the-art software GeoDict while solving for pore-scale flows within the wick microstructure. [This is unlike the trend seen in literature where the analytical expressions available in the literature for capillary pressure and relative pressure as a function of saturation are used to predict wicking

(chapter 5 of reference [1])]. The obtained numerical solutions of Richards equation were compared with the experimental results which were obtained by measuring saturations (or liquid content) of the wicks at different axial locations. Comparing of the numerical and experimental results indicated that there is a satisfying correlation between the measured saturation levels and the numerical predictions. This good agreement allows us to repose confidence in the saturations predicted using Richards equation for unsaturated flows in porous media.

4-3 Model for wicking using Richards equation

4-3-1 Mathematical Formulation

Based on the derived Richards equation in Appendix 3, Eq. A36 is the classic form of Richards equation for tracking the movement of moisture in porous media [26]. A numerical solution of this equation for predicting diffusive moisture migration under the influence of capillary pressure in 2D or 3D can be easily obtained.

If we ignore variations in the cross-sectional plane of the wick and assume the moisture flow to be one-dimensional along the vertical axis of the wick, parallel to the fiber direction, Eq. A36 (page 175) can be simplified to

$$\frac{\partial S_w}{\partial t} = \frac{\partial}{\partial z}\left(D_{zz}(S_w)\frac{\partial S_w}{\partial z}\right) - D_g(S_w)\frac{\partial S_w}{\partial z} \tag{79}$$

The coefficients $D_g(S_w)$ and $D_{ij}(S_w)$, called the diffusivity coefficient and the capillary diffusivity tensor, respectively, are formulated as

$$D_g = -\frac{\rho g K_{zz}}{\varepsilon \mu}\frac{\partial k_r}{\partial S_w} \tag{80}$$

$$D_{ij} = -\frac{K_{ij}}{\varepsilon\mu}\frac{\partial\langle p_c\rangle^f}{\partial S_w}k_r(S_w) \tag{81}$$

where k_r is the relative permeability and $\langle p_c\rangle^f$ is the capillary pressure. (As per the porous-media physics, both of these are functions of liquid saturation S_w.) Here the suffixes i and j can take values x, y and z. Note that when the z principal direction is aligned with the wick axis, the permeability tensor is diagonal in such a transversely-isotropic medium, and hence the capillary diffusivity tensor is diagonal too.

4-3-2 Physical Properties required to solve Richards equation

As the equations (80) and (81) for the diffusivity coefficient and the capillary diffusivity tensor show, the two properties, the capillary pressure $\langle p_c\rangle^f$ and the relative permeability k_r, are functions of the saturation S_w and they should be substituted with appropriate expressions in order for anyone to be able to solve the Richards equation. It is important to have smooth analytical expressions for these two quantities in order to have a trouble-free numerical solution. Some empirical correlations between the capillary pressure and saturation, and between the relative permeability and saturation have been employed in several flow studies [45, 72-76] related to soil and fibrous porous media. In this chapter, the investigation is done on four wicks, F3, F4, F6 and F7, selected from each batch of wicks showing diffusive front.

4-3-2-1 Capillary pressure and relative permeability as a function of saturation

Capillary pressure as a function of saturation in a fibrous medium is dependent on the distribution and amount of void space in porous media. The variations in a medium's microstructure have an impact on $\langle p_c\rangle^f$ because the inter-fiber spacing decide the magnitude of

local capillary pressure at liquid-air interfaces. Empirical correlations between capillary pressure and saturation for a given porous medium have been derived in several studies [45, 72-75] on soil or fibrous porous media. In this chapter, we found a direct way of generating accurate equations for capillary pressure and relative permeability as a function of saturation. In this regard, 3-D microstructures for wicks consisting of unidirectionally-aligned fibers were first generated using GeoDict, a software developed by Fraunhofer-IWTM Germany (http://www.GeoDict.com). [We neglected any kinks in the fibers.] GeoDict is a voxel-based computer program where the fluid-filled domain is represented by empty voxels while the solid fibers are represented by filled voxels. In order to generate the geometry, we used the FiberGeo module of GeoDict; first we inputted relevant properties and information, such as fiber diameter, solid volume fraction, and direction characteristics, which had been measured earlier. Then, this module started to pack the unit-cell with parallel fibers randomly. The wicks are made of fibers with approximately the same diameter that are aligned unidirectionally, we consider our wicks as an anisotropic medium directed in the vertical direction, Z axis. See Figure 37 for the unit-cells generated for the wicks F3, F4, F6 and F7.

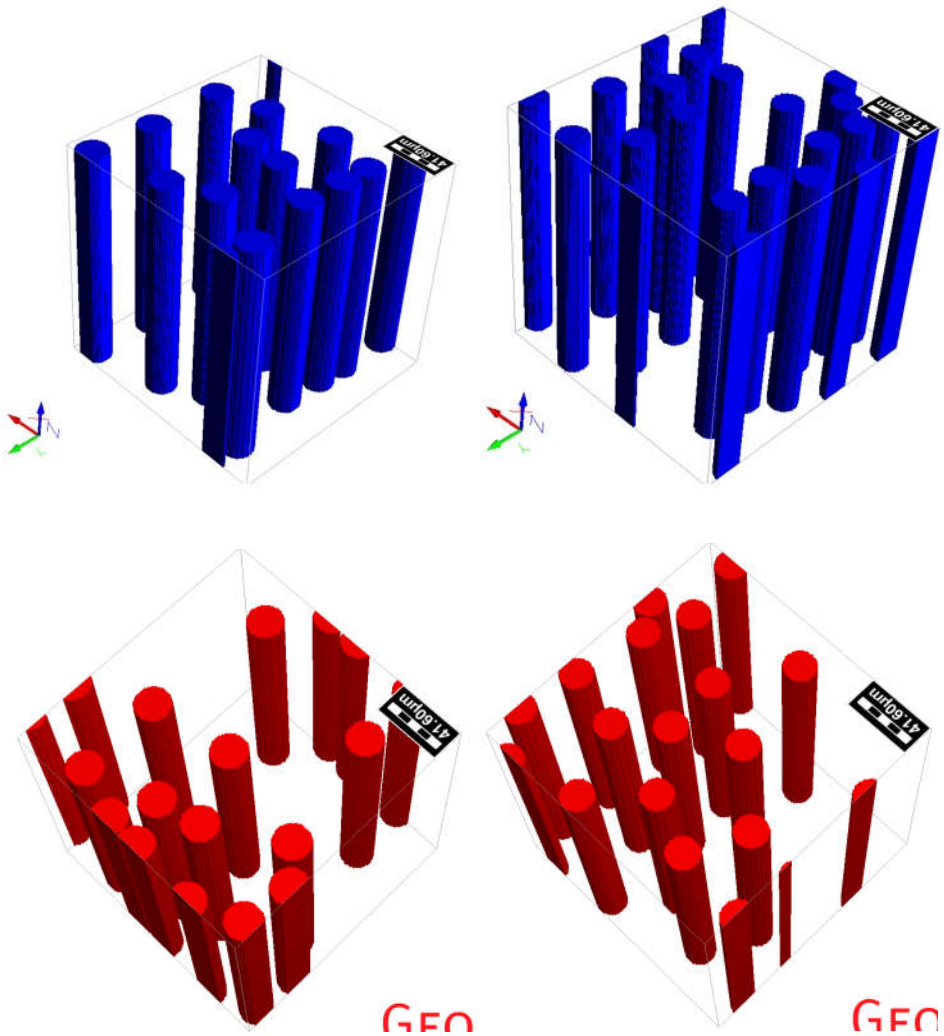
41.60µm
41.60µm
41.60µm
41.60µm
25.00µm
25.00µm

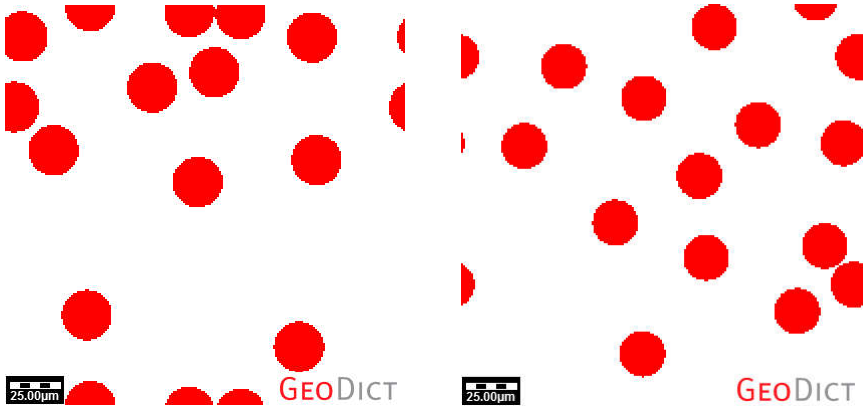

Figure 37 Unit-cells generated by GeoDict representing the fibrous microstructure of glass-fiber wicks made of unidirectional fibers (a), (b) , (c), (d) Generated 3D unit-cells for wick F3, F4, F6 and F7, respectively; (e), (f), (g), (h) Top view of the 3-D unit-cells generated by GeoDict for wicks F3, F4, F6 and F7, respectively.

In the first stage, the generated geometries were used to obtain the capillary pressure-vs-saturation plots by using the full morphology (FM) Method. The full morphology (FM) is an algorithm, which is implemented in GeoDict and uses a quasi-static geometric approach for obtaining a relationship between saturation distribution and capillary pressure within a unit cell. This method was first developed by Hazlett [77], and later used by Hilpert and Miller [78] for porous media such as soil, and has been used for fibrous media as well (e.g., Becker et al. [79],; Jaganathan et al.[71]; Ashari et al. [80]; Bucher et al. [81]). In the FM method, the void spaces in a given porous structure are fitted with spheres which represent the non-wetting phase and they are all superimposed and interconnected, establishing a continuous pathway originating from a reservoir of non-wetting fluid set at the side of the considered unit cell. The radii of spheres correspond to predetermined capillary-pressure values. By maintaining connectivity to the non-wetting phase reservoir and having their placement limited by void size, the insertion of different-sized spheres corresponding to different pressures represents the drainage process in the porous medium. For each incremental pressure, the wetting or non-wetting phase saturations can be

measured based on the ratio-by-volume of the unit-cell's void space occupied by spheres (Chapter 6 of [1]).

Figure 40 to Figure 41 are obtained by plotting the capillary pressure against the corresponding wetting-phase saturation during the drainage process for wicks F3, F4, F6 and F7, respectively.

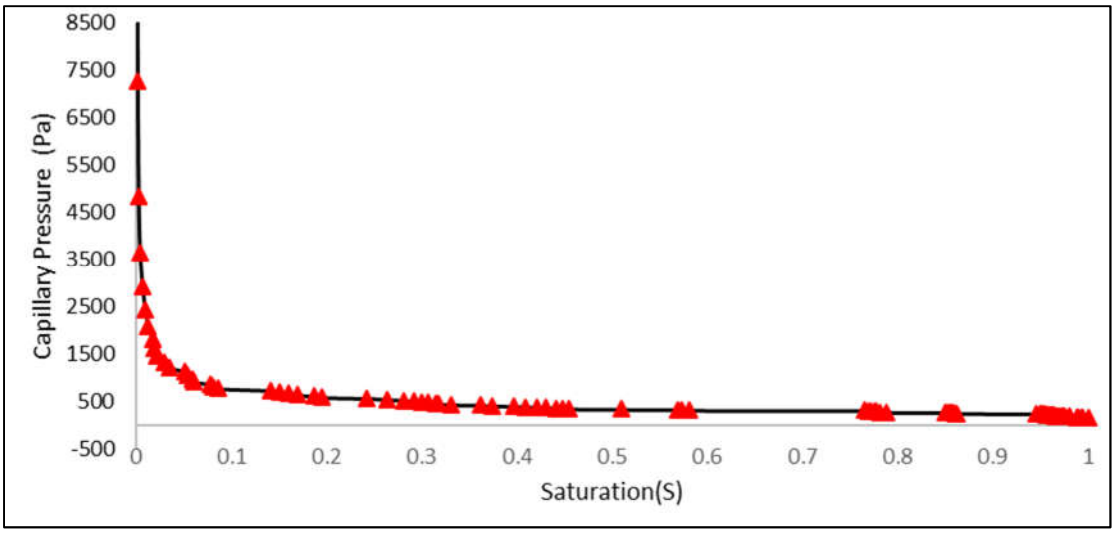

Figure 38. The capillary pressure-vs-saturation plot generated by GeoDict for wick F3

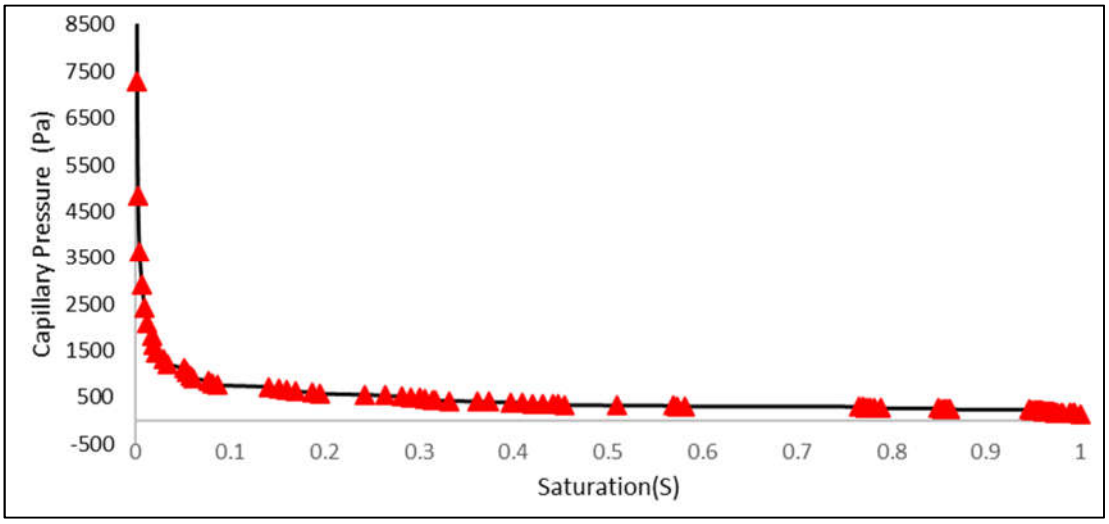

Figure 39. The capillary pressure-vs-saturation plot obtained from GeoDict for wick F4

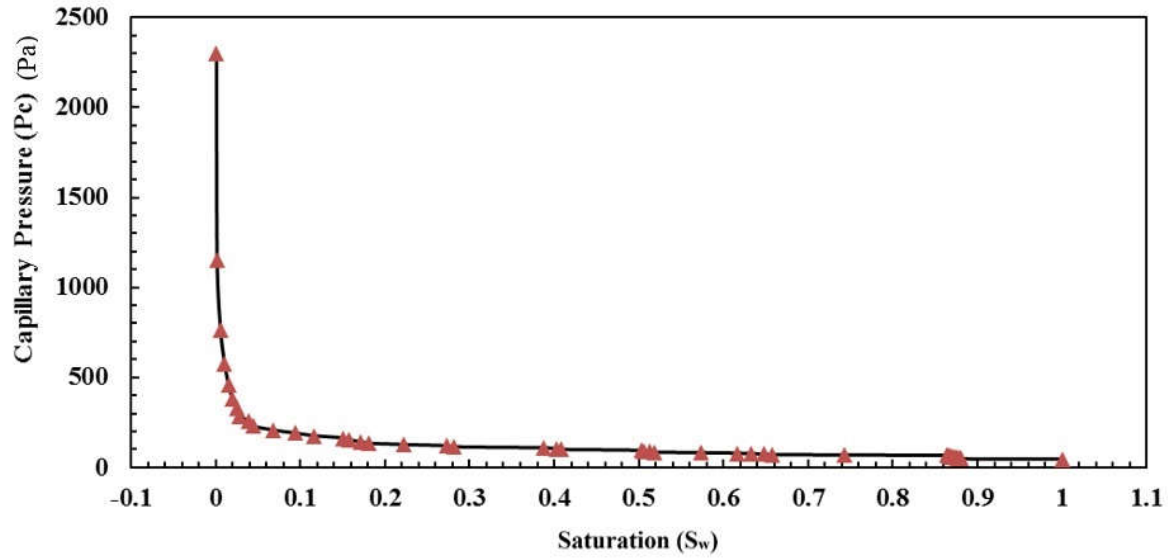

Figure 40 The capillary pressure-vs-saturation plot obtained from GeoDict for wick F6

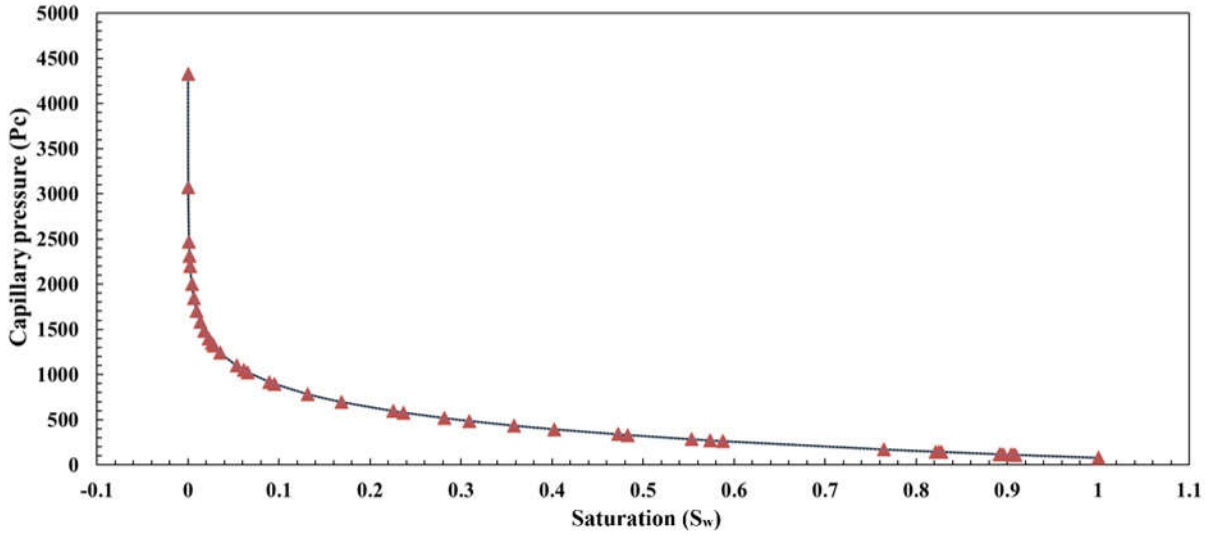

Figure 41 The capillary pressure-vs-saturation plot obtained from GeoDict for wick F7

In order to find a smooth analytical expression for the capillary pressure as a function of saturation for stable numerical simulations, our results obtained by the FM method (Figure 38 to Figure 41) are fitted with the empirical correlations for the capillary pressure–saturation relation as proposed by Van Genuchten [73], Eq 82, and Landeryou et al. [45], Eq 83. The coefficients necessary for either of the two relations are obtained from curve fitting.

Van Genuchten $$Pc(S_w) = 768.76\sqrt[4.43]{(S_w{}^{-1.29} - 1)} \quad (82)$$

Landeryou $$Pc(S_w) = -500.27\ \ln(S_w) + C \quad (83)$$

As can be seen from Figure 42 to Figure 45 which show that both these correlations display relatively satisfying agreement with the simulation results, but the Landeryou model yields a better fit. Hence the latter was selected for simulation, with its final form given as

Wick F3: $$Pc(S_w) = -951\ \ln(S_w) + 25 \quad (84)$$

Wick F4: $$Pc(S_w) = -772\ \ln(S_w) + 93 \quad (85)$$

Wick F6: $$Pc(S_w) = -348\ \ln S_w) + 78 \quad (86)$$

Wick F7: $$Pc(S_w) = -174\ \ln(S_w) + 48 \quad (87)$$

These Eqs. 84 to 87, which were obtained by curve fitting and represent the capillary pressure as a function of saturation, were used in the solution of Richards equation (Eq 79).

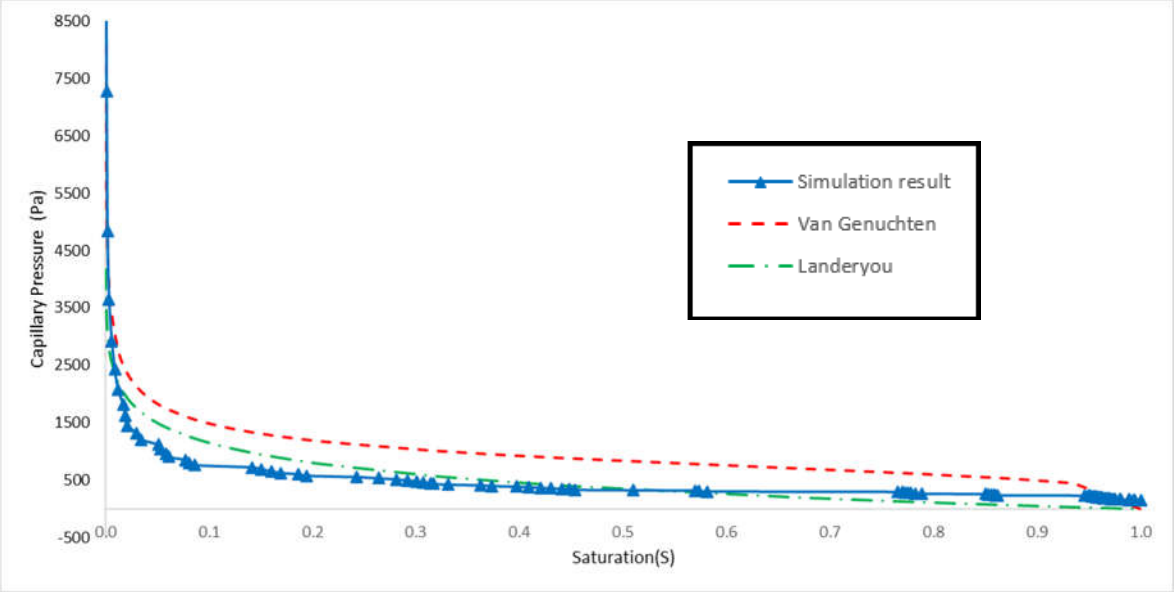

Figure 42 Results of fitting two different P_c-vs-S_w correlations to the predictions of GeoDict for obtaining the coefficients of the correlations for wick F3

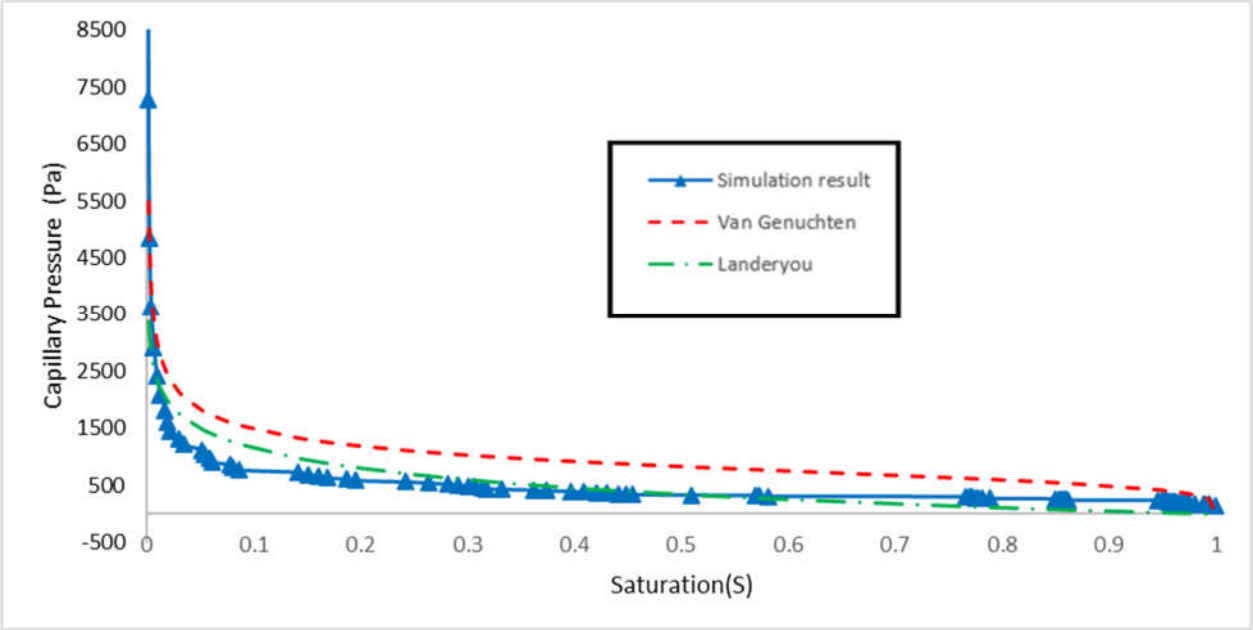

Figure 43 Results of fitting two different Pc-vs-Sw correlations to the predictions of GeoDict for obtaining the correlation coefficients for wick F4

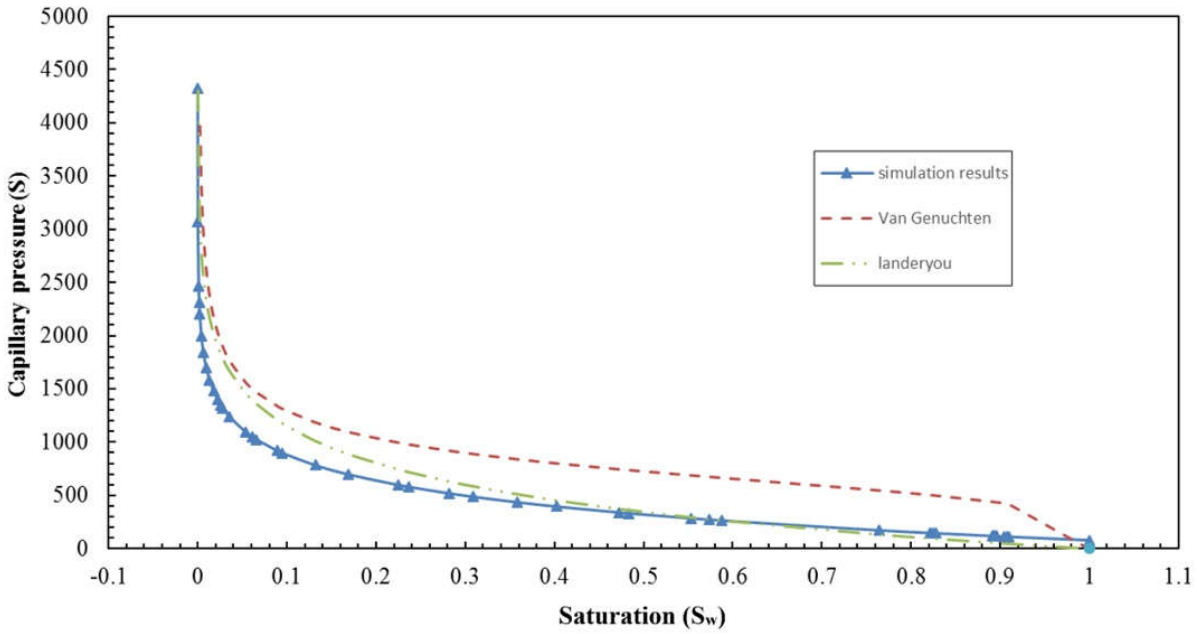

Figure 44 Results of fitting two different Pc-vs-Sw correlations to the predictions of GeoDict for obtaining the correlation coefficients for wick F6

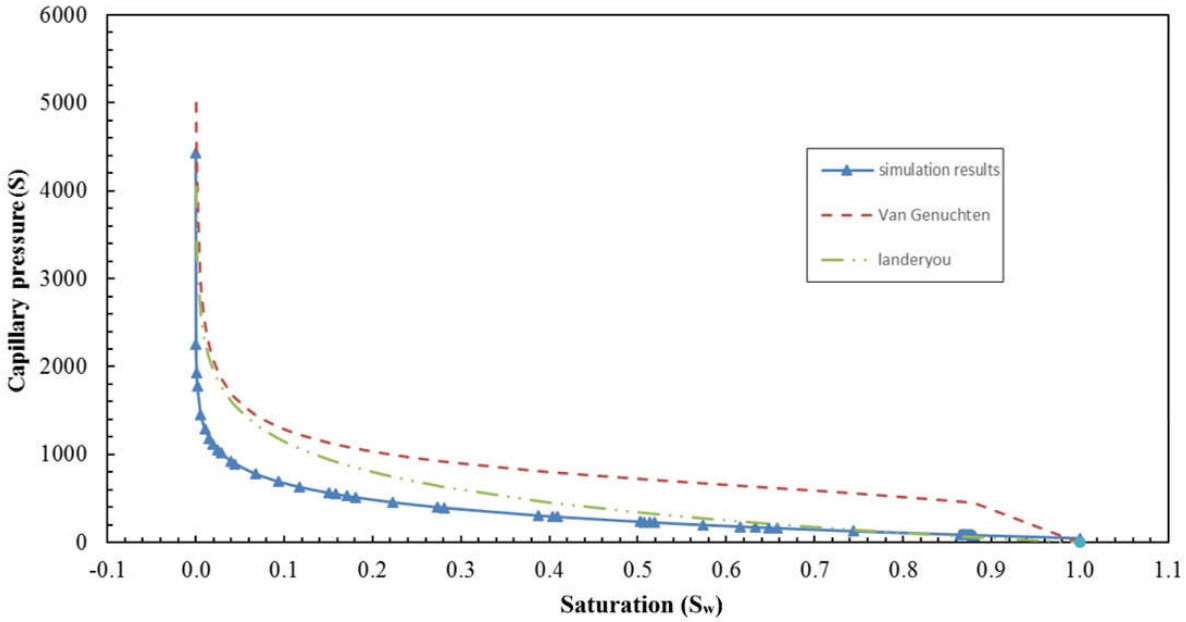

Figure 45 Results of fitting two different Pc-vs-Sw correlations to the predictions of GeoDict for obtaining the correlation coefficients for wick F7

4-3-2-2 Relative permeability as a function of saturation

Similarly, by using the FM method with the GeoDict generated 3-D unit cells, we were able to develop an expression for relative permeability as a function of saturation. Relative permeability ($k_{r,w}$) is dimensionless and has a value between 0 and 1. There have been numerous studies in the past several decades dedicated to establishing a relationship between the relative permeability and saturation in fibrous media. Brooks and Corey [76] proposed a general form for the wetting-phase relative permeability as a function of saturation in porous media as

$$k_r = S^n \tag{88}$$

where n is defined through the equation

$$n = (2 + 3\lambda)/\lambda \tag{89}$$

Here λ is the pore-size distribution index which tends to smaller values for non-uniform media

with a wider pore-size distribution. Most porous media have the *n* coefficient to lie between 2 and 4. In order to develop an appropriate equation for relative permeability as a function of saturation, we used the well-known Brooks and Corey relation to fit our relative permeability-vs-saturation values obtained from our simulations to obtain the required empirical coefficients to be n = 2.9, n=3.6, n = 2.6 and n=2.8 for wicks F3, F4, F6 and F7, respectively.

Figure 48 to Figure 49 show the relative permeability-vs-saturation plots for the wetting phase for wicks F3, F4, F6 and F7, respectively.

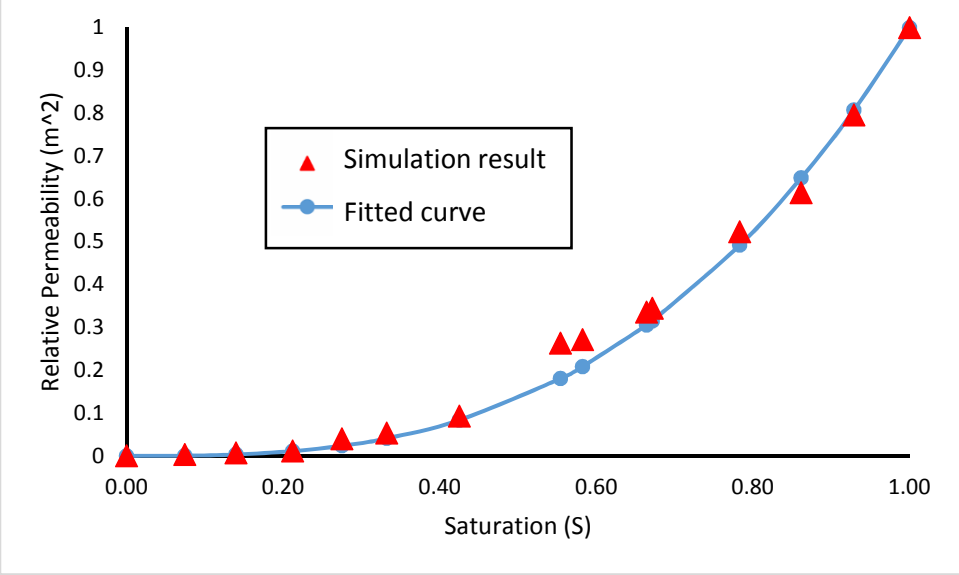

Figure 46 The Brook and Corey power-law relation fitted to the GeoDict simulation results to obtain a smooth relation for relative permeability a function of saturation for wick F3

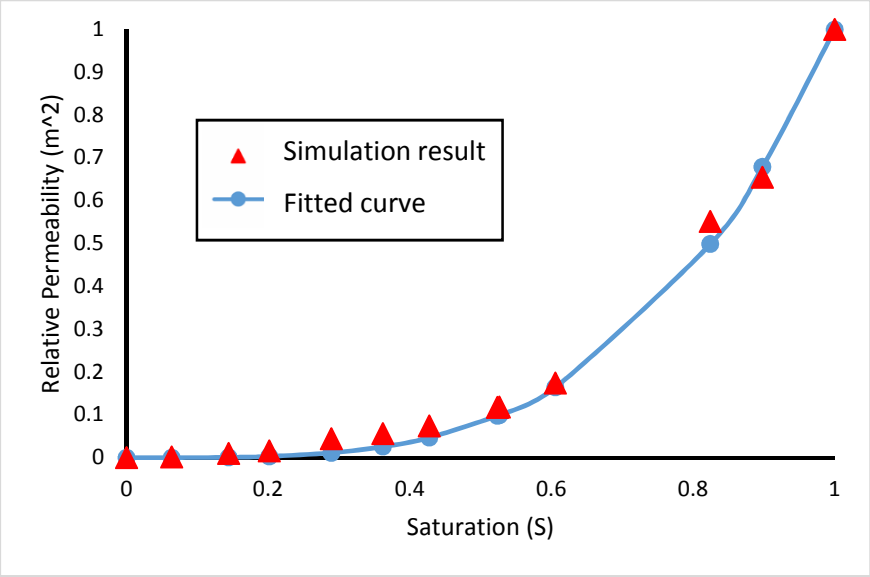

Figure 47 The Brook and Corey power-law relation fitted to the GeoDict simulation results to obtain a smooth relation for relative permeability a function of saturation for wick F4

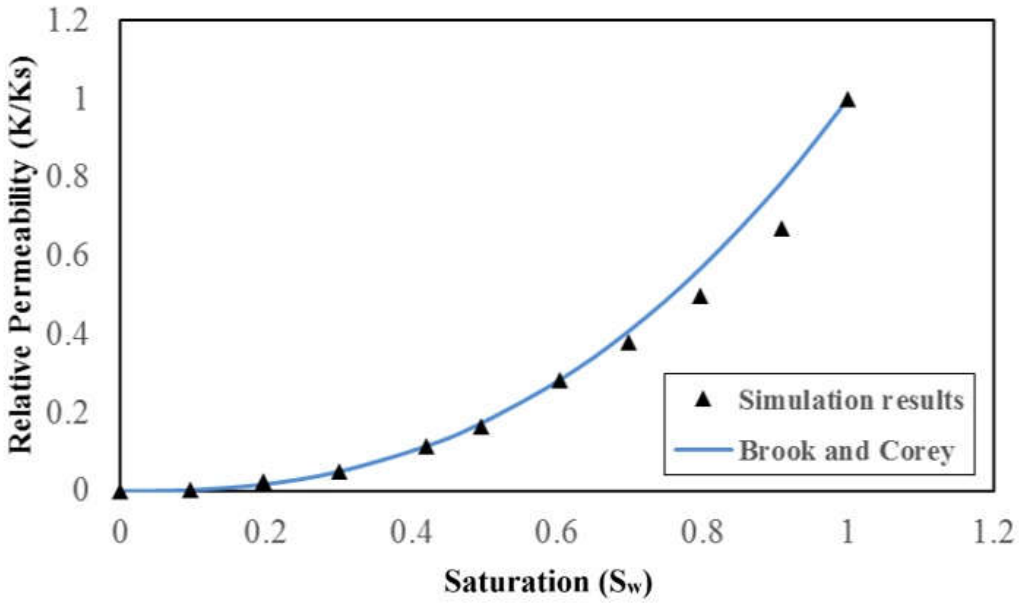

Figure 48 The Brook and Corey power-law relation fitted to the GeoDict simulation results to obtain a smooth relation for relative permeability a function of saturation for wick F6

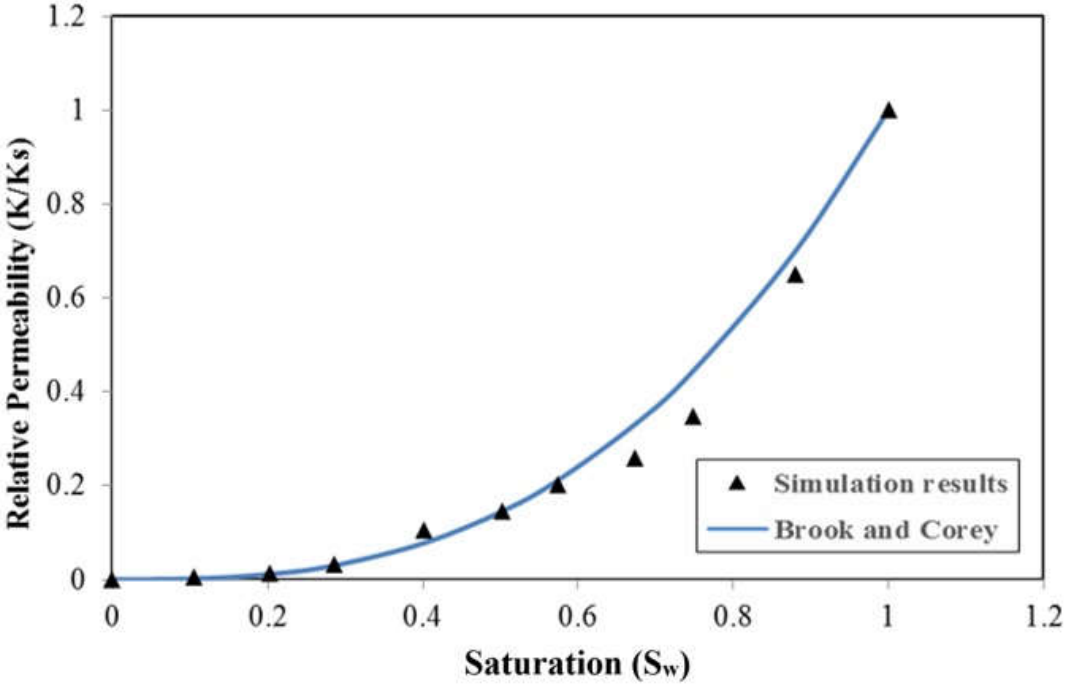

Figure 49 The Brook and Corey power-law relation fitted to the GeoDict simulation results to obtain a smooth relation for relative permeability a function of saturation for wick F7

4-3-3 Numerical and Analytical solutions

We used COMSOL and Mathematica [82] to solve the Richards equation in order to simulate the unsaturated flow during wicking in the wicks F3, F4, F6 and F7, by substituting the parameters values from Table 9 as well as employing the capillary pressure and relative permeability expressions of Equations 80 and 81, we can obtain D_g and D_{ij}.

For the Richards equation seeking to solve the saturation, as a second-order partial differential equation (PDE), the boundary conditions deemed reasonable for our wicking problem are described in Figure 50:

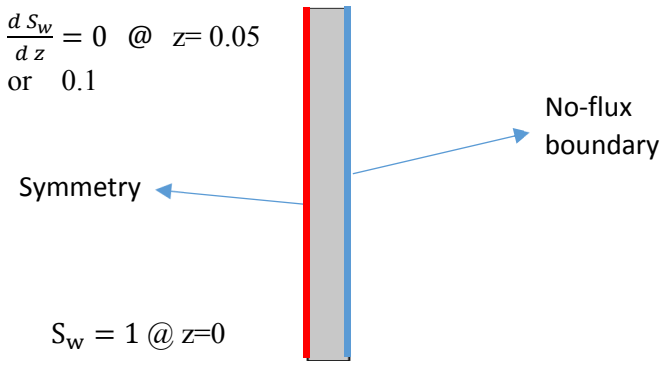

Figure 50. A schematic of the domain, and the initial and boundary conditions The initial condition is defined as

$$\boldsymbol{S_w = 0} \quad @ \quad \boldsymbol{t = 0} \; in \; \boldsymbol{0 < z \leq 0.05} \text{ for Wick F3}$$

$$\boldsymbol{S_w = 0} \quad @ \quad \boldsymbol{t = 0} \; in \; \boldsymbol{0 < z \leq 0.1} \quad \text{for Wick F4} \qquad (90)$$

Note that the height of the wicks F3, F4, F6 and F7 are equal to 0.1 m, 0.05 m, 0.2 m and 0.2 m, respectively.

Since the governing equation, Eqn. 79, is second order in z, we need two boundary conditions (b.c.s), which are proposed to be

$$S_w = 1 \quad \text{at} \quad z = 0, \; \text{and} \quad \frac{d S_w}{d z} = 0 \quad \text{at } z = z_{end} \qquad (90.5)$$

where z_{end} is the height of the solution domain that is kept much bigger that the height of the wick so that the effect of the 'insulation' or 'no-flux' b.c. at $z = z_{end}$ does not distort the solution as it evolves with time.

Although the wicking process is assumed to be 1-D and the resulting saturation to be changing only along the fiber axis, our solution domain is modeled as an axisymmetric 2D geometry of rectangular shape which is discretized using a finite element mesh consisting of quadrilateral elements. The boundary conditions listed in Eq. 90.5 are applied on the top and

bottom sides of the rectangular domain shown in Figure 50, which also describe the symmetry and no-flux conditions applied at the left and right sides of the domain. The initial condition listed in Eq. 90 is implied at the start of the simulation.

To make sure that the results obtained by Mathematica calculations are precise, we simulated the wicking process and calculated saturation levels using COMSOL as well. In this COMSOL solution, the Richards equation as a PDE is solved with exactly the same boundary and initial conditions as listed above, and the wicking process is assumed to be 1-D and the resulting saturation to be changing only along the fiber axis. However, our solution domain is modeled as an axisymmetric 2D geometry of rectangular shape which is discretized using a finite element mesh consisting of quadrilateral elements. The boundary conditions listed in Eq. 90 are applied on the left and right sides of the rectangular domain while the top and bottom sides have been imposed with the symmetry condition. The initial condition listed in Eq. 90 was imposed at the start of the simulation. In the next step, we compared the predictions of Mathematica and COMSOL with experiments which are discussed in the results and discussion section. For wicks F3 and F4, we will compared the results obtained from COMSOL with the visual result from section 4-1-3-2-2-2 and the results obtained from COMSOL and Mathematica with the experimental results obtained from the experiments explained in the following section.

4-4 Experimental procedure

In order to measure the saturation levels of the fibrous wicks during wicking, just two of fibrous wicks, F6 and F7 (glass fiber wicks), were investigated.

The wicking liquid used in our experiments was methyl caprylate ester derived from

coconut oil[1] with density $\rho_{liq} = 870\ \mathrm{Kg}/m^3$ of and viscosity $\mu = 2.072$ cP. (All these properties were characterized at room temperature, 25˚C± 2˚C.) In the following sub-sections, the procedures for measuring the saturation distribution along the wick axis and the mentioned properties are described in detail.

4-4-1 Measuring saturation along wick axis

In order to validate the numerical predictions of axial saturation distribution in the wicks, it is necessary to compare them with experimental observations. The saturation levels of the liquid were determined after 36 hours once steady-state conditions have been established. To assure the repeatability of experimental results, three (3) wicks of each type (wicks F6 and F7) were tested at each time. In the experiments, the wick was sectioned along their axes and the liquid content of the sections was measured to estimate their saturations. To accurately determine the section positions, each wick was first marked into equal parts with a length of 10 mm each (Figure 51a). Then the dry wick is weighed to estimate the weight of each part. After submerging the wick into the liquid for 36 hours from the start of dipping, each wick was immediately transferred to a pan containing liquid Nitrogen and kept there for a few seconds, which was enough for the imbibed liquid in the wick to freeze completely. After this, we were confident that the liquid content of each slice would not change during the sectioning process when pressure by hand is applied on the wick during their cutting. Also, during the transferring of the wicks into liquid Nitrogen pan, we had to ensure that no perceptible discharge of the liquid occurred. Therefore, the wick was carried very gently so that no liquid squeezed out of the wick due to hand pressure. After sectioning, every

[1] For the purposes of confidentiality, the commercial names of the wicks and wicking liquids are not released.

wick-slice was weighed and the saturation level of each wick-section was estimated using

$$S_w = \frac{(1-\varepsilon)\times m_{liq}\times \rho_{fbr}}{\varepsilon \times m_{dry}\times \rho_{liq}} \quad (91)$$

where m_{liq} is the mass of liquid absorbed into the wick and and m_{dry} is the mass of one section of the dry wick. Also, ρ_{fbr} and ρ_{liq} are the densities of glass fibers and wicking liquid, respectively. The results of measuring saturation levels of liquid along the wick axis are described in the next section.

Figure 51 Experimental procedure for measuring saturation distribution along a wick axis (a)the glass wick is marked into equal parts, (b) weighing the dry wick before immersing into the wicking liquid and achieving steady state, (c) submerging the wetted wick into liquid nitrogen to 'lock' the liquid, (d) cutting the frozen wick into the marked equal parts, (e) weighing each cut part of the frozen wick

4-5 Results and Discussion

4-5-1 Saturation as function of location for Wicks F6 and F7

In this section, the two Richards equation-based numerical solutions are compared with experiments in order to study their effectiveness in predicting axial saturation distributions in glass fiber wicks. Recall that in order to conduct a comprehensive, repeatable measurement of liquid saturation levels in fibrous wicks, three experiments each for the two wicks F6 and F7 were conducted. In presented figures which compare the results, the numerical solutions of Richards equation were obtained for the wick length of 20 cm, while the experimental results were obtained for the wick length of 6 cm. *This was because we were unable to cut more pieces of the wicks since the wicks frozen with liquid nitrogen melted quickly at room temperatures.* Hence only a partial comparison with experiments will be possible here.

The numerical solutions for saturation of Richards equation obtained using Mathematica and COMSOL, and compared with experimental results for wick F6 are shown in Figure 52. It is clear that there is a reasonable match between the numerical solutions and empirical data. Furthermore, in order to investigate the effect of gravity, the Richards equation is also numerically solved without gravity (i.e. after eliminating the term containing D_g in Eq. 79). These solutions are compared with the experimental results in Figure 53. As can be seen from Figure 52 and its comparison with Figure 53, the numerical solutions that include the gravity are more accurate as they exhibit better comparison with experimental results.

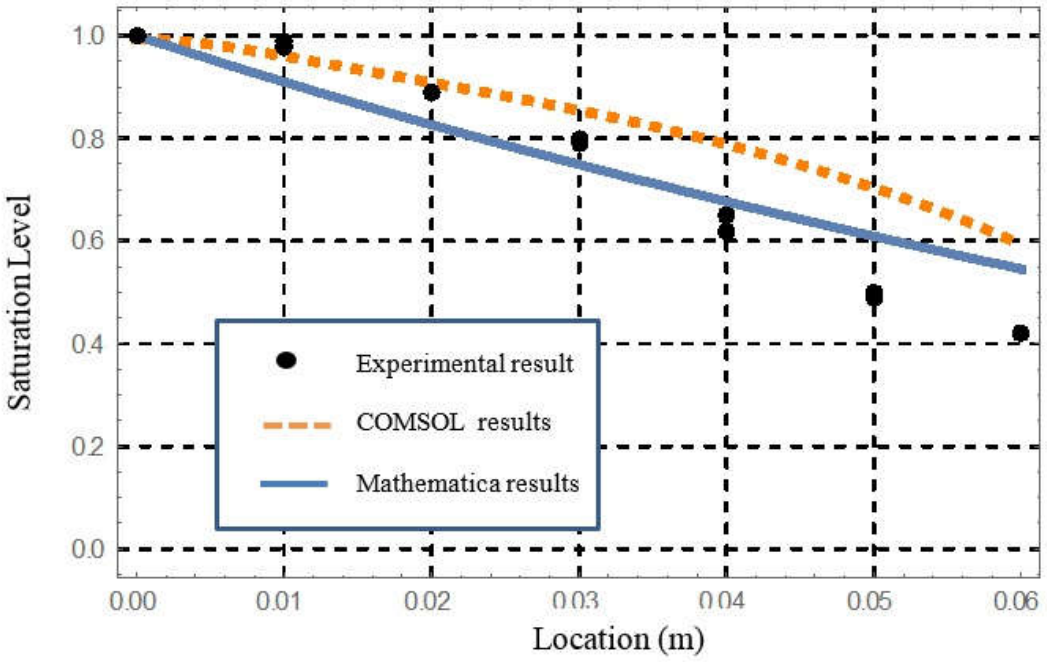

Figure 52 The numerical solutions of Richards equation (obtained after including the gravity effects) in comparison with the experimental data for wick F6

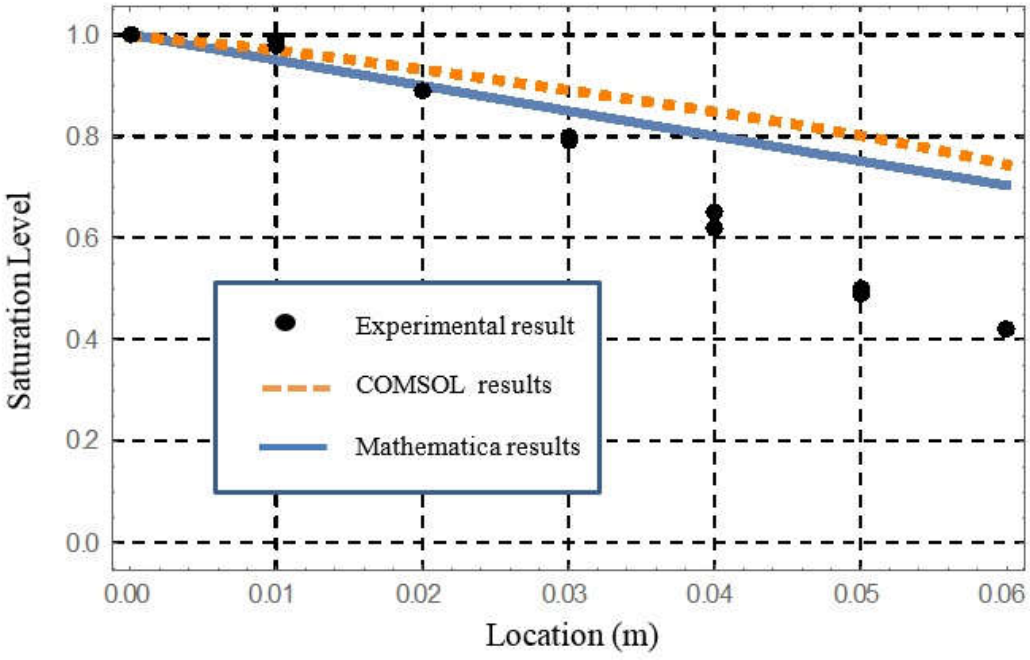

Figure 53 The numerical solutions of Richards equation (obtained after excluding the gravity effects) in comparison with the experimental data for wick F6

For the wick F7, a similar comparison between the numerical solutions and the experimentally obtained saturation values is shown in Figure 54. An additional comparison without including gravity in the simulations is presented in Figure 55. It is clear that inclusion of gravity is important in predicting the upwards movement of wetting liquid in a wick.

This similarity of observations for the two wicks F6 and F7 indicate that even over a short height of 6 cm, gravity begins to influence the results significantly though the capillary-pressure driven upwards suction plays a central role in the process.

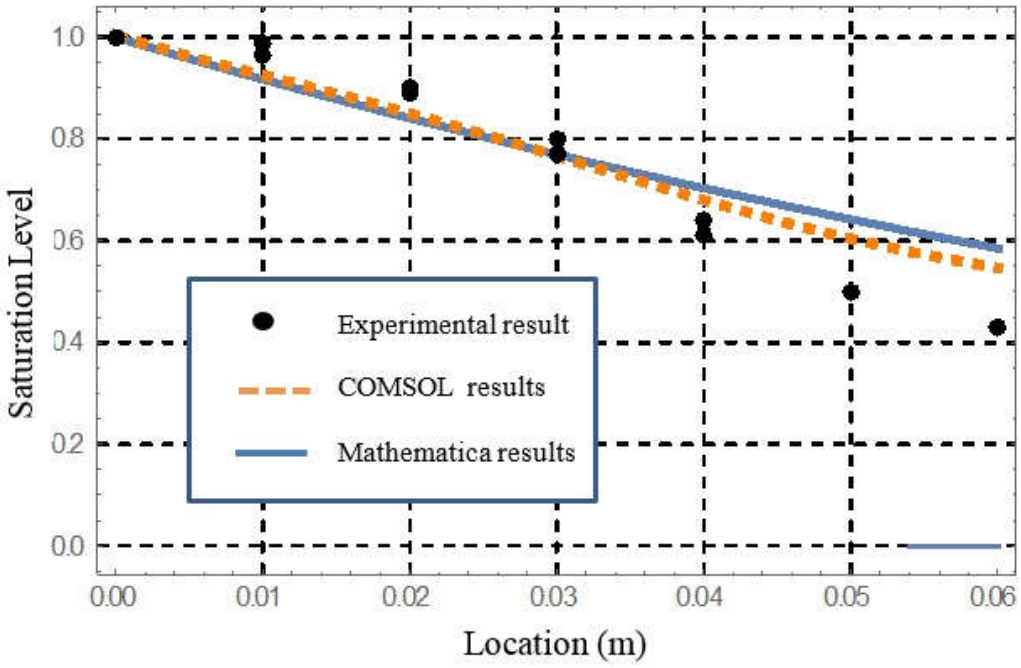

Figure 54 The numerical solutions of Richards equation (obtained after including the gravity effects) in comparison with the experimental data for wick F7

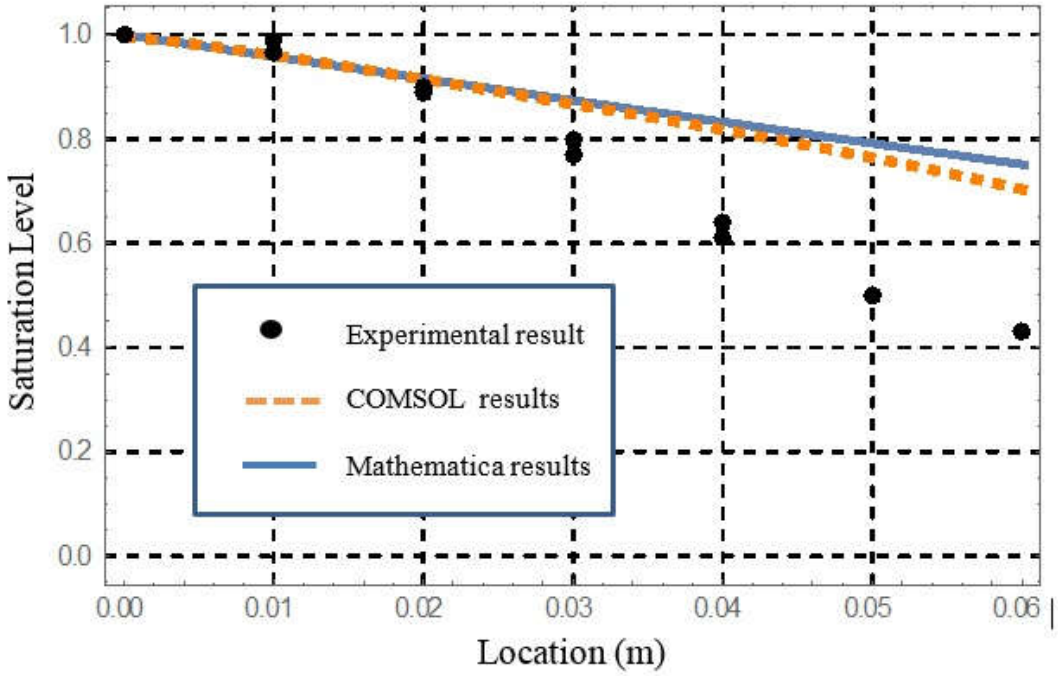

Figure 55 The numerical solutions of Richards equation (obtained after excluding the gravity effects) in comparison with the experimental data for wick F7

4-5-2 Predicting mass Absorbed into the wicks as a function of time for wicks F6 and F7

In chapter 3, we developed an expression to predict the height of the liquid front as function of time and we validated our theoretical model by measuring the liquid mass imbibed into each wick as a function of time and calculating the liquid-front height from it as follows

$$h_f = \frac{m(t)}{\varepsilon \rho_{liq} \pi R_w^2} \qquad (92)$$

As was mentioned in the introduction, due to the local pore-scale inhomogeneities caused by fiber clustering, the wetting liquid is preferentially 'pumped' along the 'channels' created by fiber clusters and thus a partially saturated wick is created during wicking. As a result, we cannot entertain a concept of having a sharp liquid-front of height h_f with 100% saturation behind the front. Hence in this part, in order to establish the accuracy of our simulations further, we will

restrict ourselves to comparing the imbibed mass predicted by our numerical simulations with that measured experimentally.

Rather than measuring the imbibed mass directly from a wicking experiment as was done in chapter 3, we will estimate the imbibed mass from our earlier-described measured saturation values along the wick axes using the equation

$$m(t) = \int_0^L \rho\, \varepsilon\, A_w\, S_w\, dz \tag{93}$$

We used this equation with the results of our numerical solutions of Richards equation in the form of saturation as a function of wick-axis location z.

After applying the results of the Richards equation in Eq. 93, the imbibed mass values were compared with the experimental results. As mentioned in the last section, the saturation values could be determined only for the first 6 cm of the 20 cm long wicks. Therefore, *the empirical imbibed-mass as a function of time cannot be determined for fibrous wicks using Eq. 93* but we know from chapter 3 that our sharp-front model, given by Eq. 22, was quite successful in predicting the imbibed mass as a function of time, which was measured using a separate experiment. Hence we will use the prediction from this theoretical model of chapter 3 as 'Experimental results'. These comparisons are presented in Figure 56 and Figure 57 for both wicks F6 and F7. Note that the solution of Richards equation at a given time is an axial distribution of saturation. Hence, at a given time, the imbibed mass estimated using Eq. 93 has a single value which is shown as a point under 'Numerical simulation results' in Figure 56 and Figure 57.

Although the theoretical model proposed in chapter 3 was not able to predict the exact height of liquid-front as there was no sharp front due to the presence of partial saturations along the wick axis, a comparison of the numerical simulation results with the experimental observations shown

in Figure 56 and Figure 57 reveals that our Richards equation solution is able to predict the amount of mass absorbed into the fibrous wicks F6 and F7 with a satisfying degree of accuracy.

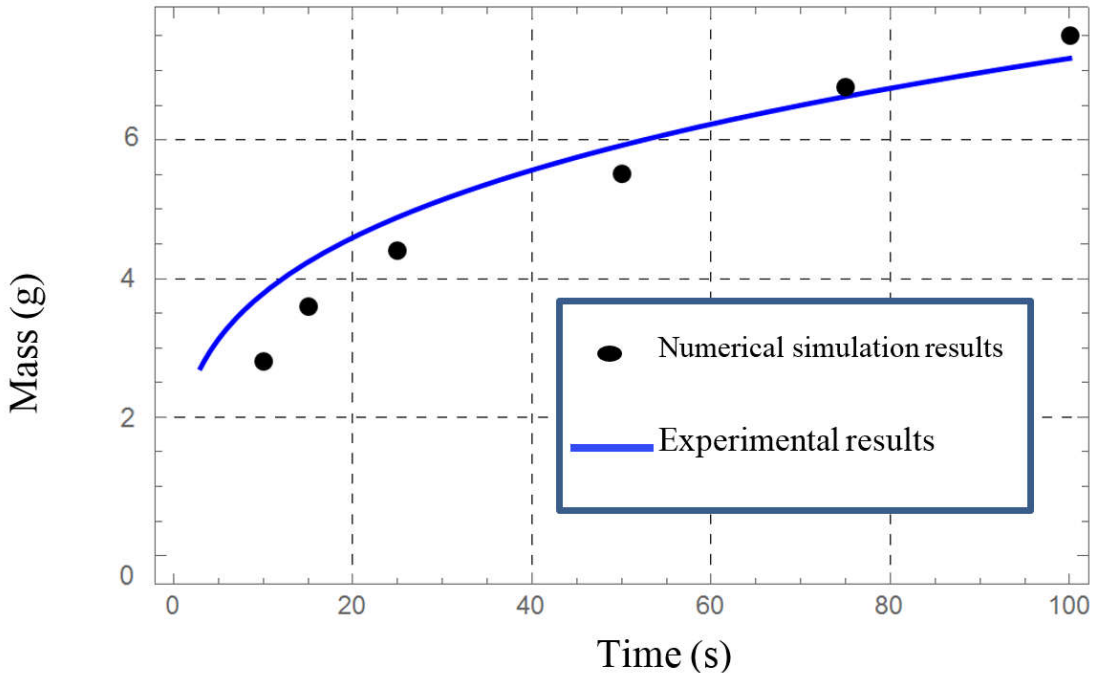

Figure 56 Comparison between the numerical simulation and experimental results for the mass of liquid imbibed into wick F6

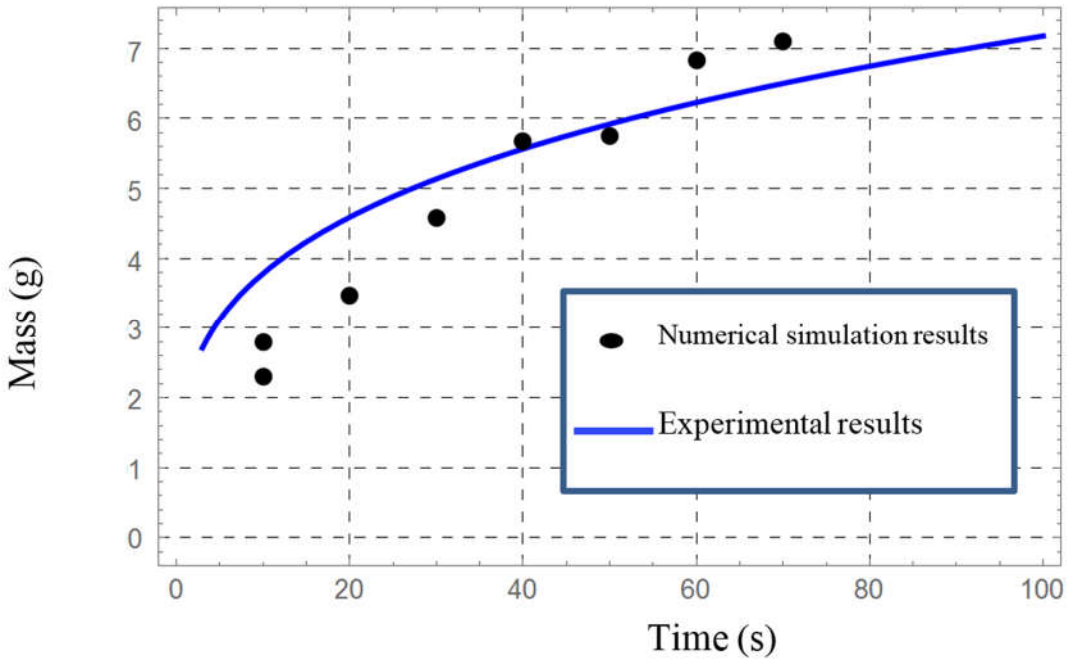

Figure 57 Comparison between the numerical simulation and experimental results for the mass of liquid imbibed into wick F7

In our developed theoretical model as well as the numerical simulations, wick properties such as the porosity and fiber diameter play critical roles, as the comparisons between Figure 53 and Figure *55* as well as Figure 56 and Figure *57* show the difference between the performance of wicks F6 and F7 that have different porosities and fiber diameters. This comparison demonstrates the effect of changes in porosity and diameter on the wicking process. As shown in Figure 57, as the porosity and fiber diameter for wick F7 is slightly higher than those for wick F6, the amount of absorbed liquid into the wick F7 is a higher. However, in the absence of any analytical expression for front height as a function of time (as was in chapter 3), a less-than-satisfactory study of the dependence of porosity and fiber diameter on front height can be established here in the present numerical study. As a result, no clear-cut optimum values of these properties can be deciphered, unlike the case where analytical results are available [83].

4-5-3 Saturation as function of location for wicks F3 and F4

In this section, the numerical solutions of Richard equation are presented in order to study their effectiveness in predicting the axial saturation distributions in fibrous wicks. The numerical predictions for saturation, obtained from COMSOL, are shown in Figure 58 and Figure 59.

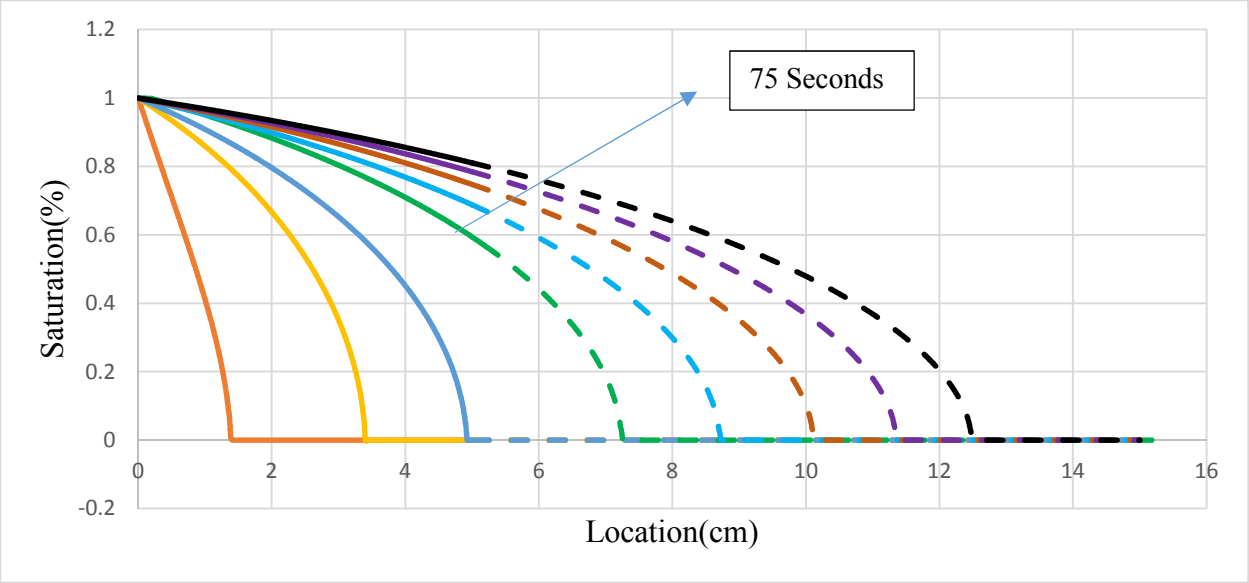

Figure 58. The evolution of numerical solutions by the Richards equation as obtained from COMSOL for wick F3. The solid curves pertain to the solution in the 'real' region while the dashed curves correspond to the solution in the extended 'imaginary' region beyond the 5 cm wick length. The saturation curve corresponding to 75 seconds is expected to be close to the saturation distribution at 75 seconds shown in (F3) of Figure 34 (Page 88).

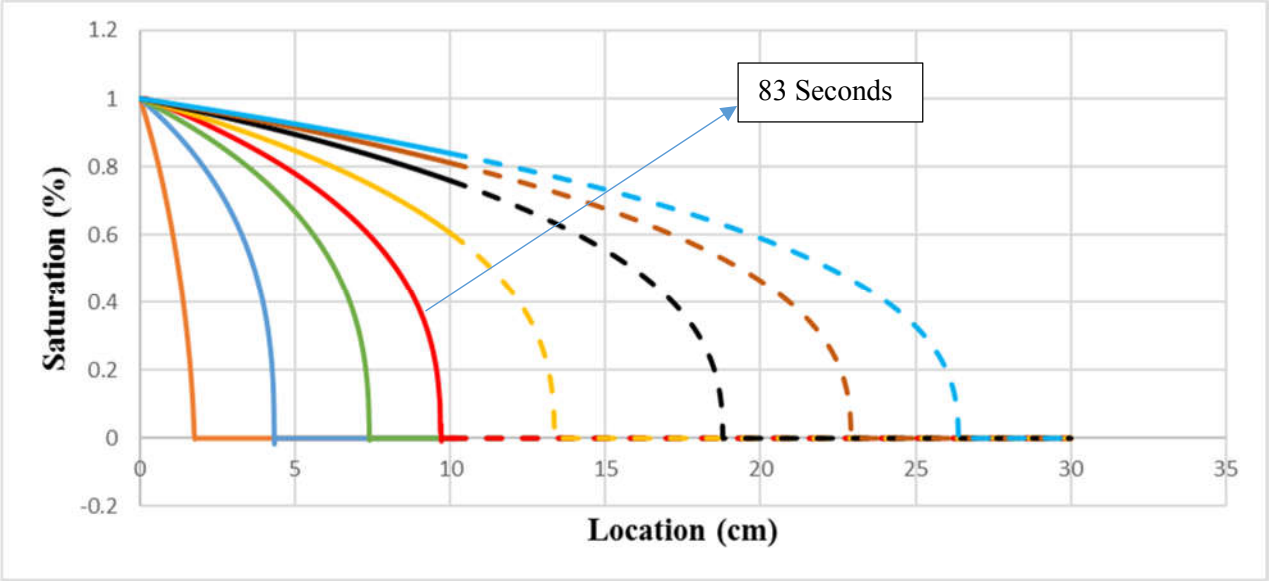

Figure 59. The evolution of numerical solutions by the Richards equation as obtained from COMSOL for wick F4. The solid curves pertain to the solution in the 'real' region while the dashed curves correspond to the solution in the extended 'imaginary' region beyond the 10 cm wick length. The saturation curve corresponding to 83 seconds is expected to be close to the saturation distribution at 83 seconds shown in (F4) of Figure 34

Figure 58 and Figure 59 show the saturation level in the wicks F3 and F4 at different times after the start of wicking process. As it can be seen from the marked curves in Figure 58 and Figure 59, expected to be close to the 75 seconds and the 83 seconds saturation-distributions for the wick F3 and F4, it can be argued that *there is a reasonable qualitative match* between the numerical predictions of saturation and the visually observed saturation in Figure 34 for the wicks F3 and F4.

(Note that we could not achieve a 'hard' comparison between the numerical and experimental saturation distributions as seen in our previous work [84] because there the experimental evaluation of saturation was done under *steady-state* condition and where the glass-fiber wick could be frozen in liquid Nitrogen and subsequently sliced and weighed, as there was no time-dependent change in saturation distribution. Any such freezing operation, which typically takes a minute at least, would allow the liquid to further move along the z axis in the wicks F3 and

F4 and thus change the saturation distributions at any chosen time.

We would like to offer a final observation on the utility of the Richards equation based wicking model. Though it is based on the more comprehensive unsaturated flow model that incorporates all the relevant aspects of two-phase flow physics through the use of the relative permeability and capillary pressure versus saturation plots, it is proving to be not that useful as the sharp-front type wicking model. For one thing, the properties such as the relative permeability and capillary pressure are quite challenging to estimate numerically (or even measure directly[26]). Secondly, important quantities such as the absorbed liquid-mass as a function of time cannot be expressed using explicit formulas such as Eqn. 23 in conjunction of Eqn. 22 where the role of various quantities (such as surface tension, contact angle, viscosity, permeability, porosity, fiber/particle diameter, etc.) is delineated clearly. Because of these advantages, the sharp-front models, despite having a rather limited and restricted flow physics, are quite useful to the users and designers of industrial wicks.

4-6 Summary and discussion

Section 4-4-1, indicated that imbibition of a liquid into a wick made of aligned fibers is characterized by distribution of partial saturation along the wick axis caused by 'pumping' of liquid along fiber clusters. In this chapter, we successfully employed Richards equation to predict saturation distribution along the wick axis. While doing this, we broke new ground on several fronts. First was the development of an appropriate form of Richards equation using the unsaturated flow theory in a transversely-isotropic porous medium. Secondly, we employed the state-of-the-art software GeoDict to determine important properties including the permeability,

relative permeability and capillary pressure directly from pore-scale simulations. Thirdly, a new liquid-N_2 based freezing technique is employed to determine experimentally the saturation along the wick length. The Richards equation-based numerical simulations were generated in 1-D using Mathematica and in 2-D using COMSOL. These results, having tallied with each other, were then compared with experimental data obtained from measuring the axial liquid-content/saturation in two different types of glass fiber wicks. Good agreements, especially after including gravity effects, were observed between the experimental results and numerical predictions. The new liquid-N_2 a new liquid-N_2 based freezing technique was unable to get the saturation distribution along the full length of the wick due to the quick thawing of the cut wick segments, and hence was unable to furnish the absorbed liquid mass vs time (m-vs-t) plot. The sharp-front model used in chapter 3, which is quite successful in replicating the m-vs-t measured through a wick-dipping experiment, was employed instead. The m-vs-t plot obtained from our two numerical simulations compared favorably with the sharp-front analytical formula. This positive result, along with the affirmation of the numerically predicted saturation distribution along the wick axis, establishes the efficacy of Richards equation in modeling imbibition of liquids in dry glass-fiber wicks.

To predict the diffuse flow-front observed in the last two fibrous wicks (F3 and F4), we employed a theoretical model based on the Richards equation to explain the gradually decreasing saturation behind liquid fronts in those wicks. An artificial unit cell of randomly arranged parallel-fibers was first created using GeoDict where we then ran some simulations to obtain the plots of the capillary pressure and relative permeability as a functions of saturation. The Richards-equation based model, solved using COMSOL, is able to predict saturation profiles as a function of time, which seem, at least qualitatively, to match the experimental observations.

Chapter 5: Investigating Liquid-Front Formation using CFD

5-1 Introduction

During the wicking process, liquid (the wetting phase) removes air (the non-wetting phase) from the pores of wicks and then then fills them up thus insuring 100% saturation. As a result, the liquid front at the pore (micro) level acts as the interface between the liquid and air phases. In some previous studies, the wettability has been measured through the rate of advance of a liquid front [85, 86]. There have been some investigations which focused on finding different parameters affecting the wicking process and to evaluate the sensitivity of liquid front to these parameters.

Hu et al [86] conducted a quantitative analysis based on a pore-scale simulation and investigated the transition of liquid fronts form from fingering to stable flow under the effect of wettability. They suggested that the progress of liquid front slows down under reduced wettability condition. Zhang et al [87]. conducted a series of displacement experiments and concluded that the front shape is highly dependent on different parameters such as the capillary number, viscosity ratio and the heterogeneity of the porous medium. Bakhshian et al [88] simulated the front movement during the drainage process using the Lattice Boltzmann method for different cases of viscosity ratios and capillary numbers. They observed that the formation of the fluid front and its transition between its different forms is strongly a function of microscopic flow patterns and invasion dynamics. They found that a low viscosity ratio causes a lower degree of saturation of the non-wetting phase at the breakthrough time (i.e., when the non-wetting fluid reaches the outlet boundary). The lower saturation level leads to a diffuse pattern of front movement and consequently leads to breaking up of fingers into droplets. In contrast, a high viscosity ratio leads to higher saturation of the non-wetting phase as a result of slow movement of the liquid front [88].

In addition to exploring the capillary number, viscosity ratio and wettability parameters, some studies focused on the formation and movement of liquid front under the effect of varying permeability. Shabina et al [89]. analyzed the capillary driven flow of a wetting phase while displacing the non-wetting phase in layered porous medium. They noted that in a stack of layers with different permeability values, the fluid front in the lower permeability (higher capillary pressure) layer will always lead. For example, in a three layered porous medium, the front leads in the small-permeability layer and is followed by the front in the medium-permeability layer, which in turn is followed by the front in the large-permeability layer. On the other hand, in a study done by Reyssat et al [90] on the imbibition process in a layered porous medium, a sharp front was observed despite the medium having layers with different a permeability values in the direction of the flow.

Among all the conducted investigations, the one by Bico and Que´re´ [91] was the first to demonstrate that the liquid front, during the spontaneous imbibition of a wetting fluid into a porous medium, has two forms: sharp and diffuse. During the imbibition process with a diffusive front, the wetting phase was found to lead in the smaller pores of a porous medium, unlike the predictions of the traditional capillary-tube bundle model. Bico and Que´re´ also discovered that a large spread in the pore size distribution is the main cause of formation of the diffusive fronts. Later, more studies were done on wicking in different type of porous media including paper napkins, towels, diapers and fractured oil reservoirs which observed the formation and progress of diffusive fronts [92-94]. Ferer et al [95] showed that, unlike the large-scale multiphase flows in porous media, the saturation front displacement at small-scale flows is a nonlinear function of time and is caused by the fingering phenomena at pore-scale.

As investigated in chapter 2, mainly three different types of liquid-fronts are observed during the imbibition of a liquid into a porous wick: sharp, semi-sharp, and diffuse. There we noticed that sometimes the same type of wicks have different types of liquid fronts: the fibrous wicks displayed both the semi-sharp and diffuse fronts. And, the main conclusions of chapters 3 and 4 indicate that the type liquid front is most important for applying the appropriate mathematical model and thus to estimate important quantities related to the wicking process such as the height of liquid front as function of time, maximum flow-rate at the top of a wick, and steady state height. In this chapter, we use FLUENT for modeling two-phase (liquid-air) flow in different porous media and tracking the movement of interface representing the liquid front. Thus the effect of microstructure on the formation and progress of liquid fronts in different wicks is studied.

5-2 Mathematical Model

5-2-1 Introduction

The existence of interface arises from the flow of two immiscible fluids (to be called phases here). Two-phase flow in complex pore cavities lead to the evolution of a complex topology of the interface. Two-phase flows at the pore (micro) scale are simulated by solving the set of Navier–Stokes equations coupled with an equation to track the interface [96]. Since our CFD (computational fluid dynamics) investigations using FLUENT are in 2D, the following equations are similarly adapted.

Continuity:

$$\frac{\partial \rho}{\partial t} + \frac{\partial (\rho u)}{\partial x} + \frac{\partial (\rho v)}{\partial y} = 0 \qquad (94)$$

X-momentum

$$\frac{\partial(\rho u)}{\partial t}+\frac{\partial(\rho uu)}{\partial x}+\frac{\partial(\rho uv)}{\partial y}=-\frac{\partial P}{\partial x}+\left[\frac{\partial}{\partial x}\left(\mu\frac{\partial u}{\partial x}\right)+\frac{\partial}{\partial y}\left(\mu\frac{\partial u}{\partial y}\right)\right]+S_x \quad (95)$$

Y-momentum

$$\frac{\partial(\rho v)}{\partial t}+\frac{\partial(\rho vu)}{\partial x}+\frac{\partial(\rho vv)}{\partial y}=-\frac{\partial P}{\partial y}+\left[\frac{\partial}{\partial x}\left(\mu\frac{\partial v}{\partial x}\right)+\frac{\partial}{\partial y}\left(\mu\frac{\partial v}{\partial y}\right)\right]+S_y \quad (96)$$

Here ρ is the fluid density, u is the fluid velocity component in the x-direction, v is the fluid velocity component in the y-direction, P is the pressure and μ is the viscosity. Sx and Sy are the source terms which include the gravity term and the surface tension contribution.

Boundary conditions:

The interface is considered as a free surface at constant pressures (with a jump due to curvature and normal stresses) but without any shear stresses. Since there is no mass exchange due to evaporation or condensation on the interface, the boundary conditions applied are as follows:

Continuity condition:

$$(V_n)_1=(V_n)_1=(V_n)_{Interface} \quad (97)$$

Normal stress balance:

$$P_2-P_1=\gamma\kappa+2\mu_2\left(\frac{\partial V_n}{\partial n}\right)_2-2\mu_1\left(\frac{\partial V_n}{\partial n}\right)_1 \quad (98)$$

Here subscript 1 stands for air (non-wetting phase) and subscript 2 denotes the wicking fluid (wetting phase), γ is the surface tension, κ is the curvature, P is the pressure. As shown in

Figure *60*, Vn is the normal velocity component, with the normal pointing from fluid 2 (wetting) into fluid 1 (non-wetting). The curvature of the interface κ, is defined through the formula

$$\kappa = \frac{1}{R'} + \frac{1}{R''} \tag{99}$$

where R' and R" are the local principal radii of curvature.

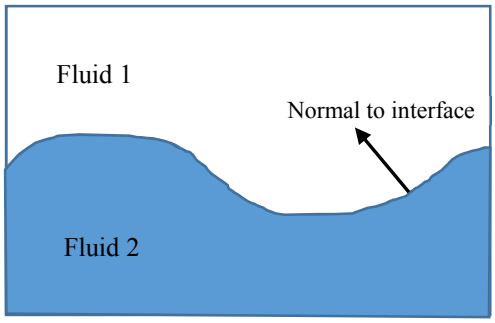

Figure 60 The interface formed between the wetting and non-wetting phases

5-2-2 VOF Method

Volume of Fluid is classified as Euler method, as it solves a scalar transport equation in the Eulerian frame [97-99]. Generally, the Euler's methods are described by a grid, which can be either stationary or non-stationary (for moving boundaries), and all the phases are treated as continuous, and specifically, the VOF method does not allow the phases to be interpenetrating. The Euler's methods follow the location and shape of the surface. Hence, in examples with moving boundaries, the grid motion can be determined by computing changes in surface locations.

For the first time in the history of volume tracking methods, DeBar [100], Hirt and Nichols [101], and Noh and Woodward [102] introduced their methods [103] in the early 1970s. DeBar's model was named KRAKEN and was based on Eulerian hydrodynamics. By using a piecewise linear approximation, it was able to model compressible non-viscous flow of several fluids in an axially symmetric (2D) region [100]. [102]. Later, models similar to DeBar's method after adding some modifications were introduced by other researchers [104] [105]. In 1982, Hirt et al developed

a novel method to track an interface known as the VOF method [101, 106]. This method uses a piecewise constant/"stair-stepped" approximation and by computing the movement of interface, calculates its location and shape in a most accurate way. Noh and Woodward's' method was called SLIC (Simple Line Interface Calculation) method and it approximates the interfaces as piecewise constant. The fluid surfaces (interfaces) are represented locally for each mixed cell and these surfaces are defined as a composition of one space dimensional components which are assumed to be straight lines in 2D (planes in 3D) and aligned with one of the logical mesh coordinates. SLIC was based on KRAKEN model, but it chooses simpler interface geometry compared to KRAKEN which makes it a better method for multiple phases within a given mixed cell. Hence, based on the three introduced methods, we can categorize most of the developed volume tracking algorithms [101, 107-111] into three interface reconstruction categories: piecewise constant, piecewise constant/stair-stepping, or piecewise linear.

There have been many investigations conducted using the VOF method in different areas involving multiple phases and using the formation of interfaces. These involved the modeling of the evaporation process [112-114], the boiling flows [115-117], and the wave formation and propagation [118-121], etc. The VOF method tracks the volume fraction of each phase instead of tracking the interface itself and the interface is reconstructed from the values of volume fraction or the fraction function [110]. In order to track the interface between the wetting and non-wetting phases, the VOF method uses a color function [103]. Color function has the properties of volume fraction as it has a value of one or zero when a control volume is entirely filled with one or the other of the phases, and a value between one and zero when an interface is present in the control volume.

As mentioned in the theory of VOF method, a function $\xi(x,y,t)$ is defined in order to track

the interface. ξ is defined to be unity at any point occupied by the wetting phase and zero at any point occupied by the non-wetting phase. Hence, during the numerical simulation, if ξ(i,j)=1 the cell i,j is full of the wetting phase, and if ξ (i,j)=0 the cell i,j is empty of the wetting phase and full of the non-wetting phase. Consequently, when the value for this function falls between 0 and 1, the cell contains the interface. Therefore, the governing equation for the tracking function becomes

$$\frac{\partial \xi}{\partial t} + \frac{\partial (\xi)}{\partial x} + \frac{\partial (\xi v)}{\partial y} = 0 \tag{100}$$

where the initial condition, i.e. ξ (x,y,0), is given by initializing the free surface geometry. The above equation states that ξ moves with the fluid in time and space. Numerical solution of this equation for ξ gives $\xi_{i,j}$ directly. The VOF method requires only one storage variable for each mesh cell to define the interface. The detailed shape is then processed after ξ is computed. In a Eulerian calculation, it is necessary to compute the flow of fluid through the mesh, which requires an averaging of the flow properties. Thus, the density and viscosity are averaged as follows:

$$\rho = \xi \rho_1 + (1 - \xi)\rho_2 \tag{101}$$

$$\mu = \xi \mu_1 + (1 - \xi)\mu_2 \tag{102}$$

For a meshbased numerical simulation, new properties based on fluid properties of both materials should be considered in the cell containing the free surface, and the governing equations should be rewritten as follows [122]:

Continuity:

$$\frac{\partial (\xi \rho_1)}{\partial t} + \nabla . \xi \rho_1 u_1 = 0 \tag{103}$$

$$\frac{\partial [(1-\xi)\rho_2]}{\partial t} + \nabla . [(1 - \xi)\rho_2 u_2] = 0 \tag{104}$$

Momentum

$$\frac{\partial(\xi\rho_1 u_1)}{\partial t} + \nabla.[\xi\rho_1 u_1 u_1] = -\Delta P_1 + \nabla.\left[\xi\mu_1\left(\nabla u_1 + \nabla {u_1}^T\right)\right] + \xi\rho_1 g + \vec{F} \quad (105)$$

$$\frac{\partial[(1-\xi)\rho_2 u_2)}{\partial t} + \nabla.[(1-\xi)\rho_2 u_2 u_2] = -\Delta P_2 + \nabla.\left[(1-\xi)\mu_2\left(\nabla u_2 + \nabla {u_2}^T\right)\right] +$$

$$(1-\xi)\rho_2 g + \vec{F} \quad (106)$$

Rider et al [103] describes the steps of the VOF method as follows. First the fluid volumes are initialized in each computational cell or control volume using a specified interface geometry. One need to compute fluid volumes in each cell containing the interface (called mixed cells) since both the wetting and non-wetting phases are present in those cells. Exact interface information is then discarded in favor of the discrete volume data which is saved as volume fractions. Since a unique interface configuration does not exist once the exact interface location is replaced with discrete volume data, interface has to be reconstructed to extract the detailed interface information and the reconstructed interface must truncate cells with a volume equal to the discrete fluid volumes [103].

As we used FLUENT to simulate the two-phase flow and track the formation and progress of the interface, control-volume formulation requires that convection and diffusion fluxes through the control volume faces be computed and balanced with source terms within the control volume itself. One of the schemes that FLUENT uses to calculate the face fluxes for the VOF model is geometric reconstruction, in which FLUENT applies a special interpolation treatment (compared to the other methods such as the Donor-Acceptor method) to the cells that lie near the interface between two phases (Figure 61).

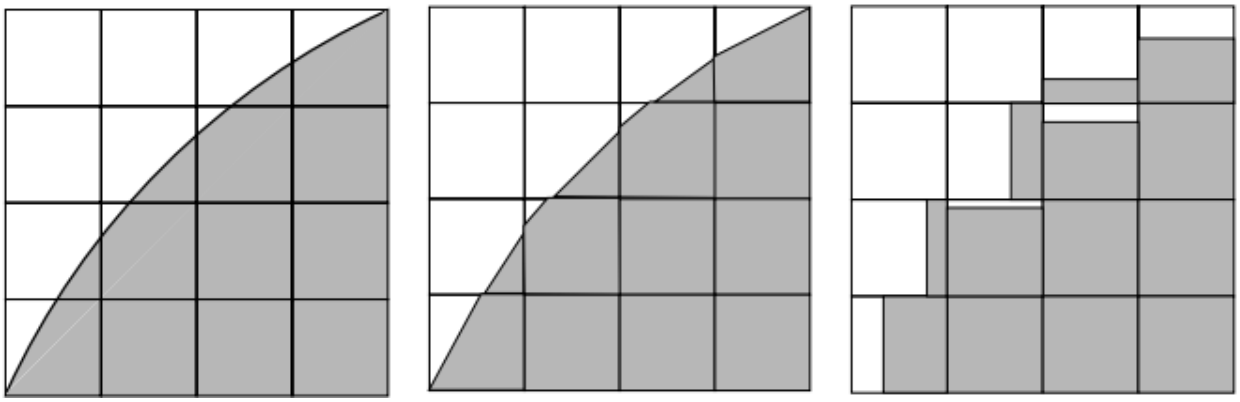

Figure 61 Comparison between the actual interface and the computed ones using different methods in FLUENT: a) actual interface, b) geometric reconstruction, c) donor-acceptor [123]

The geometric reconstruction scheme, in which the standard interpolation schemes is being used, represents the interface between fluids using a piecewise-linear approach which is one of the most accurate and applicable for general unstructured meshes. The first step of geometric reconstruction is calculating the position of the linear interface relative to the center of each partially-filled cell based on information about the volume fraction and its derivatives. The next step is calculating the amount of fluid advecting through each face using the computed linear interface representation, and information about the normal and tangential velocity distribution on the face. In the last step, based on the balance of fluxes calculated in the second step, the volume fraction in each cell is calculated [123].

In FLUENT, the surface curvature is computed from local gradients in the surface normal at the interface:

$$n = \nabla \xi_{1or2} \tag{107}$$

Hence the curvature, is defined as:

$$\kappa = \nabla . n \tag{108}$$

5-3 Case Studies

In our earlier studies listed in previous chapters, we had found that wick microstructure plays a big role in deciding whether the liquid front during wicking is sharp, semi-sharp or diffuse. All our sintered-beads wicks showed sharp fronts, while most of the fibrous wicks with fibers mostly aligned with the wick axis displayed diffuse fronts with only a few showing the semi-sharp fronts. It was also observed that the porosity also plays a role, with lower porosities in fibrous wicks giving rise to semi-sharp fronts while higher porosities (accompanied with fiber clustering) in fibrous wicks leading to diffuse fronts. Our aim here is to conduct a 2D two-phase (liquid-air) flow simulation in both particulate (bead-like) and fibrous microstructures after including the capillary pressure and gravity effects, and to see if we can validate our earlier empirical observations about the dependence of macroscopic flow-front type on particle shape and porosity.

In our present investigation, we modeled the wicking process in a series of geometries representing a porous media packed with beads or fibers. In order to have an accurate investigation on the formation and progression of liquid fronts, we created 7 (seven) different geometries to have a gradual transition from a porous medium created by spherical beads (circles in 2D) to a porous medium made of very long fiber-like ellipsoids (ellipses in 2D). To have a CFD amenable representation of our real wick microstructures, we started with circles with diameter of 20 μm and kept turning them into longer and longer ellipses with dimensions (minor diameter*major diameter) of 20*40, 20*80, 20*160, 20*320, 20*640 and 20*1280 μm as shown in Figure 62. This transition from a circle to a very long ellipse helps us to investigate the differences in shape and progress of liquid fronts in the corresponding porous media. In order to consider the effect of porosity on the formation and progress of liquid fronts, we considered two cases of 50% and 70% porosities.

In order to create unit-cells of our porous medium, we used state-of-the-art software GeoDict. To generate a unit-cell that conforms to the microstructure of our porous media, we needed to input the fiber diameter, porosity, and orientation of the fibers. Then Geodict starts to randomly pack the particles inside a cube-like unit-cell. In the following sections, we will explain the created unit-cells and simulation results.

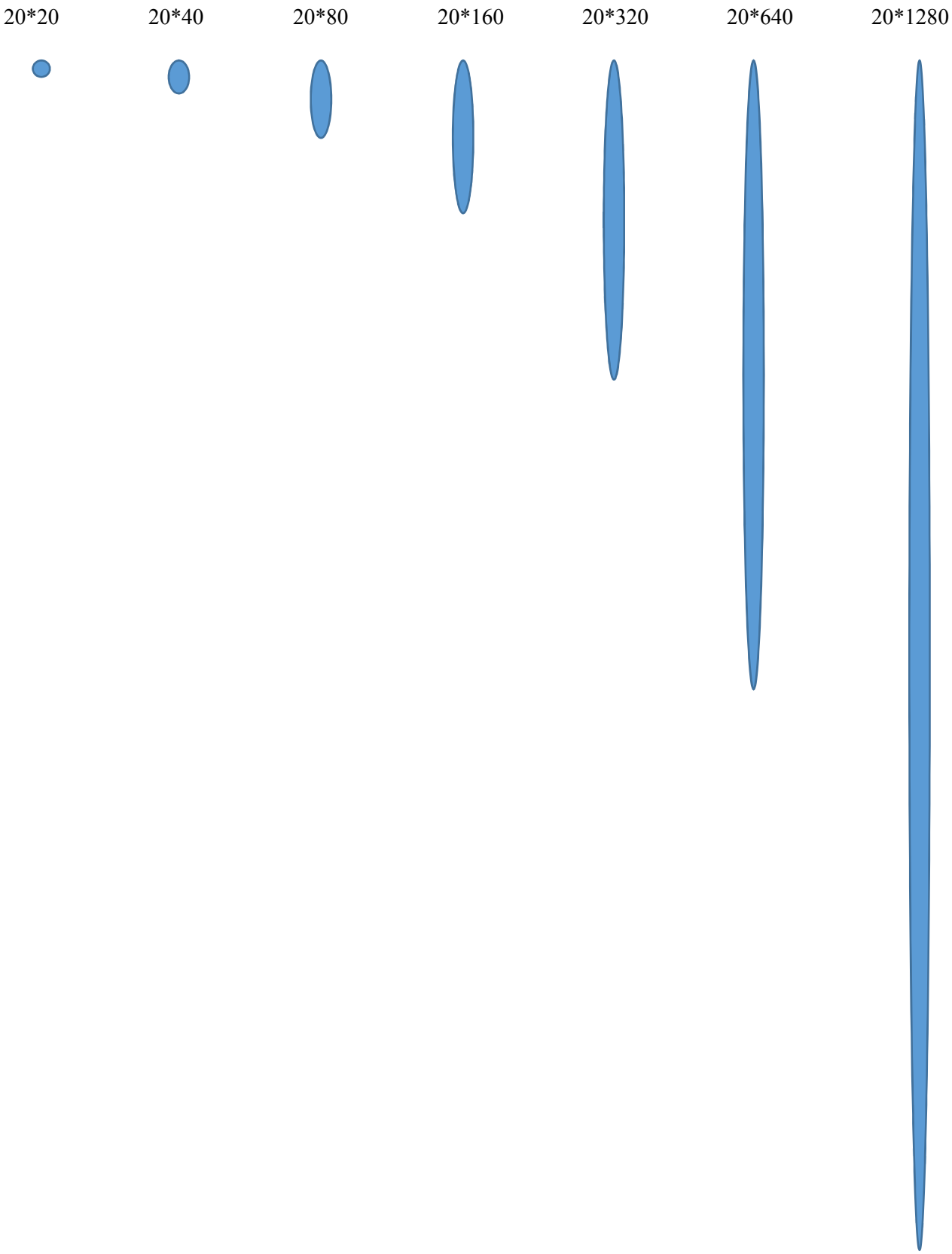

Figure 62 Sample of ellipses used to pack and create unit cells representing the investigated porous media

In order to import the unit-cells into FLUENT and to define the boundaries (Inlet, Outlet, ellipse surface, and walls), we had to do some modifications in term of making the unit-cells into geometries can be imported and read by FLUENT. Figure 63 shows an example of the original GeoDict-created unit-cell and the modified unit-cell prepared for FLUENT.

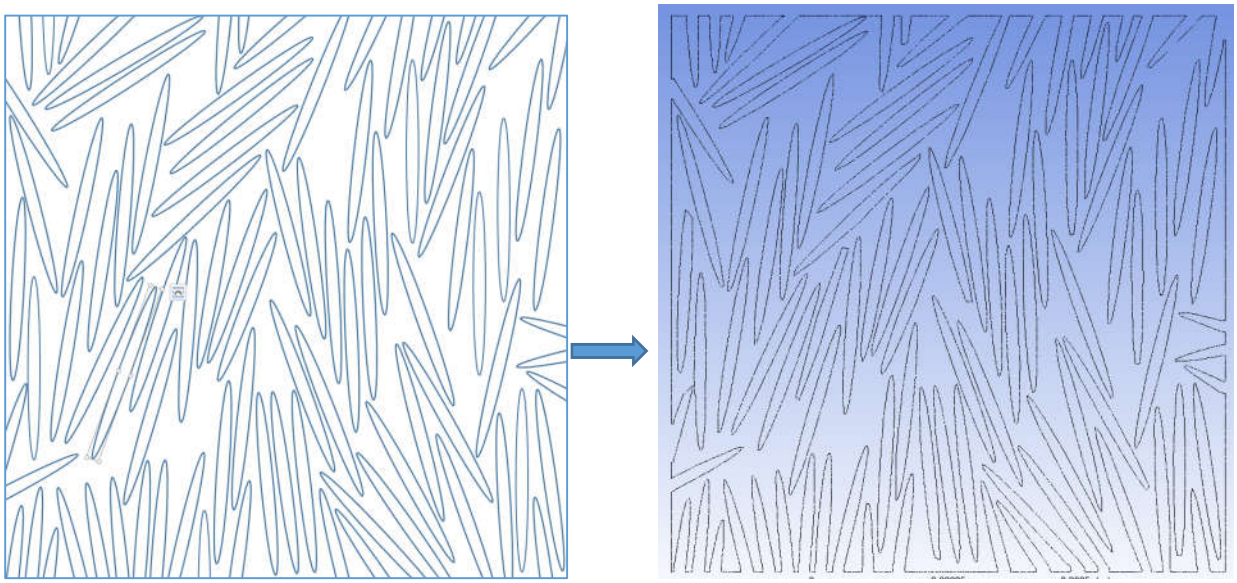

Figure 63 The process of modifying a unit-cell created by GeoDict , which is to be imported and read into FLUENT

5-3-1 Boundary condition

After preparing the geometry and importing it into FLUENT, the boundaries were defined as shown in Figure 64 and the conditions applied on the surfaces are as follow:

1-0 Pa gage pressure at the inlet

2- 0 Pa gage pressure at the outlet

3- 0 degree as the contact angle between the wicking liquid and ellipses

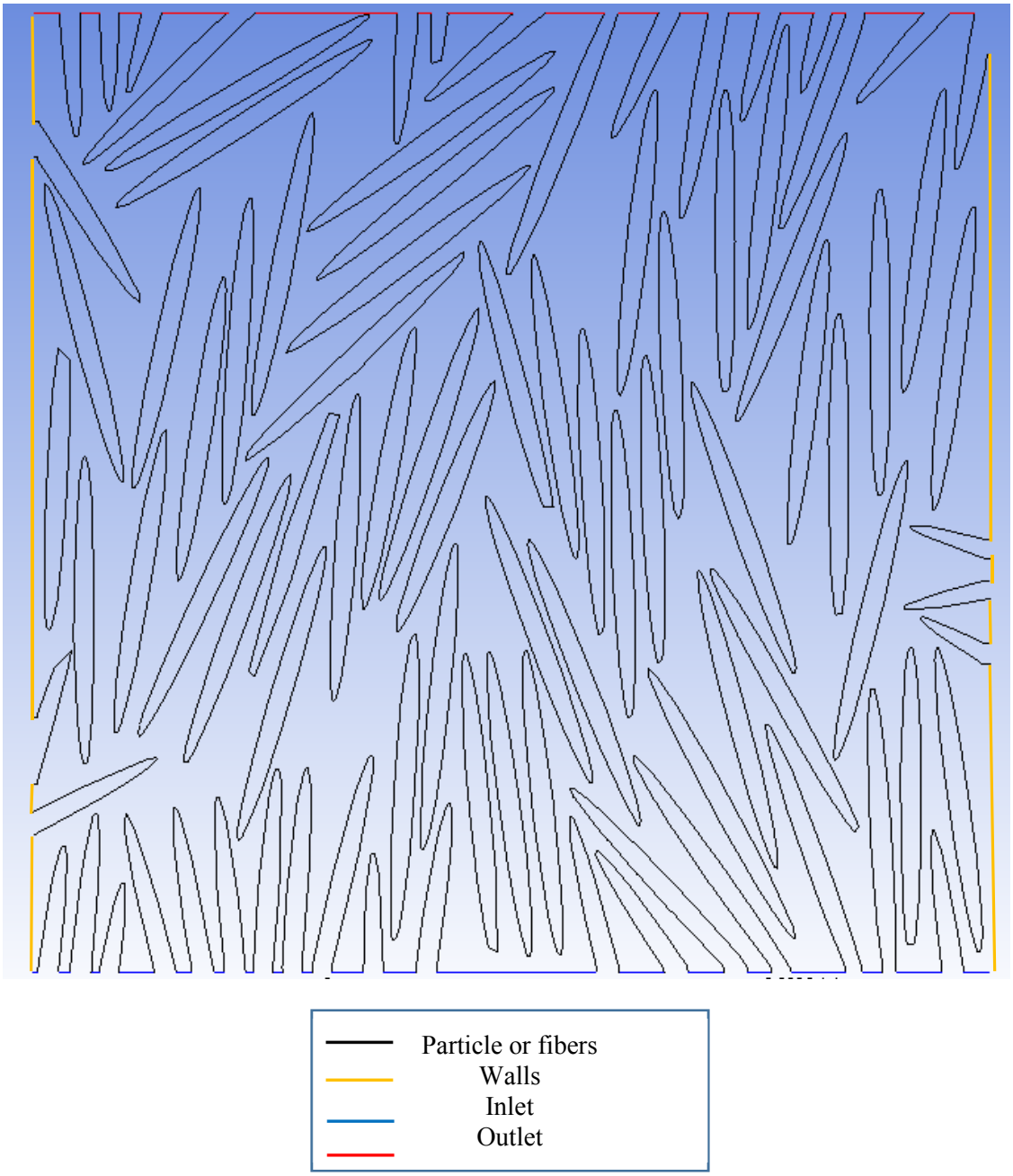

Figure 64 Boundaries of the geometry imported into FLUENT

5-3-2 Case 1: Porosity of 50%

The first studied case was that of unit-cells packed with ellipses representing particles or fibers with a porosity of 50%. As explained earlier, GeoDict packs the unit-cells by randomly arranging the ellipses. Hence, as shown in Figure 65, randomly packing the unit-cells helped us to do the investigation by cancelling bias of ellipse-cluster orientations along certain directions and allowed us to be able to generalize its outcomes along the vertical (flow) direction. Figure 65 shows the seven created unit-cells showing the gradual transition from a medium made of particles to a medium made of fibers.

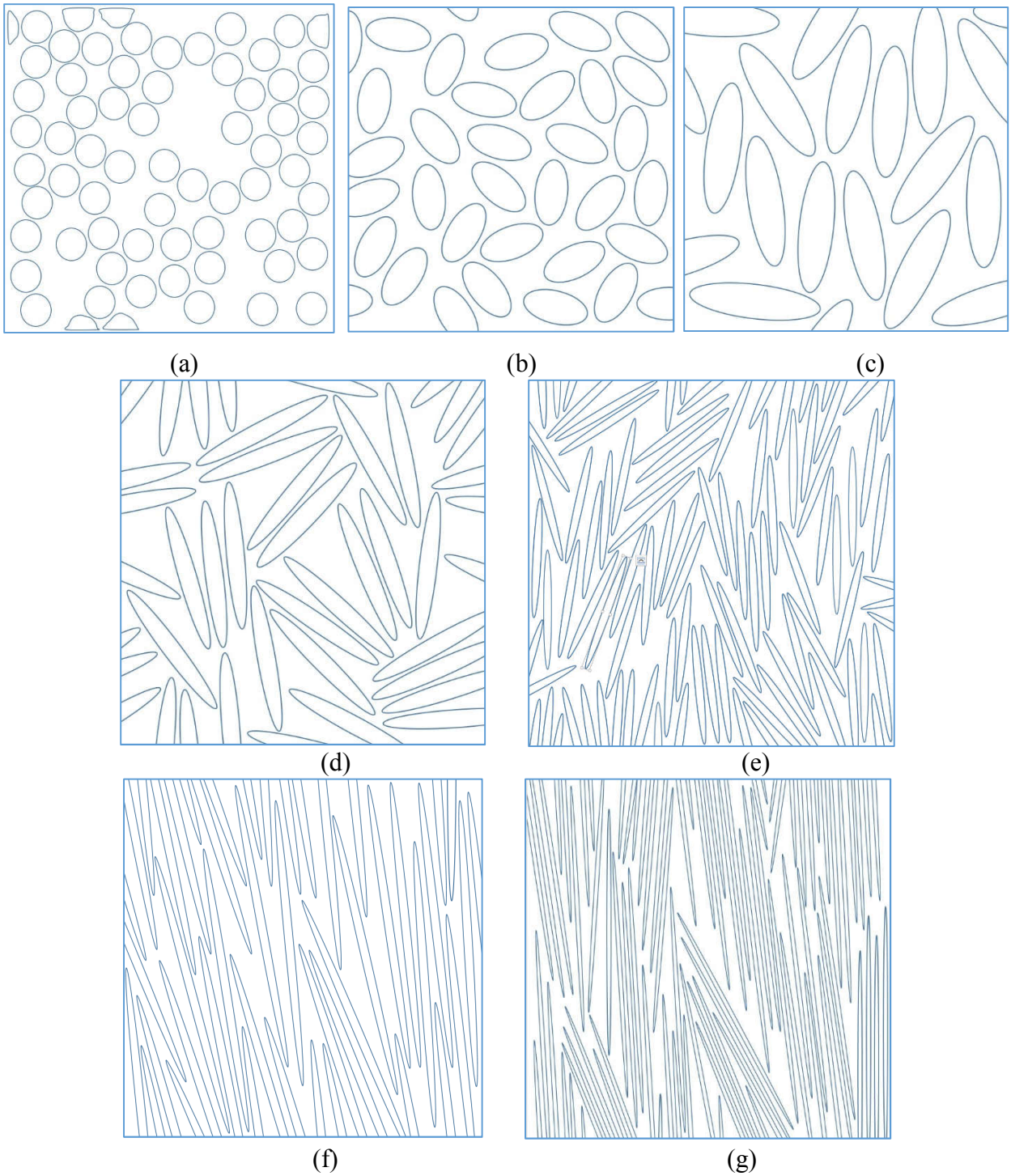

Figure 65 The unit-cells created with GeoDict representing porous media at 50% porosity: the unit cells (a) to (g) show a gradual transition from a particulate porous media to a fibrous porous media. Ellipse dimensions (minor diameter*major diameter) in unit cells: a) 20*20 µm, b) 20*40 µm, c) 20*80 µm, d) 20*160 µm, e) 20*320 µm, f) 20*640 µm, g) 20*1280 µm

5-3-3 Case 2: Porosity of 70%

The second scenario investigated was that of porosity being 70%. Like we did for porosity of 50%, we used GeoDict to create the unit-cells (Figure 66). As mentioned earlier, one benefit of having higher porosity is that we can study the effect of clustering in our simulation as well.

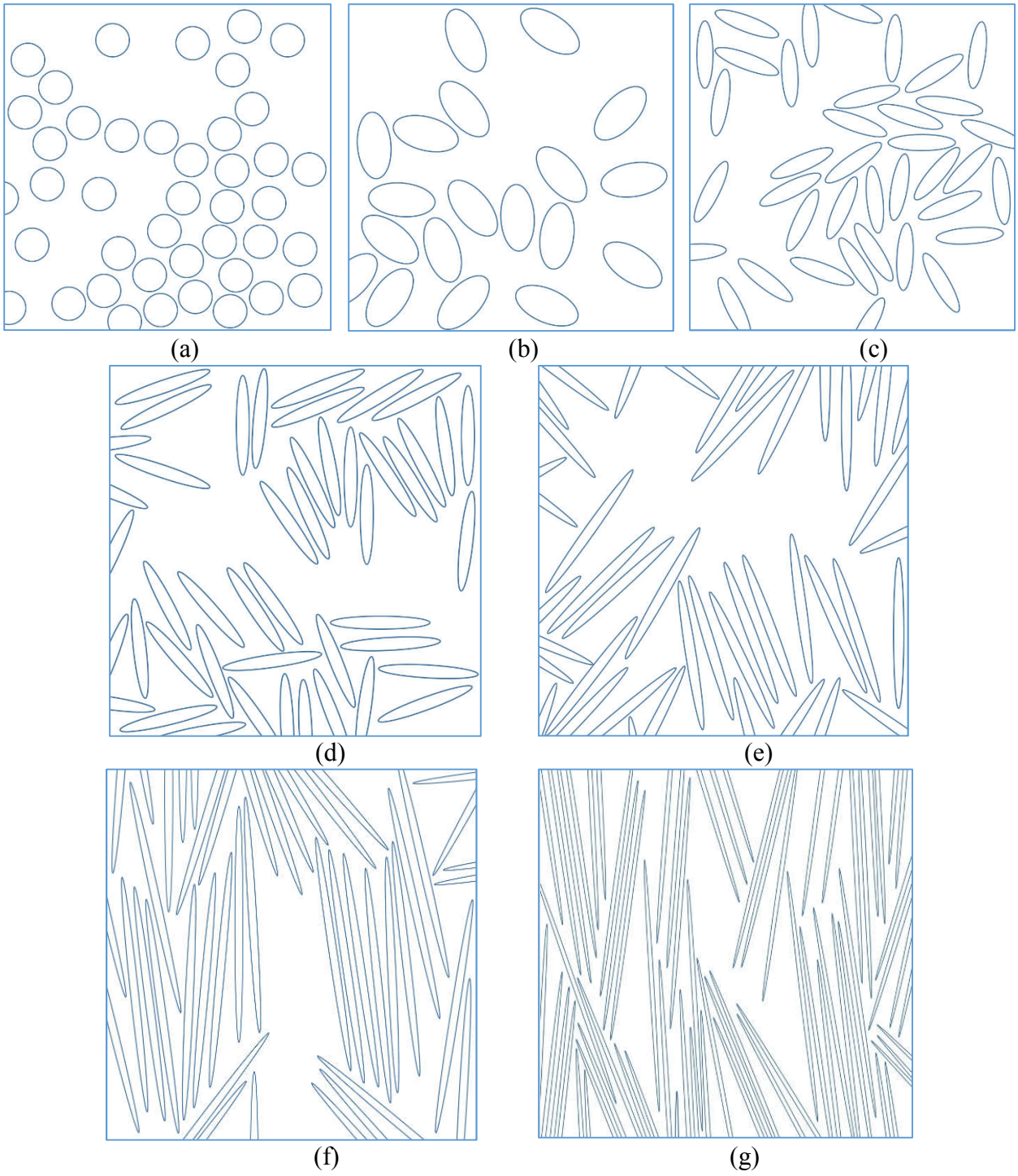

Figure 66 The unit-cells created with GeoDict representing porous media at 70% porosity: the unit cells (a) to (g) show a gradual transition from a particulate porous media to a fibrous porous media. Ellipse dimensions (minor diameter*major diameter) in unit cells: a) 20*20 µm, b) 20*40 µm, c) 20*80 µm, d) 20*160 µm, e) 20*320 µm, f) 20*640 µm, g) 20*1280 µm

5-4 Result and conclusion

After importing the prepared geometries into FLUENT, after applying the boundary conditions, and after activating the multiphase module, we are finally ready to run the simulation. In the following sub-sections, we present the results of the simulation; after interpreting them, we offer the salient conclusions.

5-4-1 Formation and progression of liquid front

Figure 67 and Figure 68 show the evolution with time of the interface between the wetting and non-wetting phases during the simulation of imbibition (wicking) process for unit-cells with porosities of 50% and 70%, respectively. To have a better understanding of the formation and progress of the interface, we showed the results corresponding to three different time steps in the same geometry.

On studying the sequence of figures from Figure 67 (a) to (g), we see clearly how the front formation is influenced by the aspect ratio of ellipses at lower porosity of 50%. For the 20*20 μm and 20*40 μm ellipses, which can consider as circular or near-circular particles, we observe a some-what flat front in the unit-cell. This means that transition from the fully wet 100% saturation to the dry 0% saturation happens over a small distance, notwithstanding the deviations caused by local heterogeneity due to clustering. This perhaps points to the front being a sharp front when looked macroscopically, and it matches with our experimental observation that (macroscopic or visual) liquid fronts in the sintered-beads wicks are invariably sharp. On replacing the circles with ellipses of 1:4 aspect ratio (i.e., with 20*80 μm dimensions), the transition from the fully wet 100% saturation to the dry 0% saturation happens over a larger distance. This trend strengthens and transition region becomes longer when the ellipses changes to 1:8 (20*160 μm) and 1:16 (20*320

μm) aspect ratios. Then the macroscopic interface which represents the visual liquid front may be transitioning to becoming a semi-sharp front. One can witness the appearance of fingers of liquids climbing preferentially in narrower spaces, thus leading to the loss of sharpness of the macroscopic fronts. Finally, for the ellipses with higher aspect ratios of 1:32 (20*640 μm) and 1:64 (20*1280 μm), the trends become stronger of the heightening of finger formation and of the elongation of the transition region. One can expect the visual front to become more and more diffuse.

A similar trend can be seen in Figure 68 (a) to (g) for 70% porosity. However, since the porosity is higher, there are more gaps in the microstructure and more evidence of clustering of 'particles' or 'fibers'. Through not much difference can be seen in the fluid distribution patterns for the three initial ellipse sizes (20*20 μm, 20*40 μm and 20*80 μm), one can however observe that the length over which the local saturation changes from 100% to 0% is now a bit longer. As a result, the macroscopic front is perhaps likely to be changing from being sharp to being semi-sharp more 'easily'. For the last four ellipse sizes (20*160 μm, 20*320 μm, 20*640 μm, 20*1280 μm), the length over which the local saturation changes from 100% to 0% is now clearly longer. Hence the visual or macroscopic fronts are going to be more diffuse. In particular, a comparison of Figures 67(g) and 68(g) reveals that for the higher porosity case the micro fronts are more 'broken up', have more pockets of air trapped, and extend over a longer length —clearly pointing to a more diffuse visual (macro) front.

As was preliminarily concluded in section 2-3, our final conclusion from Figure 67 and Figure 68 reaffirms that as the porosity increases, the liquid front type changes from sharp to semi-sharp to diffuse. In unit-cells with the lower porosity value, the particles and fibers are closer to each other and more homogeneously distributed, and consequently, the tiny micro-fronts climb uniformly in the interstitial channels to generate a sharper macro-front.

As shown in Figure 68, as the porosity increases, there is more chance of particle/fiber clustering and we observe higher concentrations of solid phase in several local areas of the microstructure. Such an existence of clustering leads to local inhomogeneities and consequently there will be faster motion of the wetting phase in these narrower channels. This leads to faster climbs of tiny micro-fronts in the clusters compared to the more 'open' regions, which causes the visual (macro) front to be more diffuse.

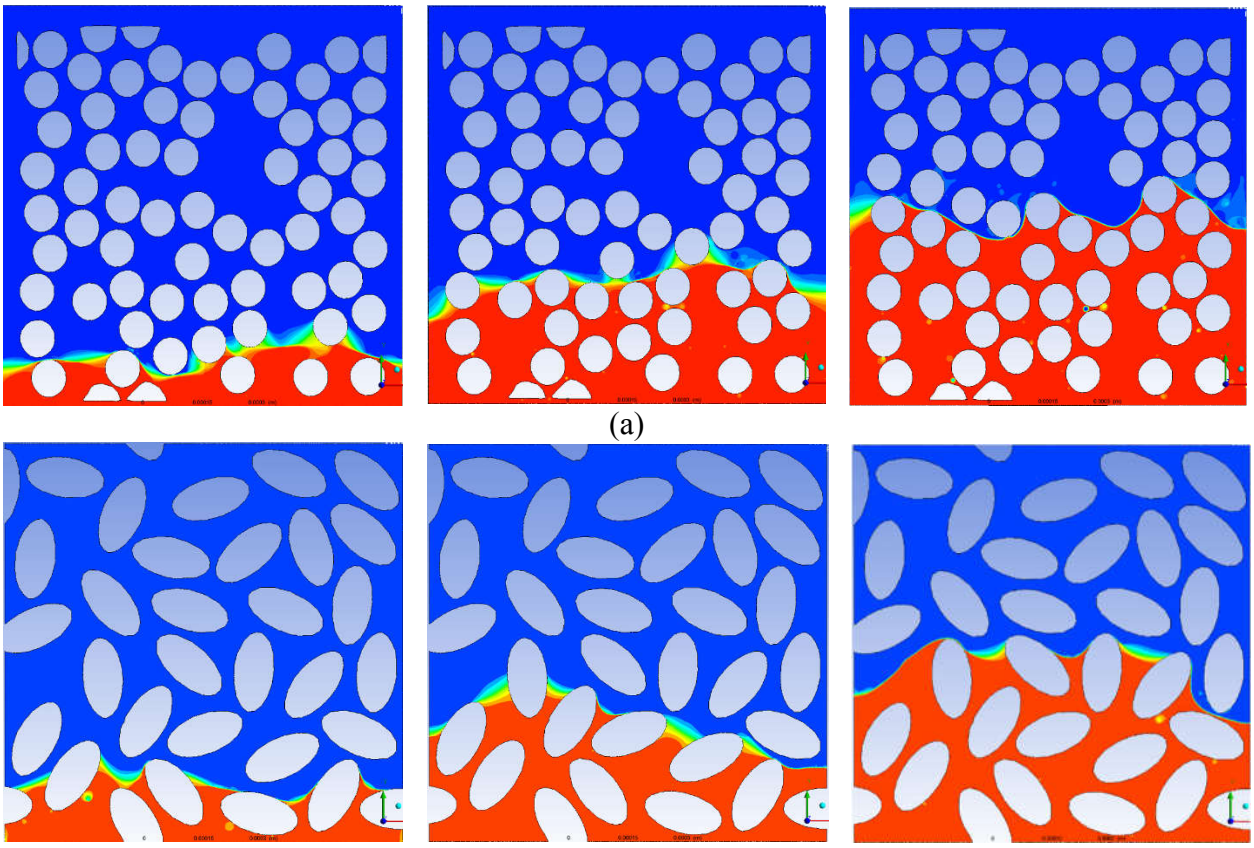

(a)

(b)

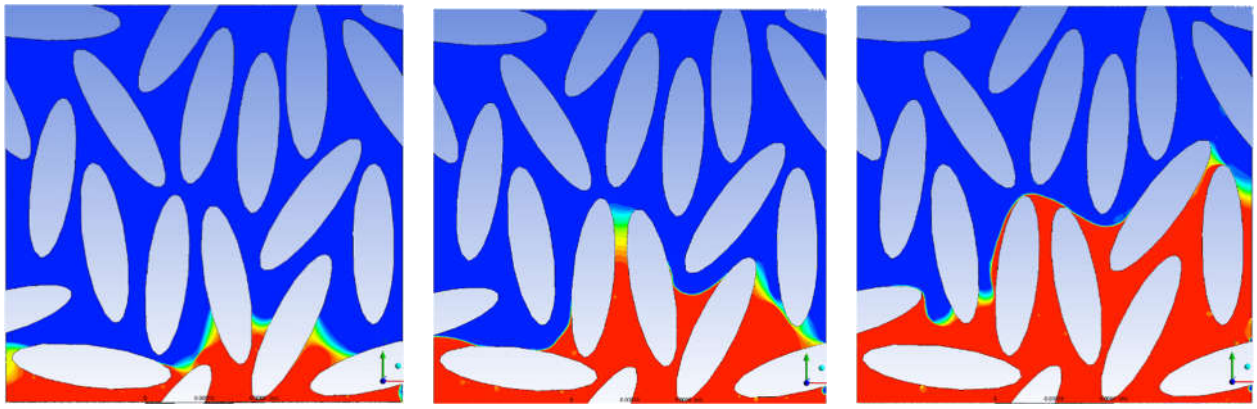

(c)

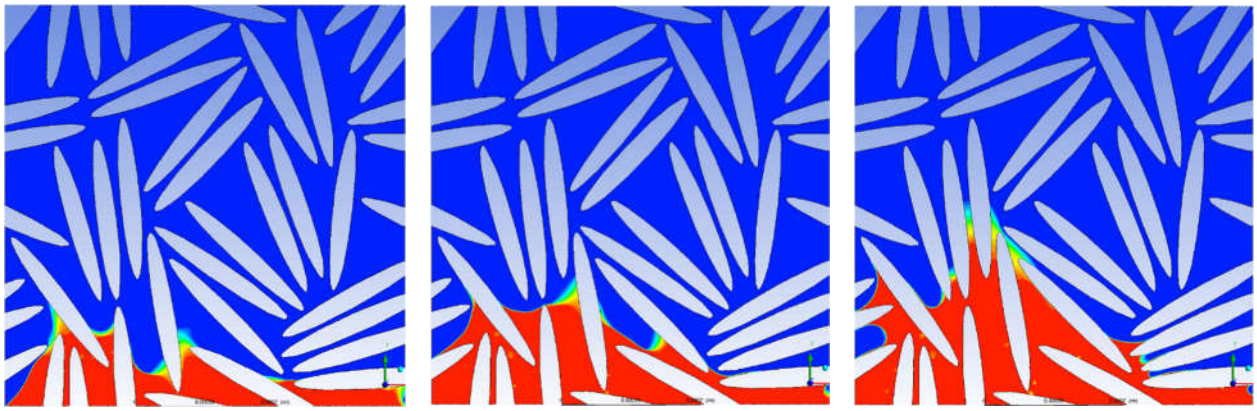

(d)

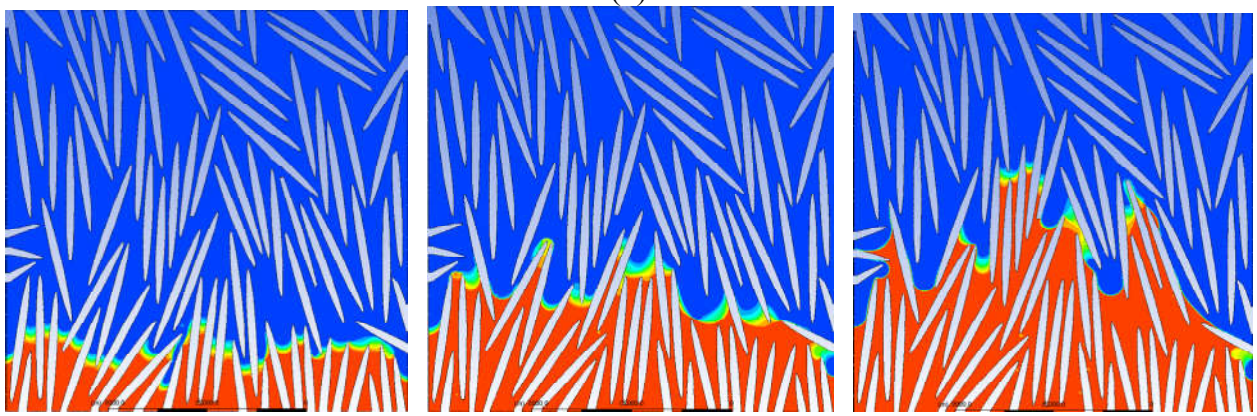

(e)

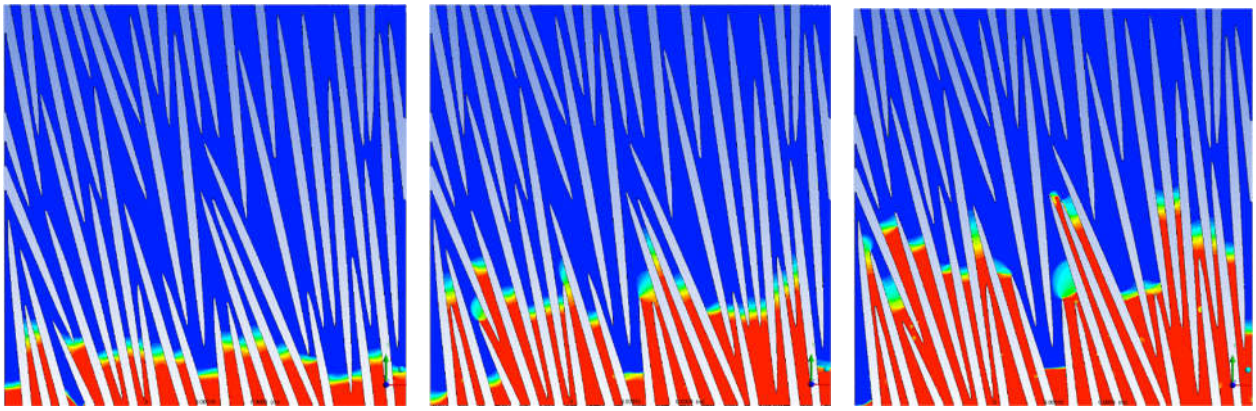

(f)

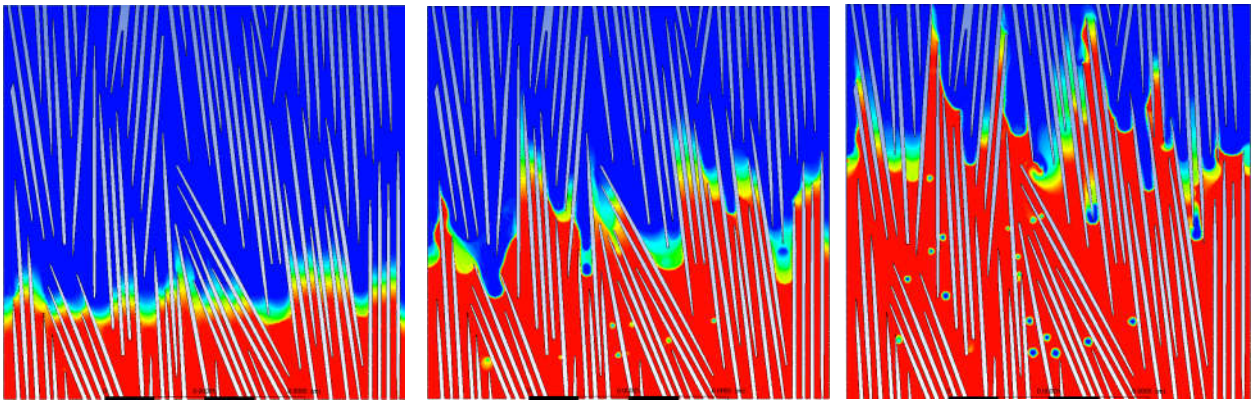

(g)

Figure 67 The movement of interface during the imbibition process in three different time steps in the unit-cells with a porosity of 50%. The dimensions of ellipses are:
a) 20*20 µm, b) 20*40 µm, c) 20*80 µm, d) 20*160 µm, e) 20*320 µm, f) 20*640 µm, g) 20*1280 µm

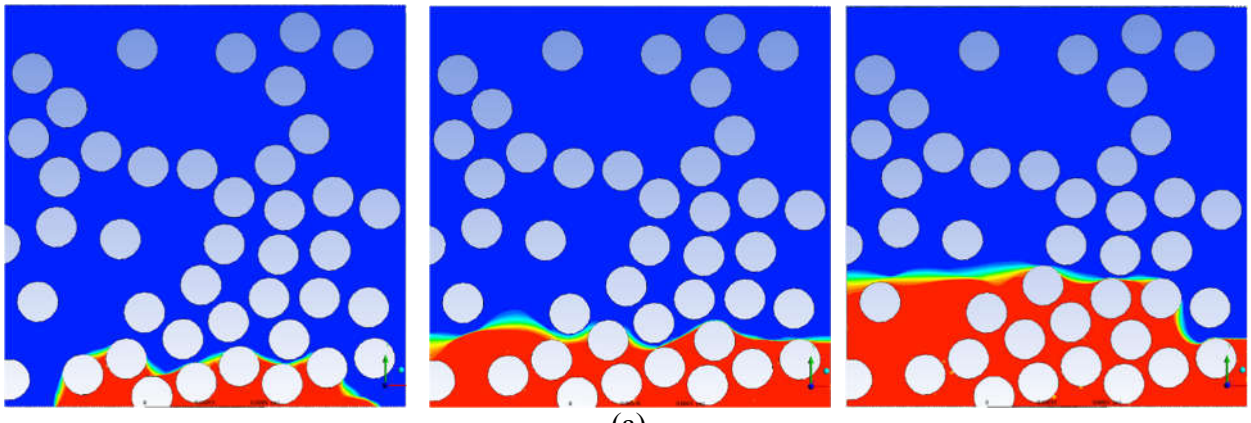

(a)

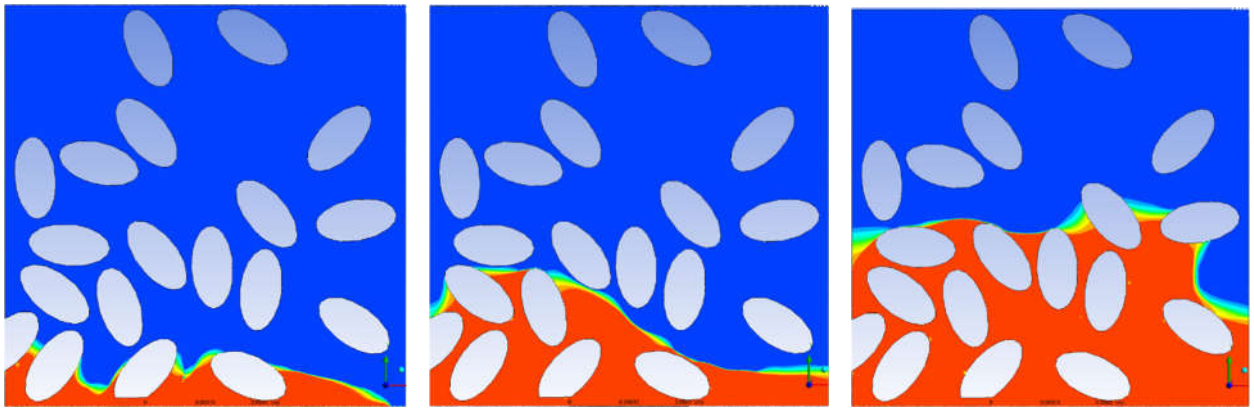

(b)

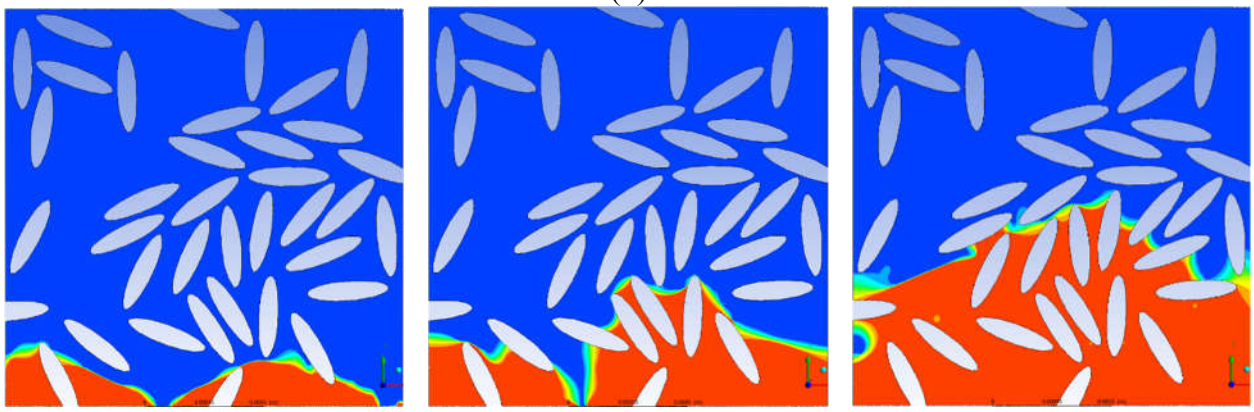

(c)

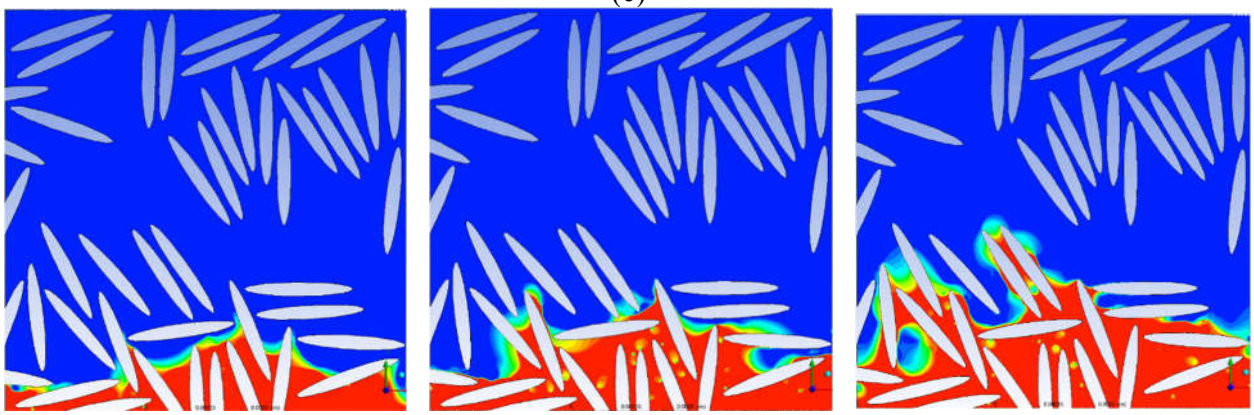

(d)

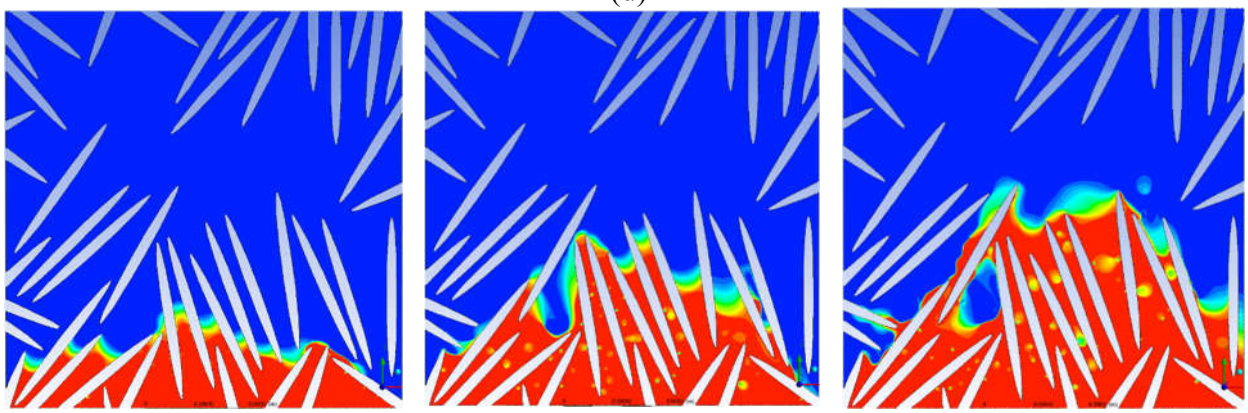

(e)

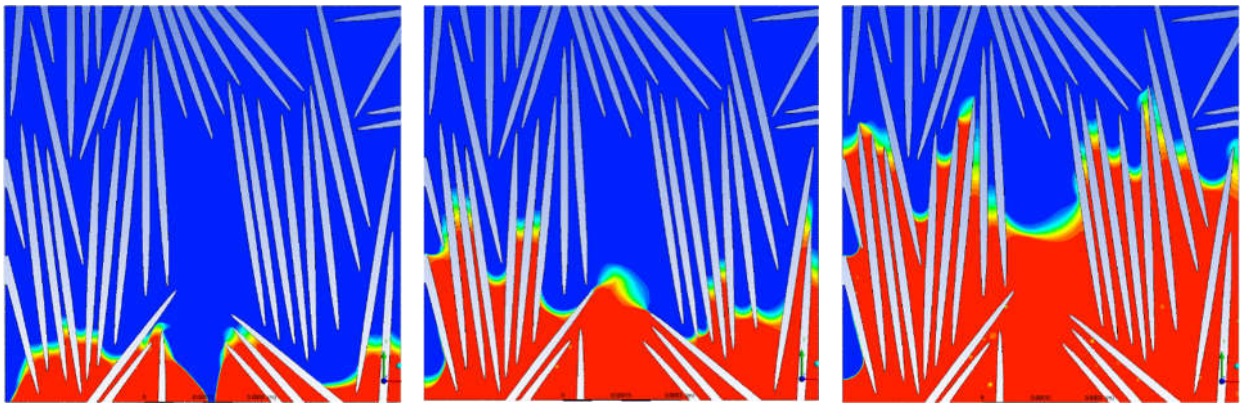

(f)

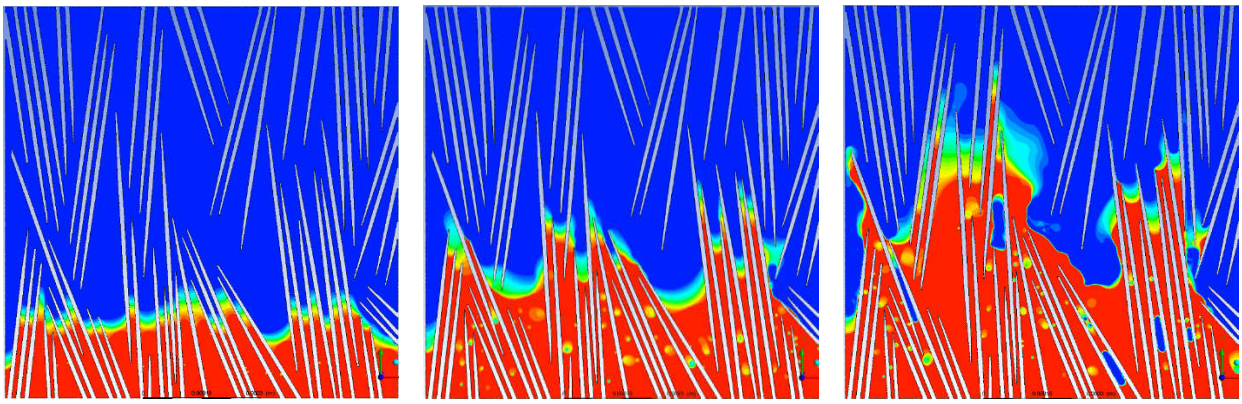

(g)

Figure 68 The movement of interface during the imbibition (wicking) process in three different time steps in the unit-cells with a porosity of 70%. The dimensions of ellipses are: a) 20*20 µm, b) 20*40 µm, c) 20*80 µm, d) 20*160 µm, e) 20*320 µm, f) 20*640 µm, g) 20*1280 µm

5-4-2 Variation of saturation as a function of position along the flow direction

As was explained in chapter 2, 3 and 4, under different conditions of sharp front and diffusive fronts, saturation become a function of time and position along the flow-direction coordinate. Under the sharp fronts, all the void space behind the visual liquid fronts are filled, completely saturated with the wicking fluid at 100% saturation, whereas under the diffusive front conditions, there is no well-defined sharp front and the saturation gradually changes from 100% to 0% over a finite length. Hence, it is important to study this dependence of saturation on location

and time in our CFD study also.

In order to make this comparison, we selected 5 different time steps and for each time step, by using the post-processor module of FLUENT, we obtained the fluid-phase distribution images at specific liquid-front positions.

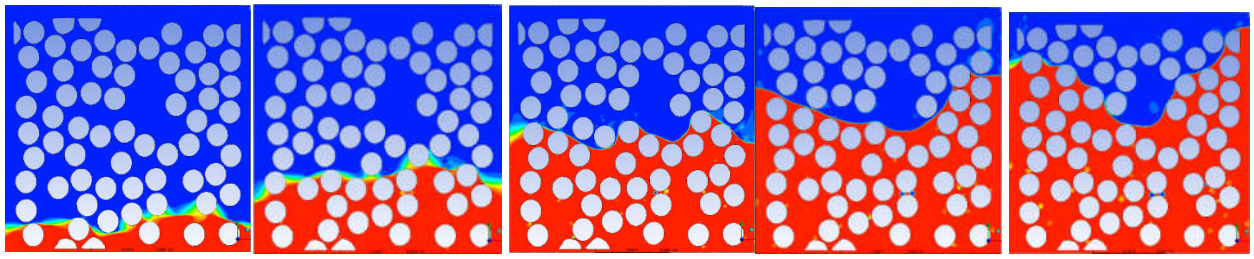

(a)

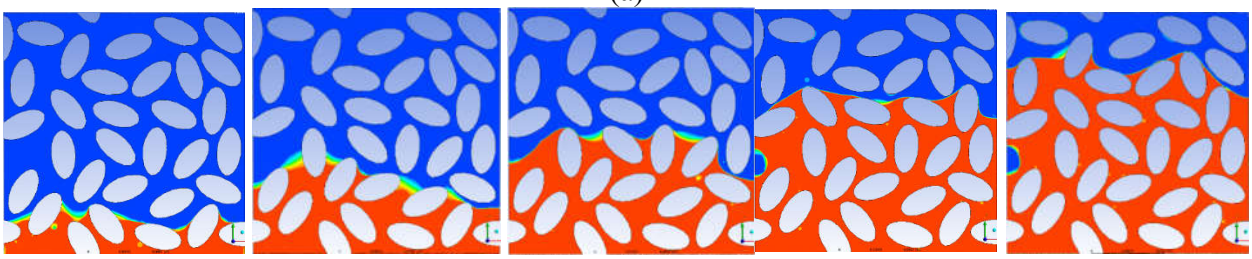

(b)

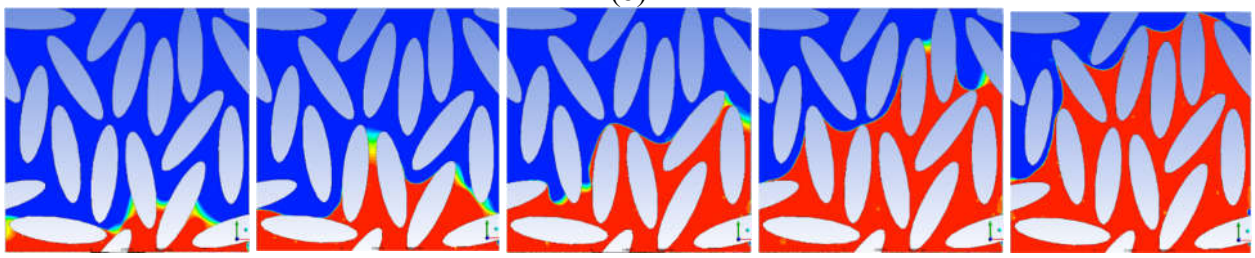

(c)

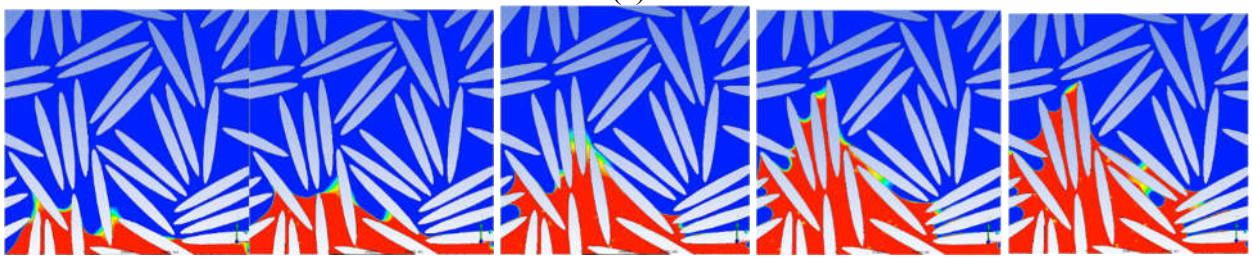

(d)

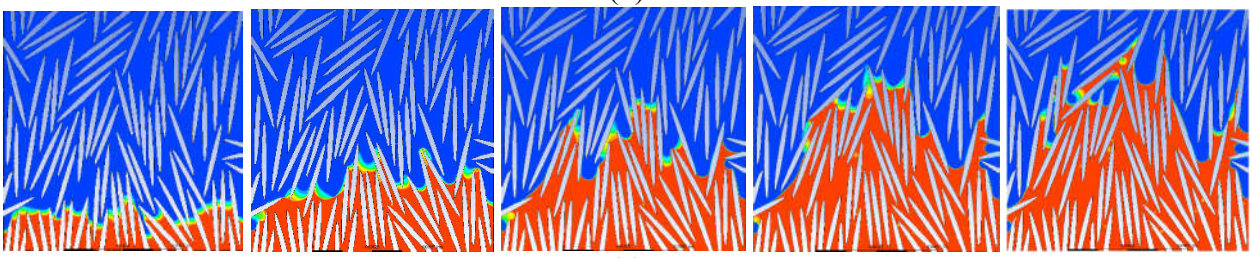

(e)

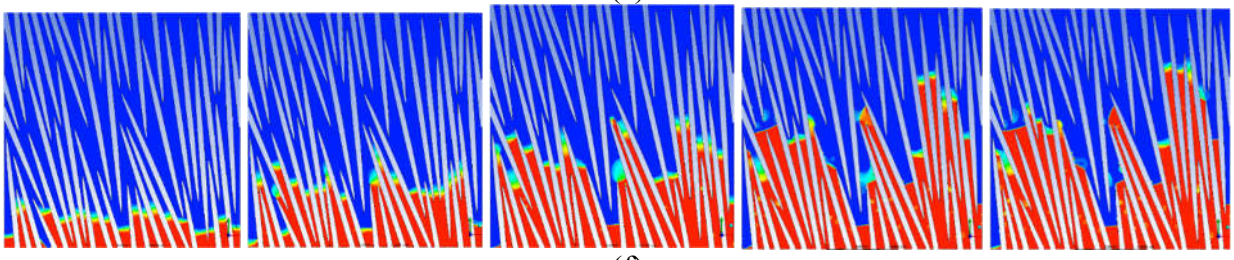

(f)

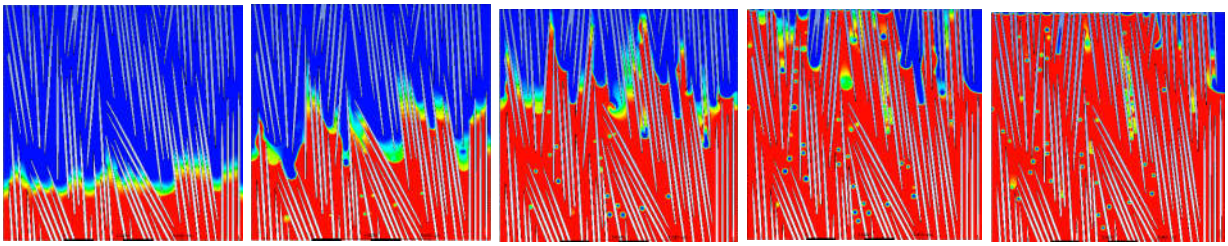

(g)

Figure 69 Five different time-steps of the wicking CFD simulation for each unit-cell having porosity of 50 %:

*a) 20*20 µm, b) 20*40 µm, c) 20*80 µm, d) 20*160 µm, e) 20*320 µm, f) 20*640 µm, g) 20*1280 µm*

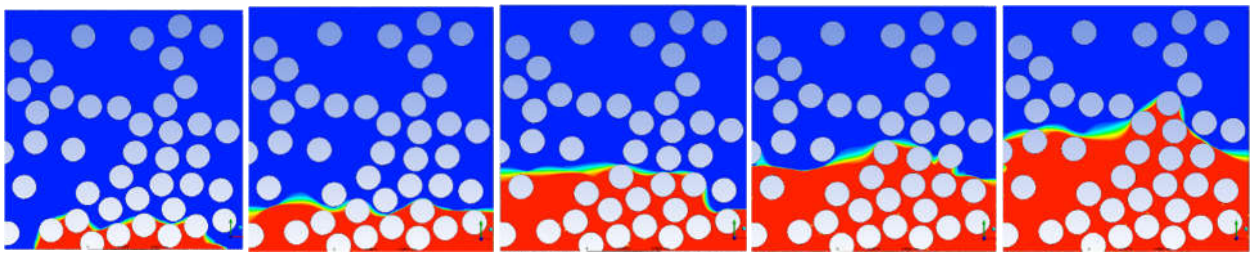

(a)

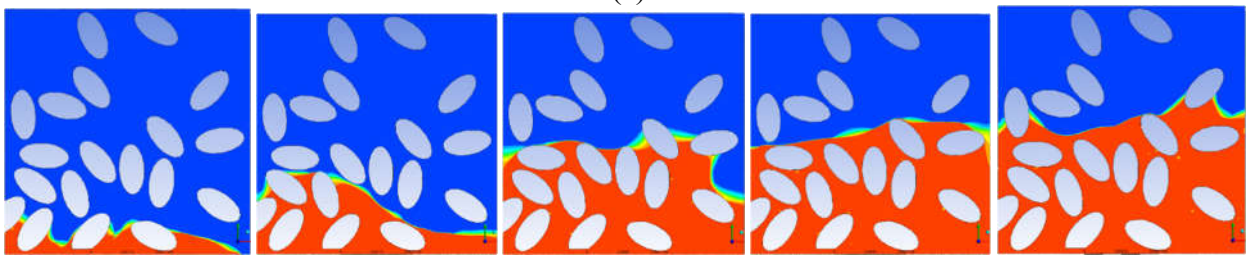

(b)

(c)

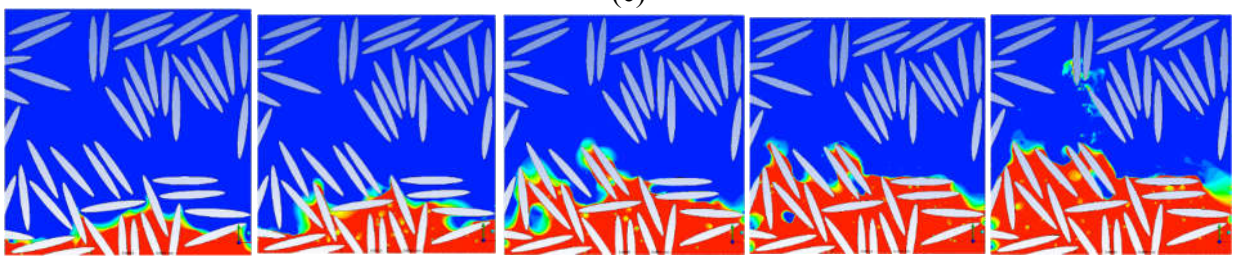

(d)

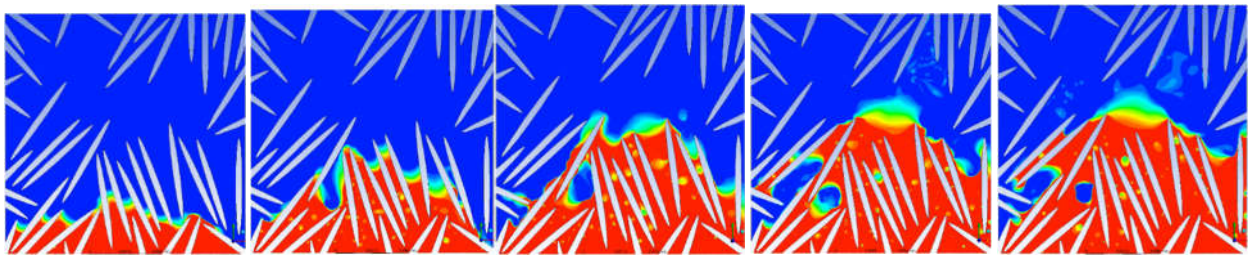

(e)

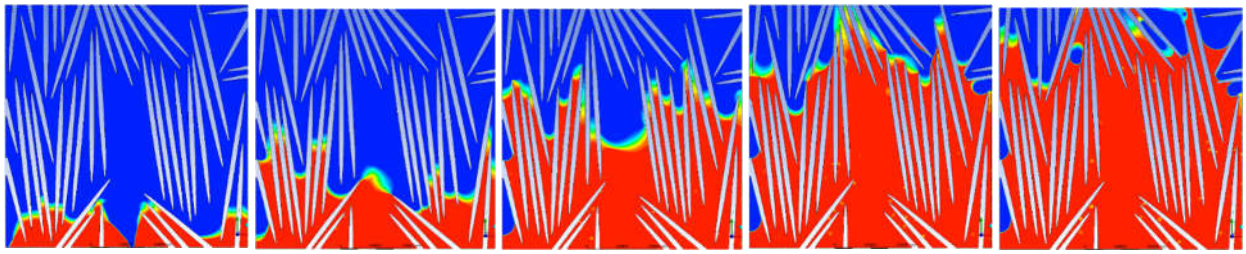

(f)

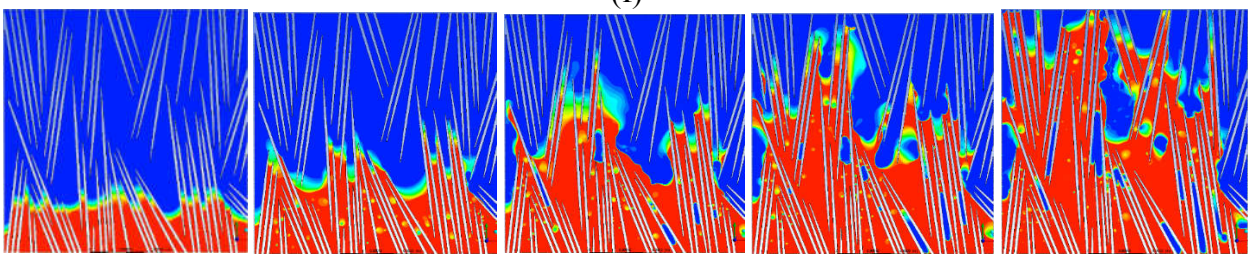

(g)

Figure 70 Five different time-steps of the wicking CFD simulation for each unit-cell having porosity of 70 %:
a) 20*20 µm, b) 20*40 µm, c) 20*80 µm, d) 20*160 µm, e) 20*320 µm, f) 20*640 µm, g) 20*1280 µm

In order to estimate saturation as a function of location along the flow direction, we discretize each image by superimposing a grid as shown in Figure 71. The grid is 25*25 and the size of each grid component is 8 micrometers.

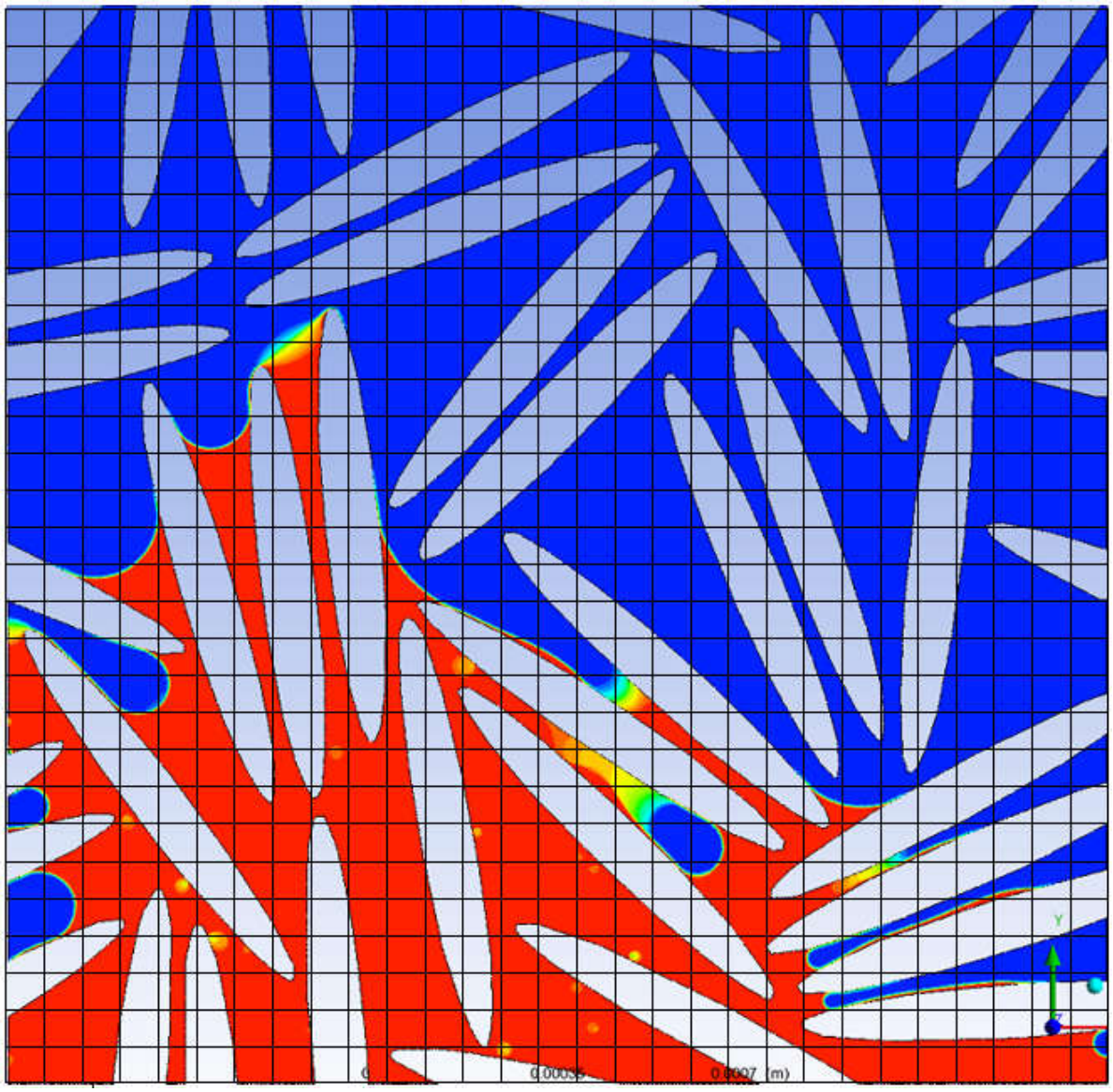

Figure 71 An example of the grid superimposed on one of the fluid-phase distribution images obtained from the FLUENT post-processor module

Putting a grid on each image enabled us to compute the saturation at each horizontal row of the grid. This was done by counting the number of squares filled by the wetting phase (red color)

and its ratio to the number of all squares in each row, excluding the squares containing the solid phase (white color). Hence, the number of squares 'filled' with the wicking liquid as well as the number of squares occupied by the solid phase enable us to estimate the saturation in that row as:

$$S = \frac{\#\text{ of squares filled with wetting phase}}{\text{total number of squares} - \#\text{ of solid phase squares}} \tag{109}$$

Figure *72* to Figure 78 show the saturation as a function of nondimensionalized location ($\frac{\text{the size of each grid component or square} \times \text{the row number}}{\text{minor radius 20 µm}}$) for all 5 time steps for all the seven investigated unit-cells for porosity of 50% (Figure 79 to Figure 85 for porosity of 30%)

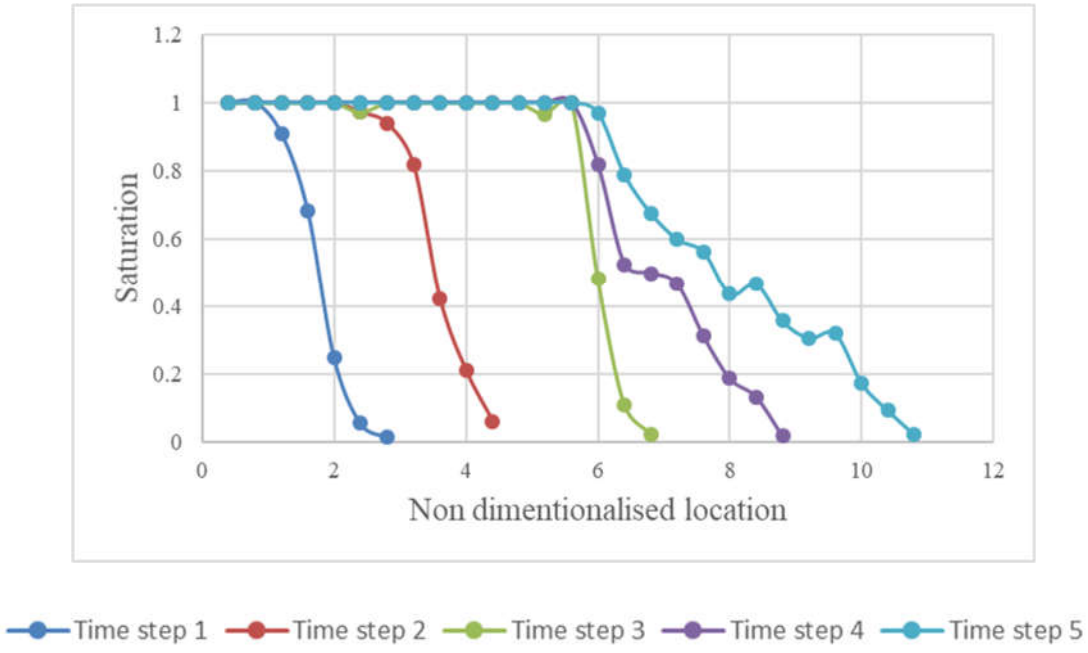

Figure 72 The graph of saturation as function of nondimensionalized flow-direction coordinate for 5 different time steps for the unit-cell packed with circles of diameter of 20 µm and with a porosity of 50%

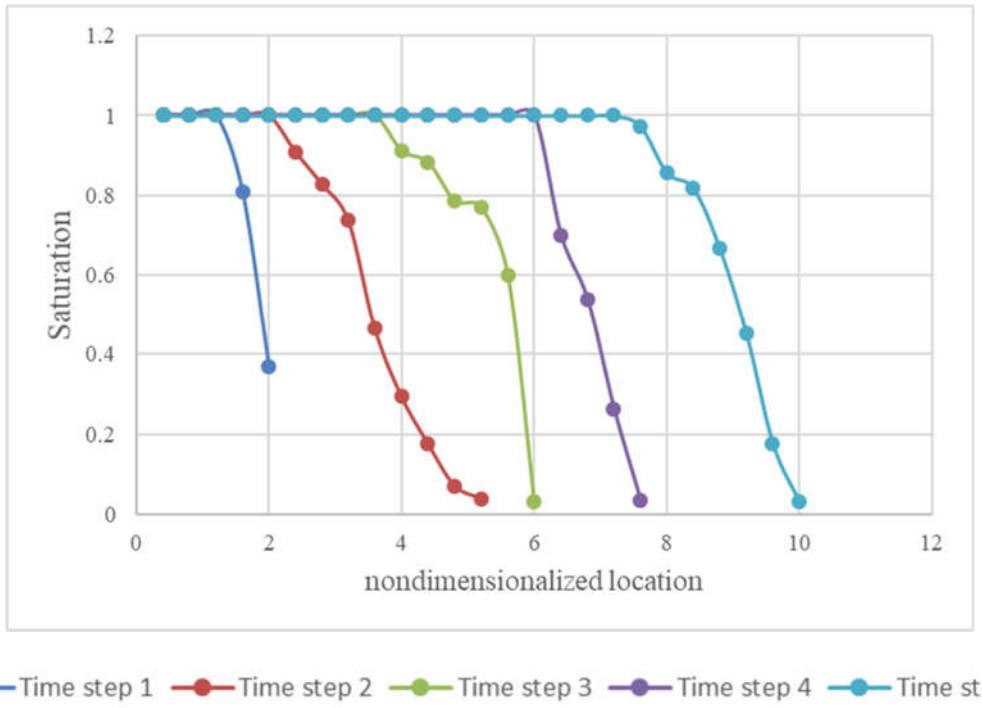

Figure 73 The graph of saturation as function of nondimensionalized flow-direction coordinate for 5 different time steps for the unit-cell packed with ellipses of dimensions 20*40 μm and with a porosity of 50%

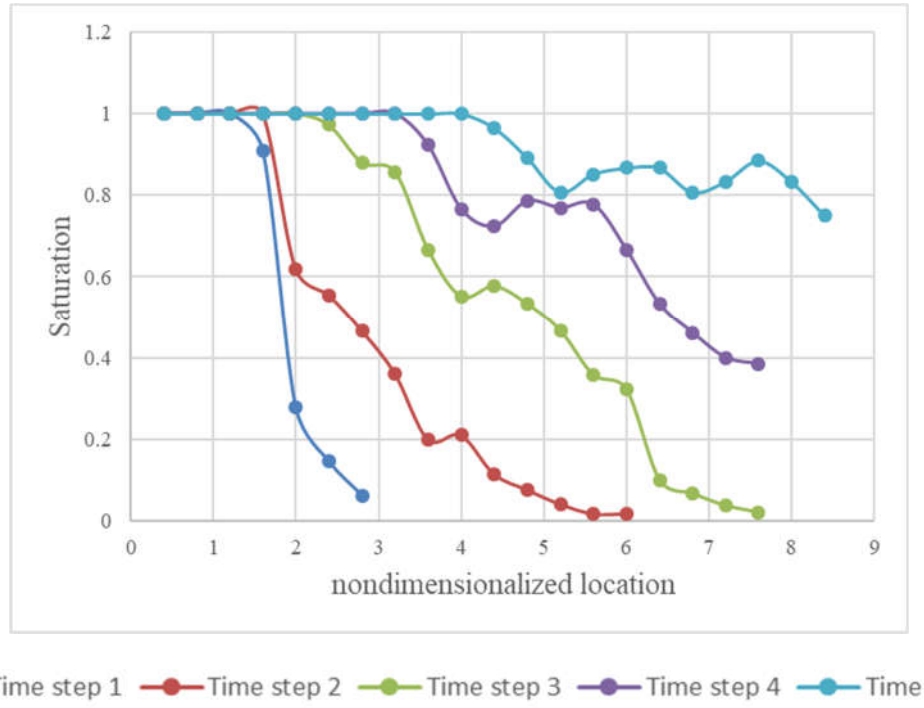

Figure 74 The graph of saturation as function of nondimensionalized flow-direction coordinate for 5 different time steps for the unit-cell packed with ellipses of dimensions 20*80 μm and with a porosity of 50%

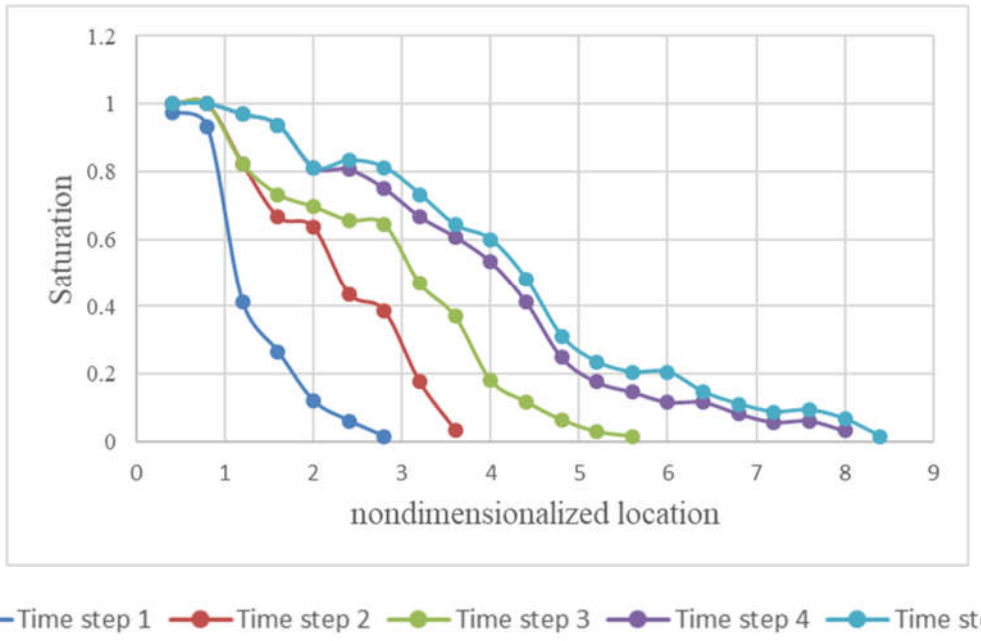

Figure 75 The graph of saturation as function of nondimensionalized flow-direction coordinate for 5 different time steps for the unit-cell packed with ellipses of dimensions 20*160 μm and with a porosity of 50%

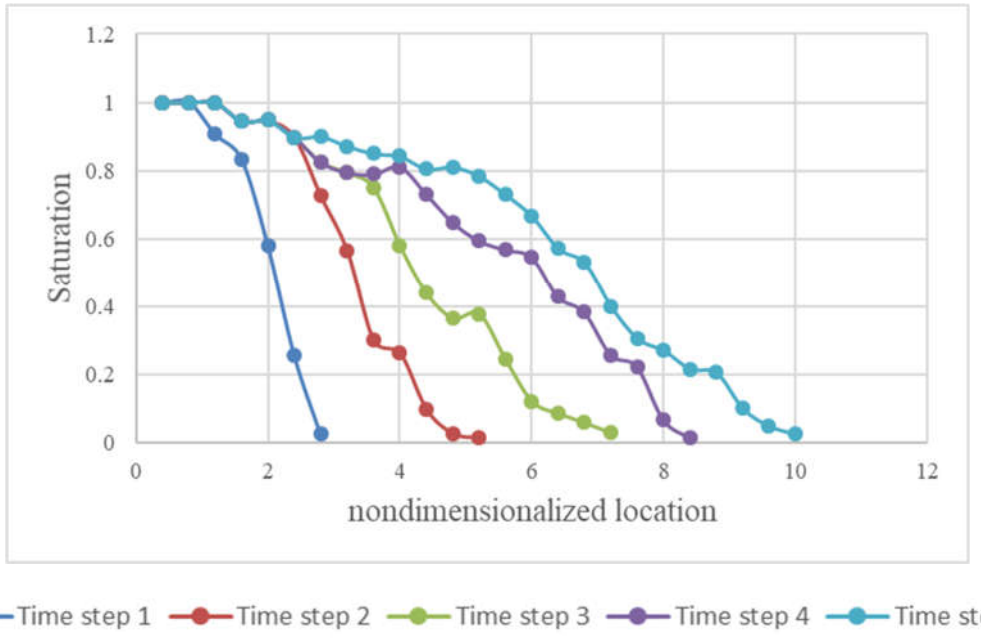

Figure 76 The graph of saturation as function of nondimensionalized flow-direction coordinate for 5 different time steps for the unit-cell packed with ellipses of dimensions 20*320 μm and with a porosity of 50%

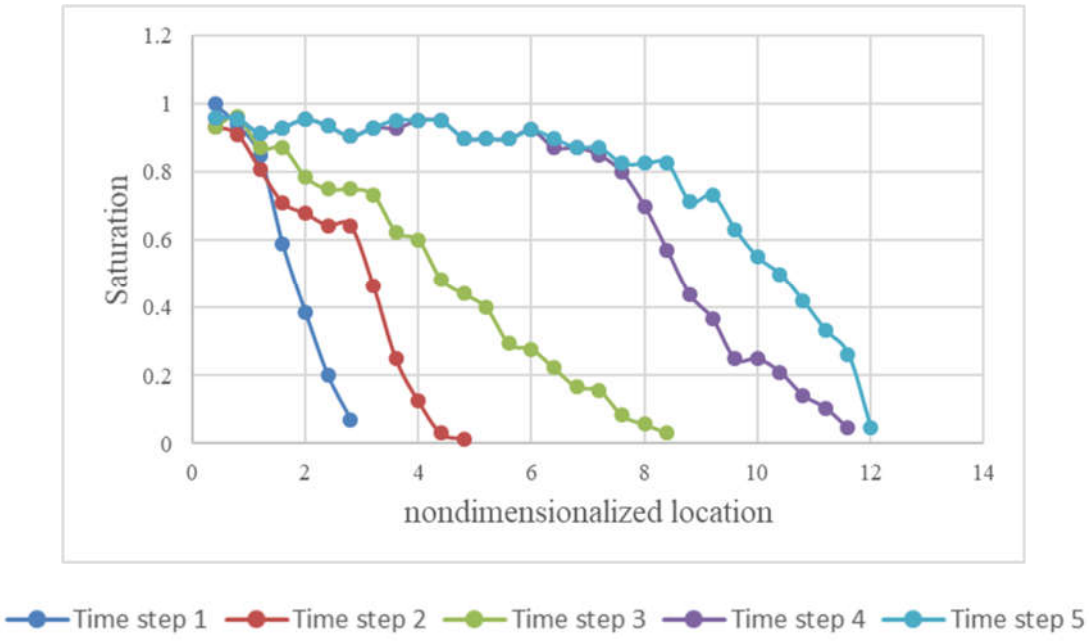

Figure 77 The graph of saturation as function of nondimensionalized flow-direction coordinate for 5 different time steps for the unit-cell packed with ellipses of dimensions 20*640 μm and with a porosity of 50%

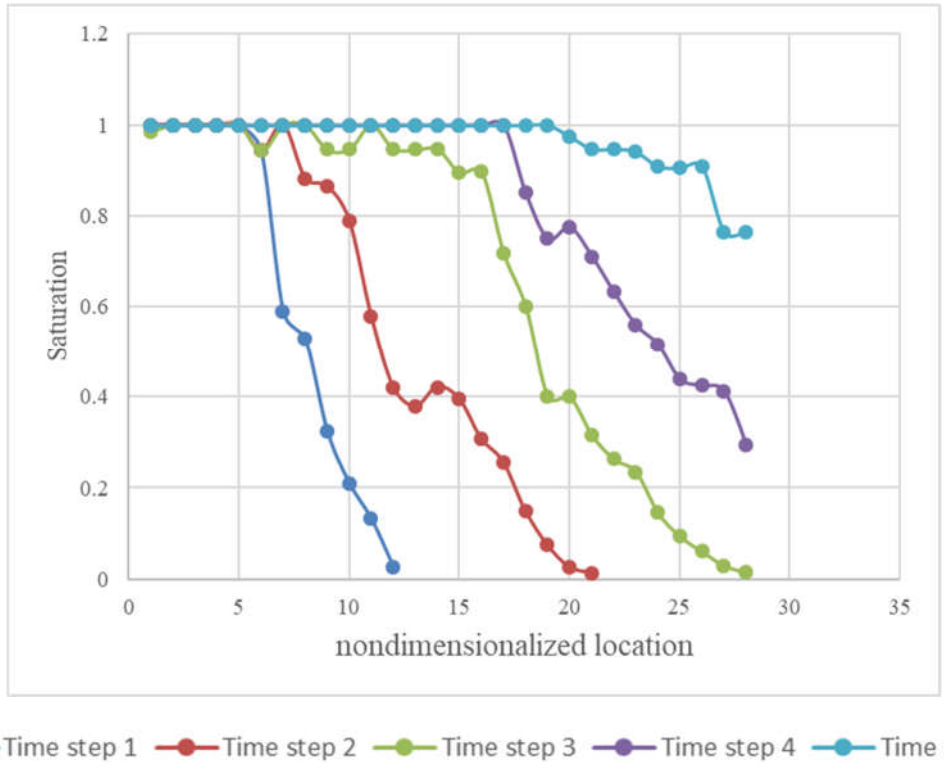

Figure 78 The graph of saturation as function of nondimensionalized flow-direction coordinate for 5 different time steps for the unit-cell packed with ellipses of dimensions 20*1280 μm and with a porosity of 50%

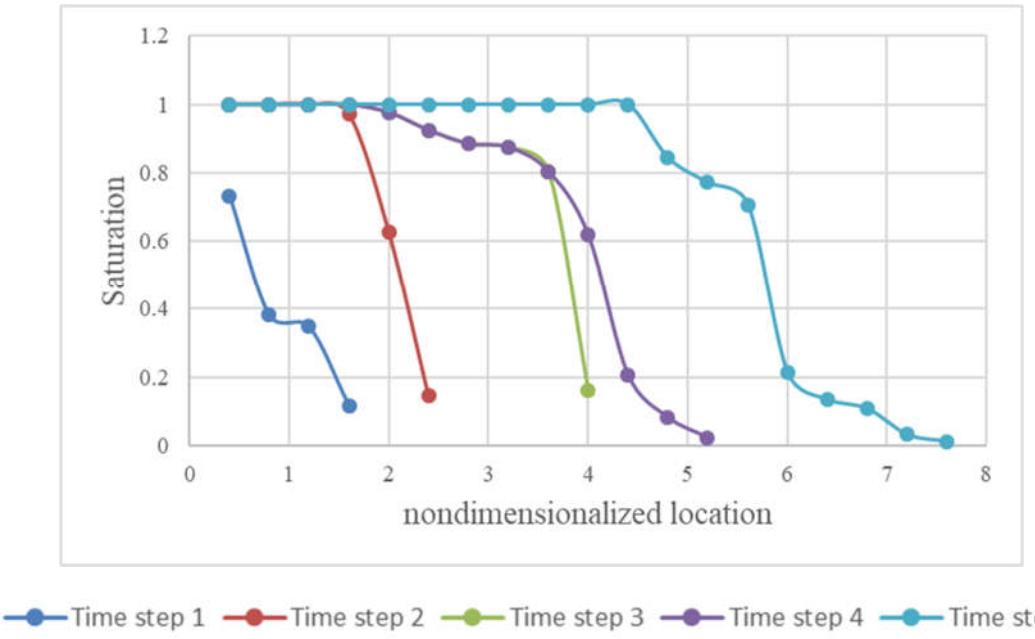

Figure 79 The saturation evolution graph for 5 different time steps for the unit-cell packed with circles of diameter of 20 μm at a porosity of 70%

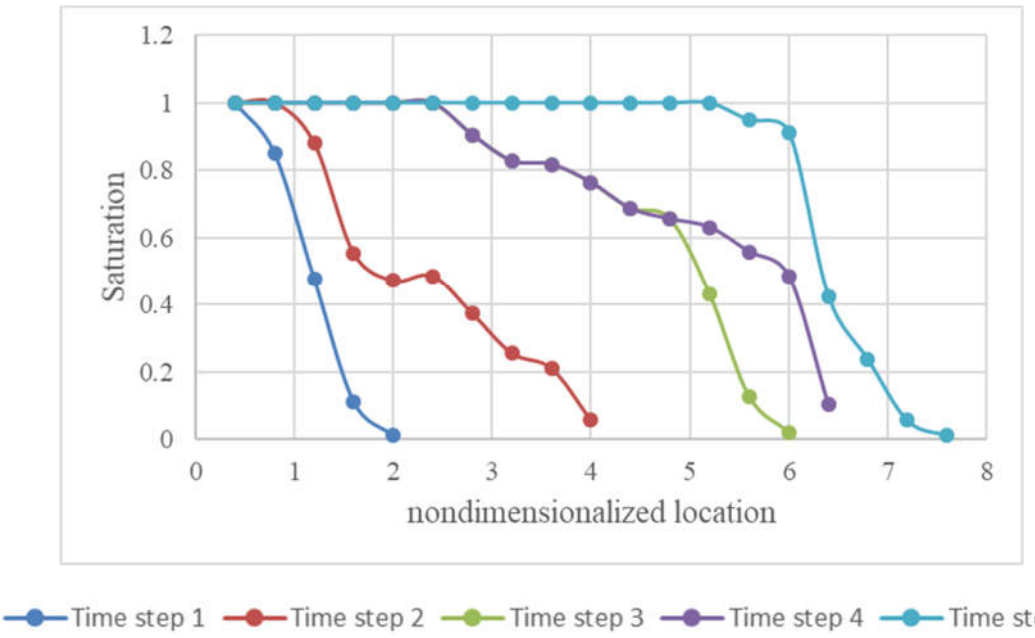

Figure 80 The saturation evolution graph for 5 different time steps for the unit-cell packed with ellipses of dimensions of 20*40 μm at a porosity of 70%

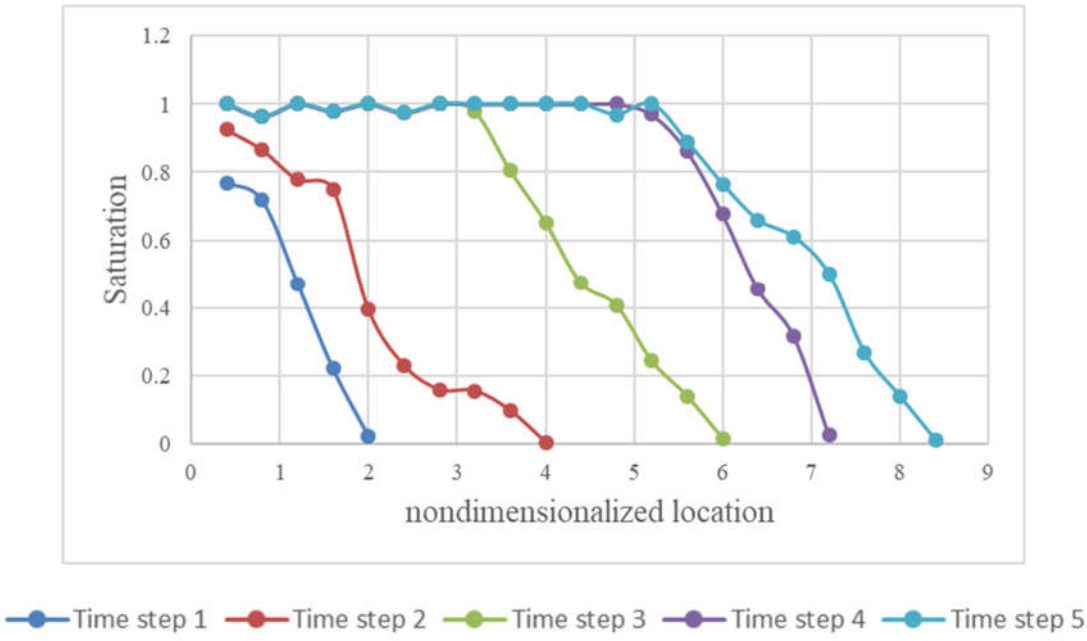

Figure 81 The saturation evolution graph for 5 different time steps for the unit-cell packed with ellipses of dimensions 20*80 µm at porosity of 70%

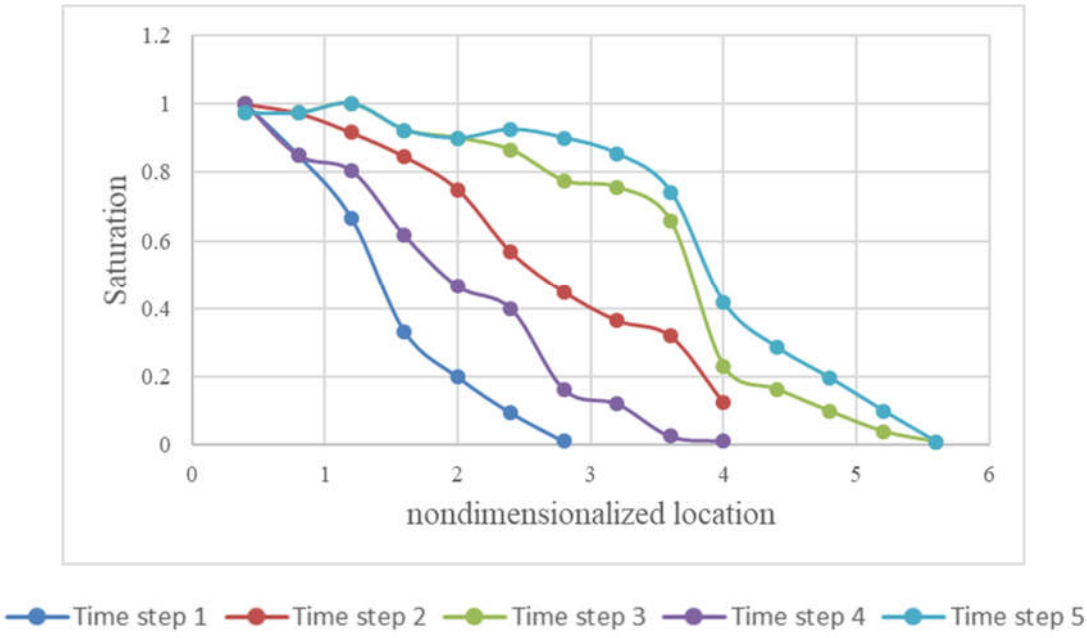

Figure 82 The saturation evolution graph for 5 different time steps for the unit-cell packed with ellipses of dimensions 20*160 µm at a porosity of 70%

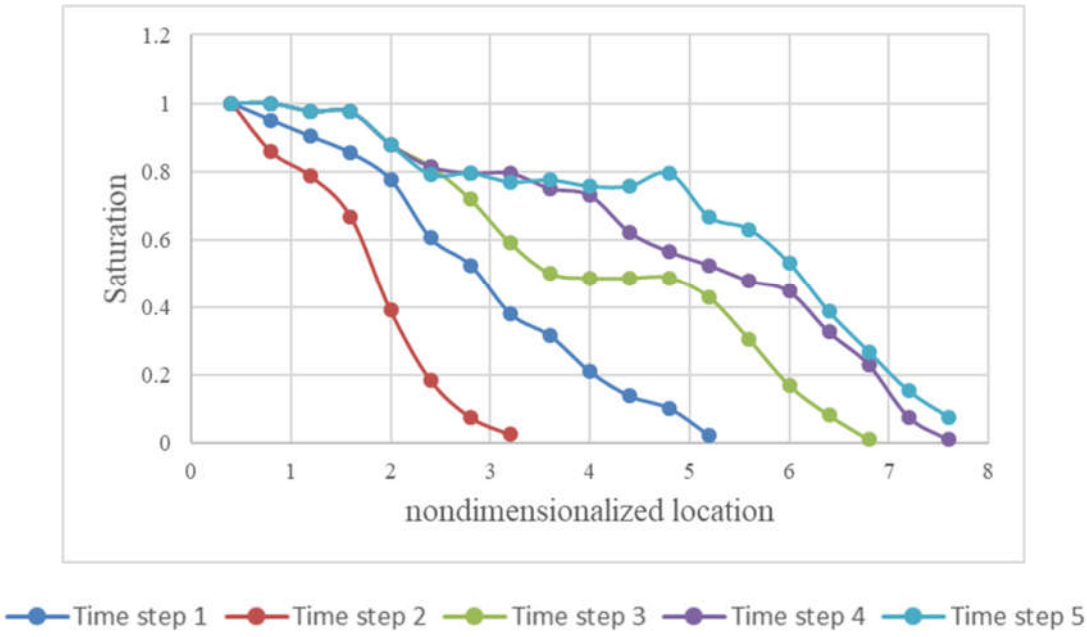

Figure 83 The saturation evolution graph for 5 different time steps for the unit-cell packed with ellipses of dimensions 20*320 µm at a porosity of 70%

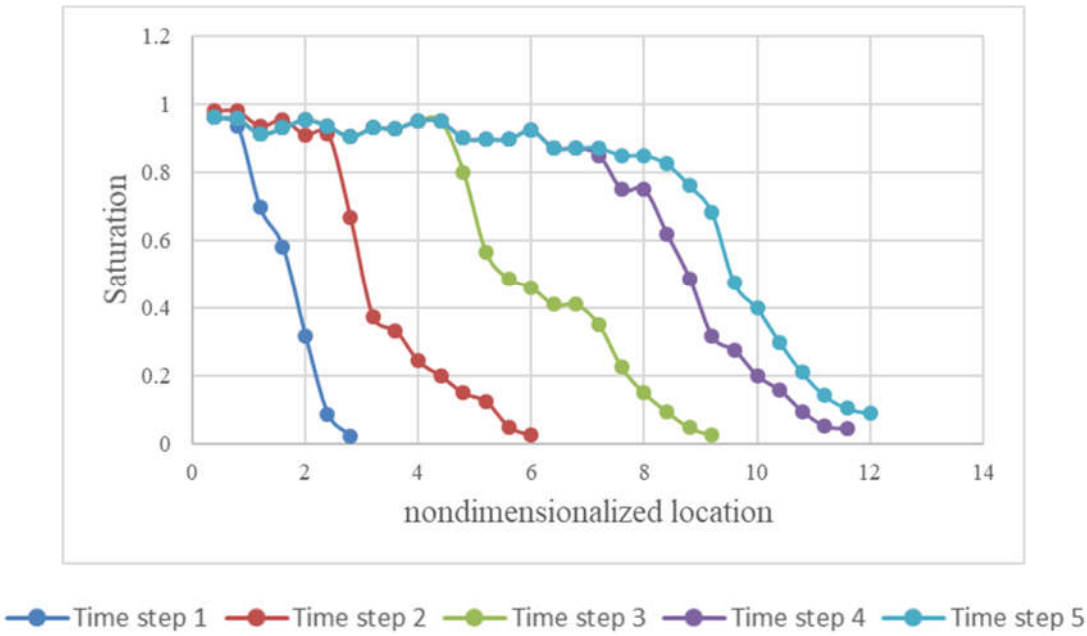

Figure 84 The saturation evolution graph for 5 different time steps for the unit-cell packed with ellipses of dimensions 20*640 µm at a porosity of 70%

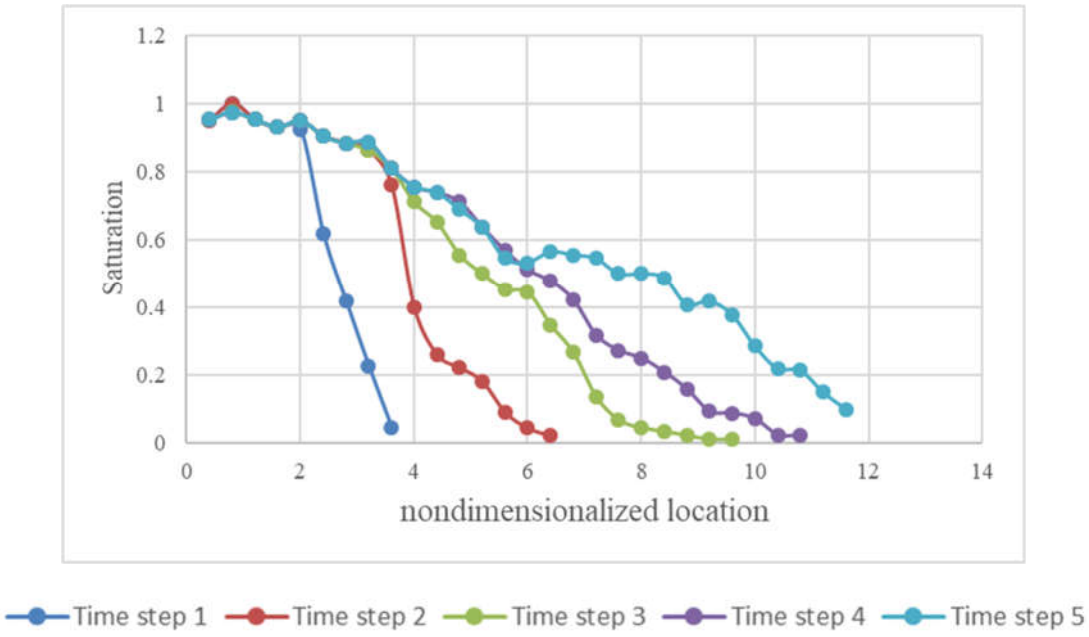

Figure 85 The saturation evolution graph for 5 different time steps for the unit-cell packed with ellipses of dimensions 20*1280 µm at a porosity of 70%

Overall, by comparing the saturation progress and evolutions shown in

Figure *72* to Figure 78 and

Figure *79* to Figure 85 we observe that in general by elongating the solid-phase shape [and in particular by substituting particles (circles) with fibers (ellipses)], the saturation profiles become more fuzzy.

As expected, having sharp fronts causes saturation graphs to be step-like for the unit-cells with 20*20 µm and 20*40 µm particles—as shown in

Figure *72* and Figure 73, and Figure 79 and Figure 80, for 50% and 70% porosities, respectively. In Figure 74 and Figure 81, for the unit-cells packed with 20*80 µm ellipses, as the saturation graph starts to become fuzzy, we can infer that the macro (visual) fronts turns from

sharp into semi-sharp. Later, for higher the aspect ratios of 1:8 (20*160 μm), 1:16 (20*320 μm), 1:32 (20*640 μm), and 1:62 (20*1280 μm), the saturation graphs definitely grow fuzzier. As the saturation profiles move away from the sharp 100%-to-0% drops and take the fuzzier shapes, it points to the existence of a diffusive front during the imbibition (wicking) process.

Considering Figure 78 and combining it with Figure 69 (g) give us an interesting and very important information about saturation distribution. From the two figures, one can argue that at lower porosity value, since there is less clustering of fibers, the saturation graph gets less fuzzy and the liquid front tends to take a less diffusive form. In addition, Figure 78 shows the saturation levels are at its high values which means that most of the grid squares are filled by the wetting phase; this is confirmed by Figure 69 (g). In contrast, we do not observe such a behavior for the unit-cell packed with ellipses of 20*1280 μm for the 70% porosity; consequences of the higher porosity are more clustering, more inhomogeneities, more micro-front formations, and finally more micro-fingers formation during the wicking process.

5-5 Summary

In this chapter, we used FLUENT to model the formation and progress of liquid front by simulating multiphase flow in the unit-cells created using ellipses. The removal of a non-wetting phase (air) by the wetting phase (wicking liquid) was successfully simulated in 2D. For our investigation, we created seven different unit-cells packed with ellipses of varying aspect ratios, starting with circular particles of aspect ratio 1 and then by increasing the ratio to represent the transition from particles to fibers.

The result showed that by increasing porosity from 50% to 70%, there is increasing

tendency of the liquid front to form fingers on the microscopic fronts leading to the formation of diffusive type visual (macroscopic) fronts. Increment in porosity causes inhomogeneities in porous media due to clustering of solid phase which leads to preferential movement of the wetting phase through narrow channels, thus leading to ‘break up’ of the micro-fronts and formation of diffused visual fronts.

Appendix 1: Derivation of Expression for Permeability in a Falling-Head Permeameter

The 1-D Darcy flow in the wick sample used in the setup of Figure 5 can be modeled using the Darcy's law for anisotropic porous media as

$$\begin{bmatrix} V_x \\ V_y \\ V_z \end{bmatrix} = -\frac{1}{\mu}\begin{bmatrix} K_x & 0 & 0 \\ 0 & K_y & 0 \\ 0 & 0 & K_z \end{bmatrix}\begin{bmatrix} \partial_x P \\ \partial_y P \\ \partial_z P \end{bmatrix} \quad \text{(A 1)}$$

For the transversely isotropic wick, $K_y = K_z$. The corresponding macroscopic mass-balance equation can be transformed as

$$\tilde{\nabla}.\tilde{V} = 0 \rightarrow \partial_x V_x + \partial_y V_y + \partial_z V_z = 0 \rightarrow -\frac{K_x}{\mu}\partial_x{}^2 P - \frac{K_y}{\mu}\partial_y{}^2 P - \frac{K_z}{\mu}\partial_z{}^2 P = 0 \quad \text{(A2)}$$

The velocity in the transverse *y,z* direction, Vy and Vx, can be neglected (i.e., Vy ~ 0, Vx~ 0) since we expect the wicking flow to be along the z (fiber) direction. As a result, the elliptic equation reduces to a simple 1-D equation for pressure as

$$\frac{d^2 P}{dz^2} = 0 \quad \text{(A3)}$$

with its general solution of the form $\mathrm{P(z)} = \mathrm{Az} + \mathrm{B}$ valid within the range $0 \leq \mathrm{z} \leq \mathrm{L}$. The boundary conditions in terms of the modified pressure (i.e., $P = P_{abs} + \rho g z$ where P_{abs} is the absolute pressure) are

$$P = p_{atm} \text{ at } z = 0 \quad \text{(A4a)}$$

$$P = p_{atm} + \rho g(h_m - L) + \rho g L = p_{atm} + \rho g h_m \text{ at } z = L \quad \text{(A4b)}$$

where h_m is the height of the liquid meniscus in the burette. (Note that, as shown in Figure 5 $h_m > L$.) On using these boundary conditions with the general solution results in the following pressure distribution inside the wick sample:

$$P(z) = \rho g\, h_m \frac{z}{L} + p_{atm} \tag{A5}$$

Use of this result with Eq. A1 leads to the expression for Darcy velocity inside the wick:

$$|v_h| = \frac{K_z}{\mu}\frac{\rho g\, h_m}{L} \tag{A6}$$

Therefore, the formula for the flow rate through the wick can be derived to be

$$Q = |v|.A = \frac{K_z A}{\mu}\frac{\rho g\, h_m}{L} \tag{A7}$$

where A is the wick cross-section area. Note that the flow rate can be related to the rate of fall of the meniscus as

$$Q = \frac{dV}{dt} = -a\frac{d\, h_m}{dt} \tag{A8}$$

where a is the burette cross-section area. From the last two equations, we get

$$\frac{d\, h_m}{dt} = -\frac{K_z A}{\mu a}\frac{\rho g\, h_m}{L} \tag{A9}$$

This can be refashioned as

$$\frac{d\, h_m}{h_m} = -Cdt \tag{A10}$$

where *C* is given by the relation

$$C = \frac{K_z A \rho g}{\mu a L} \tag{A11}$$

The general solution of Eq. A10 is given as

$$ln\,(h_m) = -Ct + C_1 \tag{A12}$$

By using the conditions

$$h_m = h_1 \quad at \quad t = t_1 \tag{A13a}$$

$$h_m = h_2 \quad \text{at} \quad t = t_2 \tag{A13b}$$

Eq. A12 can be manipulated to yield the final expression for the vertical-direction permeability of the fiber-glass wick sample as

$$ln\frac{h_2}{h_1} = -C\,(t_2 - t_1) = -\frac{K_z A\rho g}{\mu a L}(t_2 - t_1) \;\rightarrow\; K_z = \frac{\mu a L}{A\rho g(t_2 - t_1)}\,ln\frac{h_1}{h_2} \tag{A14}$$

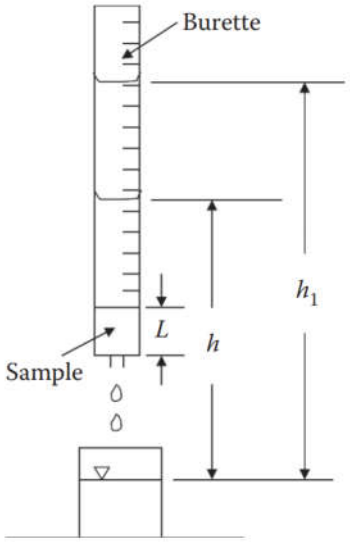

Figure A1 A schematic of falling head permeameter [1]

Note that to the best of authors' knowledge, this is a novel derivation as such a result has been obtained only for isotropic porous media [1]—its derivation for the transversely isotropic medium has been attempted only here. Also note that full permeability tensor is not obtained—

only K_x is estimated through the experiment. With y and z direction flows being not relevant in the current problem, K_y and K_z are not important and hence not estimated.

Appendix 2: Quantifying the effect of buoyancy force in the accuracy of the proposed model for absorbed mass of liquid into wicks

Let us study the various forces that come into action when the wick is submerged in a liquid. At the start of dipping the wick, the buoyancy force acts on the wick and tends to push it out of the liquid. This exertion of buoyancy force may cause some error in the estimation of the amount of liquid absorbed by the wick, and we need to investigate the effect of buoyancy force on the accuracy of our experiment.

Let us start the analysis by stating some assumptions. We assume that the portion of the wick submerged under a liquid attains instantaneous saturation because of a strong radial motion of liquid into the cylindrical wicks. This means that the initial rapidly-changing component of the buoyancy force has died down and is not included in the analysis. Let us clarify the above given statement with a little analysis. Note that the buoyancy force at the initial dipping is equal to

$$F_B = \rho_l \, V_{submerged\,wick} \; g \qquad \text{(A15)}$$

where F_B is the buoyancy force, ρ_l is the density of the liquid and $V_{submerged\,wick}$ is the volume of the submerged portion of the wick. After the liquid moves in radially into the wick and fills the pore space between fibers, the buoyancy force is given by

$$F_B = \rho_l \, (1 - \varepsilon) \, V_{submerged\,wick} \; g \qquad \text{(A16)}$$

Here ε is the porosity of the wick. If the fall of liquid level within the container in Figure 19 is very small, then $V_{submerged\,wick}$ can be taken to be a constant, and hence the buoyancy force being a constant is a good assumption.

As a result, the pore space between fibers in the submerged portion can be assumed to be completely occupied by the liquid at time $t = 0$ (Figure A2). Now as the liquid starts rising in the wick in the space between fibers, the role of the constant buoyancy force on the gained mass of liquid is explored.

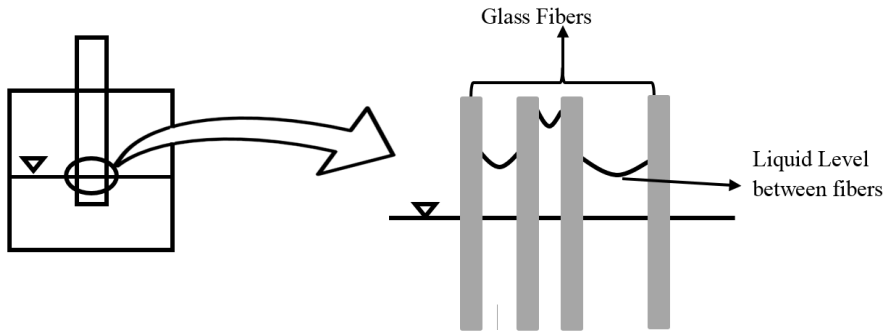

Figure A2 A schematic showing liquid menisci between glass fibers inside the wick

Force balance for the wick:

If we consider the wick held by the rod (Figure 21), the force balance for the wick can be written as

$$T(t) = M_w\,(t)\,g - F_B \qquad \text{(A17)}$$

As shown in Figure A3, F_B is the buoyancy force created due to the submergence of fibers below the outside liquid level, T is the force applied by the rod, and M_w is the mass of dry wick in addition to the mass of the liquid inside the wick that has climbed above the outside liquid-level.

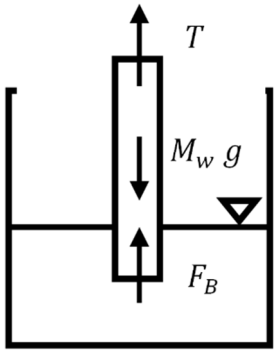

Figure A3 Force balance for the wick inserted into the liquid

Force balance for the liquid container:

Let us now consider the force balance for the liquid inside the container (*sans* the liquid climbed into the wick) as shown in Figure A4:

$$R(t) = M(t)\ g + F_B \tag{A18}$$

The mass of liquid in the container changes with time as

$$M(t) = M_{ini} - M_{abs\ liq}(t) \tag{A19}$$

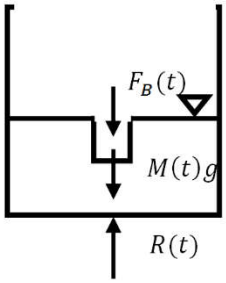

Figure A4 Force balance diagram for the liquid container without the wick

Here M_{ini} is the initial mass of the liquid inside the container which includes the initial mass of the liquid that rushed into the submerged portion of the wick to make it completely saturated. $M_{abs\ liq}$ is the time-dependent mass of the liquid absorbed subsequently into the wick and is the mass of liquid climbed above the liquid level in the container (Figure A4). R(t) is the force exerted by the balance and is equal to the force read by the balance—a decrease in this force gives the mass of the liquid absorbed into the wick.

A little thought will reveal that a constant F_B will not interfere with the wick weight-gain estimation using the balance before-and-after readings through Eqn. A18. From Eqns. A18 and A19, one can derive the following relation between a change in the balance reading, $\Delta \boldsymbol{R(t)}$, and the corresponding change in the wicked liquid-mass, $\Delta \boldsymbol{M_{abs\ liq}(t)}$:

$$\Delta R(t) = \Delta M(t)\, g \qquad \text{(A20)}$$

such that

$$\Delta M(t) = -\Delta M_{abs\ liq}(t) \qquad \text{(A21)}$$

Appendix 3: Derivation of Richards equation for a Transversely-Isotropic Porous Medium

Though the derivation of Richards equation is well known in the literature [124, 125] , the authors have not come across its derivation for glass-fiber wicks, which, due to that fact that the porous medium created by a clutch of parallel glass fibers has different flow properties along fiber-axes as compared to the direction transverse to the fibers. Such a porous medium is characterized as a transversely-isotropic medium where the permeability is in the form of a tensor, with its principal permeability along the fibers being very different from the principal permeability transverse to the fiber axis. Moreover, the transverse permeability is isotropic (not changing with direction) in the cross-sectional plane of the wick. We present this detailed derivation of Richards equation for this rather unusual case.

Under unsaturated flows in porous media where the porous medium remains partially saturated, we consider the liquid-phase saturation, S_w, (which is defined as the ratio of liquid volume within pores to the total pore volume within an averaging volume) as the primary variable in order to describe the fluid flow and redistribution. The mass balance equation for the liquid phase can be described as

$$\varepsilon \frac{\partial S_w}{\partial t} + \nabla . \langle \overrightarrow{v_w} \rangle = 0 \qquad (A22)$$

where $\langle \overrightarrow{v_w} \rangle$ is the macroscopic Darcy velocity, defined as

$$\langle \overrightarrow{v_w} \rangle = -\boldsymbol{k}_r(S_w)\boldsymbol{K}_h . \nabla \langle H \rangle^f \qquad (A23)$$

Note that $\langle\ \rangle$ and $\langle\ \rangle^f$ represent the phase average and intrinsic phase-average of any volume averaged flow quantity as defined by [126]. Here $\nabla \langle H \rangle^f$ is the gradient of the pore-averaged

piezometric head, also called the hydraulic head, which is defined as

$$H = \frac{p_w}{\rho g} + z \qquad (A24)$$

where p_w is the hydrodynamic pressure of the wetting (liquid) phase. Here μ and ρ are the liquid viscosity and density, respectively; g is the acceleration due to gravity. Also, in Eq. A23, $\boldsymbol{K}_h$ is presented as the hydraulic conductivity tensor which is defined in terms of the permeability tensor, $\boldsymbol{K}$, as

$$\boldsymbol{K}_h = \frac{\boldsymbol{K}\rho g}{\mu} \qquad (A25)$$

On substituting Eq. A24 in Eq. A23, the Darcy velocity can be re-expressed as

$$\langle \overrightarrow{v_w} \rangle = -k_r(s)\boldsymbol{K}_h . \nabla \left(\frac{\langle p_w \rangle^f}{\rho g} + z \right) \qquad (A26)$$

Since $\boldsymbol{K_h}$, the hydraulic conductivity tensor, is a function of the permeability tensor (Eq. A4), the final form of Darcy velocity can be defined as

$$\langle \overrightarrow{v_w} \rangle = -k_r \frac{\boldsymbol{K}}{\mu} . \nabla (\langle p_w \rangle^f + \rho g z) \qquad (A27)$$

On substituting Darcy velocity from Eq. A26 into Eq. A1, one can derive the equation for the saturation of the wetting phase as

$$\varepsilon \frac{\partial S_w}{\partial t} - \nabla . k_r \frac{\boldsymbol{K}}{\mu} . \nabla (\langle p_w \rangle^f + \rho g z) = 0 \qquad (A28)$$

On applying the gradient to the bracket in Eq. A27 and noticing that $\nabla \mathrm{z} = \frac{\partial \mathrm{z}}{\partial \mathrm{z}} \hat{\mathrm{k}} = \hat{\mathrm{k}}$, we get

$$\varepsilon \frac{\partial S_w}{\partial t} = \nabla . k_r \frac{\boldsymbol{K}}{\mu} . \nabla (\langle p_w \rangle^f) + \nabla . (k_r \frac{\boldsymbol{K}}{\mu} . \rho g \vec{\mathrm{k}}) \qquad (A29)$$

On using the chain rule on, assuming the liquid density to be constant, noticing that $\nabla . (\hat{\mathrm{k}}) = \frac{\partial}{\partial \mathrm{z}}$,

as well as on using the fact that the permeability tensor is diagonal, i.e.,

$$\boldsymbol{K} = \begin{bmatrix} K_{xx} & 0 & 0 \\ 0 & K_{yy} & 0 \\ 0 & 0 & K_{zz} \end{bmatrix},$$

Eq. A28 can be expressed as

$$\varepsilon \frac{\partial S_w}{\partial t} = \frac{1}{\mu}\frac{\partial}{\partial x}\left(k_r K_{xx} \frac{\partial \langle p_w \rangle^f}{\partial s}\frac{\partial s}{\partial x}\right) + \frac{1}{\mu}\frac{\partial}{\partial y}\left(k_r K_{yy} \frac{\partial \langle p_w \rangle^f}{\partial s}\frac{\partial s}{\partial y}\right) + \frac{1}{\mu}\frac{\partial}{\partial z}\left(k_r K_{zz} \frac{\partial \langle p_w \rangle^f}{\partial s}\frac{\partial s}{\partial z}\right) + \frac{K_{zz}}{\mu}\rho g\left(\frac{\partial k_r}{\partial s}\frac{\partial s}{\partial z}\right) \quad \textit{(A30)}$$

The capillary pressure, which relates the pore-averaged pressures of the liquid and air phases, can be expressed in the present case as

$$\langle p_c \rangle = \langle p_{nw} \rangle^f - \langle p_w \rangle^f \quad \textit{(A31)}$$

Since the air, the non-wetting phase, is assumed to be interconnected and its pressure equal to the atmospheric pressure, therefore

$$\langle p_w \rangle^f = p_{atm} - \langle p_c \rangle \quad \textit{(A32)}$$

In Eq. A30, both p_c and k_r are functions of saturation. Hence, on substituting Eq. A32 in Eq. A30, we can state the latter entirely in terms of the primary variable S_w as

$$\varepsilon \frac{\partial S_w}{\partial t} = -\frac{1}{\mu}\frac{\partial}{\partial x}\left(k_r(S_w) K_{xx} \frac{\partial \langle p_c \rangle^f}{\partial s_w}\frac{\partial s_w}{\partial x}\right) - \frac{1}{\mu}\frac{\partial}{\partial y}\left(k_r(S_w) K_{yy} \frac{\partial \langle p_c \rangle^f}{\partial s_w}\frac{\partial s_w}{\partial y}\right) -$$

$$\frac{1}{\mu}\frac{\partial}{\partial z}\left(k_r(S_w) K_{zz} \frac{\partial \langle p_c \rangle^f}{\partial s_w}\frac{\partial s_w}{\partial z}\right) + \frac{K_{zz}}{\mu}\rho g\left(\frac{\partial k_r}{\partial s_w}\frac{\partial s_w}{\partial z}\right) \quad \textit{(A33)}$$

The Richards equation has two main parts: one expressing the contribution of the suction pressure, and the other the contribution of the gravitational component of the total potential driving the Darcy velocity. Which of these two parts dominates depends on the boundary and initial conditions and on the stage of the process considered. Hence, in Eq. A33, all the terms are to be retained.

However, in order to simplify its form, we introduce D_g and D_{ij} (S_w), the diffusivity coefficient and the capillary diffusivity tensor, respectively, as

$$D_g = -\frac{\rho g K_{zz}}{\varepsilon \mu}\frac{\partial k_r}{\partial S_w} \qquad (A34)$$

$$D_{ij} = -\frac{K_{ij}}{\varepsilon \mu}\frac{\partial \langle p_c \rangle^f}{\partial S_w} k_r(S_w) \qquad (A35)$$

where the coefficients i and j can take values x, y and z. Note that since the permeability tensor is diagonal, the capillary diffusivity tensor is diagonal too. On using Eqs. A35 and A36 in Eq. A34, the final form of Richards equation is recovered as

$$\frac{\partial S_w}{\partial t} = \frac{\partial}{\partial x}\left(D_{xx}(S_w)\frac{\partial S_w}{\partial x}\right) + \frac{\partial}{\partial y}\left(D_{yy}(S_w)\frac{\partial S_w}{\partial y}\right) + \frac{\partial}{\partial z}\left(D_{zz}(S_w)\frac{\partial S_w}{\partial z}\right) - D_g(S_w)\frac{\partial S_w}{\partial z} \qquad (A36)$$

References

1. Masoodi, R. and K.M. Pillai, *Wicking in Porous Materials: Traditional and Modern Modeling Approaches*. 2012: CRC Press.
2. Lucas R., *Rate of capillary ascension of liquids.* Kolloid. Z., 1918. **23**: p. 15-22.
3. Bell, J.M. and F.K. Cameron, *The Flow of Liquids through Capillary Spaces.* The Journal of Physical Chemistry, 1905. **10**(8): p. 658-674.
4. Washburn, E.W., *The Dynamics of Capillary Flow.* Physical Review, 1921. **17**(3): p. 273-283.
5. O'Loughlin, M., et al., *Capillary rise dynamics of aqueous glycerol solutions in glass capillaries: A critical examination of the Washburn equation.* Journal of Colloid and Interface Science, 2013. **411**(0): p. 257-264.
6. Mullins, B.J. and R.D. Braddock, *Capillary rise in porous, fibrous media during liquid immersion.* International Journal of Heat and Mass Transfer, 2012. **55**(21–22): p. 6222-6230.
7. Mullins, B.J., R.D. Braddock, and G. Kasper, *Capillarity in fibrous filter media: Relationship to filter properties.* Chemical Engineering Science, 2007. **62**(22): p. 6191-6198.
8. Schoelkopf, J., et al., *Practical observation of deviation from Lucas–Washburn scaling in porous media.* Colloids and Surfaces A: Physicochemical and Engineering Aspects, 2002. **206**(1–3): p. 445-454.
9. Bogoyavlenskiy, V.A., A.C. Giamis, and E.J. Cotts, *Mean-field dynamics of free surface flows through obstacle arrays in a narrow passage: amendments of the Washburn model.* Fluid Dynamics Research, 2004. **35**(1): p. 23-35.
10. Levine, S., et al., *A theory of capillary rise of a liquid in a vertical cylindrical tube and in a parallel-plate channel: Washburn equation modified to account for the meniscus with slippage at the contact line.* Journal of Colloid and Interface Science, 1980. **73**(1): p. 136-151.
11. Hanžič, L., L. Kosec, and I. Anžel, *Capillary absorption in concrete and the Lucas–Washburn equation.* Cement and Concrete Composites, 2010. **32**(1): p. 84-91.
12. Lu, G., X.-D. Wang, and Y.-Y. Duan, *Study on initial stage of capillary rise dynamics.* Colloids and Surfaces A: Physicochemical and Engineering Aspects, 2013. **433**(0): p. 95-103.
13. Masoodi, R., E. Languri, and A. Ostadhossein, *Dynamics of liquid rise in a vertical capillary tube.* Journal of Colloid and Interface Science, 2013. **389**(1): p. 268-272.
14. Extrand, C.W. and S.I. Moon, *Experimental measurement of forces and energies associated with capillary rise in a vertical tube.* Journal of Colloid and Interface Science, 2013. **407**(0): p. 488-492.
15. Rideal, E.K., *On the flow of liquids under capillary pressure (CVIII.).* The London, Edinburgh, and Dublin Philosophical Magazine and Journal of Science, 1922. **44**(264): p. 1152-1159.
16. Bosanquet, C., *On the flow of liquids into capillary tubes (LV.).* The London, Edinburgh, and Dublin Philosophical Magazine and Journal of Science, 1923. **45**(267): p. 525-531.
17. Szekely, J., A.W. Neumann, and Y. Chuang, *The rate of capillary penetration and the applicability of the Washburn equation.* Journal of Colloid and Interface Science, 1971. **35**(2): p. 273-278.
18. Lavi, B., A. Marmur, and J. Bachmann, *Porous media characterization by the two-liquid method: effect of dynamic contact angle and inertia.* Langmuir, 2008. **24**(5): p. 1918-1923.
19. Fries, N. and D. Quéré, *Capillary transport processes in porous materials-experiment and model*. 2010: Cuvillier.
20. Masoodi, R., K.M. Pillai, and P.P. Varanasi, *Darcy's law-based models for liquid absorption in polymer wicks.* AIChE journal, 2007. **53**(11): p. 2769-2782.
21. Stange, M., M.E. Dreyer, and H.J. Rath, *Capillary driven flow in circular cylindrical tubes.* Physics of Fluids (1994-present), 2003. **15**(9): p. 2587-2601.
22. Masoodi, R. and K.M. Pillai, *Traditional Theories of Wicking: Capillary Models*, in *Wicking in Porous Materials: Traditional and Modern Modeling Approaches*. 2012, CRC Press. p. 31-53.

23. Lage, J., *The fundamental theory of flow through permeable media from Darcy to turbulence.* Transport phenomena in porous media, 1998. **2**.
24. Menció, A., et al., *Analysis of stream–aquifer relationships: A comparison between mass balance and Darcy's law approaches.* Journal of Hydrology, 2014. **517**(0): p. 157-172.
25. Noorduijn, S.L., G.A. Harrington, and P.G. Cook, *The representative stream length for estimating surface water–groundwater exchange using Darcy's Law.* Journal of Hydrology, 2014. **513**(0): p. 353-361.
26. Bear, J., *Dynamics of fluids in porous media*. 2013: Courier Dover Publications.
27. Barari, B. and K.M. Pillai, *Calibration of one-dimensional flow setup used for estimating fabric permeability using three different reference media.* Polymer Composites, 2014.
28. Darcy, H., *Les fontaines publiques de la ville de Dijon: exposition et application*. 1856: Victor Dalmont.
29. Masoodi, R. and K.M. Pillai, *Single-Phase (Sharp-Interface) Models for Wicking*, in *Wicking in Porous Materials: Traditional and Modern Modeling Approaches*. 2012, CRC Press. p. 97-129.
30. Pillai, K.M. and S.G. Advani, *Wicking across a fiber-bank.* Journal of Colloid and Interface Science, 1996. **183**(1): p. 100-110.
31. Masoodi, R., H. Tan, and K.M. Pillai, *Darcy's law–based numerical simulation for modeling 3D liquid absorption into porous wicks.* AIChE journal, 2011. **57**(5): p. 1132-1143.
32. Masoodi, R., H. Tan, and K.M. Pillai, *Numerical simulation of liquid absorption in paper-like swelling porous media.* AIChE journal, 2012. **58**(8): p. 2536-2544.
33. Dullien, F.A., *Porous media: fluid transport and pore structure*. 2012: Academic press.
34. Dullien, F.A.L., *4 - Selected Operations Involving Transport of a Single Fluid Phase through a Porous Medium*, in *Porous Media (Second Edition)*. 1992, Academic Press: San Diego. p. 319-332.
35. Dullien, F.A.L., *3 - Single-Phase Transport Phenomena in Porous Media*, in *Porous Media (Second Edition)*. 1992, Academic Press: San Diego. p. 237-317.
36. Richards, L.A., *Capillary conduction of liquids through porous mediums.* Journal of Applied Physics, 2004. **1**(5): p. 318-333.
37. Aker, E., et al., *A Two-Dimensional Network Simulator for Two-Phase Flow in Porous Media.* Transport in Porous Media, 1998. **32**(2): p. 163-186.
38. Gruener, S., et al., *Anomalous front broadening during spontaneous imbibition in a matrix with elongated pores.* Proceedings of the National Academy of Sciences, 2012. **109**(26): p. 10245-10250.
39. Sadjadi, Z. and H. Rieger, *Scaling Theory for Spontaneous Imbibition in Random Networks of Elongated Pores.* Physical Review Letters, 2013. **110**(14): p. 144502.
40. Heiko, R., T. Christian, and S. Zeinab, *Meniscus arrest dominated imbibition front roughening in porous media with elongated pores.* Journal of Physics: Conference Series, 2015. **638**(1): p. 012007.
41. Szekely, J., A. Neumann, and Y. Chuang, *The rate of capillary penetration and the applicability of the Washburn equation.* Journal of Colloid and Interface Science, 1971. **35**(2): p. 273-278.
42. Rideal, E.K., *CVIII. On the flow of liquids under capillary pressure.* The London, Edinburgh, and Dublin Philosophical Magazine and Journal of Science, 1922. **44**(264): p. 1152-1159.
43. Masoodi, R. and K.M. Pillai, *A General Formula for Capillary Suction-Pressure in Porous Media.* Journal of Porous Media, 1012. **15**(8): p. 775-783.
44. Corless, R.M., et al., *On the LambertW function.* Advances in Computational mathematics, 1996. **5**(1): p. 329-359.
45. Landeryou, M., I. Eames, and A. Cottenden, *Infiltration into inclined fibrous sheets.* Journal of Fluid Mechanics, 2005. **529**: p. 173-193.
46. Reza Masoodi, K.M.P., *Wicking in Porous Materials: Traditional and Modern Modeling Approaches*. 2012: CRC Press.

47. Wheeler, A.J. and A.R. Ganji, *Introduction to engineering experimentation*. 1996: Prentice Hall New Jersey.
48. Zarandi, M.A.F., K.M. Pillai, and A.S. Kimmel, *Spontaneous imbibition of liquids in glass-fiber wicks. Part I: Usefulness of a sharp-front approach.* AIChE Journal, 2018. **64**(1): p. 294-305.
49. http://www.brookfieldengineering.com.
50. Tomadakis, M.M. and T.J. Robertson, *Viscous Permeability of Random Fiber Structures: Comparison of Electrical and Diffusional Estimates with Experimental and Analytical Results.* Journal of Composite Materials, 2005. **39**(2): p. 163-188.
51. Berdichevsky, A.L. and Z. Cai, *Preform permeability predictions by self-consistent method and finite element simulation.* Polymer Composites, 1993. **14**(2): p. 132-143.
52. Gebart, B., *Permeability of unidirectional reinforcements for RTM.* Journal of composite materials, 1992. **26**(8): p. 1100-1133.
53. Bruschke, M.V. and S.G. Advani, *Flow of generalized Newtonian fluids across a periodic array of cylinders.* Journal of Rheology, 1993. **37**(3): p. 479-498.
54. GeoDict, F.-I.G., https://www.itwm.fraunhofer.de/en/fraunhofer-itwm.html.
55. Whitaker, S., *The Method of Volume Averaging*. 2013: Springer Netherlands.
56. Barari, B., S. Beyhaghi, and K. Pillai, *Fast and Inexpensive 2D-Micrograph based Method of Permeability Estimation through Micro-Macro Coupling in Porous Media.* Journal of Porous Media, 2019. **22**(7).
57. Parseval, Y.D., K. Pillai, and S. Advani, *A simple model for the variation of permeability due to partial saturation in dual scale porous media.* Transport in porous media, 1997. **27**(3): p. 243-264.
58. Vernet, N., et al., *Experimental determination of the permeability of engineering textiles: Benchmark II.* Composites Part A: Applied Science and Manufacturing, 2014. **61**: p. 172-184.
59. Roy, T., H. Tan, and K.M. Pillai, *A method to estimate the accuracy of 1-D flow based permeability measuring devices.* Journal of composite materials, 2007. **41**(17): p. 2037-2055.
60. Tan, H. and K.M. Pillai, *A Method to Estimate the Accuracy of Radial Flow—Based Permeability Measuring Devices.* Journal of composite materials, 2009. **43**(21): p. 2307-2332.
61. Barari, A., et al., *Numerical analysis of Richards' problem for water penetration in unsaturated soils.* Hydrology and Earth System Sciences Discussions, 2009. **6**(5): p. 6359-6385.
62. Berninger, H., R. Kornhuber, and O. Sander, *Fast and robust numerical solution of the Richards equation in homogeneous soil.* SIAM Journal on Numerical Analysis, 2011. **49**(6): p. 2576-2597.
63. Menziani, M., S. Pugnaghi, and S. Vincenzi, *Analytical solutions of the linearized Richards equation for discrete arbitrary initial and boundary conditions.* Journal of Hydrology, 2007. **332**(1): p. 214-225.
64. Tracy, F., *Three-dimensional analytical solutions of Richards' equation for a box-shaped soil sample with piecewise-constant head boundary conditions on the top.* Journal of Hydrology, 2007. **336**(3): p. 391-400.
65. Tracy, F.T., *Analytical and Numerical Solutions of Richards' Equation with Discussions on Relative Hydraulic Conductivity.* Hydraulic Conductivity-Issues, Determination and Applications, 2011.
66. Varado, N., et al., *Assessment of an efficient numerical solution of the 1D Richards' equation on bare soil.* Journal of Hydrology, 2006. **323**(1): p. 244-257.
67. Zlotnik, V.A., et al., *Verification of numerical solutions of the Richards equation using a traveling wave solution.* Advances in water resources, 2007. **30**(9): p. 1973-1980.
68. Gilaki, M. and I. Avdeev, *Impact modeling of cylindrical lithium-ion battery cells: a heterogeneous approach.* Journal of Power Sources, 2016. **328**: p. 443-451.
69. Balali, M.H., et al., *An overview of the environmental, economic, and material developments of the solar and wind sources coupled with the energy storage systems.* International Journal of Energy Research, 2017: p. n/a-n/a.

70. Omrani, E., et al., *New Emerging Self-lubricating Metal Matrix Composites for Tribological Applications*, in *Ecotribology: Research Developments*, J.P. Davim, Editor. 2016, Springer International Publishing: Cham. p. 63-103.
71. Jaganathan, S., H.V. Tafreshi, and B. Pourdeyhimi, *A realistic modeling of fluid infiltration in thin fibrous sheets.* Journal of Applied Physics, 2009. **105**(11): p. 113522.
72. Haverkamp, R., et al., *A comparison of numerical simulation models for one-dimensional infiltration.* Soil Science Society of America Journal, 1977. **41**(2): p. 285-294.
73. Van Genuchten, M.T., *A closed-form equation for predicting the hydraulic conductivity of unsaturated soils.* Soil Science Society of America Journal, 1980. **44**(5): p. 892-898.
74. Ashari, A., et al., *Modeling fluid spread in thin fibrous sheets: Effects of fiber orientation.* International Journal of Heat and Mass Transfer, 2010. **53**(9): p. 1750-1758.
75. Ashari, A. and H. Vahedi Tafreshi, *A two-scale modeling of motion-induced fluid release from thin fibrous porous media.* Chemical Engineering Science, 2009. **64**(9): p. 2067-2075.
76. Brooks, R. and T. Corey, *HYDRAULIC PROPERTIES OF POROUS MEDIA.* Hydorology Papers, Colorado State University 1964.
77. Hazlett, R., *Simulation of capillary-dominated displacements in microtomographic images of reservoir rocks.* Transport in porous media, 1995. **20**(1-2): p. 21-35.
78. Hilpert, M. and C.T. Miller, *Pore-morphology-based simulation of drainage in totally wetting porous media.* Advances in water resources, 2001. **24**(3–4): p. 243-255.
79. Becker, J., V. Schulz, and A. Wiegmann, *Numerical Determination of Two-Phase Material Parameters of a Gas Diffusion Layer Using Tomography Images.* Journal of Fuel Cell Science and Technology, 2008. **5**(2): p. 021006-021006-9.
80. Ashari, A. and H.V. Tafreshi, *General capillary pressure and relative permeability expressions for through-plane fluid transport in thin fibrous sheets.* Colloids and Surfaces A: Physicochemical and Engineering Aspects, 2009. **346**(1): p. 114-122.
81. Bucher, T., et al., *Modeling resistance of nanofibrous superhydrophobic coatings to hydrostatic pressures: The role of microstructure.* Physics of Fluids (1994-present), 2012. **24**(2): p. 022109.
82. http://www.wolfram.com/.
83. Beyhaghi, S., et al., *Wicking and evaporation of liquids in porous wicks: a simple analytical approach to optimization of wick design.* AIChE Journal, 2014. **60**(5): p. 1930-1940.
84. F. Zarandi, M.A. and K.M. Pillai, *Spontaneous imbibition of liquid in glass fiber wicks, Part II: Validation of a diffuse-front model.* AIChE Journal, 2018. **64**(1): p. 306-315.
85. Palmer, W., *28—THE ADVANCE OF A LIQUID FRONT ALONG A GLASS YARN.* Journal of the Textile Institute Transactions, 1953. **44**(8-9): p. T391-T400.
86. Hu, R., et al., *Wettability effects on supercritical CO2–brine immiscible displacement during drainage: Pore-scale observation and 3D simulation.* International Journal of Greenhouse Gas Control, 2017. **60**: p. 129-139.
87. Zhang, C., et al., *Influence of viscous and capillary forces on immiscible fluid displacement: Pore-scale experimental study in a water-wet micromodel demonstrating viscous and capillary fingering.* Energy & Fuels, 2011. **25**(8): p. 3493-3505.
88. Bakhshian, S., S.A. Hosseini, and N. Shokri, *Pore-scale characteristics of multiphase flow in heterogeneous porous media using the lattice Boltzmann method.* Scientific reports, 2019. **9**(1): p. 3377.
89. Ashraf, S. and J. Phirani, *Capillary displacement of viscous liquids in a multi-layered porous medium.* Soft matter, 2019. **15**(9): p. 2057-2070.
90. Reyssat, M., et al., *Imbibition in layered systems of packed beads.* EPL (Europhysics Letters), 2009. **86**(5): p. 56002.
91. Bico, J. and D. Quéré, *Precursors of impregnation.* EPL (Europhysics Letters), 2003. **61**(3): p. 348.
92. Mason, G. and N.R. Morrow, *Developments in spontaneous imbibition and possibilities for future work.* Journal of Petroleum Science and Engineering, 2013. **110**: p. 268-293.

93. Morrow, N.R. and G. Mason, *Recovery of oil by spontaneous imbibition.* Current Opinion in Colloid & Interface Science, 2001. **6**(4): p. 321-337.
94. Alava, M., M. Dubé, and M. Rost, *Imbibition in disordered media.* Advances in Physics, 2004. **53**(2): p. 83-175.
95. Ferer, M., et al., *Fractal nature of viscous fingering in two-dimensional pore level models.* AIChE Journal, 1995. **41**(4): p. 749-763.
96. Stenmark, E., *On multiphase flow models in ANSYS CFD software.* Chalmers Universiy of Technology, Sweden, 2013.
97. Parker, B. and D. Youngs, *Two and three dimensional Eulerian simulation of fluid flow with material interfaces*. 1992: Atomic Weapons Establishment.
98. Shyy, W., *Elements of pressure-based computational algorithms for complex fluid flow and heat transfer*, in *Advances in heat transfer*. 1994, Elsevier. p. 191-275.
99. Floryan, J. and H. Rasmussen, *Numerical methods for viscous flows with moving boundaries.* 1989.
100. DeBar, R., *Fundamentals of the KRAKEN code.* Technical Report UCIR-760, 1974.
101. Nichols, B. and C. Hirt. *Methods for calculating multidimensional, transient free surface flows past bodies*. in *Proc., 1st Int. Conf. Ship Hydrodynamics*. 1975. Naval Ship Research and Development Center, Bethesda, Md.
102. Noh, W.F. and P. Woodward. *SLIC (simple line interface calculation)*. in *Proceedings of the fifth international conference on numerical methods in fluid dynamics June 28–July 2, 1976 Twente University, Enschede*. 1976. Springer.
103. Rider, W.J. and D.B. Kothe, *Reconstructing Volume Tracking.* Journal of Computational Physics, 1998. **141**(2): p. 112-152.
104. Norman, M.L. and K.-H.A. Winkler, *2-D Eulerian hydrodynamics with fluid interfaces, self-gravity and rotation*, in *Astrophysical Radiation Hydrodynamics*. 1986, Springer. p. 187-221.
105. Centrella, J.M., J.M. Leblanc, and R.L. Bowers. *Numerical astrophysics*. in *Numerical Astrophysics*. 1985.
106. Hirt, C.W. and B.D. Nichols, *Volume of fluid (VOF) method for the dynamics of free boundaries.* Journal of computational physics, 1981. **39**(1): p. 201-225.
107. Ashgriz, N. and J. Poo, *FLAIR: Flux line-segment model for advection and interface reconstruction.* Journal of computational physics, 1991. **93**(2): p. 449-468.
108. Chorin, A.J., *Flame advection and propagation algorithms.* Journal of computational physics, 1980. **35**(1): p. 1-11.
109. Pilliod, J.E., *An analysis of piecewise linear interface reconstruction algorithms for volume-of-fluid methods*. 1992: U. of Calif., Davis.
110. Pilliod Jr, J.E., *Second-order accurate volume-of-fluid algorithms for tracking material interfaces.* 1997.
111. Youngs, D.L., *Time-dependent multi-material flow with large fluid distortion.* Numerical methods for fluid dynamics, 1982.
112. Piscaglia, F., et al., *A MultiPhase Dynamic-VoF solver to model primary jet atomization and cavitation inside high-pressure fuel injectors in OpenFOAM.* Acta Astronautica, 2019. **158**: p. 375-387.
113. Strotos, G., et al., *Predicting the evaporation rate of stationary droplets with the VOF methodology for a wide range of ambient temperature conditions.* International Journal of Thermal Sciences, 2016. **109**: p. 253-262.
114. Wilson, J.A., M. Haghshenas, and R. Kumar, *Phase-change mechanism for evaporation in porous media using volume of fluid: Implicit formulation of interfacial temperature.* International Communications in Heat and Mass Transfer, 2019. **103**: p. 90-99.
115. Dinsenmeyer, R., et al., *Volume of fluid approach of boiling flows in concentrated solar plants.* International Journal of Heat and Fluid Flow, 2017. **65**: p. 177-191.

116. Jeon, S.-S., S.-J. Kim, and G.-C. Park, *Numerical study of condensing bubble in subcooled boiling flow using volume of fluid model.* Chemical Engineering Science, 2011. **66**(23): p. 5899-5909.
117. Yuan, M.H., et al., *Numerical simulation of film boiling on a sphere with a volume of fluid interface tracking method.* International Journal of Heat and Mass Transfer, 2008. **51**(7): p. 1646-1657.
118. Larmaei, M.M. and T.-F. Mahdi, *Simulation of shallow water waves using VOF method.* Journal of Hydro-environment Research, 2010. **3**(4): p. 208-214.
119. Oggiano, L., et al., *Reproduction of steep long crested irregular waves with CFD using the VOF method.* Energy Procedia, 2017. **137**: p. 273-281.
120. Uddin, M.I. and M.M. Karim, *Application of Volume of Fluid (VOF) Method for Prediction of Wave Generated by Flow around Cambered Hydrofoil.* Procedia Engineering, 2017. **194**: p. 82-89.
121. Zhao, X.-z., C.-h. Hu, and Z.-c. Sun, *Numerical Simulation of Extreme Wave Generation Using VOF Method.* Journal of Hydrodynamics, Ser. B, 2010. **22**(4): p. 466-477.
122. Ketabdari, M.J., *Free Surface Flow Simulation Using VOF Method.* Numerical Simulation: From Brain Imaging to Turbulent Flows, 2016: p. 365.
123. https://www.ansys.com/products/fluids/multiphase-flows/multiphase-flows-models.
124. Pinder, G.F. and W.G. Gray, *Finite element simulation in surface and subsurface hydrology*. 2013: Elsevier.
125. Bear, J., *Dynamics of fluids in porous media.* American Else-vier, New York, 1972.
126. Whitaker, S., *The method of volume averaging*. Vol. 13. 1998: Springer Science & Business Media.

Curriculum Vitae

AMIN ZARANDI

aminfzarandi@gmail.com

PROFESSIONAL SUMMARY

- A dynamic mechanical engineer in modeling and analyses of **Thermal Analysis,** Computational Fluid Dynamics **(CFD),** and Finite Element Analysis **(FEA)** resulting in over 14 publication and $300,000 in lab grant funding
- Learned to expert proficiency several **Thermal,** CFD, and FEA software's such as **ANSYS** (FLUENT-CFX-Mechanical), **COMSOL**, and OpenFoam to contribute towards requirements of 4 funded and 6 independent projects resulting in 12 International Journal and Conference papers
- Creative and self-motivated individual with easy-integration in a multicultural environment with the unique combination of detail-oriented mindset, multi-task handling, and exceptional problem-solving skills and proven ability to meet tight deadlines by working in a fast-paced work environment

KEY SKILLS

- **Thermal** analysis, design, and simulation of electrical systems
- Computational Fluid Dynamics (**CFD**) and Finite Element Analysis (**FEA**)
- CFD and FEA software package, **ANSYS, COMSOL**, OpenFoam
- Experiments design and lab testing
- 2D/3D SolidWorks, AutoCAD, CATIA and Creo
- Code development, C++, Python, MATLAB
- Geometric dimensioning and tolerancing (GD&T)
- Designing and running experiments for **thermal and mechanical properties** characterization
- Analytical and numerical validating with experimental measurements and experiments
- Project management

PROFESSIONAL EXPERIENCE

Vibtech Consultants, Milwaukee WI
Non-Destructive Testing Intern, 2017-2019

- Performed vibration and Electro Magnetic Interference tests for research imaging devices (MRI, CT) for 50 projects
- Validated the MRI and CT images for **CFD simulations** in term of noise and accuracy
- Analyzed the data and providing solutions to make sites in compliance with sensitive medical equipment per siting requirements

University of Wisconsin-Milwaukee
Research Assistant, 2014-2019

- Developed theoretical, experimental, and numerical **(CFD/FEA)** models for flow, transport and **thermal studies** resulted in 10 projects and 14 International Journal and Conference papers
- Single and **multiphase flow** modeling of the wicking process in porous media using **ANSYS** (FLUENT-ICEM CFD) and **COMSOL** resulted in 9 International Journal and Conference papers and 300K in lab funded projects
- Designed and modeled **thermal (cooling) system** and **thermal-structural analysis** for **high power transformers** and **circuit boards** for sensitive applications
- **Designed and performed experimental tests** for model validation and calibration
- Ran virtual structure analysis system and drop test to predict different package structure performance and developed testing and experimentation for validation of results with a rapid prototype
- Created 3D images for numerical simulations utilizing Micro-CT and MRI
- Experimental and numerical simulation **data analysis**
- Co-advised and trained 3+ MSc/PhD students through their research duties in **CFD and FEA analysis**

University of Wisconsin-Milwaukee
Instructor/ Teaching Assistant, 2015-2019

- Taught **Computational Fluid Dynamics (CFD)**, **Finite Element** Simulation, Engineering Thermodynamics, Introduction to Fluid Mechanics and **Heat Transfer** for 6 semesters
- Provided front-line troubleshooting software and hardware in the **CFD** and **Heat Transfer** lab
- Defined CFD project assignments and provided examples for running different simulations

JN Consulting Engineers, Tehran, Iran
Water and Wastewater Expert, 2011-2013

- Designed pump station and water transmission pipelines for two industrial parks projects worth $2M
- Ran **CFD** models of water distribution systems networks in WaterCAD 4.5 and WaterHammer
- Reviewed and approved project AutoCAD drawings and made final changes as necessary
- Performed hydraulic CFD modeling of reservoirs resulted in two projects worth $1M
- Responsible for selecting and sizing of components along with generating schematics

IK Powertrain Co., Tehran, Iran
Mechanical Engineering Intern, 2012-2013

- Modeled ignition process by direct numerical **CFD simulating** of the spark using AVL-Fire resulted in 3 publications and development of new ignition system for Gasoline-CNG mixture
- Developed CAD model of piston+cylinder in Solidworks and created Hex-Mesh using ICEM-CFD for combustion simulation
- Selected Boundary Conditions based on the type of CFD simulation, simulated using AVL-Fire and experimental validation in collaboration with a team of 5 Scientist
- Designed and modeled **thermal system** for the new ignition system
- Conducted CFD analysis examples for the stages of combustion in an engine

COMPUTER SKILLS

- Design and simulation: **ANSYS (FLUENT, CFX, ICEM CFD, Mechanical), COMSOL**, AVL-Fire, OpenFoam, HyperMesh, SolidWorks, AUTOCAD
- Programming Language: Python, C++, MATLAB
- Other software packages: Paraview, Wolfram Mathematica, Tecplot, MS-Office

EDUCATION

- University of Wisconsin-Milwaukee, Milwaukee, WI, 2014 - 2019
  Ph.D., Mechanical Engineering; 4 GPA
  Thesis: Evaluation of Experimental, Numerical and Theoretical Heat Transfer and Wicking Models in Porous Media

- Iran University of Science and Technology, Tehran, Iran, 2010 - 2013
  M.Sc. Automotive Engineering, 3.6 GPA
  Thesis: Numerical Simulation of Spark Plug and Ignition Process in Spark Ignition Engines

- University of Kerman, Kerman, Iran, 2005 - 2009
  B.Sc., Mechanical Engineering, 3.3 GPA
  Thesis: Solar Energy and Solar Power Plants

PUBLICATIONS

Journal Papers:

- M. Amin F Zarandi, Krishna M Pillai, Salvador Arroyo, "Longitudinal and Transverse Flows in Fiber Tows: Evaluation of Theoretical Permeability Models through Numerical Predictions and Experimental Measurements", Composites Part A, 2018
- M. Amin F. Zarandi, Krishna M Pillai, Bamdad Barari, "Permeability of Flow Along and Across Fiber Bundles: Testing of Permeability Models through Tow-Scale Experiments and Simulations", American Institute of Chemical Engineers Journal (AIChE), 2018
- M. Amin F. Zarandi, Krishna M Pillai, "Spontaneous Imbibition of Liquid in Glass Fiber Wicks, Part II: Validation of a Diffuse-front Model", American Institute of Chemical Engineers Journal (AIChE), 2017
- M. Amin F. Zarandi, Krishna M Pillai, "Spontaneous Imbibition of Liquids in Glass-Fiber Wicks, Part I: Usefulness of a Sharp-Front Approach", American Institute of Chemical Engineers Journal (AIChE), 2017
- S. Paul, S. Roy, P., Amin Zarandi, Perdyomna Ghosh, K.M. Pillai, "A novel method for permeability estimation from micro tomographic images", Journal of Transport in Porous Media, 2018
- Arundhati Pillai, M. Amin F. Zarandi, Faten B. Hussein, Krishna M. Pillai, Nidal H. Abu-Zahra," Towards developing a low-cost gravity-driven arsenic filtration system using iron oxide nanoparticle-loaded PU foam", Under review, Water Quality Research Journal, March 2018

Conference Papers:

- Amin Zarandi, Krishna M Pillai," Spontaneous Liquid Imbibition in Industrial Wicks: Comparing the Effectiveness of Sharp- and Diffuse-Front Models", 10th International Conference on Porous Media (Interpore), New Orleans, 2018
- Amin Zarandi, Salvador Arroyo, Krishna M Pillai, "Permeability of Flow Along and Across Fiber Bundles: Testing of Permeability Models Through Tow-Scale Experiments and Simulations", The 14th International Conference on Flow Processing in Composite Materials (FPCM), Lulea, Sweden, 2018
- M. Amin F. Zarandi, Krishna M Pillai, "Estimating Permeability of Polyurethane (PU) Foams using 3D Micro-CT Images", 8th International Conference on Porous Media Cincinnati, Ohio, 2016
- M. Amin F. Zarandi, Krishna M Pillai, Adam Kimmel, "Darcy's Law-Based Model for Predicting Wicking of Liquids in Glass-Fiber Wicks", 6th International Conference on Porous Media (InterPore 2014), Milwaukee, Wisconsin, 2014
- M. Amin F. Zarandi, M. Baloo, "Numerical Investigation of Parameters of Ignition System Effects on Performance and Emissions of Gasoline-Fueled SI Engine", International Conference on Mechanical, Civil and Material Engineering (ICMCME), Bangkok, Thailand, 2014
- M. A. Faghihi Z. "Investigation of the Effect of Spark Plug Gap on Power Performance and Combustion Characteristics in a Gasoline Fueled SI Engine", International Conference on Automotive and Vehicle Technologies (AVTECH13), Istanbul, Turkey, 2013
- M. Amin F. Zarandi, Javad Marzbanrad, "HCCI Control by Variable Valve Actuation (VVA) and Fast Thermal Management (FTM)", 20th Annual International Conference on Mechanical Engineering (ISME2010), Shiraz University, Shiraz, Iran, 2012

ACADEMIC PROJECTS

- Analyzed, simulated thermal system for high power transformers
- Modeled wicking and combustion in a wick in order to optimize lamp design in tiki torch
- Used wicking models to design a high through-put, fully-wet wick for a piezo-electric incense dispenser
- Analyzed, simulated and designed thermal system for ignition system designated for gasoline-CNG fuel mixture
- Simulated curing thermal process in bioprinting tissue in 3D bioprinters

AWARDS & HONORS

- Chancellor's Award, University of Wisconsin-Milwaukee (2015, 2016, 2018)
- Graduate Student Travel award, University of Wisconsin-Milwaukee (2016, 2018)
- Diversity and Inclusion Award Nominee, 2017, University of Wisconsin- Milwaukee
- Exemplary Leadership Award Nominee, 2017, University of Wisconsin- Milwaukee
- Holding the highest teaching evaluation score in Mechanical Engineering Department, UW-Milwaukee since Spring 2015